UNIVERSITY OF
Southampton
School of Engineering Sciences

Astronautics Research Group

# An Empirical Model of Long-Term Thermospheric Density Change

by

**Arrun Saunders**

**Thesis for the degree of Doctor of Philosophy**

**June 2012**

UNIVERSITY OF SOUTHAMPTON

## ABSTRACT

SCHOOL OF ENGINEERING SCIENCES

ASTRONAUTICS RESEARCH GROUP

Doctor of Philosophy

# AN EMPIRICAL MODEL OF LONG-TERM THERMOSPHERIC DENSITY CHANGE

by Arrun Saunders

Predicting the positions of satellites in Low Earth Orbit (LEO) requires a comprehensive understanding of the dynamic nature of the atmosphere. For objects in LEO the most significant orbit perturbation is atmospheric drag, which is a function of the local atmospheric density from a layer in the atmosphere called the thermosphere. For long-term predictions of satellite orbits and ephemerides, any density trend in the thermosphere is a necessary consideration, not only for satellite operators, but also for studies of the future LEO environment in terms of space debris. Numerous studies of long-term thermospheric density change have been performed. Predictions by Roble & Ramesh (2002), along with evidence by Keating (2000), Emmert *et al.* (2004), Marcos *et al.* (2005), Qian *et al.* (2006) and Emmert *et al.* (2008), strongly suggest the existence of such a phenomenon. Therefore, the objective of the research presented in this thesis is to provide a novel method to evaluate quantitatively thermospheric density change.

Satellite drag data is an effective medium through which one can investigate local thermospheric density and changes thereof. There are many ways of determining atmospheric density, but inferring thermospheric density from satellite drag data is a relatively cost-effective way of gathering in-situ measurements. To do this, knowledge about a satellite's physical properties that are intrinsic to atmospheric drag is required. A study by Saunders *et al.* (2009) highlighted problems with estimating a satellite's physical properties directly from data given explicitly by Two-Line Element (TLE) sets. This prompted an investigation into ways to estimate ballistic coefficients: a required satellite parameter associated with drag coefficient and area-to-mass ratio. A novel way of estimating satellite ballistic coefficients was derived and is presented in this thesis. Additionally, novel consideration of atmospheric chemical composition was applied on long-term drag coefficient variability. Using a quantitative estimate of a ballistic coefficient one can propagate numerically a satellite's orbit and predict the effects of atmospheric drag. Given an initial satellite orbit from TLE data, one approach is to use an orbital propagator to predict the satellite's state at some time ahead and then to compare that state with TLE data at the same epoch. The difference between the semi-major axes of the initial orbit and that after the orbit propagation is then integrated and can be used to estimate the global average density. The method employed in this study utilises this process. To achieve this, a specially developed, computer-based, numerical orbital propagator was written in the programming language C/C++. The underlying theories and implementation tests for this propagator are presented in this thesis.

# Contents

# List of Figures

# List of Tables

## Published Works

◇ **Lewis. H. G.**, Newland R. J., Swinerd G. G. and Saunders A., (2008) A New Analysis of Debris Mitigation Using Networks, paper presented at the 59th International Astronautical Congress, Glasgow, Scotland, September/October 2008.

◇ **Saunders, A.**, Lewis H. G. and Swinerd G. G., (2009), A New Tool for Satellite Re-entry Predictions, paper presented at the Fifth European Conference on Space Debris, Darmstadt, Germany, March-April 2009.

◇ **Lewis. H. G.**, Swinerd G. G., Newland R. J. and Saunders A., (2009), Active removal study for on-orbit debris using DAMAGE, paper presented at the Fifth European Conference on Space Debris, Darmstadt, Germany, March-April 2009.

◇ **Lewis. H. G.**, Swinerd G. G., Newland R. J. and Saunders A., (2009), The Fast Debris Evolution Model, *Advances in Space Research*, 44, 5, September 2009.

◇ **Saunders, A.**, Swinerd G. G. and Lewis H. G., (2009), Preliminary Results to Support Evidence of Thermospheric Contraction, paper presented at the 10th Advanced Maui Optical and Space Surveillance Technologies Conference, Maui, Hawaii, September 2009.

◇ **Saunders, A.**, Swinerd G. G. and Lewis H. G., (2010), Deriving Accurate Satellite Ballistic Coefficients from Two-Line Element Data, *J. Spacecraft & Rockets* 2010-12-A32023.

◇ **Lewis H. G.**, Saunders, A. Swinerd G. G. and Newland R. J., (2010), Effect Of Thermospheric Contraction On Remediation Of The Near-Earth Space Debris Environment, *J. Geophys. Res.,* doi:10.1029/2011JA016482.

◇ **Saunders, A.**, Lewis H. G. and Swinerd G. G., (2010), Further Evidence of Long-Term Thermospheric Density Change Using a New Method of Satellite Ballistic Coefficient Estimation, *J. Geophys. Res.,* doi:10.1029/2010JA016358.

## Oral Presentations

◇ **Preliminary Results to Support Evidence of Thermospheric Contraction**, 10th Advanced Maui Optical and Space Surveillance Technologies Conference, Maui, Hawaii, September 2009.

◇ **Further Evidence of Long-Term Thermospheric Density Change Using a New Method of Satellite Ballistic Coefficient Estimation**, 6th Workshop on Long-Term Changes and Trends in the Atmosphere, Colorado, U.S.A, June 2010.

◇ **Effect Of Thermospheric Contraction On Remediation Of The Near-Earth Space Debris Environment**, 6th Workshop on Long-Term Changes and Trends in the Atmosphere, Colorado, U.S.A, June 2010.

## Poster Presentations

◇ **A New Tool for Satellite Re-entry Predictions**, 5th European Conference on Space Debris, Darmstadt, Germany, March-April 2009.

## Conferences & Workshops Attended

◇ **37th COSPAR Scientific Assembly**, Montreal, Canada, July 2008.

◇ **5th European Conference of Space Debris**, Darmstadt, Germany, March-April 2009.

◇ **10th AMOS Technologies Conference**, Maui, Hawaii, September 2009.

◇ **6th Workshop on Long-Term Changes and Trends in the Atmosphere**, Colorado, U.S.A, June 2010.

# DECLARATION OF AUTHORSHIP

I, Arrun Saunders,

declare that the thesis entitled:

**An Empirical Model of Long-Term Thermospheric Density Change**

and the work presented in the thesis are both my own, and have been generated by me as the result of my own original research. I confirm that:

- this work was done wholly or mainly while in candidature for a research degree at this University;
- where any part of this thesis has previously been submitted for a degree or any other qualification at this University or any other institution, this has been clearly stated;
- where I have consulted the published work of others, this is always clearly attributed;
- where I have quoted from the work of others, the source is always given. With the exception of such quotations, this thesis is entirely my own work;
- I have acknowledged all main sources of help;
- where the thesis is based on work done by myself jointly with others, I have made clear exactly what was done by others and what I have contributed myself;
- parts of this work have been published as:

1. Saunders, A., Lewis H. G. and Swinerd G. G., (2009), A New Tool for Satellite Re-entry Predictions, paper presented at the fifth European Conference of Space Debris, Darmstadt, Germany, March-April 2009;
2. Saunders, A., Swinerd G. G. and Lewis H. G., (2009), Preliminary Results to Support Evidence of Thermospheric Contraction, paper presented at the 10th Advanced Maui Optical and Space Surveillance Technologies Conference, Maui, Hawaii, September 2009;
3. Saunders, A., Swinerd G. G. and Lewis H. G., (2010), Deriving Accurate Satellite Ballistic Coefficients from Two-Line Element Data, *J. Spacecraft & Rockets* 2010-12-A32023;
4. Saunders, A., Lewis H. G. and Swinerd G. G., (2010), Further Evidence of Long-Term Thermospheric Density Change Using a New Method of Satellite Ballistic Coefficient Estimation, *J. Geophys. Res.,* doi:10.1029/2010JA016358.

Signed: ..........................................................................................................

Date: ..............................................................................................................

# Acknowledgements

There are so many people that have contributed to making my time researching such a wonderful period. There are some people that deserve special recognition.

Hugh and Graham, I could not have hoped for better supervisors. You always showed unfaltering encouragement, support and friendship throughout my time researching. As a result, these years have been some of the best of my life, thank you.

My parents, Tony, Kim, and my brother Carl, thank you for all your love, support and interest over the years to get me where I am now; I couldn't have done it without you.

Julie, thank you for your love, kindness, encouragement and keeping me sane in the last stages of writing up. You have been a saint!

Sam, no-one else took more of an interest in my re-entry predictions and $F_{10.7}$ solar flux than you did. You have been a truly wonderful friend throughout, thank you.

Roger, Pete and the late Simon, you provided my inspiration for mathematics and engineering and to constantly better myself; Simon I wish you could be here to read my thesis.

Finally, I would like extend my sincere thanks to my two Viva examiners, John and Adrian, for their careful readings and comments of my thesis. In particular, I would like to thank John for flying from the U.S. just for my Viva examination, in addition to his continued support during the correction process.

# Nomenclature

| **Symbol** | **Definition** |
|---|---|
| $a$ | Semi-major axis |
| $a_{ij}$ | Runge-Kutta-Fehlberg-Horn coefficients |
| $\mathrm{a}_\mathrm{p}$ | Geomagnetic 3-hourly index (nT) |
| $A$ | Projected surface area |
| $\mathrm{A}_\mathrm{p}$ | Geomagnetic daily index |
| $AU$ | Astronomical Unit = 1.49597870691$\times 10^{8}$ km |
| $b_i^\star()$ | Continuous step gradient function |
| $B^*$ | TLE Satellite ballistic parameter |
| $\bar{C}$ | Cosine geopotential coefficient |
| $C_d$ | Drag coefficient |
| $C_r$ | Reflectivity coefficient |
| $e$ | Eccentricity |
| $\hat{\mathbf{e}}$ | Luni-solar unit position vector |
| $E_r$ | Earth's equatorial radius = 6,378.1363 km |
| $f$ | Lagrange orbital force |
| $F$ | Wind factor |
| $\mathrm{F}_{10.7}$ | Solar Flux at 10.7 cm wavelength |
| $g()$ | Gaussian function |
| $G$ | Universal Gravitational constant |
| $G()$ | Cumulative Gaussian function |
| $h$ | Integration step size |
| $h_{\delta/\zeta}$ | Associated altitude, ballistic coefficient / density. |
| $i$ | Inclination |
| $\mathbf{k}$ | Runge-Kutta-Fehlberg-Horn gradient coefficients |
| $Kn$ | Knudsen Number |
| $\mathrm{K}_\mathrm{p}$ | Geomagnetic 3-hourly index (logarithmic) |
| $l$ | Characteristic length |
| $m$ | Satellite mass |
| $M_{\oplus,\otimes,\odot}$ | Mass of celestial body |
| $M$ | Mean anomaly |
| $n_M$ | Mean mean motion |
| $p$ | Semi-latus rectum = $a(1-e^2)$ |
| $P$ | Solar radiation pressure = 4.56$\times 10^{-6}$ N/m$^{2}$ |
| $\bar{P}$ | Legendre polynomial |
| $P_{\text{solar}}$ | Solar Activity Factor |
| $\mathbf{r}$ | Geocentric position vector |
| $\ddot{\mathbf{r}}$ | Geocentric acceleration vector |

| **Symbol** | **Definition** |
|---|---|
| rhs$()$ | Force model function |
| $R$ | Radius |
| $\mathbf{s}$ | Perturbing body's position vector |
| $\bar{S}$ | Sine geopotential coefficient |
| $t$ | Time |
| $\bar{t}_{cpu}$ | Computational run-time |
| $T$ | Temperature |
| $U$ | Geopotential |
| $\mathbf{v}$ | Geocentric velocity vector |
| $\mathbf{V}$ | Model wind velocity vector |
| $x$ | Cartesian coordinate |
| $y$ | Cartesian coordinate |
| $\mathbf{y}(t)$ | State vector at time '$t$' |
| $z$ | Cartesian coordinate |

| **Greek Symbol** | **Definition** |
|---|---|
| $\alpha$ | Accommodation coefficient |
| $\gamma$ | Equinox deviation |
| $\delta$ | Ballistic coefficient = $\frac{C_d A}{m}$ |
| $\delta_{0m}$ | Legendre normalising coefficient |
| $\Delta$ | Difference, or small step |
| $\zeta$ | Thermospheric density comparison parameter |
| $\eta$ | Gaussian mean |
| $\theta$ | Obliquity of the ecliptic = 23.43929111° |
| $\lambda$ | Geocentric longitude |
| $\lambda^{\star}$ | Mean free path |
| $\mu$ | Celestial body gravitational constant = $GM$ |
| $\nu$ | Shadow function |
| $\rho$ | Density |
| $\sigma$ | Standard deviation |
| $\tau$ | Time step fitting parameter |
| $\phi$ | Geocentric latitude |
| $\Phi$ | Increment function |
| $\omega$ | Argument of perigee |
| $\omega_f$ | Fourier spectral analysis angular frequency |
| $\omega_r$ | Angular rotation rate |
| $\omega_\gamma$ | Vernal equinox precession rate |
| $\Omega$ | Longitude of ascending node |

| Abbreviation | Definition |
|---|---|
| AETHER | An Earth orbital propagator for Thermospheric analysis |
| AFSPC | United States Air Force Space Command |
| AGI | Analytical Graphics, Inc. |
| AMOS | Advanced Maui Optical and Space Surveillance |
| CIRA | COSPAR International Reference Atmosphere |
| COSPAR | Committee on Space Research |
| Dst | Disturbance Storm Time geomagnetic index (nT) |
| EUV | Extreme Ultraviolet |
| Envisat | Environmental Satellite |
| ESA | European Space Agency |
| HSA | High Solar Activity |
| HWM | Horizontal Wind Model |
| J2000.0 | Reference system of epoch Julian Date 2451545.0 |
| JB | Jacchia-Bowman |
| JGM | Joint Gravity Model |
| LEO | Low Earth Orbit |
| LSA | Low Solar Activity |
| MET | Marshall Engineering Thermosphere |
| MSIS | Mass Spectrometry and Incoherent Scatter |
| MLT | Mesosphere and Lower Thermosphere |
| NASA | National Aeronautics and Space Administration |
| NRLMSISE | Naval Research Laboratory MSIS Extended |
| NOAA | National Oceanic and Atmospheric Administration |
| RK4 | Runge-Kutta 4th Order Method |
| $RK4^1$ | RK4: 1 second integration step size |
| RKFH | Runge-Kutta-Fehlberg-Horn 7th Order Method |
| $RKFH^2$ | RKFH: 2 second integration step size |
| SAF | Solar Activity Factor |
| SEM | Solar EUV Monitor |
| SGP4 | Simplified General Perturbations 4 |
| SME | Sun, Moon and Earth |
| SMLTM | Spectral Mesosphere/Lower Thermosphere Model |
| SRP | Solar Radiation Pressure |
| STK | Satellite Tool Kit |
| TEME | True Equator Mean Equinox |
| TLE | Two-Line Element |
| USSSN | U.S. Space Surveillance Network |
| UV | Ultravoilet |

# 1 Introduction

Long-term atmospheric evolution and climate change are active areas of study. Though evidence shows that significant changes in the atmosphere are occurring, causes have yet to be globally accepted. Is the atmosphere secularly changing through natural processes alone? Or have the changes been incurred by anthropogenic activities? The rate at which average global temperatures in the troposphere have increased suggests the latter, which is further supported by a statistical correlation with the *anthropogenic* increase in greenhouse gas concentrations since the start of the industrial revolution. As greenhouse gasses propagate up through the atmosphere their interactions with naturally occurring gas species cause changes in atmospheric density structure. To try and answer the questions posed above, theoretical hypotheses have been made about the changes that these interactions may cause. Now, practical tests of these hypotheses are becoming abundant, which provide valuable contributions to our understanding of our planet. This thesis describes a method of detecting long-term atmospheric density changes and provides results to compare with previous studies and hypotheses.

## 1.1 The Atmosphere: A Brief Description

Planetary atmospheres are generally complex systems consisting of numerous gas species that cause variations in the atmospheric structures of temperature and density. Earth's atmosphere is divided into five layers classified by their temperature regimes. The upper boundary of each layer is known as a 'pause' (eg. tropopause, stratopause, mesopause and thermopause), whereby the vertical temperature gradient changes sign, i.e. stops decreasing and starts increasing and *vice versa*. Each regime encompasses different energetic processes that gives rise to a vertical temperature profile. Figure 1 shows the variation of temperature and density with altitude during high and low solar activity, as predicted by Naval Research Laboratory's empirical atmospheric model using Mass Spectrometry and Incoherent Scatter Radar from the ground up to the exosphere, released in the year 2000 (NRLMSISE-00). The general principles for the atmospheric energetics will be described in relation to specific heating processes.

It comes as no surprise that the primary energy input into the atmosphere is the Sun. For the majority of the atmosphere, the manner in which the solar energy is absorbed by the locally present atmospheric species governs the resulting temperature. From the ground up, the first of layer is called the troposphere, in which the cause of atmospheric temperature is slightly different. Due to the proximity of this layer with the Earth's surface, the temperature is largely due to the Earth's black-body radiation yielding a temperature of approximately 256 K. In addition to this energy input, local air temperature here is determined via absorption of a mixture of direct solar radiation and reflected radiation from the ground and surrounding gasses. The 'Greenhouse effect' encompasses these absorption processes that cause further warming in the troposphere due to the gasses of carbon dioxide, methane and, mostly, water vapour. These atmospheric species can efficiently trap infrared radiation, leading to a net warming effect. Owing to the radiation trapping ability and the relative density, the troposphere is termed

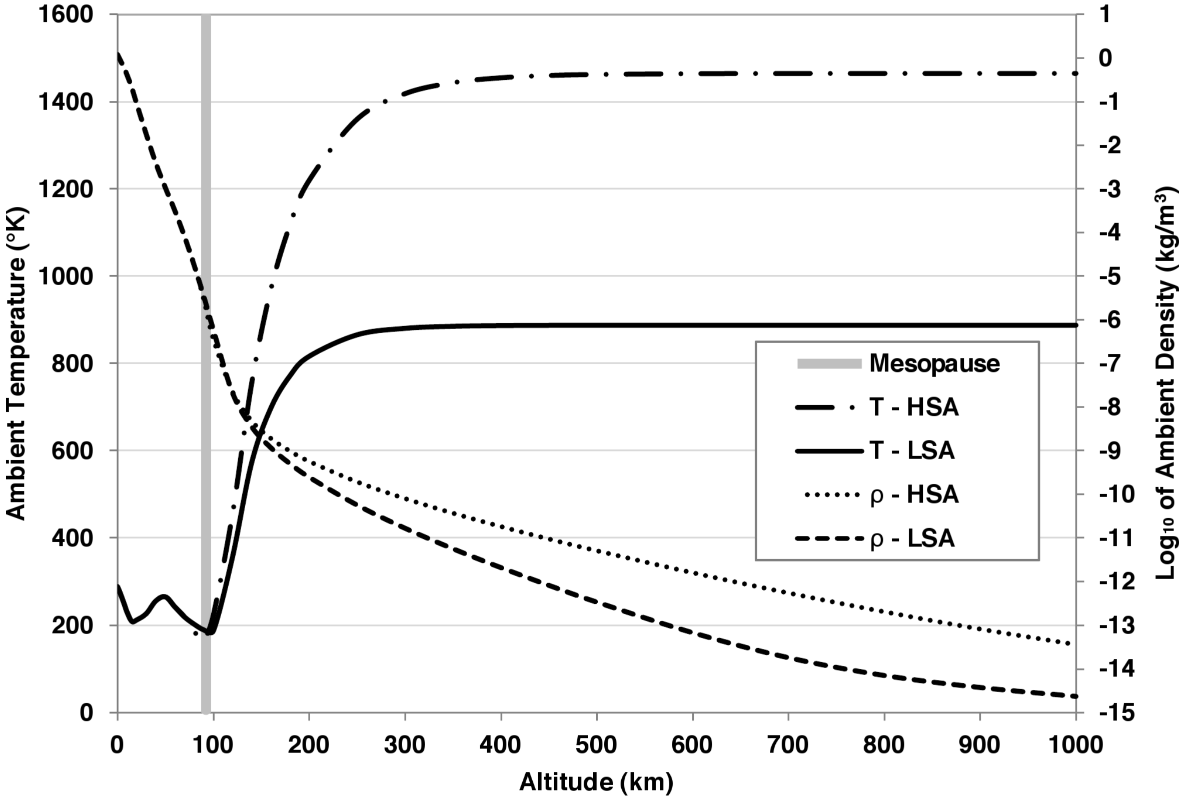

Figure 1: *Average atmospheric temperature ($T$) and density ($\rho$) according to the NRLMSISE-00 empirical atmospheric model for high solar activity (HSA) and low solar activity (LSA).*

'optically thick', meaning radiation is generally absorbed, rather than emitted. As one ventures into higher altitudes, the atmosphere becomes increasingly optically thin with more radiative emission than absorption. For this reason, in the troposphere, there exists a lapse rate in temperature with increasing altitude until the tropopause is reached at 15 km with an ambient temperature of approximately 215 K.

Above the tropopause is the stratosphere. Here, the temperature is primarily governed by chemical processes involving ozone. Ozone is formed photochemically from molecular oxygen. The ozone layer is manifested due to the unique conditions that exist at this altitude: any lower then there is insufficient short-wave radiation to energise the photochemical process; and any higher leads to insufficient amounts of molecular oxygen. The radiative lapse rate from the troposphere continues for only a short way into the stratosphere until solar UV and visible radiation is absorbed by the ozone layer. The absorption of solar radiation by ozone releases the energy into the surrounding atmosphere as heat, resulting in a negative lapse rate that increases temperature to approximately 265 K at 50 km altitude, known as the stratopause.

Above 50 km, the mesospheric density is so low that collisions between gaseous species becomes highly infrequent. At mesospheric and lower thermospheric altitudes, the heating processes take on different modes. The primary mechanisms are; the absorption of solar UV and EUV radiation; auroral heating and particle precipitation down the Earth's magnetic field lines; the release of chemical energy and processes occurring lower in the atmosphere that are transferred upwards molecular and eddy heat conduction; and radiative cooling from carbon dioxide, oxides of nitrogen, ozone and atomic oxygen infrared emissions [97]. For high-energy solar radiation, i.e. those with wavelengths less than 200 nm, all incident flux is absorbed above altitudes of 80 km and re-distributed in radiated air-glow, stored chemical energy and direct heating of the neutral atmosphere. As a result, the thermosphere exhibits the most significant thermal variation in the atmospheric temperature profile, hence its name.

Below 150 km, the absorption of solar UV by molecular oxygen is the dominant heat source, whereby the molecular bonds are broken to produce atomic oxygen, which is transported to the lower thermosphere around 90 km. This will later be shown to play a key role in the net energy loss mechanism involved in long-term thermospheric cooling.

The main radiative cooling processes originate from infrared cooling from a number of gas species spread over a range of altitudes. In the upper thermosphere, the radiation from atomic oxygen is the dominant radiative heat loss process. In the middle thermosphere, it is the infrared radiation originating from oxides of nitrogen. In the lower thermosphere, infrared radiation from carbon dioxide is the dominant heat loss process. The largest uncertainty of radiative heat loss is the contribution from the interaction of carbon dioxide and atomic oxygen, which extends from the middle atmosphere into the lower thermosphere [97]. With carbon dioxide being a greenhouse gas, its effect can be linked to anthropogenic forcings.

As altitude increases, the ambient temperature in the thermosphere tends to an asymptotic value known as the exospheric temperature, which is one of several parameters commonly used to define the state of the thermosphere. Assuming fixed conditions at the base of the thermosphere, the temperature, composition, and mass density profiles can be derived from the exospheric temperature. The neutral gas heating in the thermosphere mainly occurs within the altitude range of 150-300 km. In the upper thermosphere, the same heating mechanisms as well as additional neutral heating caused by thermal conduction down the Earth's magnetic field lines, which heat the present ions and electrons. This heating, controlled by magnetospheric-ionospheric interactions, peaks between the altitude band of 150-300 km and may be responsible for the magnitude of the exospheric temperature. In addition to absorption of solar UV irradiance, the thermosphere is also heated by the dissipation of electrical current from the magnetosphere and by precipitation of energetic particles along magnetic field lines.

The thermopause is defined as the altitude at which the mean free path of the atmospheric particles is approximately equal to the vertical scale height of the atmosphere [93]. The plots of temperature in Figure 1 asymptote to the constant exospheric temperature at different altitudes, demonstrating how the altitude at which the thermopause resides varies depending on solar activity. The lowest layer through which satellites or objects orbiting the Earth travel is the thermosphere, unless they are returning to Earth. As detailed above, solar activity strongly affects the atmosphere, be it due to the rotation of the Earth relative to the Sun, or by the irradiance from the Sun over the 11-year solar cycle. When the atmosphere is in direct sunlight or when solar activity is high, the atmosphere swells in size. Conversely during local night time or low solar activity the atmosphere contracts. Therefore, when studying the thermosphere it is important to recognise the variation in altitude over which the thermosphere spans. Owing to this large variation in thermopause altitude, there is no discrete boundary whereby atmospheric drag perturbations significantly decrease. The mass density continues to decrease approximately exponentially with altitude, but at a lesser rate due to the dominance of atomic helium and hydrogen in atmospheric composition and their ballistic trajectories within this rarefied regime.

## 1.2 The Atmosphere and The Space Environment

As the space environment becomes increasingly populated with existing and newly-launched objects, mechanisms affecting satellite and space debris orbits are of great relevance to the process of orbit determination. One of the perturbing factors affecting an object in Low Earth Orbit (LEO) is aerodynamic drag caused by the object's movement through the Earth's atmosphere. As the drag encountered by satellites depends on the local mass density of the atmosphere, comprehensive knowledge of the behaviour of the atmosphere is necessary when predicting future orbital evolution. In particular, long-term secular trends in atmospheric density are very important when predicting lifetimes of objects in LEO.

Knowledge of atmospheric density trends has applications over a wide range of operational space-related disciplines. Considering the space debris environment, it is important to monitor and stabilise the population of the orbiting objects as the consequences of a collision can be catastrophic. Objects with very little mass can have enough kinetic energy to completely destroy a satellite or space station due to the velocities associated with orbiting the Earth. For example, in 2009, at the point of collision between the Kosmos 2251 and Iridium 33 satellites their relative velocity was approximately 11.7 km/s. Through the interaction between the atmosphere and the debris object, be it a defunct satellite or a fleck of paint, the acceleration due to drag reduces the orbit altitude of the object in a secular manner. If this process is allowed to continue the orbiting object will eventually vaporise in the increasingly dense atmosphere or in rare cases re-enter back to Earth. This process of degrading a satellite's orbit is the only sink mechanism for the space debris population. Evidence for the effectiveness of this sink mechanism can be seen during times of high solar activity, whereby the atmosphere swells and the removal rate of space debris objects increases. Conversely, the opposite effect happens during times of low solar activity when the atmosphere contracts. Lewis *et al.* [71] demonstrated this via the oscillatory behaviour in the effective number of orbiting objects in LEO over multiple solar cycles. A long-term, secular decline in thermospheric density would mimic the atmospheric response during the transition from high to low solar activity. As a result, the effectiveness of the atmosphere to act as a sink to the space debris population would be decreased.

Lewis *et al.* [69, 70] demonstrated the potentially damaging effect a long-term thermospheric density decline may have on the space debris population. Owing to the consequences that an over-populated space debris environment may pose, regulatory bodies have begun to implement guidelines regarding the generation of space debris. These guidelines recommend mitigation practices that reduce or eliminate unwanted orbiting objects in the LEO environment after their operational lifetimes. Methods for achieving the reduction in practice include: manoeuvring the satellite into an orbit that will decay, due to the effect of atmospheric drag, within 25 years; manoeuvring the satellite into a ‘graveyard’ orbit above LEO; or de-orbiting the satellite so that it burns up in the lower atmosphere or re-enters back to Earth. All solutions incur additional costs with no commercial benefit. Manoeuvring the satellite into a different orbit after its operational life time requires additional fuel and therefore cost, which is actively avoided when designing a satellite system. Augmenting the effect of atmospheric drag requires the natural sink provided by atmospheric density, the effectiveness of which would reduce with a long-term thermospheric density decline. Therefore, a larger device would be needed to augment the diminishing atmosphere in order to comply with the environmental guidelines. This again introduces additional complexity, mass and ultimately cost into the spacecraft system design.

Long-term thermospheric density trends can affect the design of spacecraft in the early design phase. Operational lifetime and orbit type are important parameters when designing a satellite system. For some orbits, perigee-raising manoeuvres are necessary to counteract the natural orbital degradation due to atmospheric drag. With the reduction of atmospheric drag caused by a decline in thermospheric density, perigee-raising manoeuvres would be less frequent, therefore using less propellant and requiring smaller propellant tanks. Not only would there be a saving in propellant costs, the overall mass of the spacecraft could be reduced, which would reduce the costs associated with the initial launch and orbit insertion. However, the benefits of a thermospheric density decline on a spacecraft’s design are likely to be outweighed by the incurred restrictions imposed by compliance with space debris guidelines, as described in the previous paragraph.

## 1.3 Measuring the Thermosphere

As technology has evolved, the number of satellites and other man-made Earth-orbiting objects has grown from one in 1957 to approximately 14,000 tracked objects larger than 10 cm in size at the time of writing this thesis. With such a presence in orbit, methods of measuring atmospheric density structure and composition in the thermosphere have become more abundant. One way to measure the mass density is by analysing the acceleration due to atmospheric drag on satellites in the Earth’s atmosphere. This acceleration, $\ddot{r}_{drag}$, is related to the local atmospheric density $\rho$ by

$$\ddot{r}_{drag} = -\frac{1}{2}\rho v^2 \frac{C_d A}{m}, \tag{1}$$

where $C_d$ is the satellite’s drag coefficient, $A$ is the satellite’s projected surface area, $m$ is the mass of the satellite and $v$ is the satellite’s velocity relative to the atmosphere.

The tracking data of numerous orbiting objects provides a wealthy resource with which to gain in-situ measurements of globally averaged thermospheric density. As such, the scientific community has greater scope to explore and understand the near-Earth environment. Investigations into thermospheric density evolution have relevance ranging from geophysical studies of the solar-terrestrial environment to the interactions that take place within the atmosphere between the different altitude regimes. Furthermore, deepening one’s understanding of the behaviour of the atmosphere can further other fields of research, such as orbit evolution and satellite propagation. In this study, in-situ thermospheric density measurements are primarily used to investigate long-term secular change. However, the method of measuring thermospheric density also provided a novel development in the field of astrodynamics [107].

One way to derive a long-term secular trend is by comparing data gathered from observations with data derived numerically. Numerically derived data can be produced by simulating satellite orbits using an computer program called an orbital propagator. Among other perturbations, which will be described in detail later, the effect of atmospheric drag is modelled using equation (1). The observational data used in this study were Two-Line Element (TLE) sets produced by the United States Air Force Space Command (AFSPC). TLE data provides the mean orbital parameters of an osculating orbit at a particular epoch, derived using observations from ground radar stations. This data, freely available via www.space-track.org [113], comprises more than 86,000,000 TLE sets for more than 35,000 orbiting and since decayed satellites. The database is updated on a daily basis.

An Earth orbital propagator for thermospheric analysis, named AETHER[1] and written in the programming language C++, was created to produce the numerically derived data. AETHER includes perturbations due to gravity anomalies of zonal and tesseral harmonics up to order and degree 20. In an ideal orbit around a non-rotating Earth, the forces due to the Earth's gravity would be conservative. However, as the Earth is spinning beneath an orbiting satellite, as well as external perturbing forces tugging at the satellite, the effects of gravitational harmonics become non-conservative and require careful calculation. In addition to this, AETHER also models the effects of atmospheric drag using the NRLMSISE-00 model to estimate ambient density. This force of atmospheric drag is a monotonic force in that it manifests as a continuously varying stream of resistance that is never repeated exactly, other than approximate periodic variations due to the atmosphere's natural behaviour. All other perturbations modelled by AETHER are non-conservative. These include the effects of gravity due to the Moon and Sun as well as perturbations due to solar radiation pressure. To give an indication of the significance of atmospheric drag in comparison with other perturbations experienced by a satellite in LEO, Figure 2 shows the order of magnitudes of the various perturbations modelled by AETHER. The values in Figure 2 agree with the values obtained by Doornbos [24] and Montenbruck & Gill [76].

## 1.4 Outline of Thesis

This Section describes the order in which the different topics are presented throughout this thesis. Chapter 2 provides a literature review of the current state of thermospheric density research. Chapter 3 follows on from the literature review and states the objectives of this research study. Chapter 4 describes the criteria used to select TLE sets and gives a list of physical parameters for each of the satellite's orbits used to obtain the density trend results.

Chapter 5 describes the methodology of all practices undertaken in this study. Section 5.1

---

[1] In Greek mythology, Aether is the personification of the 'upper sky', space and heaven. She is the air that the other Gods breathed.

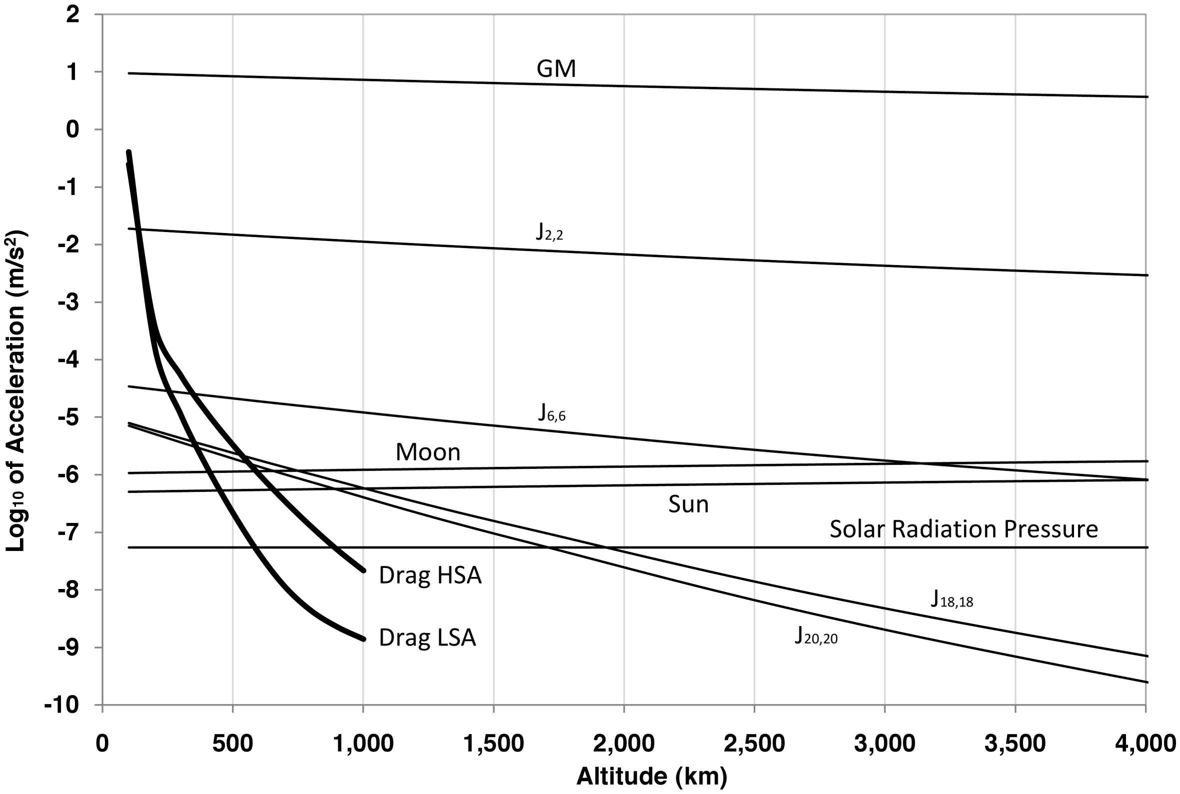

Figure 2: *The order of magnitudes of the various perturbations modelled in AETHER. Satellite properties include a drag coefficient,* $C_d$ *= 2.2, a coefficient of reflectivity,* $C_r$ *= 1.2 and an area to mass ratio of* $1 \times 10^{-8}$ *km*$^2$*/kg. The plots of Drag cease at 1,000 km due to the density data being derived from the NRLMSISE-00 density model, which by definition only extends up to the exobase.*

deals with how satellite orbits are propagated and describes in detail the creation of the numerical orbital propagator, AETHER. The underlying theories necessary to propagate a satellite orbit with high accuracy are presented. For each satellite orbit perturbation the application of the theory was then validated to demonstrate correct implementation. Section 5.2 describes the theory and iterative process used to determine empirically a satellite's ballistic coefficient, a necessary satellite characteristic when propagating an orbit in an atmosphere. Section 5.4 describes the process of using the orbit derived density data to infer a long-term thermospheric density and the methods used to analyse the data.

Chapter 6 presents initial studies that were conducted before obtaining final results. Both of the studies were published through conference proceedings and the final through a special section of the Journal of Geophysical Research: Space Physics that dealt with long-term changes in the atmosphere. In addition to testing the practices performed in this study, this process also highlighted improvements that could be made to gather the final results more efficiently and with higher quality.

Chapter 7 presents the final results. Then, Chapter 8 compares the results from this study with those from previous studies. An analysis of the errors in the final results is made. The validity of the results is discussed and their significance is placed into the context of the state-of-the-art.

Finally, in Chapter 9, conclusions are drawn concerning the degree to which the objectives of the project have been achieved, and the possible areas of further work that could be undertaken.

# 2 Literature Review

This Chapter summarises the current state of research in the domains of thermospheric density change and associated methods. First there is a description of the research surrounding long-term evolution of the thermosphere and the possible factors that may cause thermospheric density change. Next, the source and form of the TLE observational data used for this study is presented. The methods of their production and the ways in which it can be used are outlined. The estimation of a satellite's ballistic coefficient plays a significant role in using ephemeris data to study upper atmospheric density. As a result an analysis of the methods used in previous studies is presented. Then, continuing on from ballistic coefficient estimation, a description and discussion of the most recent methods used in previous studies to infer thermospheric density from observational data is presented, and how this is used to predict secular thermospheric density change.

## 2.1 The Thermosphere and Thermospheric Contraction

During the last 30 years there has been a lively debate on whether atmospheric changes caused by human activity will have significant long-term effects on the structure of the atmosphere and the general climate of the Earth. Brasseur & Hitchman [12] predicted a doubling of the carbon dioxide mixing ratios by the end of the $21^{st}$ century [12]. As a result, temperatures in the mesosphere and lower thermosphere (MLT) are expected to cool by 50 K and 10 K for a doubling of the carbon dioxide and methane atmospheric concentrations respectively [96]. As a gas decreases in temperature, its volume reduces if it is kept at a constant pressure. A similar process can happen in the atmosphere. Therefore, this temperature decrease in the MLT would collapse its density structure and result in an overall contraction of the atmosphere. Atmospheric composition strongly affects the radiative balance of the MLT and upper thermosphere, and is therefore a significant driving force behind thermospheric density change [27].

Roble & Ramesh [98] explored radiative balance changes and feedbacks due to the increase in carbon dioxide (the primary cooling agent of the MLT) and other greenhouse gases. They proposed that concentrations of greenhouse gas species in the MLT are directly proportional to concentrations in the troposphere. The greenhouse gases would then absorb energy from hot, energetic, oxygen atoms (which are primarily produced by photolysis of oxygen gas molecules) that would then be emitted into space as infrared radiation, thus resulting in a net loss of energy from the upper atmosphere. With the additional loss of energy caused by increased carbon dioxide concentrations, the thermosphere as a whole exhibits a contraction. To date, this is the suspected primary driver of secular thermospheric density change.

Brasseur & Hitchman [12] presented evidence suggesting that changes in carbon dioxide concentration also affect stratospheric ozone, and this may counter the effect of the collapsing density structure in the MLT. Ozone absorbs ultraviolet (UV) radiation, thereby causing a temperature increase with altitude between the tropopause and the stratopause. Absorption of UV radiation by ozone prevents the vast majority of this potentially harmful radiation reaching the sensitive biological processes that occur near the ground i.e. life. The absorption results in an expansion in the stratosphere. Brasseur & Hitchman also showed that stratospheric ozone amounts will increase if temperatures decrease. Therefore, ozone concentrations and temperature are observed to be inversely proportional in the upper stratosphere. In the middle atmosphere (tropopause to mesopause, 15-80 km), increases in carbon dioxide concentration would lead to more infrared radiation emitted to space and, thus, lower temperatures. So, carbon dioxide increases should lead to corresponding ozone increases resulting in an expansion. However, most of the infrared radiative cooling occurs in the MLT. This is due to the transfer of energy to carbon dioxide being predominantly achieved via a specific vibrational mode [98], from specific atoms such as atomic oxygen. As these types of gas species are more abundant in the MLT, cooling will have a more significant effect in the thermosphere than in the stratosphere. Moreover, as thermospheric density is approximately ten orders of magnitude less than that in the stratosphere, subtle energy changes from radiative cooling would be more significant in the thermosphere than they would in the stratosphere. As a result this, and the fact that stratospheric atomic oxygen is sparse, the expansion due to stratospheric ozone production will have a negligible effect on thermospheric density.

From model estimates by Akmaev & Fomichev [1], the increase in carbon dioxide concentrations of 313 parts per million (ppm) to 360 ppm observed over the last four decades produced a predominantly negative temperature response in the MLT. The cooling was estimated to be around 3 K in the mesosphere, vanishing at the mesopause, and then reaching 10-15 K in the thermosphere. It was proposed that mechanisms such as the depletion of ozone (e.g. from chlorofluorocarbons, or CFCs) in the middle atmosphere contributed substantially to the negative temperature trend. This suggested that the magnitude of the long-term density trend detected in the thermosphere may, in part, be attributed to the contraction caused by the depletion of ozone from CFCs. The emissions of CFCs into the atmosphere has been significantly reduced, but they can endure in the stratosphere for decades. Eventually, as the CFC concentrations dwindle, so will the negative temperature response. Therefore, account of this must be made when projecting an empirical model of long-term density change into the future.

Venus provides an example of the extent to which radiative cooling from carbon dioxide can affect an atmosphere. The Venusian atmosphere consists of approximately 95% carbon dioxide, as well as having an abundance of atomic oxygen above altitudes of 140 km [53]. Consequently, radiative cooling plays a vital role in the heat budget of the upper atmosphere [22]. The temperature profile of the Venusian atmosphere, from data obtained by the Vega mission [125] and outlined by Zasova *et al.* [129], shows a similarly stratified, yet relatively compact, atmosphere to that of Earth. The effect of the long-term radiative cooling caused a contraction of the atmosphere into a denser profile [129]. However, in the case of Venus, the upper atmosphere (>100 km) cannot be accurately termed as a thermosphere due to the day-night variation in its behaviour. Schubert *et al.* [109] used data from the Pioneer Venus mission [126] to highlight the contrast between the day-side and night-side temperature profiles. The day-side temperatures increase from approximately 180 K with altitude to an exospheric temperature of approximately 300 K; this forms the thermosphere. However, on the night-side there is a ‘cryosphere’ whereby temperatures decrease with altitude to around 100 K. This complex behaviour is created through a combination of a ‘thermostatic effect’ from the radiative cooling of carbon dioxide and heating due to solar extreme-ultraviolet (EUV) radiation. The thermostatic effect was later supported by Akmaev [2] who conducted experiments into the thermospheric resistance to ‘greenhouse cooling’. They suggest that after a period of radiative cooling, a balance with other thermospheric chemical processes would be attained, whereby the thermosphere would have a natural ability to resist the influence of the radiative forcing. In summary, the Venusian atmosphere is an example of the possible long-term effect of radiative cooling from the interaction between carbon dioxide and atomic oxygen. Overall, the atmosphere contracts and upper thermospheric altitudes become increasingly rarefied.

The first empirical study of density change in Earth’s thermosphere, driven by theoretical predictions of atmospheric response to increasing carbon dioxide concentrations, was made by Keating *et al.* [56] in 2000. This study used the long-term orbital decay of five satellites with perigee altitudes between 323 and 404 km averaging at 358 km. The results provide evidence of an average decline in thermospheric densities of 9.8 ±2.5% over the 20 years between 1976 and 1996. Their method incorporated an analytical approach given by King-Hele [63], and used orbital elements taken directly from TLE sets. This study by Keating *et al.* paved the way for future studies and demonstrated the potential resource of the TLE data to be used for studies into the thermospheric density structure. However, the method employed could only achieve relatively limited accuracy due to the use of the averaged orbital parameters taken directly from the TLE sets. As this study only considered satellite with relatively localised perigee altitudes, little information was presented about an altitude dependence of thermospheric cooling.

In 2004 Emmert *et al.* [28] used a more accurate method of predicting thermospheric densities using TLE data [92] for 27 long-lived near-Earth satellites. The data covered all levels of solar variability spanning the time period of 1966-2001. The results indicated a density trend of -2% per decade at 200 km altitude and increasing to -5% per decade at 700 km. This supported the idea of the upper atmosphere being affected by cooling mechanisms in the lower atmosphere. This study gave density trends at 27 discrete altitudes inferred from each orbiting object. They did this by using a drag weighted average altitude for each object and using that altitude to associate a density trend. Therefore, there is scope to present a more detailed picture of atmospheric change by using derived density ratios from multiple satellites that lie within specified altitude bins. Also, the method outlined by Picone *et al.* and used here by Emmert *et al.* employed an analytical propagator that provided numerical data with which the TLE sets were compared. Analytical propagators can achieve high computational speed but usually at a cost of low accuracy. The determination of thermospheric density from orbit evolution would therefore benefit from a high-accuracy numerical propagator such as AETHER.

In 2005, Marcos *et al.* [73] used the data from five satellites (four of which were used by Keating *et al.* [56]) in conjunction with an accurate method of deriving thermospheric densities given by Bowman *et al.* [8], to infer a long-term thermospheric density decline over the period 1970 to 2000. The results described a secular neutral density decrease of 1.7% per decade at 400 km. Their results were the most conservative to date and only predicted a value of thermospheric density decline at a single altitude. By using a theoretical general circulation model, Qian *et al.* [94] also predicted a 1.7% per decade secular density change at 400 km over the same 30-year period. They estimated a more severe average secular decline if the analysed time period was extended to include the minimum of solar cycle 24 (2008). The theoretical data with which the satellite drag data was compared was from yet another source to those used previously by Emmert *et al.*. Therefore, this provided an additional source with which to compare results of long-term thermospheric density change.

The depletion of stratospheric ozone, observed over the last few decades by satellites, along with the increase in water vapour in the atmosphere, is expected to cause a cooling in the middle atmosphere. In 2006, Akmaev *et al.* [3] used a Spectral Mesosphere/Lower Thermosphere Model (SMLTM) to simulate the effects of this cooling. The model extended up to a maximum altitude of 200 km. They predicted a declining density trend of 6.5% per decade at 110 km and reducing to 4% per decade at 200 km. The SMLTM model has been widely accepted to produce accurate simulations of atmospheric climatology and dynamics in the MLT. Also, the maximum altitude of 200 km analysed by the SMLTM is the minimum altitude from which thermospheric density data is obtained via the satellite TLE data. Therefore, the results of the study by Akmaev *et al.* provide a relatively good source of comparison for the lower-altitude results obtained by the study presented in this thesis.

Later in 2008, Emmert *et al.* [30] performed a similar study to their 2004 study, this time using approximately 5000 orbiting objects. The results at 400 km showed an overall density trend of -2.68 $\pm$0.49% per decade and trends of -5 and -2% per decade at solar minimum and maximum, respectively. They used the same method by Picone *et al.* as their 2004 study. However, the additional amount of satellite data greatly increased the signal strength of their derived long-term density decline with respect to any errors associated with their method. As this study used their previous 2004 study to hone the techniques of deriving long-term thermospheric density changes, the long-term changes that have occurred at the altitude of 400 km are now well understood. The extension of their results to include effects from solar variability also suggest a link with long-term density change. However, only results from the one discrete altitude of 400 km were presented.

Other than the daily variations due to the Earth's rotation, the thermosphere and atmosphere in general are largely affected by the state of the Sun. Thermospheric structure is altered by the Sun primarily by EUV irradiation and the effect of the solar wind. The latter carries with it a myriad of charged particles that affect the geomagnetic field, which in turn affect the atmospheric density structure.

Historical records are sparse in terms of solar EUV emissions. However the solar flux emitted in the electromagnetic spectrum at a wavelength of 10.7 cm ($F_{10.7}$) has been recorded daily since the mid 20th century. The National Oceanic and Atmospheric Administration (NOAA) [85] provides these daily indices. Figure 3 shows the $F_{10.7}$ for the 40-year historical period 1970-2010.

Richards *et al.* [95] introduced a 'solar activity factor' $P_{\text{solar}}$ that related the EUV flux to the $F_{10.7}$. Liu *et al.* [72] later performed a study comparing the relationship between $F_{10.7}$ and

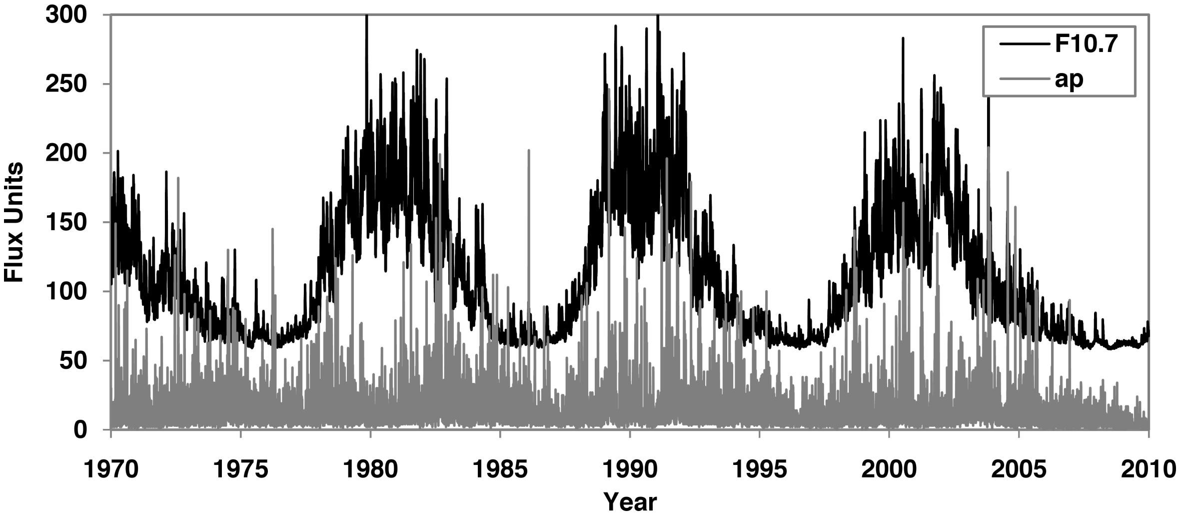

Figure 3: *Indices obtained from the NOAA databases [85 & 87] for the* $F_{10.7}$ *(*$10^{-22}$ *W/sm*$^2$*) and* $a_p$ *(nT) for 1970-2010.*

EUV radiation using daily-averaged data gathered from the Solar EUV Monitor (SEM) on board the Solar Heliospheric Observatory [111], launched in 1995. In the period 1996 and 2005, the relationship between the $F_{10.7}$ and EUV flux was shown to be non-linear as represented by

$$P_{\text{solar}} = \frac{(\mathrm{F}_{10.7} + \mathrm{F}_{10.7\mathrm{A}})}{2}, \tag{2}$$

where $F_{10.7A}$ is the 81-day averaged value of the daily $F_{10.7}$ index. Owing to the restricted historical availability of other solar flux indices, empirical atmospheric models have no choice but to use the $F_{10.7}$ index as a proxy for estimating the sun's effect on the upper atmosphere. Therefore, the $F_{10.7}$ flux can be used with reasonable accuracy as a proxy measurement for the EUV flux. However, it is important to realise that using the $F_{10.7}$ index does compromise the accuracy with which the atmosphere can be analysed.

Energy from the solar wind heats the thermosphere via electrical currents and energetic particles travelling down the EarthŠs field lines [97], and contributes to the magnitude of the exospheric temperature. The physical processes involved in this interaction are still poorly understood. The Earth's geomagnetic field strength has been recorded using various indices, since the early part of the 20th century. The most commonly used indices are the $a_p$ and the logarithmic equivalent $K_p$ index. Figure 3 shows the daily-averaged values of $a_p$ during the 40-year historical period. These are measured every three hours using stations around the world at varying geographic latitudes [87]. The resulting values are then averaged to produce a world wide state of the geomagnetic field. Both the solar $F_{10.7}$ flux and the geomagnetic indices are used as inputs to empirical atmospheric models in determining the current state of the atmosphere.

In 2010, Emmert *et al.* [32] used globally averaged thermospheric density derived from satellite drag data to study the thermosphere during the prolonged minimum in solar activity between cycles 23 and 24 (2007-2009). The value of $F_{10.7}$ at the trough of this solar cycle was 3.7% lower than the four previous solar cycle minima. The results of the study gave anomalously low density values at 400 km, an altitude at which thermospheric densities are relatively well understood. These low density values were 10-30% lower than expected from previous climatological conditions. The study reported that the density anomalies commenced before 2006 and it was surmised that they were larger than expected due to the radiative cooling from the increased carbon dioxide concentrations. Later, the National Centre for Atmospheric Research in Boulder, Colorado, used a general circulation model to predict the electrodynamic state of the thermosphere and ionosphere. They concluded that primary cause of low thermospheric density during the solar minimum was the unusually low levels of solar EUV irradiance [112]. The radiative cooling due to the carbon dioxide concentrations then served to exaggerate the anomalously low density values.

## 2.2 Two-Line Element Sets and the SGP4 Propagator

An example of a Two-Line Element set is given by:

```
1 02389U 66070A   99007.96524080 +.00011091 +00000-0 +87872-3 0 00886
2 02389 081.4293 188.7532 1664776 214.3889 133.7624 11.96865383328703
```

A TLE set consists of various satellite and orbit parameters for a specific satellite at a specific time or epoch. These parameters are described below for the TLE example above [114].

- Line 1: `02389U`: unclassified (`U`) satellite US Space Surveillance Number (USSSN) identification number.
- Line 1: `66070A`: this is the satellite's international designation number. The `66` denotes 1966 as the year of launch with `070` denoting the 70th launch in 1966 and the letter `A` denoting the primary satellite released on that particular launch.
- Line 1: `99007.96524080`: ephemeris epoch, 007.96524080$^{\text{th}}$ day of the year 1999.
- Line 1: `+.00011091`: 1st derivative of the mean motion with respect to time (orbital revolutions/day$^2$).
- Line 1: `+00000-0`: 2nd derivative of the mean motion with respect to time (orbital revolutions/day$^3$);
- Line 1: `+87872-3`: $B^*$ drag term (Earth radii$^{-1}$);
- Line 1: `0 00886`: element set type (`0`), sequential satellite TLE number (`0088`) and checksum (`6`);
- Line 2: `02389`: USSSN satellite identification number.
- Line 2: `081.4293`: orbit inclination $i$ (degrees).
- Line 2: `188.7532`: longitude of ascending node $\Omega$ (degrees).
- Line 2: `1664776`: eccentricity $e$ (decimal point assumed e.g. 0.1664776).
- Line 2: `214.3889`: argument of perigee $\omega$ (degrees).
- Line 2: `133.7624`: mean anomaly (degrees).
- Line 2: `11.96865383`: mean motion $n$ (revolutions per day).
- Line 2: `32870`: revolution number.
- Line 2: `3`: checksum.

All the information provided in the TLE set is used to estimate a satellite's ephemeris. However, there are two parameters of particular relevance: the $B^*$ number, a 'supposed' measure of the ballistic coefficient of the satellite, and the mean motion, which provides an accurate estimate of the semi-major axis of the satellite's orbit. The latter is the parameter through which orbital degradation is analysed.

A TLE set is produced using a differential correction technique, combining several observations of a satellite's position, to determine an orbit. The program used for this task is the Simplified General Perturbations 4 propagator (SGP4). The SGP4 is a fully analytical propagator that provides the method to convert TLE sets into state vectors, which can be used for orbit propagation using a numerical propagator, such as AETHER. The SGP4 is a freely available software, which can be easily compiled - with minor adjustments. It was included within AETHER as a TLE translation module. The state vector output from the SGP4 is in the coordinate system of True Equator Mean Equinox of epoch (TEME). This translates to the $x$-axis of a Euclidean coordinate system ($x$, $y$, $z$) parallel to the direction of the mean vernal equinox; the $z$-axis parallel to the Earth's rotational axis (in a northerly sense), with the $y$-axis completing the right-handed orthogonal coordinate system.

The term 'fully analytical', used to describe the functionality of the SGP4 propagator, means that it does not propagate the satellite's orbit in discrete steps. Instead, SGP4 uses an extensive set of formulae that have been derived by analytical theory to describe how the various perturbations affect a satellite's orbit.

The user manual for the SGP4 propagator by Hoots & Roehrich [48] states explicitly that the orbital parameters given in a TLE set must be decompiled using the same analytical theory used to produce the TLE set. This is because some periodic variations are averaged out to produce mean values of the orbital elements for the TLE set. To recover the original state vector, these periodic variations need to be reinstated, which can be done by the SGP4 propagator. Figure 4 shows a typical comparison between the three Keplerian orbital elements ($a$, $e$, $i$) obtained directly from the TLE sets (dashed line) and those calculated from the state vector output of the SGP4 using equations given by Chobotov [20] (solid line). The periodicities that are averaged out in the TLE sets but present in the state vector output, are clearly visible in the plot of eccentricity, and somewhat with the plot of semi-major axis. Though the trends in the different data derivatives of semi-major axis and inclination behave similarly, the magnitudes differ. This difference is an approximately constant throughout the time series. This shows that only the rate of change, and not the magnitude, provides a reliable parameter when a comparison is made between the data derivatives.

The accuracy of a satellite ephemeris derived TLE sets depends on how they are being used. If one is trying to determine an orbit directly from the mean orbital elements given in a TLE, the accuracy of the resulting ephemeris is relatively low with an ephemeris error of the order of tens of kilometres. This is due to the elements in the TLE being given as a mixture of Kozai and Brouwer values [90 & 122 & 123]. In 1959, Kozai [66] and Brouwer [14] presented differing theories that described the secular, short-term and long-term variations in a satellite's orbit. Both have their advantages and disadvantages but both are used in the formulation of the

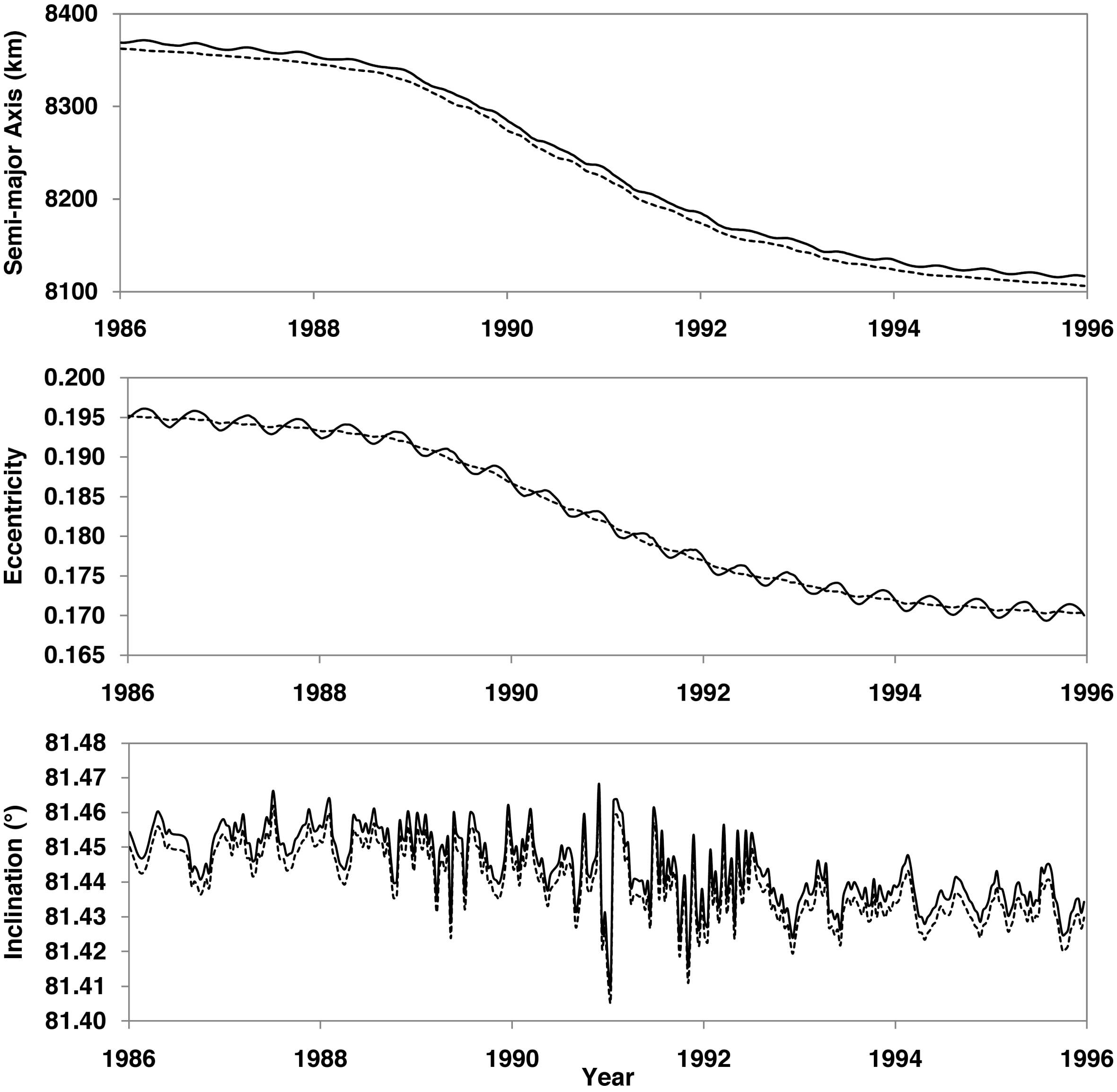

Figure 4: *The time series of the three Keplerian orbital elements of semi-major axis* $a$*, eccentricity* $e$ *and inclination* $i$ *over a 10-year period for satellite ID 02389. The solid line represents elements derived from the state vector output of the SGP4 and the dashed line represents those obtained directly from the TLE sets.*

TLE sets. For the purposes required here, they are both used to try and calculate an osculating orbit. However, they differ in the way they treat the secular, short-term and long-term periodic variations. Errors are introduced into the Keplerian elements given in the TLE as a result of the mixture of methods. An osculating orbit is the instantaneous orbit a satellite would follow if all perturbing forces were removed. By using the SGP4 propagator to convert the mean orbital elements given by the TLEs back into state vectors, the periodicities that were originally removed are reinstated. As state vectors the TLEs provide satellite ephemerides to an accuracy of hundreds of metres to a few kilometres [124].

The accuracy of TLE data ephemerides for a single satellite varies between each TLE set with unknown magnitude. This means there is no covariance carried over with the TLE data

[124], hence making errors difficult to identify and reduce. The covariance is defined as a probability distribution that describes the amount of error that a parameter may contain. When analysing long-term changes from TLE data, it was necessary to adjust the epoch separation between the utilised TLE sets to increase the magnitude of orbital variations relative to the ephemeris errors.

In general, the physical location that is described by a TLE ephemeris at the fiducial epoch of the TLE set is in proximity to the ascending node. Technically, an ephemeris is a table of state vectors. However, when referred to in this text, a TLE ephemeris denotes the SGP4 state vector at the TLE epoch. Figure 5 shows the typical $z$-component of a state vector derived from a time series of TLE data. As the TEME coordinate system has the $z$-axis aligned with the rotational axis of the Earth, with the origin in the equatorial plane, a $z$-value of zero in the state vector defines the plane of the ascending node. This being the case, periodic oscillations in the derived values of argument of perigee $\omega$, longitude of ascending node $\Omega$ and true anomaly $\theta$ coincide with the precession of the argument of perigee due to the perturbations arising from the oblateness of the Earth. This is known as the zonal gravitational harmonic, $J_2$. These periodic oscillations shown in Figure 6 are produced as a result of the orbit's nodal precession through the TLE set ephemeris location. It also shows that these three Keplerian elements derived using the the state vector output from the SGP4 are practically identical to the values obtained when using the orbital elements given explicitly in the TLE sets.

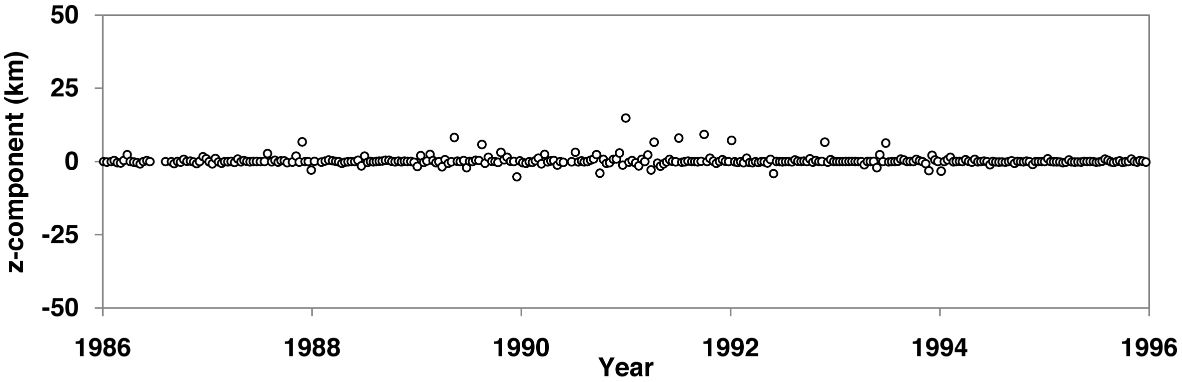

Figure 5: *The $z$-component of a the state vector for Satellite ID:02389 derived from TLE sets via the SGP4 propagator over a 10-year period.*

The accuracy of the TLE ephemerides can be improved using multiple TLE state vectors produced by the SGP4 propagator in a differential correction process to determine an orbit [124]. Similarly, the Analytical Graphics Inc. (AGI) software 'Satellite Tool Kit' (STK) [5] can produce an ephemeris that is constructed by propagating the satellite from one TLE to the next. This produces a piece-wise construction of an orbit. Both methods are computationally expensive and impractical for many TLE sets. At first glance it appears that an improvement in accuracy of the TLE ephemerides is being achieved with no extra data being added. These methods essentially use multiple observations of relatively inaccurate TLE ephemerides and, via numerical methods, produces one comparatively accurate ephemeris.

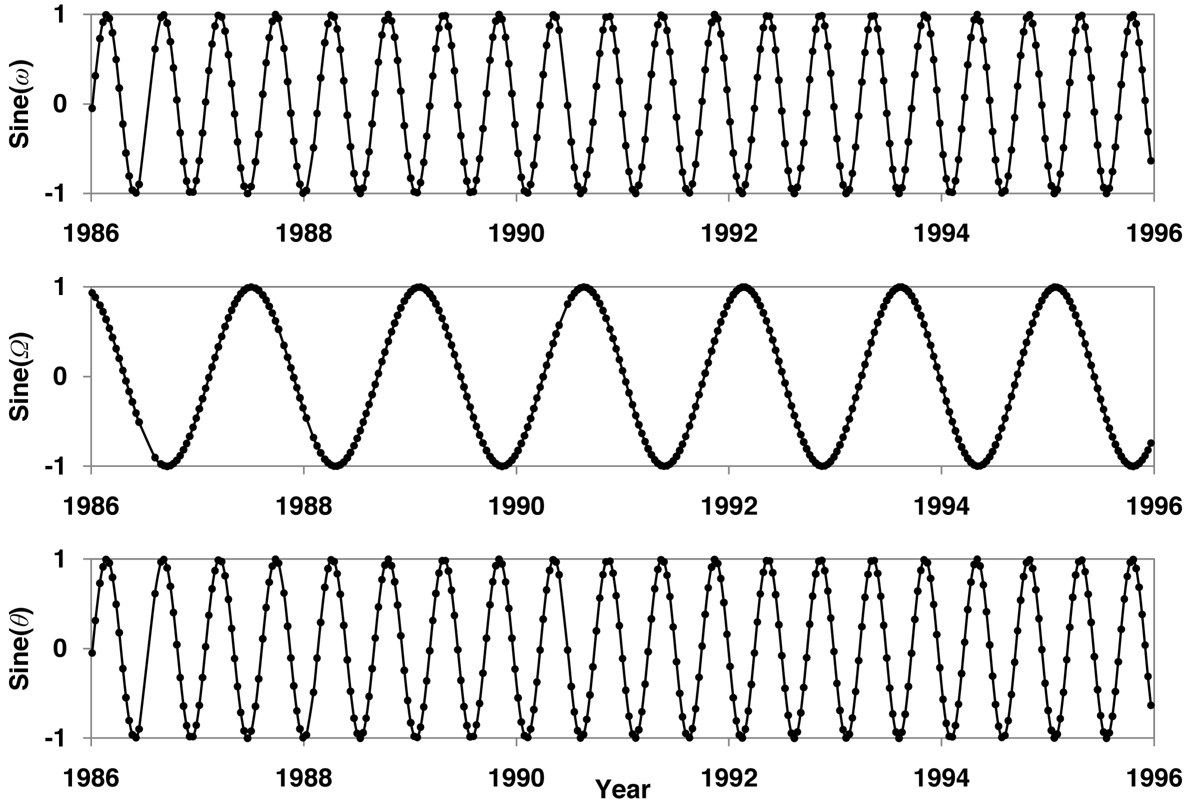

Figure 6: *The time series of the three Keplerian orbital elements of argument of perigee $\omega$, longitude of ascending node $\Omega$ and true anomaly $\theta$ for Satellite ID:02389. The solid line represents elements derived from the state vector output of the SGP4 and the black dots represent those obtained directly from the TLE sets.*

Another way to increase the accuracy of ephemerides derived from TLE sets was reported by Muldoon *et al.* [82] and uses a data-driven approach to predict future orbital parameters. Their method utilises the SGP4 propagator and naïve predictors. These are purely statistical prediction models that have no additional knowledge about the workings of the system under analysis. Firstly, by considering each orbital parameter separately, they train the naïve predictors to apply polynomials and periodic functions to the historical TLE data. These functions are then used to obtain a new TLE set at a desired epoch. The ephemeris accuracy achievable using this method is in some cases the same and other cases better than that achieved by the SGP4 alone. Again, the method reported by Muldoon *et al.* is computationally expensive. Also, further investigations into specific cases whereby the method would guarantee an increase in accuracy have not been published. As such, with no efficient method of identifying TLE sets that guarantee an improvement in ephemeris accuracy, their method is, at present, impractical.

## 2.3 The Ballistic Coefficient

The ballistic coefficient, $\delta$, is a parameter that describes a physical characteristic of a satellite. It defines the extent to which a satellite is perturbed when flying through an atmosphere. It is often the main source of error when calculating the acceleration due to drag - via equation (1) - of a satellite in LEO. Here it is defined by

$$\delta = \frac{C_d A}{m}, \tag{3}$$

where $C_d$ is the satellite's drag coefficient, $A$ is the projected area of the satellite perpendicular to the velocity vector and $m$ is the spacecraft's mass. The determination of $A$ presents some difficulty for uncontrolled objects, or objects of unknown configuration. However, it is the satellite's drag coefficient that presents the most difficulties as its value depends on the aerodynamic regime and atmospheric composition at the spacecraft's location, which are often unknown.

The flow regime is classified according to the Knudsen number,

$$Kn = \frac{\lambda^{\star}}{l}, \tag{4}$$

where $\lambda^{\star}$ is the mean free path of the atmospheric molecules and $l$ is the characteristic length of the satellite. In LEO, the Knudsen number is much greater than one, meaning continuum flow regime properties can no longer be applied. This generally means that macroscopic properties, such as density, pressure and temperature cannot be applied to the flow, which would enable a relatively simple theoretical calculation of $\delta$. That said, under the circumstances considered in atmospheric space-flight, density can be considered a continuous parameter. However, parameters such as the drag coefficient of a satellite need to be determined either by using empirical methods or rarefied flow theory - the opposite to continuum flow theory whereby the flow is considered as discrete particles.

The flow regime can also vary according to the local atmospheric chemical composition. The interaction, or energy transfer, of varying gas species with a satellite's surface can significantly affect the drag coefficient [21]. The degree of energy transfer between an atmospheric molecule and a satellite surface is expressed in terms of the accommodation coefficient,

$$\alpha = \frac{T_{if} - T_r}{T_{if} - T_s}, \tag{5}$$

where $T_r$ is the temperature of the molecules reflected from a satellite's surface, $T_s$ is the temperature of the satellite's surface molecules and $T_{if}$ is the temperature of the incident flow. The surface properties of a satellite's external faces affect the accommodation coefficient as well as the material of which it is made. The accommodation coefficient can be thought of as a momentum-transfer coefficient, and as such, it can influence the magnitude of atmospheric drag. Different materials 'accommodate' the impacting molecules for different lengths of time. In addition to this, the length of time of 'accomodation' varies depending on the specific molecule - different gas species are 'accomodated' for different lengths of time. The chemical composition of the thermosphere changes with altitude [91], as seen in Figure 7. Therefore, the accommodation coefficient is altitude dependent, affecting the drag coefficient and, in turn affecting the ballistic coefficient.

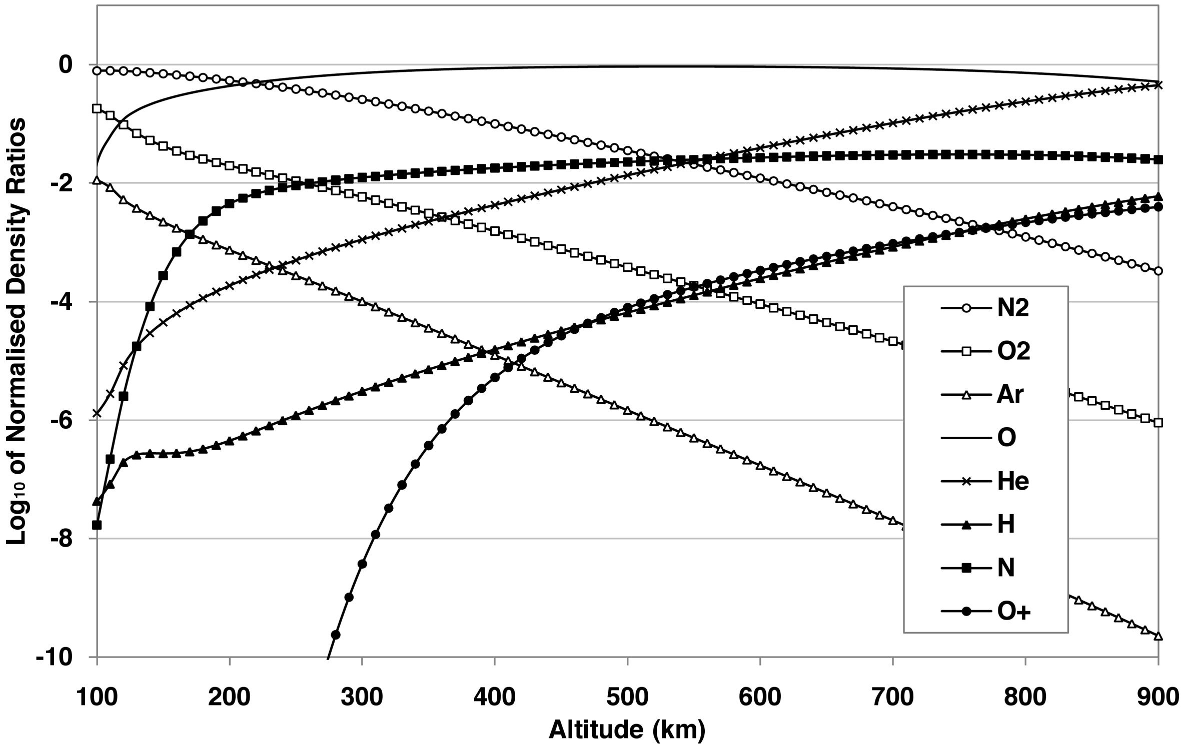

Figure 7: *The altitude-dependence of the chemical composition of the atmosphere. Shown are the normalised density ratios of the individual gas species according to the the NRLMSISE-00 empirical atmospheric model [91]. They are normalised to the local total atmospheric density.*

For simple objects, such as spheres or cubes, that are in stable, low eccentricity orbits (i.e. orbits in which local atmospheric density does not significantly vary) it is possible to obtain a relatively accurate estimate of their ballistic coefficient. However, most satellites are not simple shapes and may also have varying projected areas due to rotation relative to their velocity vectors. As a result, a number of methods have been investigated to estimate a satellite's ballistic coefficient. These methods are outlined below.

- **Using the $\mathbf{B}^*$ drag term directly from the TLE sets**: from Hoots & Roehrich [48], $B^*$ is defined as

$$B^* = \frac{1}{2}\delta R_\oplus \rho_0, \tag{6}$$

where $R_\oplus$ is the equatorial radius of the Earth (6378.135 km), and $\rho_0$ is an assumed atmospheric density (2.461×$10^{-5}$ kg/m$^2 R_\oplus$). This gives $\delta$ as

$$\delta = 1.2741621 \times 10^{-5} B^* \quad \text{(km}^2\text{/kg)}. \tag{7}$$

A problem with the use of equation (7) is that $B^*$ is treated as a fitting parameter in the process of producing the specific TLE set. It is possible that the estimated value of $B^*$ is completely unrelated to drag effects at times when other perturbations are significant. Therefore, it is possible that $B^*$ may take a negative value giving a negative of $\delta$ from equation (7), which is of course impossible for a ballistic coefficient defining drag effects [120]. This leads to an inaccurate and unreliable method of estimating a satellite's ballistic coefficient.

- **Using satellite dimensions and estimating drag coefficient**: this method requires a database of satellite physical parameters. The Database and Information System Characterising Objects in Space (DISCOS) [65] is one such source. DISCOS can be accessed online and satellite characteristics for a limited number of satellites can be retrieved. For example, spacecraft mass and average cross-sectional area can be obtained. Estimating a drag coefficient and using equation (3) can then provide an estimate for the satellite's ballistic coefficient.

This method requires a large amount of preparation to collect satellite information. Also, DISCOS does not carry data on all orbiting objects, so other methods would be required to predict ballistic coefficients for those satellites where data is lacking. Using different methods to calculate ballistic coefficients for numerous satellites can introduce an inconsistency into the analysis. This could produce an artificial bias in some results, skewing the analysis of the phenomenon being studied. Further, results have shown that the drag coefficient of a satellite varies with altitude [9 & 21] and, so, to estimate a ballistic coefficient would require altitude information (contained in the TLE data) and satellite characteristics (DISCOS or some other database) to be able to predict $\delta$ with reasonable accuracy.

- **Averaging multiple estimates from differentially-corrected orbit fits**: Bowman [7] used satellite tracking data from 40 satellites over the period 1970-2000 to estimate 'true' ballistic coefficients for use in the High Accuracy Satellite Drag Model (HASDM) [116] developed by the U.S. Air Force Space Command. HASDM is used to calculate atmospheric density variations and uses data obtained from a number of selected satellites. With the aid of an orbital perturbation model and satellite observational data, a batch least squares algorithm was used to determine an orbit and obtain an estimate of ballistic coefficient. The observable value in this approach was the product of the true atmospheric density and the true ballistic coefficient. Therefore, in order to extract an estimate for the ballistic coefficient, this approach relied on the Jacchia 1970 empirical atmospheric model [50] to provide estimates of atmospheric density. This method assumes that the density estimates provided by the Jacchia 1970 model are correct, which is not necessarily true. However, the model density may still be biased in some way. Taking an average of many ballistic coefficient estimates reduces the assumption to one that assumes the Jacchia 1970 density model is at least unbiased over extended periods of time.

The ballistic coefficient estimated during the orbit determination process is different from the 'true' ballistic coefficient as it relies on an empirical model to provide neutral density estimates. However, by taking the average of 3,200 estimated values, Bowman obtained an accurate estimate of the 'true' values of ballistic coefficient. This method was validated using the theoretical ballistic coefficient of orbiting spheres with known physical parameters.

Taking an average of multiple estimates of ballistic coefficient does not provide a robust value of ballistic coefficient. A satellite's true ballistic coefficient can vary over time. In an earlier study, Bowman [6] described the variation of the drag coefficient with solar activity and altitude. During times of low solar activity the chemistry of the upper atmosphere, for a given altitude, changes as it contracts. Therefore, during a historical period that spans complete solar cycles, or significant portions of complete cycles, the drag, and therefore the ballistic coefficient will vary. However, the variations in chemistry were reported to have significant effect only above approximately 500 km. From data given by Moe & Bowman [75], the drag coefficient of orbiting objects is seen to vary approximately linearly with altitude below 500 km. Figure 8 shows drag coefficient data derived for orbiting spheres during sunspot minimum and maximum.

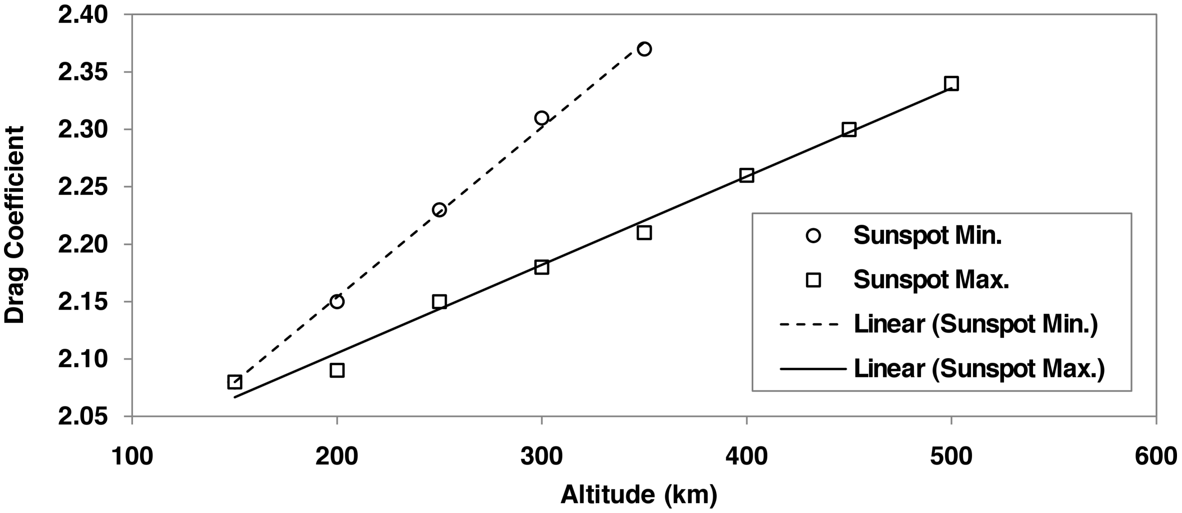

Figure 8: *The altitude-dependent nature of drag coefficients derived for spheres, orbiting during sunspot minimum and maximum. Data provided by Moe & Bowman [75].*

• **Comparison with satellites of known ballistic coefficient**: presented by Picone *et al.* [92] and used in the studies by Emmert *et al.* [28, 29 & 30], this approach uses TLE data and the SGP4 propagator. A time series of ballistic coefficients are estimated using

$$\delta^M(t_{ik}) = \frac{\frac{2}{3}\mu^{\frac{2}{3}}[n_M(t_{ik})]^{-\frac{1}{3}}\Delta_{ik}n_M}{\int_{t_i}^{t_k}\rho^M v^3 F \mathrm{d}t}, \quad (8)$$

where $\mu = GM$, the gravitational constant of the Earth, $n_M$ is the Kozai mean motion (given directly by the TLE sets), the subscripts $i$ and $k$ denote the pair of TLE sets between which the ballistic coefficient is determined, $\rho^M$ is the density derived from the NRLMSISE-00 empirical atmospheric model, $v$ is the inertial orbital speed and $F$ is a dimensionless factor that accounts for the rotation of the atmosphere. The value of the ballistic coefficient is assigned to the time $t_{ik} = \frac{t_i+t_k}{2}$ and $\Delta_{ik}n_M$ is the difference in the Kozai mean motion between the consecutive TLE sets.

Bowman [7] showed that highly accurate estimates of ballistic coefficient can be achieved by averaging multiple measurements taken over many orbit periods. Theoretical estimates for orbiting satellites with known relatively simple geometry and surface composition, can be used as scaling parameters for other satellites with more complex shapes. Picone *et al.* used such scaling parameters to adjust the average of the measured ballistic coefficients derived from equation (8) to produce a ‘true’ estimate of ballistic coefficient. Theoretical predictions of ballistic coefficients for simple shapes were estimated to an accuracy of 5-10% [21]. The ballistic coefficient of the satellite under investigation (denoted by subscript $I$) can be related to that of a reference satellite (denoted by subscript $R$) by

$$\delta_I^T = \left\langle \delta_I^M \right\rangle \frac{\delta_R^{Th}}{\left\langle \delta_R^M \right\rangle}, \tag{9}$$

where the two objects are orbiting in similar historical time periods. The brackets signify long-term averages, calculated over a time period much greater than the propagation time between TLE epochs, but much less than the timescale of secular thermospheric change. Here $\delta^T$ denotes the satellite’s ‘true’ ballistic coefficient, $\delta^{Th}$ represents the theoretical value ($C_D \frac{A}{m}$) and $\delta^M$ denotes the measured value of the ballistic coefficient obtained by the time series of TLE data and equation (8).

The use of TLE data to obtain an estimate for the ballistic coefficient and to infer atmospheric density values creates a circular argument. As such, Picone *et al.* solved this problem by the use of reference objects with simple, and therefore accurately predictable ballistic coefficients. The key assumption using this method is that if two orbiting objects experience atmospheric drag at the same time and location, the density should be the same for both. Applying this assumption over may objects reduces the ambiguity of ballistic coefficient estimates to thermospheric density estimates to a semi-arbitrary scaling of only the ballistic coefficients estimated of just the small number of reference objects.

## 2.4 Deriving Thermospheric Densities from Two-Line Element Sets

A summary of the methods used in the empirical studies previously outlined in section 2.1 to derive thermospheric densities from satellite drag data is given below. All the methods follow the same general principle of quantifying the change in the semi-major axis and related parameters such as the mean motion and its inverse, the orbital period. Doing this provides information about the magnitude of atmospheric drag, which from equation (1) is a function of atmospheric density.

The method used by Keating *et al.* [56] utilises analytical theory from King-Hele [59] and the satellite drag data from the AFSPC TLE sets.

Firstly, the rate of change of the mean motion, $n$, as a function of time was determined using a 20th degree polynomial. The rate of change of the orbital period $P$ was then calculated using

$$\frac{\mathrm{d}P}{\mathrm{d}t} = -\frac{(\frac{\mathrm{d}n}{\mathrm{d}t})P}{n}. \tag{10}$$

An expression given by King-Hele [63] uses the rate of change of the mean motion from equation (10) to calculate a product of ballistic coefficient and atmospheric density given by

$$\delta\rho = -\frac{\frac{\mathrm{d}P}{\mathrm{d}t}}{3}\sqrt{\frac{2e}{\pi a H}}\left[1 - 2e + \frac{5e^2}{2} - 3e^2 - \frac{H}{8ae}\left(1 - 10e + \frac{7H}{16ae}\right)\right], \tag{11}$$

where $e$ is the orbit eccentricity and $a$ is the orbit's semi-major axis. $H$ is the density scale height derived from NASA's 1999 model, the Marshall Engineering Thermosphere (MET99) [51], which is an updated version of the Jacchia 1970 empirical atmospheric model. In equation (11), the ballistic coefficient is defined by

$$\delta = \frac{FSC_D}{m}, \tag{12}$$

where

$$F = \left(1 - \frac{r_p}{v_p}\alpha\cos i\right)^2, \tag{13}$$

is a parameter accounting for the co-rotation of the atmosphere with the Earth. In equation (13), $r_p$ and $v_p$ are the satellite's geocentric radius and velocity at perigee respectively, $\alpha$ is the angular velocity of the co-rotating atmosphere and $i$ is the satellite's orbital inclination.

The use of $\delta\rho$ in equation (11) removes the need to estimate a value for the ballistic coefficient. Instead, Keating estimates the regression coefficient $K$ for each satellite-year of data by plotting the product $\delta\rho$ against densities derived from the MET99 model ($\rho_{MET99}$) and using a least-squares fit. This leads to

$$\delta\rho = K\rho_{MET99}. \tag{14}$$

Therefore, from equation (14), $K$ was used as a proxy for changes in density, under the assumption of a constant ballistic coefficient.

A method for computing atmospheric density values from satellite drag data presented by Bowman *et al.* [8] was used in the 2005 study by Marcos *et al.* [73]. This method used energy dissipation rates of satellite orbits to infer absolute values for atmospheric temperature and, ultimately, density. As a satellite orbits through an atmosphere, it is retarded by atmospheric drag. This retardation can be thought of as a loss in orbital energy, or energy dissipation. Quantifying this energy dissipation, and the rate at which it occurs, is the method taken by Bowman *et al.* and is used to infer information about atmospheric density between two observations.

By using a differential correction technique and a general orbital perturbation model, orbits were fitted to observations given by the U.S. Space Surveillance Network (USSN) to obtain the six Keplerian elements ($a$, $e$, $\theta$, $i$, $\Omega$, $\omega$) as well as a ballistic coefficient [7]. The perturbation model included the empirical Earth Gravity Model (EGM96) published in 1996 truncated at gravitational harmonic order and degree 48. Initially the full EGM96 model with gravitational harmonics of order and degree 70 was used to obtain highly accurate values of fitted orbits and ballistic coefficients to be used as reference. Then in an effort to reduce the computational effort, the truncation at order and degree 48 was deemed adequate, relative to the reference values, to provide sufficient accuracy when analysing the orbital energy dissipation rates.

The perturbation model also included third-body gravitational effects from the Sun and Moon as well as accelerations due to solar radiation pressure and atmospheric drag. The atmospheric model used to predict density was the modified version of the empirical Jacchia 1970 model [50] used in the HASDM program [116].

Bowman *et al.* gives the energy dissipation rate (EDR) of a satellite's orbit subject to atmospheric drag as

$$\bar{\dot{\varepsilon}} = \frac{B}{2\Delta t}\int_0^{\Delta t} \rho_{J70}\mathbf{v}_{atm}(\mathbf{v}_{atm} \bullet \mathbf{v}_{sat})\mathrm{d}t, \tag{15}$$

where $B$ is the satellite ballistic coefficient derived from the orbit fitting, $\Delta t$ is the time span over which the EDR is calculated, $\rho_{J70}$ is the model density derived from the modified Jacchia 1970 model and $\mathbf{v}$ is the atmosphere-relative velocity and inertial velocity of the satellite with subscript '$atm$' and '$sat$' respectively. The EDR was then calculated on a daily basis using

$$\bar{\dot{\varepsilon}} = \frac{B}{2 \times 86,400}\sum_{j=0}^{M} \rho_{J70}\mathrm{f}(\mathbf{v})dt, \tag{16}$$

where $M = 86,400/dt$, $dt$ = 1 and 6 second(s) for orbit eccentricities, $e >$ 0.01 and $e \leq$ 0.01 respectively for the $j^{th}$ ephemeris, and

$$\mathrm{f}(\mathbf{v}) = \mathbf{v}_{atm}(\mathbf{v}_{atm} \bullet \mathbf{v}_{sat}). \tag{17}$$

To avoid the circular argument of using a model density to obtain a 'true' density, a correction in the observed EDRs was needed as these relied on the empirically derived value of ballistic coefficient. From the method presented by Bowman [7] the 'true' ballistic coefficient $\bar{B}$

was calculated from numerous empirically derived values. This ‘true’ value was then used to calculate a corrected version of the EDR,

$$\bar{\dot{\varepsilon}}_{COR} = \frac{\bar{B}}{2\Delta t}\int_0^{\Delta t}(\rho_{J70} + \frac{\partial \rho}{\partial Q}\Delta Q)\mathrm{f}(\mathbf{v})\mathrm{d}t, \tag{18}$$

where $\Delta Q$ is a perigee height correction. It was found that ephemeris errors occurring during the orbit fitting process were adversely affecting the EDR estimates. Ephemeris errors resulted from orbit fits with unevenly spaced observations. To reduce these errors a least-squares fit of perigee height with empirically derived ballistic coefficient was necessary in order to ultimately obtain an accurate calculation of density. The observed and corrected values for EDRs were then related to the temperature difference $\Delta T_c$ between the modified Jacchia 1970 empirical atmospheric model and the observed temperature computed by the EDR value using

$$\bar{\dot{\varepsilon}}_{OBS} = \bar{\dot{\varepsilon}}_{COR} + \Delta T_c \frac{\partial \bar{\dot{\varepsilon}}_{COR}}{\partial T_c} + \frac{1}{2}\Delta T_c^2 \frac{\partial^2 \bar{\dot{\varepsilon}}_{COR}}{\partial T_c^2}. \tag{19}$$

Here the partial derivatives of $\bar{\dot{\varepsilon}}$ are obtained in the same manner as equation (15) with the partial derivatives of $\rho_{J70}$ with respect to $T_c$ being derived from the modified Jacchia 1970 empirical model. This process is presented in greater detail in Bowman [8].

The quadratic equation (19) was then solved for $\Delta T_c$, from which an average daily density value was derived.

The method used by Emmert *et al.* [28, 29 & 30] and Lean *et al.* [68] when deriving thermospheric densities was first reported by Picone *et al.* [92]. The method derived total mass density from TLE sets by integrating numerically the differential equation (20) (below), which describes the influence of atmospheric drag on the orbital mean motion. The integration requires only the use of the SGP4 propagator. A single estimate of atmospheric density using this method requires two TLE sets, TLE$_1$ and TLE$_2$ and their epoch is given by $t_1$ and $t_2$ respectively. The orbital mean motion is directly affected by atmospheric drag and, so, by summing the change in orbital mean motion over a specified period of time provides information about atmospheric drag and, hence, density. In the absence of gravitational perturbations, atmospheric drag on a satellite will continually reduce the semi-major axis $a$ of an osculating orbit. The rate of change of $a$ is given by

$$\dot{a} = \frac{2a^2 v}{\mu}\ddot{r}_{drag}, \tag{20}$$

where $\ddot{r}_{drag}$ is the acceleration due to drag defined by equation (1), $\mu$ is Earth’s gravitational constant and $v$ is the satellite’s velocity relative to the atmosphere. The variable $a$ in equation (20) is converted to the mean mean motion $n_M$ as outlined in the Appendix Section A2 of Picone *et al.* [92]. When solar radiation pressure is negligible, as is often the case for objects in LEO, the rate of change of the mean mean motion can be given by

$$\dot{n}_M = \frac{3}{2} n_M^{\frac{1}{3}} \mu^{-\frac{2}{3}} \rho \delta v^3 F, \tag{21}$$

where $\delta$ is the ballistic coefficient and $F$ is the wind factor accounting for the co-rotation of the atmosphere given previously by equation (13). It is equation (21) that is to be integrated numerically in order to obtain an estimate of atmospheric density.

Picone *et al.* used the SGP4 propagator to integrate the right hand side of equation (21) from the epoch of TLE$_1$, $t_1$ to that of TLE$_2$, $t_2$, to give

$$\Delta_{1,2}n_M \cong \frac{3}{2}\mu^{-\frac{2}{3}} \oint_{t_1}^{t_2} n_M^{\frac{1}{3}} \rho \delta v^3 F \mathrm{d}t, \tag{22}$$

where

$$\Delta_{1,2}n_M = n_{M(t_2)} - n_{M(t_1)}, \tag{23}$$

which is calculated directly from the parameters given in the two TLE sets. Between $t_1$ and $t_2$ Emmert *et al.* used the SGP4 propagator to predict the orbital speed, $v$, over the satellite's orbit path. As the SGP4 propagator calculates the satellite's ephemeris at discrete times, the orbit path is made up of line elements relating to the satellite's instantaneous velocity vector. The contour integration sign $\oint$ is used to denote an approximately closed path integral. As the integration of the orbital parameters in the right-hand-side of equation (22) would yield the change in orbital mean motion, $\Delta_{1,2}n_M$, the density $\rho$ must represent the atmospheric density through which the spacecraft travels. Therefore, by rearranging equation (22) given by

$$\rho(t_{1,2}) \equiv \frac{\frac{2}{3}\Delta_{1,2}n_M \mu^{\frac{2}{3}}}{\oint_{t_1}^{t_2} n_M^{\frac{1}{3}} \delta v^3 F \mathrm{d}t}, \tag{24}$$

the average density, $\rho(t_{1,2})$, was obtained and assumed to apply at the time $t_{1,2} = \frac{(t_1+t_2)}{2}$, for simplicity. This density estimate was derived in a similar manner to the ballistic coefficient defined by equation (8) and (9). For this reason, the estimation of the ballistic coefficient previously defined can be used with equation (24) without introducing any inconsistency in the density analysis.

The last step before a atmospheric density estimate can be made was to replace $n_M$ in the denominator of equation (24) by $n_M \approx \frac{\{n_M(t_1)+n_M(t_2)\}}{2}$, giving

$$\rho(t_{1,2}) \cong \frac{\frac{2}{3}\mu^{\frac{2}{3}} \left\{ n_M^{-\frac{1}{3}} \right\} \Delta_{1,2}n_M}{\oint_{t_1}^{t_2} \delta v^3 F \mathrm{d}t}. \tag{25}$$

To analyse the results of this study with respect to altitude, methods of how density estimates have previously been assigned to altitudes are also important. Here, to associate an altitude to the density estimate given by equation (25), Emmert *et al.* used a drag weighted average, between the epochs of $t_1$ and $t_2$, of ephemeris height, local time and latitude. The drag weighting factor $\lambda$ was given by

$$\lambda = \rho_{mod} v^3 F, \tag{26}$$

where $\rho_{mod}$ was the density derived from the NRLMSISE-00 empirical atmospheric model.

## 2.5 Summary

A thorough review of the fundamental areas of importance when studying thermospheric density have been covered in this literature review. Motivations for the studies have been described, which were all generally based on the issue of global climate change.

Thermospheric density change was predicted by theoretical investigations before empirical evidence for long-term trends was discovered. It is generally accepted that energy loss through radiative transfer in the thermosphere is caused by carbon dioxide and nitrous oxides and their interaction with atomic oxygen. Carbon dioxide and nitrous oxides are greenhouse gasses and their concentrations have steadily increased above natural levels in the atmospheric since the start of the industrial revolution. The understanding of the role of carbon dioxide in thermospheric cooling has been strengthened by the study of similar phenomena on Venus, a planet whose atmosphere has high concentrations of carbon dioxide as well as atomic oxygen, especially in the thermospheric regions.

Solar radiation is the main cause of large amplitude density variations in the thermosphere. Measurements of solar radiation can now be made over a wide spectrum of wavelengths. However, historically, the measurements were more limited due to the technological capabilities of the time, and only a few wavelengths could be measured and documented. Space-age technological advancement has provided new ways to measure a broader spectrum of solar radiation. However, to make density estimates using the TLE database, one can only use the historically available solar radiation measurements. These need to serve as proxies to the historically unavailable measurements of parameters that directly affect the upper atmosphere, such as EUV radiation. Furthermore, the investigation by Emmert *et al.* [32] into the minimum of solar cycle 23-24, and its affect on thermospheric densities, raises the question as to whether thermospheric density analysis during the years 2008-2010 can be made in the same manner as that of earlier years. This is due to the use of empirical atmospheric models being used as comparison tools. These models were based on a dataset whereby the solar radiation did not reach the extreme low levels as they did during minimum of solar cycle 23-24. As such, they cannot act as a base for comparison during such times of low solar radiation without being subjected to extensive accuracy studies.

The study by Keating *et al.* [56] served as a successful precursor to later empirical studies, demonstrating the relevance of further investigations into long-term thermospheric density change. The studies by Emmert *et al.* (2004) [28], Marcos *et al.* (2005) [73] and Emmert *et al.* (2008) [30] all continued the empirical investigations into long-term density change in the thermosphere. These three studies used more accurate methods of deriving density values from TLE data. However, Marcos *et al.* [73] still used only five satellites over a 30-year period. Emmert *et al.* [28 & 30], on the other hand, used an improved method with more satellites (27 and approximately 5000 respectively) and over the maximum historical duration made permissible by the availability of reliable TLE data. A commonality among all empirical investigations into long-term thermospheric density change, and that is that all studies report a density decline.

The study by Emmert *et al.* depended on an analytical propagator for the integration of satellite orbits. Numerical integration can provide higher accuracy orbital propagation than that achievable by analytical propagators, such as the SGP4 [76]. To date, all the empirical studies into long-term thermospheric density all aim to estimate a density value and associate that value with an altitude and epoch. However, no study simply compares *changes* in density, relative to a specific epoch and altitude, to infer long-term density change without subsequently converting into a specific density value. However, the method by Marcos *et al.* does calculate energy dissipation rates for satellite orbits, which is essentially equivalent to the rate-of-change of semi-major axis. Simply analysing the change in semi-major axis could lead to a more efficient way of analysing bulk TLE data, which could enhance any signal of long-term thermospheric density change, and further the field of research.

It is also important to highlight the fact that in all methods described above, whereby a ballistic coefficient is estimated for a satellite, the actual value predicted is essentially meaningless as it is only used as a proxy to indicate long-term changes in density. Therefore, unless additional consideration is taken into long-term variability of ballistic coefficient, the resulting assumption would be that there is no long-term trend in the ballistic coefficient estimates.

Data from the TLE sets are most accurate when using them in the form of a state vector. Greater ephemeris accuracy and precision can be achieved by the use of computational and numerical methods. Vallado [124] described a piecewise method using the STK software. This piecewise method involved determining accurately a single ephemeris from multiple TLE observations. This could be performed many times and the derived ephemerides could then used to attain a more accurate picture of orbit evolution. Muldoon *et al.* [82] presented a data-driven approach, using purely statistical methods, again requiring additional, bespoke, software. Though Muldoon *et al.* developed this method for the application of future conjunction analysis of space debris objects, the concept could be applied to create a more accurate ephemeris using TLE sets surrounding a particular epoch of interest. Both methods would require considerable computational effort. Particularly in the case of Muldoon *et al.*, who did not consider computational effort when formulating their method. They believed that potential users of such a numerical process would be limited to analysing only a small number of objects. If the analysis extended to a substantial amount of objects, clusters of computers would need to be at their disposal. Another key disadvantage of such methods is the loss in temporal resolution of orbital ephemerides. This is due to the available number of accurate ephemeris data points necessarily being less than the original, less accurate, observational data.

Methods to infer ballistic coefficients for orbiting satellites have been presented. Each method has limitations, with the estimated value of a ballistic coefficient being dependent on how it is to be used. Most methods presented here rely on an empirical density model of the atmosphere to predict satellite orbit evolution and hence infer a ballistic coefficient. This is a valid method as many peer reviewed studies have estimated the ballistic coefficient in such a way. The important point to remember with methods using empirical models to estimate ballistic coefficients is that they all assume the density estimate from the models are correct. This is the assumption one must make in order to progress with such methods. However, care should be taken to correctly acknowledge the limitations of such assumptions, especially when analysing density itself. Applications for this facet are mostly associated when using propagators with estimated values of ballistic coefficient. In these cases, the ballistic coefficient and propagator must operate under the same assumptions in order to be compatible. In conclusion, the ambiguity of estimating ballistic coefficients and predicting density must be carefully considered in order to generate meaningful results about long-term secular thermospheric density change.

Empirically determining a ballistic coefficient via orbit iteration is a novel way of predicting a satellite's ballistic coefficient. If it is done using comparisons of numerical data with observational data then variations in flow regime during the observation period must be considered. For example, the value of a ballistic coefficient depends on the flow regime in which the satellite is orbiting. Owing to solar cycle variation, the flow regime at a given altitude changes. Therefore, if the observational period is less than that of the solar cycle then the variation in flow regime would not be intrinsically taken into account. Post-processing of the derived values of ballistic coefficient would need to be done in order to obtain an accurate long-term average value. One drawback of this method is the computational run-time. However, highly accurate values of ballistic coefficient could be obtained if the numerical data was produced using a numerical propagator. Therefore, development of an efficient process would be required to successfully estimate ballistic coefficients using orbit iteration. The method used by Emmert *et al.* to estimate a varying ballistic coefficient over a historical period is robust and suitably accurate. However, there is a requirement to find reference objects and then assign them to specific historical time periods. This makes the process of deriving long-term density changes less efficient than it could otherwise be. In addition to using a numerical orbit propagator in conjunction with orbit iteration, it would be beneficial if a method was developed through which only TLE data for a relatively small time period could be used to accurately infer a ballistic coefficient. A more detailed explanation and discussion of using orbit iteration to obtain ballistic coefficient values is deferred until Chapter 5.2.

# 3 The Research Objectives

Is the thermosphere secularly changing? If so, by how much? The previous chapter has presented evidence that may provide an answer to these questions. However, these are the questions that this study attempts to answer using novel methods. To do this the research objectives that were made are outlined below.

1. A detailed understanding of the data provided by the TLE sets was required. The sources of error associated with using TLE data needed to be identified, and any issues resolved, before attempting to infer a signal connected with long-term density change. Therefore, methods to suppress errors in the TLE data needed to be determined. Once the ways in which the TLE sets can provide the most precise satellite ephemerides were understood, justifiable conclusions of thermospheric density could then be made;

2. The development of a sufficiently accurate, numerical, orbital propagator was required. As the ‘workhorse’ of this study, the propagator was dedicated to handling TLE data. It needed to be equipped with all perturbations whose magnitudes are significant relative to measurements of thermospheric density. The implementation of the analytical perturbation theories needed to be tested and validated against independent sources;

3. A novel way needed to be derived to estimate an accurate satellite ballistic coefficient. A crucial part of empirical thermospheric density analysis is the accurate representation of a satellite’s physical properties. This parameter was estimated in such a way that it did not depend on drag calculations throughout the historical period of utilised data. This was done so that the drag estimates used to infer thermospheric density were independent to how the ballistic coefficient was determined;

4. The derivation of a robust mathematical theory that extracts thermospheric density information from satellite drag data was required. Once the tools for propagating accurately satellite orbits were developed, the theory of interpreting satellite drag data to infer a relative long-term density change needed to be developed. Also, to enrich the conclusions made from the drag data, methods to analyse greater details of the long-term signal (altitude and solar flux dependence as well as other periodicities) were developed.

# 4 The Observational Two-Line Element Data

Two-line element sets derived from the observations of 41 satellites, listed in Table 1, were selected to provide the observational data used in this study. The selection requirements that were used are listed below.

- The data must be observations of the same object. Sometimes foreign objects in adjacent orbits can be incorrectly recognised and documented in the TLE data. This obviously gives false ephemeris predictions of desired satellite.
- The data must have high temporal fidelity i.e. TLE sets approximately 10 days, or less, apart for a significant proportion of the historical period (1970-2010).
- The orbits represented by the TLE sets needed have perigee altitudes that continuously lie between 100-700 km for the majority of the historical period. The range of perigee altitudes exhibited by the satellites under observation are shown in Figure 9.

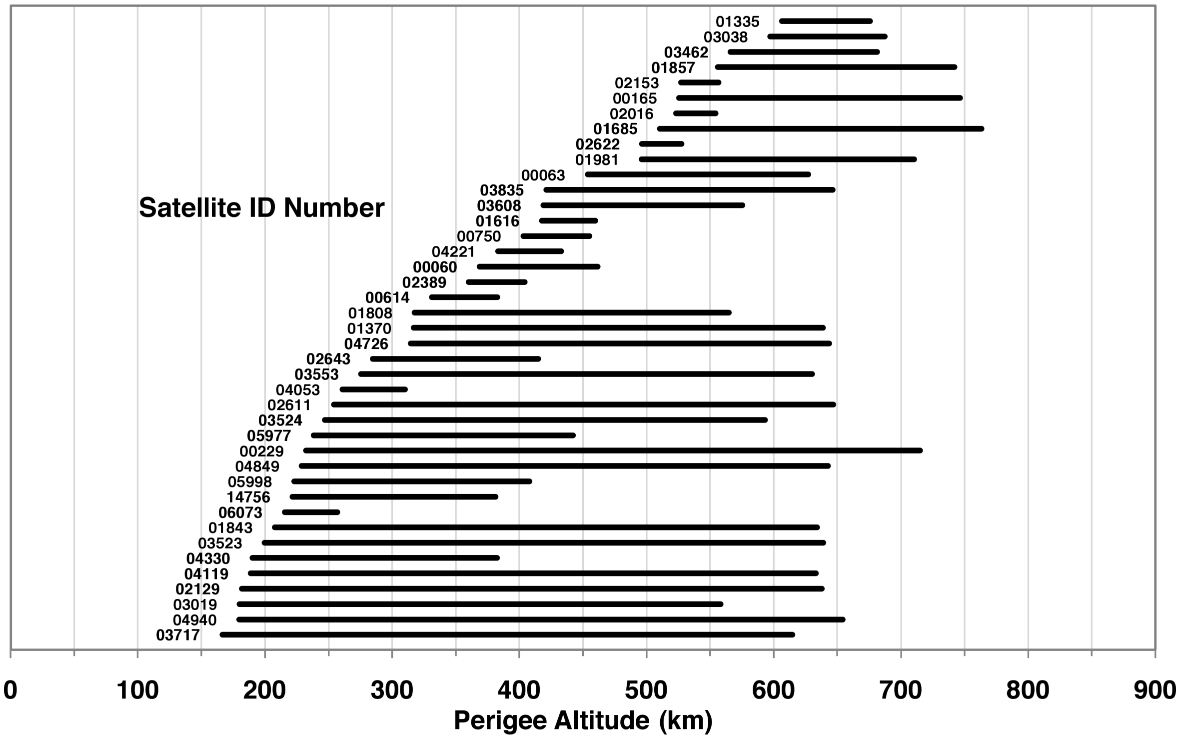

Figure 9: *The range of perigee altitudes covered by the 41 satellite used in this study.*

Table 1: *The TLE data from the 41 satellites used in this study.*

| Satellite ID Number | Historical Period | Perigee Altitude (km) | Eccentricity | Average Inclination (°) |
|---|---|---|---|---|
| 00060 † ⋆ ◇‡ | 1970 - 2010 | 461.5 - 368.6 | 0.1133 - 0.0194 | 49.94 |
| 00063 †‡ | 1970 - 2010 | 627.1 - 453.6 | 0.0087 - 0.0012 | 48.55 |
| 00165 †‡ | 1970 - 2010 | 746.5 - 525.5 | 0.0059 - 0.0000 | 47.92 |
| 00229 † | 1970 - 2002 | 715.0 - 232.2 | 0.0097 - 0.0006 | 48.29 |
| 00614 † ⋆ ◇‡ | 1970 - 2010 | 382.7 - 331.1 | 0.2097 - 0.0925 | 82.09 |
| 00750 †‡ | 1970 - 2010 | 455.1 - 403.1 | 0.3154 - 0.1938 | 60.85 |
| 01335 ‡ | 1970 - 2010 | 675.7 - 606.3 | 0.0944 - 0.0531 | 56.13 |
| 01370 †‡ | 1970 - 2004 | 638.8 - 316.8 | 0.0808 - 0.0005 | 56.07 |
| 01616 ‡ | 1970 - 2010 | 459.7 - 417.6 | 0.1778 - 0.1185 | 144.23 |
| 01685 ‡ | 1970 - 2010 | 763.3 - 510.4 | 0.0044 - 0.0000 | 32.32 |
| 01808 †‡ | 1970 - 2002 | 564.6 - 317.6 | 0.1435 - 0.0005 | 79.80 |
| 01843 † | 1970 - 2002 | 634.1 - 207.6 | 0.0131 - 0.0004 | 64.98 |
| 01857 ‡ | 1970 - 2010 | 742.2 - 555.8 | 0.0101 - 0.0016 | 32.03 |
| 01981 ‡ | 1970 - 2010 | 710.5 - 496.0 | 0.0038 - 0.0000 | 32.44 |
| 02016 †‡ | 1970 - 2010 | 554.3 - 523.2 | 0.1386 - 0.1195 | 34.11 |
| 02129 † | 1970 - 2002 | 637.8 - 181.7 | 0.0220 - 0.0009 | 98.30 |
| 02153 †‡ | 1970 - 2010 | 556.6 - 527.1 | 0.1511 - 0.1313 | 79.78 |
| 02389 † ⋆ ◇‡ | 1970 - 2010 | 404.3 - 360.1 | 0.2274 - 0.1405 | 81.45 |
| 02611 | 1970 - 2002 | 646.8 - 254.1 | 0.0103 - 0.0003 | 93.39 |
| 02622 †‡ | 1970 - 2010 | 527.5 - 496.3 | 0.2401 - 0.2248 | 99.11 |
| 02643 ⋆‡ | 1970 - 2010 | 414.8 - 284.6 | 0.6937 - 0.6327 | 26.34 |
| 03019 †‡ | 1970 - 2002 | 558.2 - 179.8 | 0.0308 - 0.0001 | 64.07 |
| 03038 ‡ | 1970 - 2010 | 687.4 - 597.0 | 0.0979 - 0.0572 | 56.31 |
| 03462 ‡ | 1970 - 2010 | 681.2 - 566.0 | 0.0058 - 0.0012 | 32.05 |
| 03523 † | 1970 - 2001 | 639.1 - 199.4 | 0.1007 - 0.0005 | 62.29 |
| 03524 † | 1970 - 2001 | 593.1 - 246.8 | 0.1021 - 0.0013 | 62.33 |
| 03553 †‡ | 1970 - 2004 | 630.0 - 275.5 | 0.1027 - 0.0023 | 62.26 |
| 03608 ‡ | 1970 - 2010 | 575.3 - 418.7 | 0.1072 - 0.0158 | 62.53 |
| 03717 † | 1970 - 2001 | 614.6 - 166.4 | 0.0956 - 0.0032 | 62.32 |
| 03835 ‡ | 1970 - 2010 | 646.3 - 421.2 | 0.0048 - 0.0000 | 81.19 |
| 04053 | 1970 - 2010 | 310.1 - 260.7 | 0.2779 - 0.1025 | 30.35 |
| 04119 † | 1970 - 2002 | 633.3 - 188.6 | 0.0051 - 0.0000 | 81.18 |
| 04221 †‡ | 1970 - 2010 | 432.9 - 383.2 | 0.1701 - 0.0818 | 102.83 |
| 04330 † ⋆ ◇‡ | 1970 - 2003 | 382.4 - 190.1 | 0.2636 - 0.0019 | 31.08 |
| 04726 † | 1970 - 2001 | 643.5 - 314.5 | 0.0996 - 0.0014 | 62.84 |
| 04849 †‡ | 1971 - 2005 | 642.7 - 228.7 | 0.0048 - 0.0000 | 81.21 |
| 04940 † | 1970 - 2001 | 654.1 - 179.6 | 0.1021 - 0.0005 | 62.79 |
| 05977 ‡ | 1970 - 2010 | 442.1 - 238.1 | 0.7274 - 0.6114 | 29.58 |
| 05998 ‡ | 1970 - 1999 | 407.8 - 222.8 | 0.7222 - 0.5646 | 28.16 |
| 06073 †‡ | 1972 - 2010 | 257.0 - 215.4 | 0.4193 - 0.2195 | 52.17 |
| 14756 ‡ | 1973 - 2010 | 381.2 - 221.6 | 0.6707 - 0.5166 | 26.60 |

† satellites used in the study by Emmert *et al.* [28]
⋆ satellites used in the study by Keating *et al.* [56]
◇ satellites used in the validation exercise by Saunders *et al.* [105]
‡ satellites used in the validation exercise by Saunders *et al.* [106]

# 5 Methodology

This Section presents the methodology required to fulfil the research objectives. There are four sections: orbital propagation via numerical integration; the determination of a satellite's ballistic coefficient; a method to infer thermospheric density information from satellite drag data; and the derivation of long-term secular density change.

## 5.1 Orbit Propagation

The research objectives outline the necessity for the ability to propagate numerically a satellite orbit over a period of time given an initial ephemeris. TLE data provides this ephemeris. Thus, an Earth-orbital propagator for thermospheric analysis (AETHER) was created for this study. This subsection presents the tools and methods used when performing orbital propagation. AETHER was written in the computing language C/C++. Throughout this subsection, describing the numerical orbit propagation, the various subroutines that make up AETHER are explained. For additional detail and clarity, some of AETHER's code is presented in Section 11.2 of the Appendices. However, for those readers less literate in computational programming, understanding the code is not a prerequisite for comprehension of the main text.

The basis of numerical orbit propagation involves predicting a future state given an initial state. The initial state is given as a state vector, which describes an object's position and velocity. Secondly, calculations of the perturbing accelerations are made and combined to give an acceleration vector. A parameter intrinsic to numerical orbit propagation is the time step, or integration step. This defines how far in the future the prediction is to be made. The future position vector is calculated by multiplying by the initial velocity vector by the time step. Similarly, the future velocity vector is calculated by multiplying the combined acceleration vector by the time step. This process is repeated until some specified condition is reached, usually after a pre-defined period of time, and is the principle of numerical orbit propagation.

A state vector contains six elements: three Cartesian components for both position and velocity ($\mathbf{r} = r_x, r_y, r_z$ and $\mathbf{v} = v_x, v_y, v_z$). A state vector is required for the initial condition of a satellite's ephemeris. The perturbing acceleration vector is a sum of all the component accelerations from the various sources, some of which are outlined in Figure 2, and given by

$$\ddot{\mathbf{r}} = \ddot{\mathbf{r}}_{Earth} + \ddot{\mathbf{r}}_{Drag} + \ddot{\mathbf{r}}_{Moon} + \ddot{\mathbf{r}}_{Sun} + \ddot{\mathbf{r}}_{SRP}, \tag{27}$$

where the subscript $Earth$ denotes the gravitational acceleration of the Earth, $Drag$ denotes the aerodynamic drag due to the atmosphere, $Moon$ and $Sun$ indicate the effects of the Moon and Sun's gravity and $SRP$ denotes perturbations due to solar radiation pressure.

Numerical orbital propagation can be broken down into three main components: the mathematical representation of the virtual environment, i.e. the coordinate system, through which the orbit will be propagated, the numerical integration technique, and the calculation of the perturbing accelerations given in equation (27). The next subsection defines the coordinate system used by AETHER, and how it acts as the reference frame when propagating orbits.

### 5.1.1 Coordinate Systems

As a significant portion of the perturbations modelled in AETHER are based in a geocentric coordinate system, that is one relative to the geometric shape of the Earth, it is logical that AETHER also used a coordinate system that is also geocentric. The TEME coordinate system used by the TLE data, in which the output state vector is based, is geocentric and has the $xy$-plane coincidental with Earth's equatorial plane. With a position vector $\mathbf{r}$ given in the TEME coordinate system the calculations of geocentric latitude $\phi$, longitude $\lambda$ and altitude $h$ are simply defined by

$$\phi = \arcsin\left(\frac{r_z}{|\mathbf{r}|}\right), \tag{28}$$

$$\lambda = \arctan\left(\frac{r_y}{r_x}\right) - \mathrm{GST}, \tag{29}$$

$$h = |\mathbf{r}| - E_r\left[1 - 0.0033528197\sin(\phi)\right], \tag{30}$$

where $E_r$ is the Earth's equatorial radius and $\mathrm{GST}$ is the Greenwich Sidereal Time. Note that the calculation of the inverse Tangent function when deriving the longitude $\lambda$ is quadrant dependent. In equation (30) the calculation of altitude departs from a simple subtraction of the Earth's radius from the distance of the satellite from the centre of the Earth due to the Earth being an oblate spheroid.

Therefore, the coordinate system that AETHER used for orbit propagation of TLE state vectors was that of the TEME system [58], which is described by:

- the $z$-axis aligning with the instantaneous North pole;
- the $x$-axis aligning with the mean direction of the vernal equinox of epoch;
- and the $y$-axis completing the right-handed system.

Over approximately 25,765 years the vernal equinox rotates a full 360° on the celestial sphere. This is due to the precession of the Earth's rotational axis. The precession rate per year of the vernal equinox $\omega_\gamma$ is therefore given by

$$\omega_\gamma = \frac{360^\circ}{25,765} = 0.01397244 \ \text{°/year.} \tag{31}$$

Over the last 50 years spanning the historical TLE data set, the direction of the vernal equinox has moved by approximately 0.692°. Errors of the order of kilometres can occur by not accounting for this angular change when predicting accurate ephemerides.

The ephemerides for the relative positions of the Sun, Moon and Earth are given in the reference frame J2000.0. This coordinate system uses a dynamical-equinox of epoch J2000.0 inertial reference system, where the epoch of J2000.0 is the Julian date of noon on January 1st 2000 GMT (JD 2451545.0) [128]. This coordinate system is described with

- the $z$-axis normal to the ecliptic plane;
- the $x$-axis aligned with the mean direction of the vernal equinox of J2000.0;

- and the $y$-axis completing the right-handed system.

The description ‘mean’ signifies that nutation effects in the Earth’s rotation are averaged.

Directional vectors describing the positions of third-bodies needed to be manipulated for correct alignment within the TEME coordinate axes. To transpose vectors given in the coordinate systems of J2000.0 to that of the TEME system required two matrix rotations. Figure 10 shows the difference between the TEME and J2000.0 coordinate systems. The order in which the vectors are rotated is important when applying matrix algebra to coordinate systems. Therefore, to convert from J2000.0 to the TEME system the order of the two rotations are described below.

1. Aligning the $x$-axes: the vernal equinox needed to be converted from J2000.0 to the mean equinox of epoch via a rotation about the $z$-axis by an amount calculated from equation (31);
2. Aligning the $z$-axes: the celestial pole of J2000.0 needed to be parallel with the tilt of the Earth’s rotational axis, which required a rotation about the $x$-axis of 23.43929111° [78].

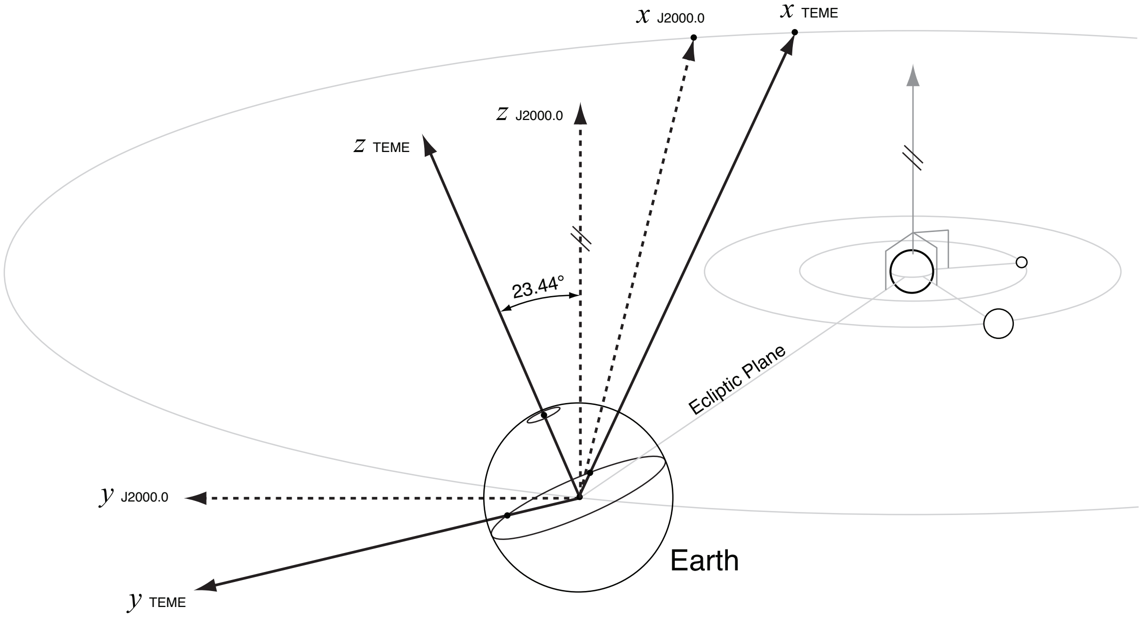

Figure 10: *The orientations of the TEME and J2000.0 coordinate systems.*

This rotation of the J2000.0 coordinate system about the $z$ and $x$-axis required the matrix transformation given by

$$\begin{Bmatrix} X_{TEME} \\ Y_{TEME} \\ Z_{TEME} \end{Bmatrix} = \begin{Bmatrix} \cos(\gamma) & -\sin(\gamma)\cos(\theta) & \sin(\gamma)\sin(\theta) \\ \sin(\gamma) & \cos(\gamma)\cos(\theta) & -\cos(\gamma)\sin(\theta) \\ 0 & \sin(\theta) & \cos(\theta) \end{Bmatrix} \begin{Bmatrix} X_{J2000.0} \\ Y_{J2000.0} \\ Z_{J2000.0} \end{Bmatrix}, \tag{32}$$

where $\gamma$ is the deviation from the equinox of Julian date 2451545.0 to that of TLE epoch and $\theta$ is the tilt of the Earth’s rotational axis (23.43929111°). AETHER’s coding for this matrix transformation between the coordinate systems of TEME and J2000.0 is outlined in Section 11.2.2 of the Appendix.

### 5.1.2 Numerical Integration Method

To carry out the orbital propagation, a numerical integration technique is required. The entire process would be compromised if the numerical integration technique was of inadequate precision. There are many numerical integrations techniques that provide varying levels of precision. Therefore, careful selection of the numerical integration method is required to obtain reliable results.

Numerical orbit propagation periodically calculates state vectors at discrete time intervals separated by a time step $\Delta t$. As the orbital perturbations vary over a satellite's orbit, the smaller the time step, the less the perturbations will vary from their previous state, which will produce a more accurate orbit propagation. However, using smaller time steps means a larger number of perturbation calculations per orbit, which has the undesired effect of increasing computational effort.

Previous studies by the author [102 & 103] used a 4th Order Runge-Kutta (RK4) integration method to perform orbital propagation. The RK4 was sufficiently accurate for these studies due to the distances involved (the gravitational sphere of influence of the planet Mars) and the relatively small rate of change of the perturbing acceleration vector. Therefore, for orbit propagations where the rate of change of acceleration vector is small, the RK4, with its low requirement of computational effort, is a suitable integration method. When calculating relative positions of the Earth, Moon and Sun for luni-solar and SRP perturbations for this study the RK4 technique is used. For this reason, a description of the RK4 shall be presented here and takes the form of

$$\mathbf{y}\left(t+\Delta t\right)=\mathbf{y}(t)+\Delta t\boldsymbol{\Phi}, \tag{33}$$

where $\mathbf{y}(t)$ is the satellite's state vector at time $t$. The variable $\boldsymbol{\Phi}$ denotes the increment function, which is a propagated state vector. It is calculated from the weighted mean of four vector gradients given by

$$\boldsymbol{\Phi}=\frac{1}{6}\left(\mathbf{k}_1+2\mathbf{k}_2+2\mathbf{k}_3+\mathbf{k}_4\right). \tag{34}$$

The gradients are defined by

$$\mathbf{k}_1=f\left[t,\mathbf{y}(t)\right], \tag{35}$$

$$\mathbf{k}_2=f\left[t+\frac{\Delta t}{2},\mathbf{y}(t)+\frac{\Delta t}{2}\mathbf{k}_1\right], \tag{36}$$

$$\mathbf{k}_3=f\left[t+\frac{\Delta t}{2},\mathbf{y}(t)+\frac{\Delta t}{2}\mathbf{k}_2\right], \tag{37}$$

$$\mathbf{k}_4=f\left[t+\Delta t,\mathbf{y}(t)+\Delta t\mathbf{k}_3\right]. \tag{38}$$

where the function $f[...]$ is the calculation of all the perturbing accelerations due to the gravity of the Earth, Moon and Sun.

The rate of change of the perturbing acceleration vector, affecting a satellite in LEO, is much greater than that affecting the Earth, Moon and Sun. Therefore, to accurately propagate orbits of satellites in LEO, the numerical integrator needed to be more sophisticated for two main reasons described below.

1. The epochs at which the TLE ephemerides are associated are not at regular intervals in time. They may take any value. Therefore a variable integration step size and/or a continuous (analytical) method was required so that the propagation time coincides perfectly with the TLE epochs under comparison.
2. The rate of change of the accelerations from the various perturbations in LEO is large hence making orbital propagation significantly more sensitive to errors. Therefore, a more accurate prediction of the acceleration vector was required than can be achieved with the RK4 technique.

From Montenbruck & Gill [76] a method is outlined by Horn [49], whereby a six-stage Runge-Kutta-Fehlberg method is adapted to give a seven-stage continuous method. This adaptation allows the method to produce data that is unevenly spread throughout time, if required. As it does not necessarily produce data at discrete intervals in time, it can essentially be thought of as a continuous method. The seven-stage Runge-Kutta-Fehlberg-Horn (RKFH) method, outlined below, can be used with a predefined integration step size that is constant over every TLE comparison the orbital propagator executes. In addition, it can be made to coincide exactly with the TLE epochs using a fitting parameter to propagate the orbit from the penultimate integration step to the TLE epoch, which is generally not equal to the integration step size.

The RKFH method is given by

$$\mathbf{y}\left(t+\sigma\Delta t\right)=\mathbf{y}(t)+\tau\Delta t\mathbf{\Phi}, \tag{39}$$

where $\tau$ is the fitting parameter for the penultimate step to the TLE epoch and all other symbols have their original meaning from the RK4 method above. The increment function $\mathbf{\Phi}$ is now given by

$$\mathbf{\Phi}=\sum_{i=1}^{7} b_i^{\star}\left(\tau\right)\mathbf{k}_i. \tag{40}$$

The coefficients used to calculate the continuous step function $b_i^{\star}$ in equation (40) are detailed in Section 11.3 of the Appendix. The method for calculating the vector coefficients $\mathbf{k}_i$ is defined by

$$\mathbf{k}_i=\text{rhs}\left[\mathbf{y}(t)+\Delta t\sum_{j=1}^{i-1} a_{ij}\mathbf{k}_j\right]. \tag{41}$$

The coefficients $a_{ij}$ are specific to the RKFH method and are detailed in Section 11.4 of the Appendix. The Horn method is an adaptation of the six-stage Runge-Kutta-Fehlberg method and both use the same coefficients $a_{ij}$. The seventh gradient calculation only requires previous gradient calculations as shown by

$$\mathbf{k}_7=\text{rhs}\left[\mathbf{y}(t)+\Delta t\left(\frac{1}{6}\mathbf{k}_0+\frac{1}{6}\mathbf{k}_4+\frac{2}{3}\mathbf{k}_5\right)\right]. \tag{42}$$

The coding for both the RK4 and RKFH methods are detailed in Sections 11.2.3 & 11.2.4 in the Appendix.

Investigations were conducted into varying the integration step size and comparing the position displacement errors in relation to a theoretical orbit. The theoretical orbit used Keplerian theory, which is a simple two-body system using an Earth-centred inverse square law gravity field and no other orbital perturbations. The displacement error was measured after an orbital propagation time equal of 96,000 seconds (1.1 days). This is the time between consecutive TLE epochs for the well-observed European Space Agency's Environmental Satellite (Envisat) [34]. The initial ephemeris conditions used an altitude of 500 km, at a longitude and declination of 0°. The initial velocity vector was calculated to give a zero-inclination circular orbit with an orbital speed of 7.61268 km/s. The results showed that after the 1.1-day propagation period with an integration step size of 2 seconds the displacement error between the numerical and theoretical positions was approximately 10 $\mu$m. This level of precision produces an accuracy that is greater than that of the TLE ephemerides by approximately six orders of magnitude, therefore incurring an unnecessary amount of computational effort.

This study required a more rigorous approach to optimising the integration step size, as a trade-off between precision and computational load. It was important that orbital propagation provided sufficiently accurate ephemerides at an acceptable level of computational run-time. Similarly to investigations described above, the determination of integration step size for AETHER used a comparison between the numerically propagated orbits and orbit parameters based on Keplerian theory. The errors in the orbital semi-major axis of the numerically propagated orbits were used to determine the necessary level of precision, again using only an Earth-centred inverse square law gravitational field.

An initial experiment was conducted using integration step sizes of 2.5, 5, 10, 20, 40, 80, 160 and 320 seconds. Circular orbits were used for simplicity as this meant the theoretical semi-major axis was equal to the magnitude of the position vector. Therefore any errors occurring from the numerical integration were simple to identify. The propagation was performed over an arbitrary integration time of 2 days to allow a measurable errors to manifest. Figure 11 shows the errors in the semi-major axis after a 2-day propagation period for the various step sizes.

Figure 11 shows spurious behaviour in the errors in semi-major axis for orbits with altitudes greater than 3,200 km and integration step sizes of less than 40 seconds. These behaviours demonstrate the effect of the limited precision of the numerical values used within AETHER. As the orbits increase in size and the integration step size reduces, the number of steps required to propagate a full orbit increases. Although extremely small (up to AETHER's numerical value$\times 5 \times 10^{-17}$), the cumulative effect of the errors associated with rounding to the precision used by AETHER became apparent when there were a large number of integration steps required to complete the orbit. This spurious behaviour was experimental evidence for the limiting accuracy attainable by AETHER. In these specific orbit scenarios, it is the precision of the numerical values used in AETHER that returns the accuracy, which from Figure 11 shows errors with orders of magnitude less than $10^{-9}$ km.

From [124], the ephemerides derived from TLE data in their most accurate form can provide an accuracy of approximately 100 metres. Estimating thermospheric density essentially

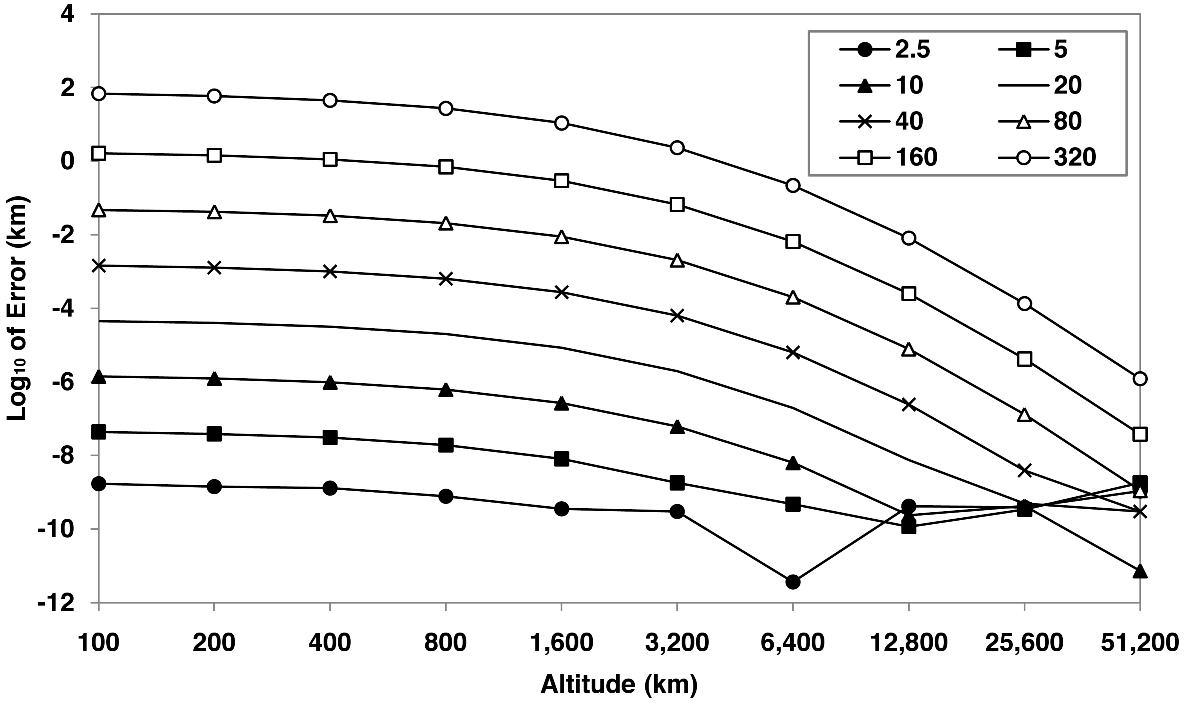

Figure 11: *The magnitudes of errors in the semi-major axis between a numerically propagated and theoretical Keplerian orbit after a 2-day propagation period for the various integration step sizes (in seconds).*

relies on accurately measuring the size of orbits. Therefore, reducing the error in this measurement will make the signal of any density change clearer, and easier, to detect. To qualitatively increase the signal-to-error ratio of long-term thermospheric density variations, the required accuracy from the numerical integrator was set at approximately two orders of magnitude less than the expected ephemerides errors associated with the TLE data. From Figure 11, this implied an integration step size of no more than 20 seconds and a propagated ephemeris error of less than 1%.

The accuracy dependence on semi-major axis is an additional feature presented in Figure 11. More specifically, this is a dependency on the magnitude of the perturbing acceleration. This makes intuitive sense: for satellite orbits subjected to large perturbing accelerations, the rate of change of velocity vector will also be comparatively large. Therefore, to sustain ephemeris accuracy, the acceleration vector, and hence the velocity vector, would need to be evaluated and corrected with high frequency, implying a small integration step size. For satellites with high eccentricity, the magnitude of the acceleration vector varies significantly as the satellite moves through its orbit. As a result, a variable integration step size was deemed the solution as this could provide the optimal step size relative to the magnitude of the acceleration vector.

The error returned from a 20-second step size in a 100-km altitude orbit ($\epsilon_{20}$) was used as the target accuracy when determining a variable step size model based on the magnitude of the acceleration vector. This error was approximately $10^{-4.5}$ km. More simulations were performed, than shown in Figure 11, to obtain a trend of step size with acceleration magnitude that yielded the same accuracy as that of $\epsilon_{20}$. From this data set an empirical model was derived. A best fit power function was applied to the data using the method of least squares. Figure 12 shows the trend of step size with respect to the acceleration magnitude as well as the empirically derived power function. The power function fitted the data points with $R^2$ = 1.0000.

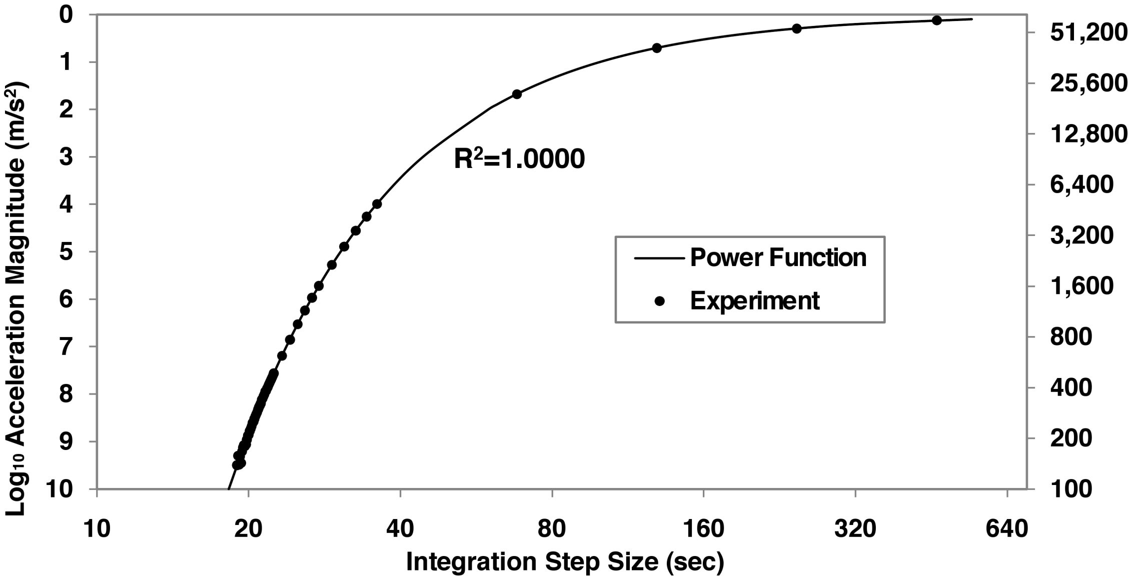

Figure 12: *The variation of integration step size with altitude that returned the equivalent accuracy as* $\epsilon_{20}$. *The best fit power function is shown, which gave* $R^2$ *= 1.0000.*

The function presented in Figure 12 is dependent on the magnitude of the summed acceleration vector from all perturbations included in AETHER. The function takes the form

$$\Delta t = 0.4847\ddot{\mathbf{r}}^{-0.7989}, \tag{43}$$

where $\ddot{\mathbf{r}}$ is the summed acceleration vector given by equation (27). The implementation of this variable step size in AETHER is presented in Section 11.2.1 of the Appendix: lines 0218-0225.

Numerical propagation using a variable integration step size is most beneficial in this study when analysing satellites in highly eccentric orbits. As this study deals with satellite orbits in the atmosphere, the perigee altitudes of the analysed orbits will be in a region of high-magnitude acceleration perturbations and thus implying the use of a small integration step size. However, as the satellites are propagated through the apogee regions, regions of relatively low-magnitude acceleration perturbations, a large step size can be used to make the method more efficient.

The aim of using a variable integration step size is to retain sufficient orbital propagation accuracy across the full range of analysed orbits as well as decrease the required computational effort. Therefore, experimental simulations with varying orbital geometry were conducted and used to analyse the effectiveness of the variable step size function defined above. The considered orbital geometries had perigee altitudes between 100 and 600 km at intervals of 100 km and eccentricity values from 0.0 to 0.4 at intervals of 0.1. This dataset was representative of the majority of the utilised TLE data.

Initially, a set of experimental simulations was performed to establish a baseline for comparison with the variable step size results. This was done for all orbit geometries defined previously using a total integration period of two days and an integration step size of 20 seconds. The errors in semi-major axis between the propagated orbits and the equivalent theoretical Keplerian orbits were again used to gauge the accuracy of the integration method. As the integration period of two days was fixed as was the integration step size, the computational run-time for all orbit geometries was relatively equal, as expected. Variations could only be from the computer's processor performance, the amplitudes of which were approximately 10%. To establish a baseline run-time, against which improvements could be normalised and compared, the average run-time of all the experimental simulations was used, which is denoted by $\bar{t}_{cpu}$. The run-times, normalised against $\bar{t}_{cpu}$, and errors in semi-major axis for each experiment are shown with respect to perigee altitude in Figure 13.

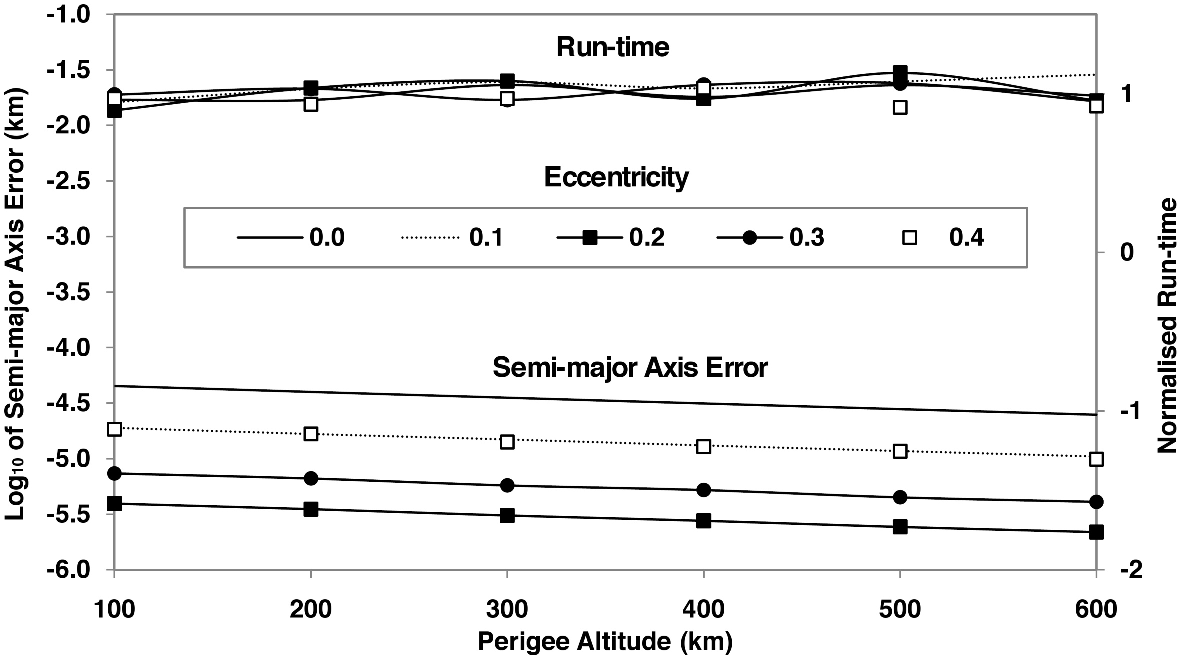

Figure 13: *The normalised run-times against $\bar{t}_{cpu}$ and errors in semi-major axis for each orbit geometry: perigee altitudes 100 - 600 km and orbit eccentricities 0.0 - 0.4.*

Next, the variable integration step size function, defined by equation (43), was included in AETHER and the experimental simulations were repeated using the same orbital geometries as before. The results are shown in Figure 14. As intended, the errors from the semi-major axis comparison did not exceed the target $\epsilon_{20}$ accuracy of $10^{-4.5}$ km. Figure 14 presents successfully the aim of this exercise of reducing the computational run-time for orbits with high eccentricity. The cost of this reduction in computational run-time was the diminished accuracy of the higher eccentricity orbits. As their accuracies did not degrade beyond the $\epsilon_{20}$ accuracy, there was no practical loss in propagation fidelity. It shows that, originally, the propagations were attaining an unnecessary level of accuracy, at the cost of computational run-time.

From Figure 14, the normalised run-times for each value of eccentricity were averaged and plotted against eccentricity, as shown in Figure 15. A linear regression line was fitted through the datum points to obtain a function that could be used to determine the benefit of this method when using the full TLE data. The fit of the regression line gave $R^2$ = 0.9761.

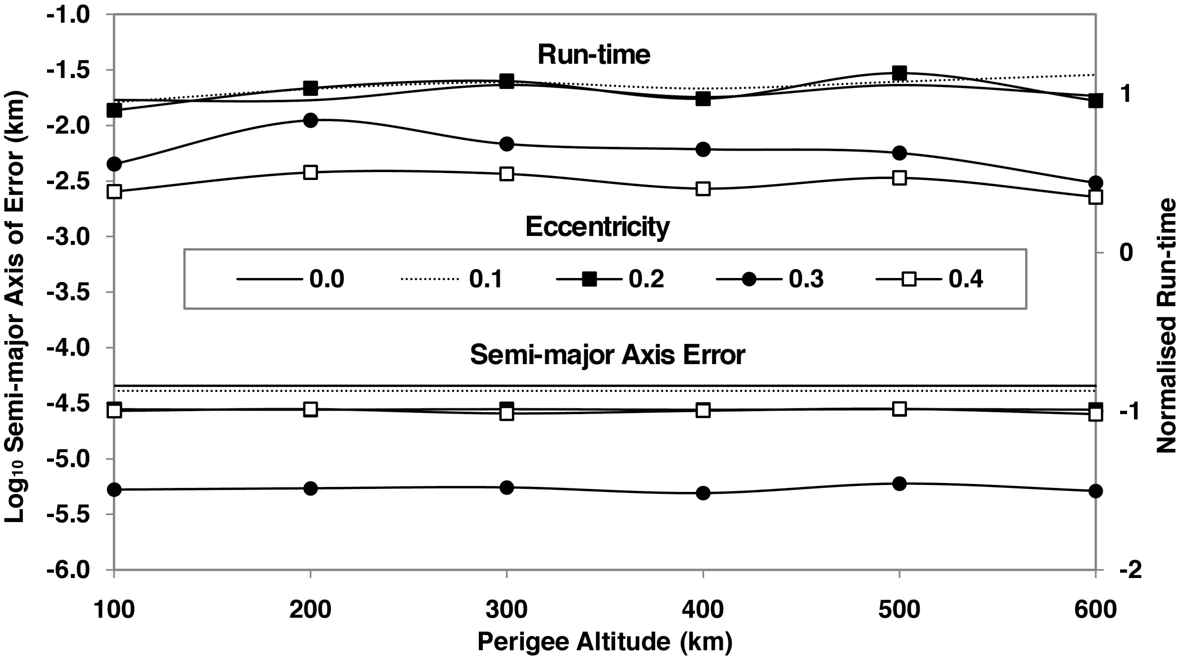

Figure 14: *With the addition of the variable integration step size function, the results from the repeated experiments analysing the normalised run-time and errors in semi-major axis for the same orbit geometries as in Figure 13.*

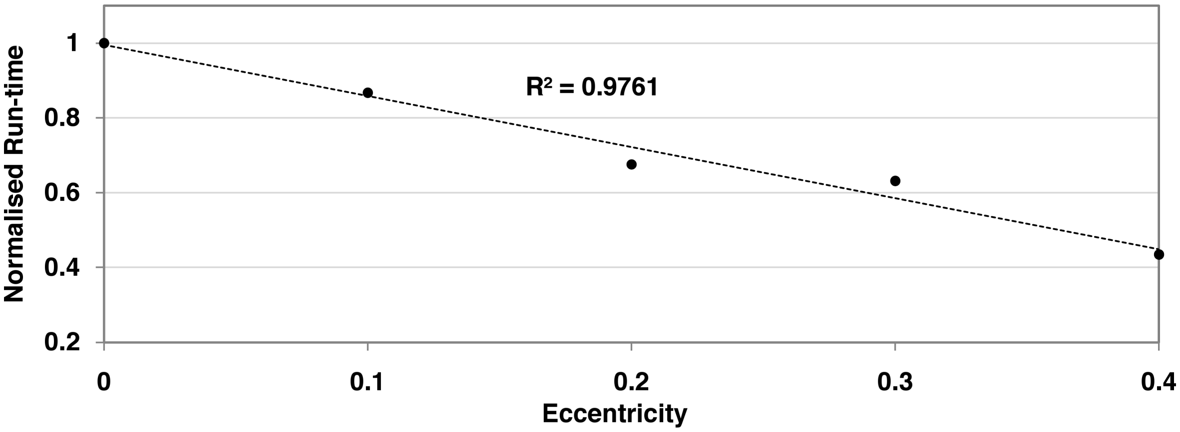

Figure 15: *The average values of run-time plotted with their associated value of eccentricity, from Figure 14, with a best-fit linear regression line. The values of run-time were again normalised using* $\bar{t}_{cpu}$ *and the fit of the regression line gave* $R^2$ *= 0.9761.*

The function of the linear regression line was given by

$$t_{cpu} = -1.3659986 * e + 1, \tag{44}$$

and only to be used as a guide to estimate the benefits of using the variable integration step size function with eccentricities analysed in this optimisation process.

To demonstrate the variable integration step size function in action, a test orbit was selected and the variation of step size was recorded throughout orbital propagation by AETHER. The orbit geometry had a perigee altitude of 100 km and an apogee altitude equal to that of a geostationary orbit (35,863 km), implying an eccentricity of 0.734. The variation of orbital altitude along with the calculated integration step size for this test case is shown in Figure 16.

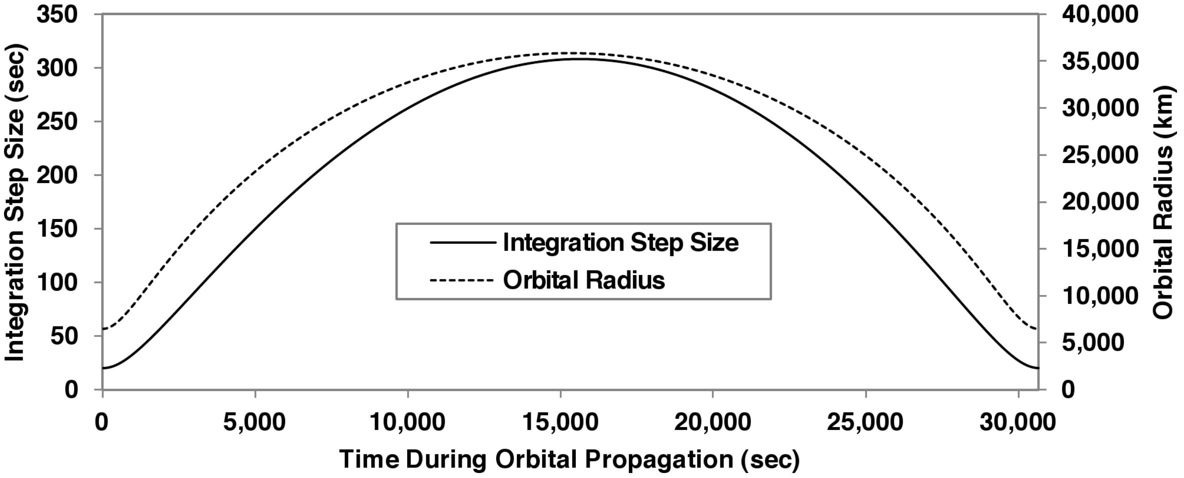

Figure 16: *The variation of orbital altitude along with the calculated integration step size for the test orbit: perigee = 100 km, apogee = 35,863 km (Geostationary orbit value) &* $e$ *= 0.694.*

The averaged eccentricities of the 41 satellites whose orbital historical TLE data contributed to this study were used to obtain an expected improvement in run-time using equation (44). Figure 17 shows the results. For any datum point with a normalised run-time value less than one meant that there would be a saving in run-time compared to the time it would take to propagate the orbit with a constant step size of 20 seconds. It is clear that a reduction in the run-time for many of the 41 satellites would be obtained.

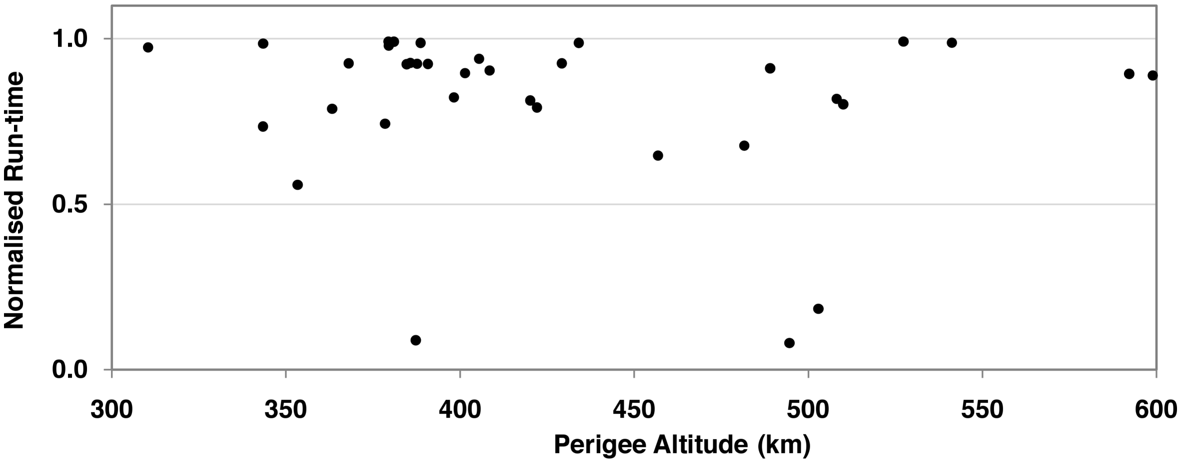

Figure 17: *The expected improvement in computational run-time for the 41 satellites whose orbital historical TLE data contributed to this study.*

During this optimisation process no orbital perturbations were included in the analysis. However, it was the magnitude of the acceleration vector that was used to determine the variable integration step size, which is the sum of all satellite perturbations as well as primary gravity. Therefore, the analysis holds for orbit propagation when perturbations are included in the acceleration vector.

### 5.1.3 The Earth's Gravity Field

Owing to the Earth's spherical asymmetry, a radially symmetric acceleration field, such as that defined by the inverse square law

$$\ddot{\mathbf{r}}_{grav} = -\frac{\mu}{r^3}\mathbf{r}, \tag{45}$$

is not sufficient for accurate geocentric orbital propagation. Here $\ddot{\mathbf{r}}$ is the acceleration vector and $\mathbf{r}$ is the position vector of the satellite, both with the origin at the centre of the Earth (geocentric). $\mu$ is the gravitational constant of the Earth (398600.4415 km$^3$/s$^2$) and $r$ is the magnitude of the geocentric position vector. Instead, a function based on spherical harmonics was used, as given by Roy [100] and Kaula [52]. In this approach, the variations in the gravity field are defined by the values of the normalised coefficients ($\bar{C}_{nm}$ and $\bar{S}_{nm}$), usually taken from a standard geopotential model. In spherical coordinates, the acceleration due to an asymmetric Earth gravity model can be expressed as

$$\ddot{\mathbf{r}}_{Earth} = \nabla\frac{GM}{r}\sum_{n=0}^{\infty}\sum_{m=0}^{n}\frac{R_E^n}{r^n}\bar{P}_{nm}\left\{\sin\phi\right\}\left(\bar{C}_{nm}\cos\left(m\lambda\right)+\bar{S}_{nm}\sin\left(m\lambda\right)\right), \tag{46}$$

where $R_E$ is the equatorial radius of the Earth, $\lambda$ denotes geocentric longitude and $\bar{P}_{nm}\left\{\sin\phi\right\}$ are normalised Legendre polynomials of order $n$ and degree $m$, in which the spherical harmonics are expanded in terms of the Sine of geocentric latitude $\phi$. The gradient function is defined as

$$\nabla\left\{U\right\} = \left(\frac{\partial U}{\partial x}\mathbf{i}+\frac{\partial U}{\partial y}\mathbf{j}+\frac{\partial U}{\partial z}\mathbf{k}\right). \tag{47}$$

Equation (46) defines acceleration in terms of spherical coordinates and needs to be converted to Cartesian coordinates for use in AETHER. Then, the gradient of the function needs to be obtained for the accelerations to be successfully calculated. The process, presented below, for converting the gradient of the geopotential acceleration from spherical coordinates to Cartesian coordinates is provided by Vallado [120]. To express $U$ in terms of Cartesian coordinates as opposed to spherical coordinates, the chain rule must be applied giving

$$\ddot{\mathbf{r}}_{grav} = \left(\frac{\partial U}{\partial r}\left(\frac{\partial r}{\partial \mathbf{r}}\right)+\frac{\partial U}{\partial \phi}\left(\frac{\partial \phi}{\partial \mathbf{r}}\right)+\frac{\partial U}{\partial \lambda}\left(\frac{\partial \lambda}{\partial \mathbf{r}}\right)\right), \tag{48}$$

where

$$\mathbf{r} = x\mathbf{i}+y\mathbf{j}+z\mathbf{k}. \tag{49}$$

Dividing equation (48) into its Cartesian components for the explicit accelerations gives

$$\ddot{x} = \frac{\partial U}{\partial r}\frac{\partial r}{\partial x}+\frac{\partial U}{\partial \phi}\frac{\partial \phi}{\partial x}+\frac{\partial U}{\partial \lambda}\frac{\partial \lambda}{\partial x}, \tag{50}$$

$$\ddot{y} = \frac{\partial U}{\partial r}\frac{\partial r}{\partial y}+\frac{\partial U}{\partial \phi}\frac{\partial \phi}{\partial y}+\frac{\partial U}{\partial \lambda}\frac{\partial \lambda}{\partial y}, \tag{51}$$

and

$$\ddot{z} = \frac{\partial U}{\partial r}\frac{\partial r}{\partial z}+\frac{\partial U}{\partial \phi}\frac{\partial \phi}{\partial z}+\frac{\partial U}{\partial \lambda}\frac{\partial \lambda}{\partial z}. \tag{52}$$

Individually taking the partial derivative of the function $U$ with respect to the spherical components yields

$$\frac{\partial U}{\partial r}=\frac{GM}{r^2}\sum_{n=2}^{\infty}\sum_{m=0}^{n}\left(\frac{R_E}{r}\right)^n(1+n)\,\bar{P}_{nm}\left\{\sin\phi\right\}\left(\bar{C}_{nm}\cos\left(m\lambda\right)+\bar{S}_{nm}\sin\left(m\lambda\right)\right), \tag{53}$$

$$\frac{\partial U}{\partial \phi}=\frac{GM}{r}\sum_{n=2}^{\infty}\sum_{m=0}^{n}\left(\frac{R_E}{r}\right)^n\frac{\partial\left(\bar{P}_{nm}\left\{\sin\phi\right\}\right)}{\partial\phi}\left(\bar{C}_{nm}\cos\left(m\lambda\right)+\bar{S}_{nm}\sin\left(m\lambda\right)\right), \tag{54}$$

and

$$\frac{\partial U}{\partial \lambda}=\frac{GM}{r}\sum_{n=2}^{\infty}\sum_{m=0}^{n}\left(\frac{R_E}{r}\right)^n m\bar{P}_{nm}\left\{\sin\phi\right\}\left(\bar{S}_{nm}\cos\left(m\lambda\right)-\bar{C}_{nm}\sin\left(m\lambda\right)\right). \tag{55}$$

The remaining portions of the spherical partials of equations (50)-(52) with respect to the Cartesian components are given in vector form below in equations (56)-(58) for the final explicit definitions of the Cartesian acceleration components given by

$$\ddot{x}=\left\{\frac{1}{r}\frac{\partial U}{\partial r}-\frac{z}{r^2\sqrt{x^2+y^2}}\frac{\partial U}{\partial\phi}\right\}x-\left\{\frac{1}{x^2+y^2}\frac{\partial U}{\partial\lambda}\right\}y, \tag{56}$$

$$\ddot{y}=\left\{\frac{1}{r}\frac{\partial U}{\partial r}-\frac{z}{r^2\sqrt{x^2+y^2}}\frac{\partial U}{\partial\phi}\right\}y+\left\{\frac{1}{x^2+y^2}\frac{\partial U}{\partial\lambda}\right\}x, \tag{57}$$

and

$$\ddot{z}=\frac{1}{r}\frac{\partial U}{\partial r}z+\frac{\sqrt{x^2+y^2}}{r^2}\frac{\partial U}{\partial\phi}, \tag{58}$$

where

$$\ddot{\mathbf{r}}_{grav}=(\ddot{x},\ddot{y},\ddot{z}). \tag{59}$$

The coding for this process is presented in section 11.2.5 of the Appendix: lines 0311-0351.

Equation (46) requires the normalised Legendre polynomials to order and degree 20. The normalisation comes in the form of

$$\bar{P}_{nm}=\sqrt{\frac{(2-\delta_{0m})(2n+1)(n-m)!}{(n+m)!}}P_{nm}. \tag{60}$$

where

$$\delta_{0m}=\left\{\begin{array}{c}1,\,m=0\\0,\,m\neq 0\end{array}\right\}. \tag{61}$$

The Legendre polynomial is then,

$$P_{nm}(x)=\frac{1}{2^n n!}(1-x^2)^{\frac{m}{2}}\frac{\mathrm{d}^{n+m}}{\mathrm{d}x^{n+m}}(x^2-1)^n, \tag{62}$$

where

$$x\equiv\sin(\phi). \tag{63}$$

Deriving the Legendre polynomials using equation (62) becomes extremely cumbersome much beyond order five. Therefore, a more efficient method can be used that employs a recursive algorithm [120] given by

$$P_{n,0}(x) = \frac{1}{n}\left\{(2n-1)xP_{n-1,0}(x) - (n-1)P_{n-2,0}(x)\right\}, \tag{64}$$

$$P_{n,m}(x) = P_{n-2,m}(x) + (2n-1)P_{1,1}(x)P_{n-1,m-1}(x), \tag{65}$$

and

$$P_{n,n}(x) = (2n-1)P_{1,1}(x)P_{n-1,n-1}(x), \tag{66}$$

where

$$P_{0,0}(x) = 1, \tag{67}$$

$$P_{1,0}(x) = x = \sin(\phi), \tag{68}$$

and

$$P_{1,1}(x) = \cos(\phi). \tag{69}$$

One of the latest geopotential models is the 70th order Joint Gravity Model 3 (JGM3) [117]. A comparison of all the relevant perturbations encountered by a satellite are represented in terms of their magnitude from Figure 2 and Montenbruck & Gill [77]. From these, it is apparent that gravitational perturbations of order $n \geq 20$ are orders of magnitude smaller than atmospheric drag accelerations at equivalent altitudes. Therefore, the maximum detail of the asymmetric gravitational model required for orbital propagation in this study allows the JGM3 model to be truncated at order $n = 20$. However, it will be shown later that lower precision of the gravity model is acceptable to further reduce computational effort when inferring long-term thermospheric density trends.

For every orbit propagation step in AETHER, the Legendre polynomials are re-calculated. Recalling that each step requires seven gradient calculations for the RKFH method, each of which requires the calculation of 210 Legendre polynomials (20 + 19 + 18 + ... + 1), it is clear that calculation of this acceleration contributes to the majority of the computational run-time. A truncated version of the coding for the Legendre polynomials is presented in Section 11.2.5 of the Appendix: lines 0296-0309.

During the implementation of the JGM3 in AETHER, several checks were made to ensure the propagator was functioning correctly. As the propagation method is iterative, it was necessary to ensure cumulative errors were being made. This method was verified by plotting the magnitudes of the acceleration produced by the JGM3 for the entire globe. If there were no numerical discontinuities between the variation of the accelerations then there could be no cumulative computational errors in the code. As the magnitudes of accelerations calculated from the gravity harmonics of order $\geq 3$ are orders of magnitude smaller than those of order 2, Figure 18 shows only the gravity harmonics $\geq 3$ for the JGM3.

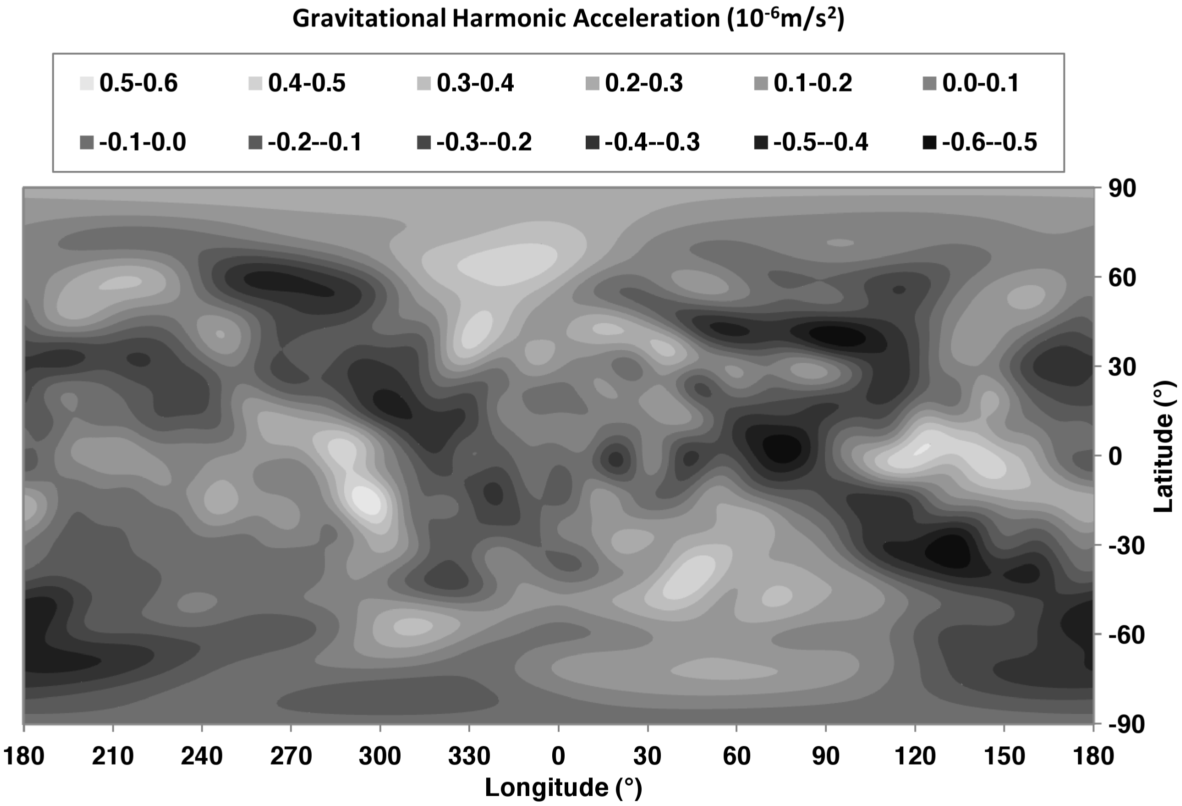

Figure 18: *The deviation of Earth gravity harmonics of order* $\geq$*3 for the JGM3 from the* $\frac{GM}{r^2}$ *component. Note no cumulative effect over the Earth.*

### 5.1.4 Empirical Atmospheric Model

It is necessary to predict the atmospheric density at a satellite's position when modelling the effects of atmospheric drag during orbit propagation. To do this, a mathematical model of the atmosphere is required to provide a density estimate, $\rho$, in the calculation of atmospheric drag, which is repeated here for clarity:

$$\ddot{r}_{drag} = -\frac{1}{2}\rho v^2 \frac{C_d A}{m}, \tag{70}$$

The analytical models discussed here are based on a theoretical framework (using mathematical functions), the parameters of which are determined empirically. The three models that were studied in detail are:

1. CIRA-72 [19]: The Committee on Space Research (COSPAR) produced this international reference atmosphere (CIRA) in 1972. It is an empirical model of the neutral temperature and density of the thermosphere derived from atmospheric drag effects on satellite orbits. The input parameters specifying the atmospheric state are: altitude; geocentric latitude; sun declination; hour angle of sun; fraction of tropical year; magnetic index ($K_p$); a three-solar-rotation average of $F_{10.7}$; and previous day $F_{10.7}$. The model calculates neutral temperature, total density, and the densities of $N_2$, $O_2$, O, He, Ar, and H.
2. MSIS-86 [43]: Similar to the CIRA-72, this is an empirical model of neutral temperature and density of the thermosphere derived by in-situ mass spectrometry and incoherent scatter (MSIS) radar data in the years leading up to 1986. The input parameters are: date; time (UT); altitude; geocentric latitude and longitude; local solar time; daily averaged magnetic index ($A_p$); a three-solar-rotation average $F_{10.7}$; and the previous day $F_{10.7}$. A history of three-hourly magnetic indices ($a_p$) can be used for higher resolution detail during magnetic storms. The model calculates neutral temperature, total density, and the densities of $N_2$, $O_2$, O, He, Ar, and H.
3. NRLMSISE-00 [91]: This model is based on a broader range of observational data sets including in-situ mass spectrometry, incoherent scatter radar, solar occultation measurements of molecular oxygen, numerous drag and satellite accelerometer measurements as well as orbit derived densities. The NRLMSISE-00 requires the same inputs as the MSIS-86 model with the exception of $A_p$. Instead, the NRLMSISE-00 uses the higher temporal resolution index of $a_p$. In addition to the densities of the species calculated by the MSIS-86 model, this model also includes predictions of atomic nitrogen and a high altitude (>500 km) 'anomalous oxygen' ($O^+$) component of total mass density that is not in thermal equilibrium at the local atmospheric temperature.

The CIRA-72 and MSIS-86 atmospheric models predict a neutral or total thermospheric density, meaning the atmospheric composition does not take account of ionised gas species that can potentially alter atmospheric temperature and density. Assuming a neutral atmosphere allows the temperature and density to be derived from analytical theory with greater simplicity.

The inclusion of ionic gas species requires additional electromagnetic physics, which in turn requires the empirical atmospheric model to include a more complicated analytical framework. Keating et al. [55] demonstrated that an appreciable $O^+$ component can exist and this contributes significantly to high-altitude drag and total mass density. In addition, the mass density attributable to other ionic species (e.g. $H^+$, $He^+$) was minor in comparison to $O^+$ under the conditions studied. As the $O^+$ component is not associated with neutral thermospheric composition, its omission introduces a source of error in any atmospheric model that does not explicitly account for it. This is the key difference between neutral (total) density and effective density which is the parameter experienced by satellites. Ultimately the exclusion of $O^+$ could result in an over estimation of the derived thermospheric densities because satellites would encounter more drag than predicted. Therefore, it is an important requirement for this study that the chosen atmospheric model includes the 'anomalous oxygen' component, and the NRLMSISE-00 is one such atmospheric model.

All the models mentioned here do not depend on calendar year and, therefore, do not exhibit any form of long-term density change. Instead, they show a snapshot of the atmosphere, represented by the best fit to the data available at the time the model was created. Therefore, the NRLMSISE-00, and others, will highlight any secular trend in the observed TLE data over long periods of time. To demonstrate the detail of the three atmospheric models described above, Table 2 shows the included atmospheric variations in the calculations for thermospheric density.

Table 2: *The included variations within the empirical atmospheric models. The bullet points represent the inclusion of the specific atmospheric variation and $T_{exo}$ is the exospheric temperature.*

| Variation | CIRA-72 | MSIS-86 | NRLMSISE-00 |
|---|---|---|---|
| Independent of year | ● | ● | ● |
| Solar $F_{10.7}$ Flux effect on mean $T_{exo}$ | ● | ● | ● |
| Symmetrical Annual | ● | ● | ● |
| Symmetrical Semi-annual | | ● | ● |
| Asymmetrical Annual | | ● | ● |
| Asymmetrical Semi-annual | | ● | ● |
| Diurnal | ● | ● | ● |
| Semidiurnal | | ● | ● |
| Daily Geomagnetic | ● | ● | ● |
| All UT & Longitudinal | | ● | ● |
| Combined Geomagnetic, UT & Longitudinal | | ● | ● |
| Terdiurnal | | ● | ● |
| Departures from diffusive equilibrium | | | ● |

As the models are created using a 'best fit' to the observed data sets, errors associated with each model can be calculated. Picone *et al.* [91] performed a statistical analysis and gave a comparison between the three atmospheric models and Jacchia's data, which was originally used to formulate the CIRA-72. Table 3 shows bias values of atmospheric density taken from Table 1 of Picone *et al.* [91], which vary with geomagnetic activity. Further, the Table shows the largest residuals occur during periods high geomagnetic activity.

Table 3: *The statistical comparison of the three empirical models to Jacchia's data.* $A_p$ *represents the daily average of the 3-hourly geomagnetic* $a_p$ *index.*

| $A_p$ | Altitude (km) | CIRA-72 | MSIS-86 | NRLMSISE-00 |
|---|---|---|---|---|
| $\leq 10$ | 200-400 | -0.04 | -0.06 | -0.06 |
|  | 400-800 | -0.07 | -0.08 | -0.07 |
| All | 200-400 | -0.07 | -0.06 | -0.07 |
|  | 400-800 | -0.09 | -0.07 | -0.08 |
| $\geq 50$ | 200-400 | -0.12 | -0.07 | -0.05 |
|  | 400-800 | -0.17 | +0.01 | -0.01 |

Table 3 shows no significant difference in the mean residuals between the MSIS-86 and the NRLMSISE-00. Therefore, the chemistry considered in the model and the coverage of observations were the deciding factors when choosing between this two models.

From the three empirical atmospheric models considered here, the model chosen to provide the atmospheric density estimates for the calculation of atmospheric drag was the NRLMSISE-00 model. This was mainly for two reasons: the inclusion of the anomalous oxygen component in the density prediction, and the largest set of observational data was used in its development. This will generally lead to a closer approximation to the 'true' atmospheric state. This is to say that, over widely varying geophysical conditions, the changes in the atmosphere will be more accurately represented by the NRLMSISE-00 atmospheric model.

Doornbos [25] has suggested that the most accurate and up-to-date model for representing density changes due to the solar EUV input is the Jacchia-Bowman 2006 (JB2006) [10] empirical atmospheric model. However the EUV indices it requires have only been available since the late 1990's. Therefore, using the JB2006 model would not be possible in this research project, which requires atmospheric density calculations for earlier historical periods. In addition, the JB2006 model does not accurately capture the variations due to geomagnetic activity as it uses Jacchia's code from the early 1970's (the same code used in CIRA-72). The JB2008 [119] empirical atmospheric model, a successor to both the NRLMSISE-00 and JB2006 model, was introduced in 2008. The JB2008 introduces the use of a new index to represent geomagnetic activity, the Disturbance Storm Time (Dst) index. The Dst index is measured hourly, instead of 3-hourly as is the case with the $a_p$ and $K_p$ indices, possibly leading to greater temporal resolution of predictions of atmospheric state. However the JB2008 uses the same EUV indices as the JB2006 thus remaining unsuitable for historical use.

The NRLMSISE-00 model requires various inputs to calculate atmospheric density. The NRLMSISE-00 model requires inputs of location, time of day, time of year, solar EUV irradiance, and magnetospheric energy input. For EUV and magnetospheric energy, the proxies of $F_{10.7}$ and $a_p$, respectively are used. NOAA provides these indices in various formats from measurements obtained through ground-based radar stations. The measurement of $F_{10.7}$ incorporates variabilities that require adjustment before use as inputs into the NRLMSISE-00 atmospheric model. The database of indices provided by NOAA contain three forms of $F_{10.7}$ [86]: observed magnitudes of $F_{10.7}$; adjusted magnitudes to remove a 7% variation caused by the annually-changing Earth-Sun distance; and absolute $F_{10.7}$ magnitudes that are further refined by a multiple of 0.9, to compensate for uncertainties in antenna gain and $F_{10.7}$ radiation reflected from the ground. These refinements performed by NOAA aim to provide the $F_{10.7}$ flux radiated from the Sun. However, for this study the $F_{10.7}$ radiation incident upon the Earth's atmosphere is the desired measurement. Therefore, it is the observed values that are used in the calculations of the NRLMSISE-00 density model.

Figure 19 shows a typical example of the data provided by the Dominion Radio Astrophysical Observatory databases [23] [accessed via NOAA 85 & 87]. The temporal resolution of the $F_{10.7}$ and $a_p$ data is daily and three-hourly respectively. To achieve a smooth variation in density calculation using the NRLMSISE-00 model in this study, linear interpolation of the daily $F_{10.7}$ flux index was performed to obtain intermediate $F_{10.7}$ values. Thus, the black line in Figure 19 precisely represents the $F_{10.7}$ input to the NRLMSISE-00 model as used in AETHER.

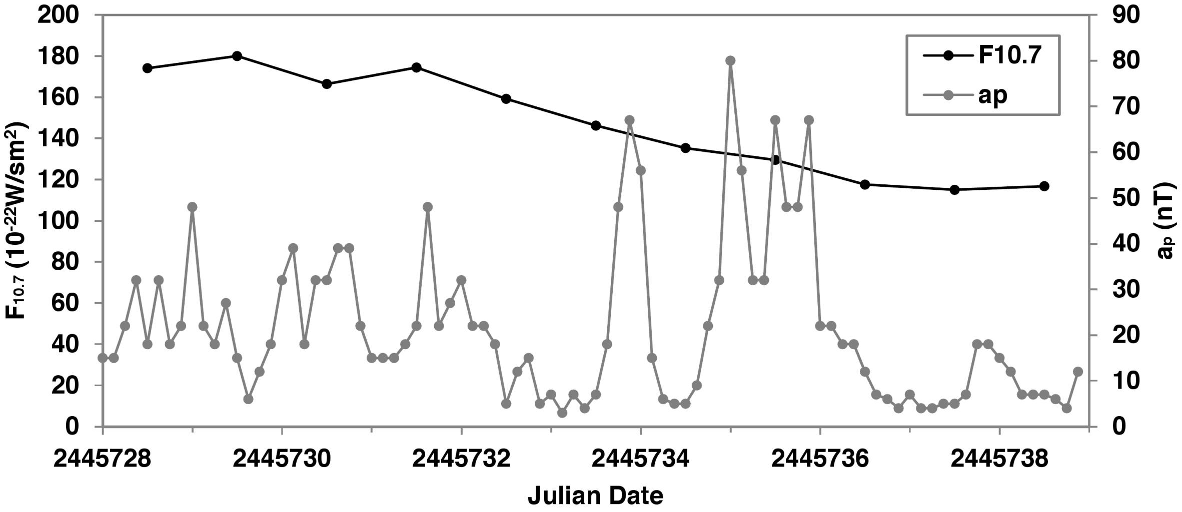

Figure 19: *The variation of the daily $F_{10.7}$ and three-hourly $a_p$ indices obtained from the NOAA databases [85 & 87] over an 11-day period. The plots show the highest temporal resolution available from the data sources.*

The variation of the geomagnetic index $a_p$ is not as smooth as that of the $F_{10.7}$ index. NOAA provides the $a_p$ index at three-hourly intervals for this reason. To calculate atmospheric density, the NRLMSISE-00 model requires an array of $a_p$ measurements ranging in time from the epoch of interest. The variation of the $a_p$ changes on a much finer time scale than that of $F_{10.7}$. Therefore, there is no justification to interpolate between measurements. As the epoch of propagation varies continuously, the nearest temporal value of the discretely measured $a_p$ values were used for the NRLMSISE-00 input array. The coding for calculations of $F_{10.7}$ and $a_p$ in AETHER are presented in Sections 11.2.6 & 11.2.7 of the Appendix.

With the publication of the NRLMSISE-00 model, the FORTRAN source code was also released. This code calculates the atmospheric parameters, such as density, given the required inputs. Brodowski [13] later published a version of the NRLMSISE-00, written in C++, which is used to calculate thermospheric density in AETHER.

### 5.1.5 Thermospheric Wind Model

Equation (1) requires the velocity of the satellite relative to the atmosphere to determine the acceleration due to drag. Following King-Hele [59], a theoretical approach is used whereby the velocity term in equation (1) is multiplied by a dimensionless factor $F$, depending on the position of the satellite relative to the Earth. This ‘wind factor’, defined by King-Hele [59], is given by

$$F \cong \left(1 - \frac{r\omega_r}{v}\cos i\right)^2, \tag{71}$$

where $r$ is the distance from the centre of the Earth, $v$ is the magnitude of the satellite’s inertial velocity, $\omega_r$ is the angular rotation rate of the Earth and $i$ is the satellite’s orbital inclination. Here, the entire atmosphere is assumed to co-rotate with the Earth. This is not accurate, as the atmosphere is a dynamic system with complex currents that do not co-rotate exactly with the Earth. For a more detailed representation of average atmospheric winds, the Horizontal Wind Model of 1993 (HWM-93) [47] can be employed. This takes the form of a computationally expensive mathematical model providing zonal and meridional wind profiles from average climatological and various geophysical conditions.

To derive thermospheric density trends, the method, by Picone *et al.* [92] and used in the studies by Emmert *et al.* [28 & 30], used

$$\mathbf{F} = \frac{\mathbf{v} - \mathbf{V}}{v^2}\left\{\frac{\mathbf{v} - \mathbf{V}}{|\mathbf{v} - \mathbf{V}|} \cdot \frac{\mathbf{v}}{v}\right\}, \tag{72}$$

to calculate the wind vector $\mathbf{F}$. Here $\mathbf{V}$ is the velocity vector of the wind, derived from a model such as HWM-93, and $\mathbf{v}$ is the inertial velocity vector of the satellite.

Differences between equation (71) and (72) typically amount to less than 3% when $\mathbf{V}$ is derived from the HWM-93 [92]. Therefore, to save on computational effort no empirical thermospheric wind model is included in AETHER. For further, more detailed, studies this is one factor to include that would increase the accuracy of the thermospheric density measurements.

The co-rotation of the atmosphere with the Earth is modelled in AETHER even though thermospheric wind velocities relative to the Earth are not. Excluding the effect of atmospheric co-rotation can lead to errors in the estimation of atmospheric drag by about 11%, which increases with altitude.

In AETHER’s coordinate system (TEME), the velocity vector $\mathbf{W}$ of a perfectly co-rotating atmosphere will have a constant $W_z$ component of zero. Therefore, only the $W_x$ and $W_y$ components require consideration. Assuming a perfect co-rotation implies an increasing velocity vector with altitude and the angular rotational velocity of the atmosphere will be equal to that of the Earth’s. In reality this is not the case as Coriolis and viscous effects cause a shearing effect between the layers of the atmosphere. Therefore, in a reference frame relative to the stars, such as TEME, the atmosphere will complete one rotation about its axis after one sidereal day (86,164 seconds). The atmospheric wind vector is then given by

$$\mathbf{W} = \frac{2\pi|\mathbf{r}|\cos\phi}{86,164}, \tag{73}$$

where $\mathbf{r}$ is the satellite's position vector and $\phi$ is the geocentric latitude. The vector $\mathbf{W}$ can now be separated in to its Cartesian components. To do this a consideration of the relative vector geometries is required. Figure 20 shows an example of the atmospheric wind velocity at a position, $\mathbf{r}_{xy}$, in the TEME coordinate system.

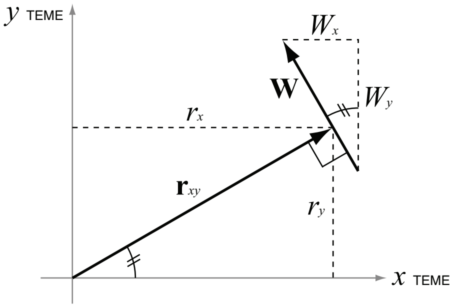

Figure 20: *The relative geometries of a position vector* $\mathbf{r}_{xy}$ *in the* $xy$*-plane to that of the co-rotating atmospheric wind vector* $\mathbf{W}$*.*

Therefore, the atmospheric wind vector can be given by

$$\mathbf{W} = \left\{ \begin{array}{c} W_x \\ W_y \\ W_z \end{array} \right\} = \left\{ \begin{array}{c} \frac{-r_y}{r_{xy}} |\mathbf{W}| \\ \frac{r_x}{r_{xy}} |\mathbf{W}| \\ 0 \end{array} \right\}, \tag{74}$$

where $r_{xy} = \sqrt{r_x^2 + r_y^2}$. Therefore, the velocity vector of the satellite relative to the atmosphere, used in equation (1), is given by

$$\mathbf{V_w} = \mathbf{v} - \mathbf{W} = \left\{ \begin{array}{c} v_x - W_x \\ v_y - W_y \\ v_z \end{array} \right\}. \tag{75}$$

where $\mathbf{v}$ is the geocentric satellite velocity vector. The coding that describes the co-rotating atmosphere in AETHER is presented in Section 11.2.5 for the Appendix: lines 0221-0244.

### 5.1.6 Luni-Solar Perturbations

To model the effects of the Moon and Sun's gravity on satellite orbits, an analysis of the orbital accelerations relative to the reference frames used in AETHER was required. In an inertial reference frame, the acceleration of an Earth orbiting satellite due to a perturbing body (subscript $\otimes$) is given by

$$\ddot{\mathbf{r}} = GM_{\otimes}\frac{\mathbf{s}-\mathbf{r}}{|\mathbf{s}-\mathbf{r}|^3}, \tag{76}$$

where $G$ is the universal gravitational constant, $M_{\otimes}$ is the mass of the perturbing body and $\mathbf{s}$ and $\mathbf{r}$ are the position vectors of the perturbing body and satellite respectively, relative to the Earth. As the Earth is orbiting the Sun it is subject to an acceleration $\ddot{\mathbf{r}}_{Earth}$ given by

$$\ddot{\mathbf{r}}_{Earth} = GM_{\otimes}\frac{\mathbf{s}}{|\mathbf{s}|^3}. \tag{77}$$

Therefore, in a reference frame centred on the Earth, subtracting equation (77) from equation (76) gives

$$\ddot{\mathbf{r}} = GM_{\otimes}\left\{\frac{\mathbf{s}-\mathbf{r}}{|\mathbf{s}-\mathbf{r}|^3} - \frac{\mathbf{s}}{|\mathbf{s}|^3}\right\}. \tag{78}$$

After simplification of equation (78) the gravitational perturbations caused by the Moon and the Sun for each vector component are given by

$$\ddot{\mathbf{r}}_{Moon/Sun} = \frac{GM_{\otimes}r}{s^3}\left[-\hat{\mathbf{e}}_r + 3\hat{\mathbf{e}}_{\otimes}^2\hat{\mathbf{e}}_r\right] = \left\{\begin{array}{c}\ddot{r}_x\\ \ddot{r}_y\\ \ddot{r}_z\end{array}\right\} = \frac{GM_{\otimes}r}{s^3}\left\{\begin{array}{c}-\hat{e}_{rx} + 3\hat{e}_{\otimes x}^2\hat{e}_{rx}\\ -\hat{e}_{ry} + 3\hat{e}_{\otimes y}^2\hat{e}_{ry}\\ -\hat{e}_{rz} + 3\hat{e}_{\otimes z}^2\hat{e}_{rz}\end{array}\right\}, \tag{79}$$

where $\hat{\mathbf{e}}$ denotes the unit vector pointing in the direction of the perturbing body (subscript $\otimes$) and satellite (subscript $r$), in the geocentric frame.

Calculating luni-solar perturbations requires the position vectors of the Moon and Sun at each propagation time-step. Precise ephemerides for solar system bodies can be obtained from the NASA Horizons system [128]. This is done using an email request system, whereby the user submits a query via email detailing the desired date and celestial body. An automated response replies with the requested information. To automate the Horizons email system in AETHER would not be practical, as the ephemerides need to be re-evaluated at every integration time step and this would take too long to execute. The solution to this was to request Sun, Moon and Earth (SME) ephemerides for multiple dates, at intervals of 10 days for the historical period of 1970-2010. Then, to predict a more precise estimate of the SME positions, AETHER uses a 4th order Runge-Kutta propagator initialised using the nearest 10-day ephemerides of the SME data to give the positions at the exact time required. The coding for these processes are presented in lines 0122-0180 of Section 11.2.5 and all of Sections 11.2.8 & 11.2.9 of the Appendix.

The force model used to propagate the barycentric Moon and Earth positions takes into account the accelerations from each other and the Sun. To propagate the Sun's barycentric position, linear interpolation between the Horizons' SME 10-day positions gave sufficient accuracy, with a maximum position error of approximately 20 km. This position error would yield a maximum change in the direction of the acceleration vector due to the Sun of approximately $8.02\times10^{-6}$ degrees, which is negligible. Figure 21 shows the discrete 10-day interval locations of the Sun in the J2000.0 coordinate system given by the Horizons system.

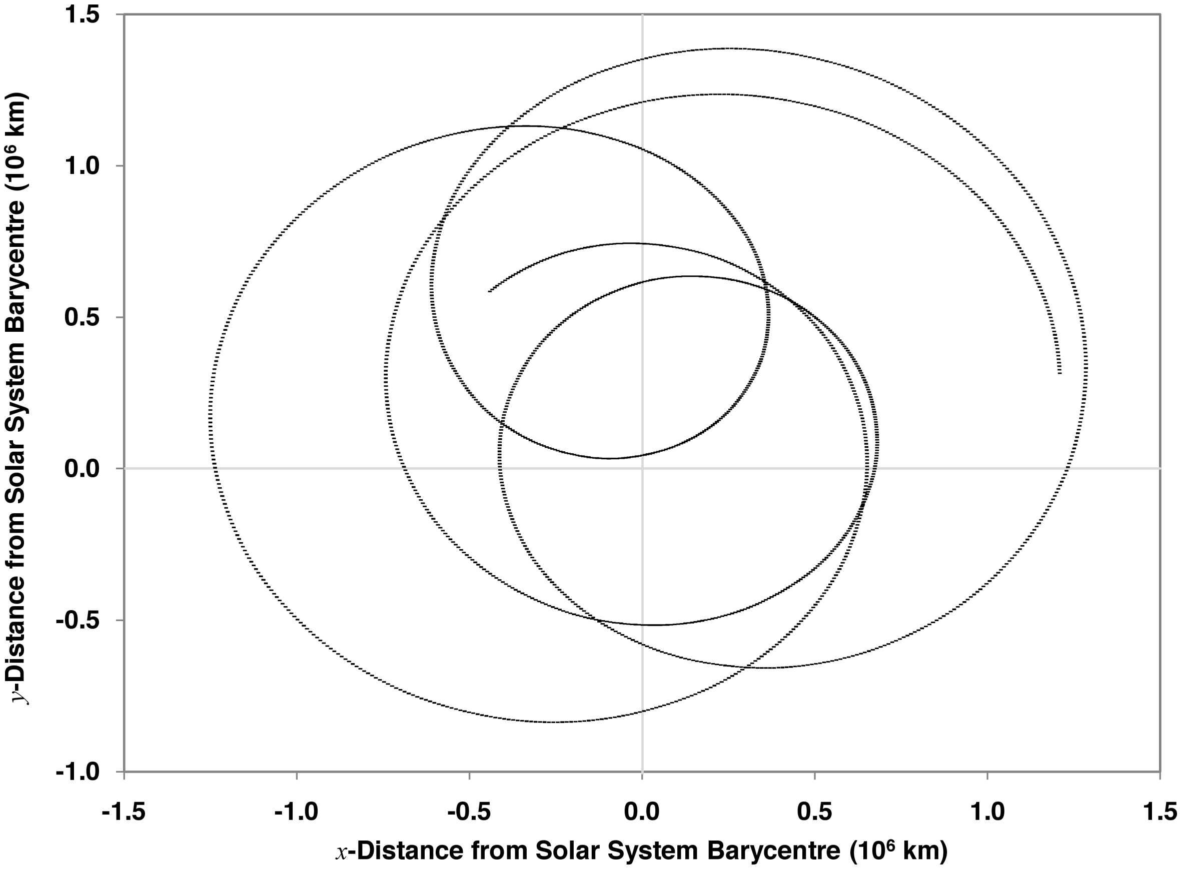

Figure 21: *The discrete 10-day interval locations of the Sun in the J2000.0 coordinate system given by the Horizons system. The $z$ component of the Sun's position also varies, although generally with an amplitude of one order of magnitude less than the $x$ and $y$ component.*

Horizon returns the ephemerides in the J2000.0 coordinate system, with the origin at the Solar System barycentre. Therefore, two steps are required to convert to the TEME coordinate system as used by AETHER and the TLE data. The first is to apply a rotation matrix to the SME ephemerides. Then, to obtain the Moon and Sun position vectors relative to the Earth, a translation of the origin from the Solar system barycentre to the position of the Earth is done by simple vector subtraction, for example,

$$\mathbf{r}_{\otimes TEME} = \mathbf{r}_{\otimes J2000.0} - \mathbf{r}_{Earth J2000.0}. \tag{80}$$

To test the implementation of luni-solar perturbations, propagations by AETHER were compared to the same propagations using the Astrogator propagator of the STK software [5]. For both propagators, only the perturbations due to luni-solar gravity were included with primary gravity. Four sample propagations were performed at three month intervals to obtain various orientations of the Moon and the Sun relative to the Earth as shown in Figure 22. The satellite orbit used for comparison was an equatorial geostationary geometry, at zero longitude. The satellite's altitude was the parameter used to compare the perturbations with the results from AETHER and STK, the results of which are shown in Figure 23.

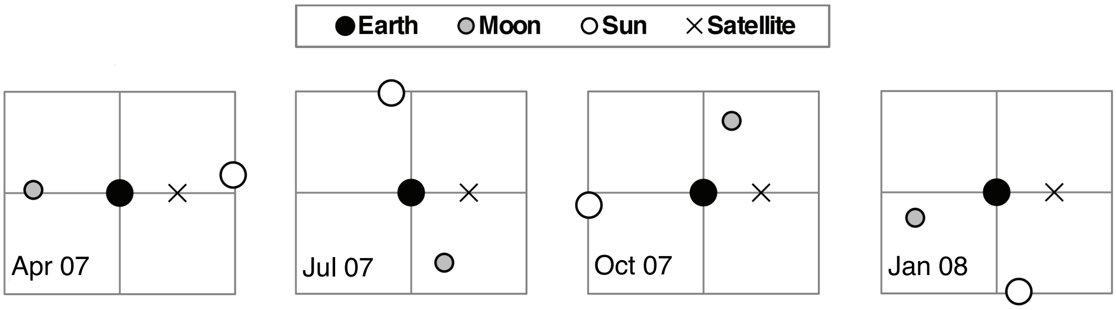

Figure 22: *The orientations of the Moon, Sun and Satellite relative to the Earth for each propagation, shown in the* $xy$ *plane of the TEME system coordinate.*

The geostationary orbit configuration was chosen because it is sensitive to luni-solar perturbations. The maximum deviation between the results of AETHER and STK were found to be approximately 1 km. With the semi-major axis for a geostationary orbit being approximately 42,164 km, the results implied a position error of 0.002% of the position vector. For calculations of satellite ephemerides in LEO this would equate to a position error of less than 1 % of the TLE ephemeris error. In addition to the quantitative error, the general trends of the altitude variation from AETHER reflect those of STK, suggesting that the handling and calculation of the luni-solar direction vectors behave as expected. However, there are differences. One explanation could be due to ephemerides used to estimate the relative positions of the Earth, Moon and Sun. Both use NASA JPL as the source but, interpolation methods between the discrete ephemerides may vary, yielding a slightly different position. Also, the trends in Figure 23 seem to suggest a damping of the amplitude of the altitude variation in AETHER with respect to that of STK. This could be due to slightly different values of astronomical constants within the workings of the two propagators. Variations of mass estimates of the different bodies, in addition to varying precision used by both propagators, could contribute to the differences observed.

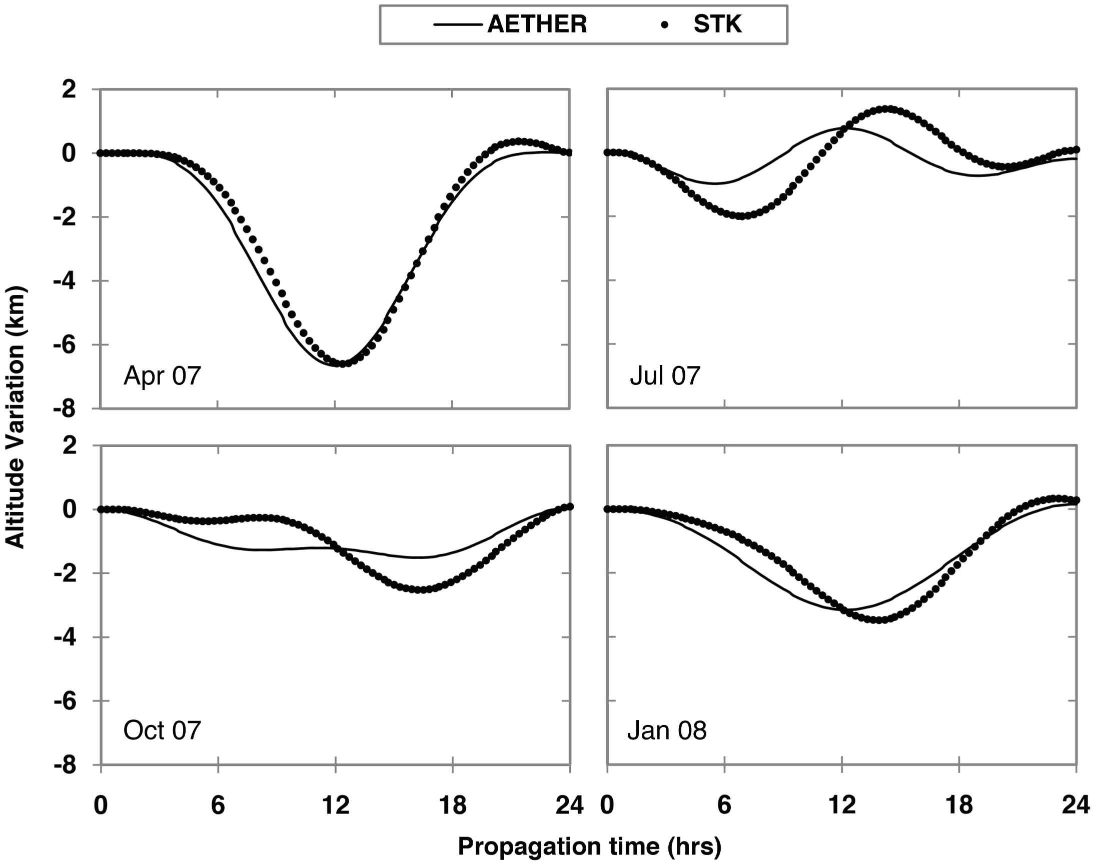

Figure 23: *The change in the satellite's altitude during one 24-hour orbit cycle, for the propagations in AETHER and STK.*

### 5.1.7 Solar Radiation Pressure

Above altitudes of approximately 600-700 km, and depending on solar activity, the perturbation caused by the force of sunlight becomes significant compared to drag. This perturbation is commonly known as Solar Radiation Pressure (SRP). Including the perturbation due to SRP is necessary to achieve precise orbit propagation for satellite orbits above altitudes of 500 km. From Aksnes [4] and Montenbruck & Gill [79], the acceleration due SRP can be approximated by

$$\ddot{\mathbf{r}}_{SRP} = -P_{\odot} C_r \frac{A}{m} \frac{\mathbf{r}_{\odot}}{r_{\odot}^3} AU^2, \tag{81}$$

where $P_{\odot}$ is the pressure of solar radiation (4.56×10$^{-6}$ N/m$^2$) [74], $C_r$ is the reflectivity coefficient of the satellite, $\frac{A}{m}$ is the area to mass ratio of the satellite, $\mathbf{r}_{\odot}$ is the position vector of the Sun relative to the satellite with magnitude $r_{\odot}$ and $AU$ is a constant denoted by the average distance from the Earth to the Sun. It is known as the Astronomical Unit (1.49597871×10$^8$ km). From Fortescue *et al.* [35] and Aksnes [4], $C_r$ can take any value between 0 and 2. However, results by van der Ha & Modi [36] show that a sensible average value for $C_r$ is 1.25.

The area-to-mass ratio in equation (81) is one of the parameters used to calculate the ballistic coefficient and so can be derived using

$$\frac{A}{m} = \frac{\delta}{2.2}, \tag{82}$$

where the drag coefficient $C_d$ of the satellite under investigation is assumed to be 2.2. In reality, $C_d$ varies, as discussed earlier, between a value of 2 and 4. Attaining values near 4 could only be possible if the atmospheric particles were reflected in a specular manner, which is highly unlikely in real situations. However, assuming a small amount of reflection, which is the case for most satellites, a value of 2.2 provides a good estimate for deriving the area-to-mass ratio.

Solar radiation pressure only perturbs a satellite's orbit when there is direct line of sight between any part of the Sun and the satellite. Therefore, as a satellite can pass through the shadow of the Earth, equation (81) applies neither consistently nor uniformly. To address this issue a shadow function, $\nu$, [80] can be used that modifies equation (81) giving

$$\ddot{\mathbf{r}}_{SRP} = -\nu P_{\odot} C_r \frac{A}{m} \frac{\mathbf{r}_{\odot}}{r_{\odot}^3} AU^2. \tag{83}$$

Figure 24 shows how the shadow function varies with the position in the satellite's orbit.

The shadow function used in AETHER calculates the angles subtended by the Earth and Sun as viewed from the satellite and, using vector geometry, calculates the proportion of the Sun that is obscured by the Earth [80]. The assumption that the Earth is spherical is used to calculate the shadow, resulting in a slight error at Northerly latitudes due to the Earth's oblateness. Also, as the propagation of a satellite position is essentially in jumps relating to the integration time step, the exact point of shadow entry and exit will not necessarily coincide with propagated ephemeris. This would produce very small errors in the calculation of semi-major axis. However, the magnitude of these errors over a 10-day period would be negligible

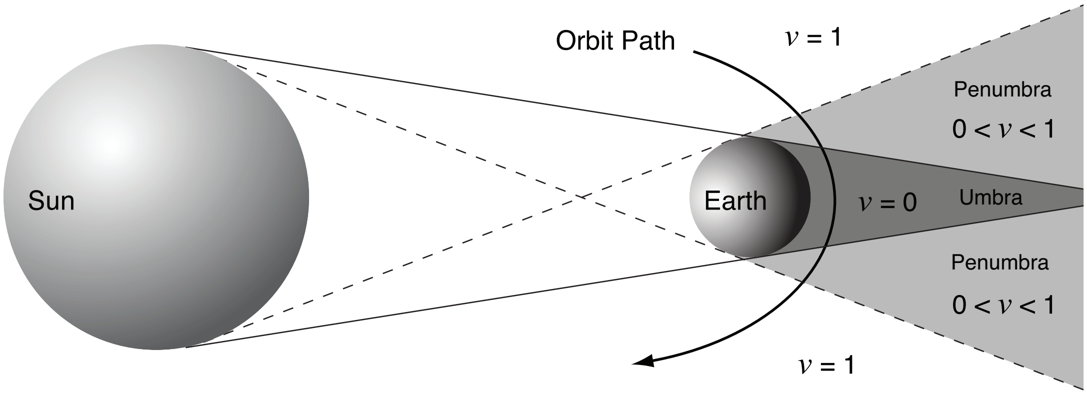

Figure 24: *The variation of the shadow function $\nu$ during an orbit passing through the Earth's shadow. Not to scale.*

compared to the overall change in semi-major axis due to other perturbations. The coding for the calculations of SRP and the shadow function can be seen in Section 11.2.5 of the Appendix: lines 0251-0281.

To validate the theory behind the SRP perturbations described above, Aksnes [4] presented a study of the effects of SRP on the Keplerian elements of a spherical satellite's orbit. This was done using a semi-analytical algorithm, based on the expressions derived by Kozai [67], to integrate the equations of motion for the balloon satellite, DASH 2, (ID 00624) over an orbital period. Two orbit configurations were analysed. The first was such that the satellite did not enter the Earth's shadow during one orbital period, and the second included a complete shadow passage; that is, a shadow entry and exit. Due to some inconsistencies in the theory presented in the literature by Aksnes [4] and Kozai [67], the theory used for the validation of AETHER is detailed below.

The initial conditions for the satellite taken from an analysis by Slowey [110] are presented below in the form of the standard six Keplerian orbital elements.

Epoch = 38400.0 MJD
$a$ = 10,085.44 km
$e$ = 0.025422
$i$ = 88.3924°
$M$ = 0.95623 + 8.57299($t_{\text{MJD}}$-38400) revs
$\omega$ = 227.493° - 0.98308($t_{\text{MJD}}$-38400)°
$\Omega$ = 45.38124° - 0.05638($t_{\text{MJD}}$-38400)°
$C_r$ = 1.105
$\frac{A}{m}$ = $3.79\times10^{-6}$ km$^2$/kg

Here, $t_{\text{MJD}}$ is the modified Julian date (MJD) of the epoch under investigation and is calculated by

$$\text{MJD} = \text{Julian Date} - 2400000.5. \tag{84}$$

From Kozai [67] the change in the semi-major axis due to SRP for a Sun-lit portion of a satellite's orbit between two positions with eccentric anomalies $E_1$ and $E_2$ is given by

$$\mathrm{d}a = 2a^3 F \left| S(0)\cos E + T(0)\sqrt{1-e^2}\sin E \right|_{E_1}^{E_2}, \tag{85}$$

where the parameter $F$ denotes the acceleration due to SRP given by

$$F = P_{\odot}\frac{C_r A}{\mu m}\frac{\mathbf{r}_{\odot}}{r_{\odot}^3} AU^2. \tag{86}$$

In equation (85) the direction cosines $S(...)$ and $T(...)$, which are a function of the true anomaly $\theta$, are given by

$$\begin{aligned} \left\{\frac{S(\theta)}{T(\theta)}\right\} = & -\cos^2\left(\frac{i}{2}\right)\cos^2\left(\frac{\epsilon}{2}\right)\left\{\frac{\cos}{\sin}\right\}(\lambda_{\odot} - \theta - \omega - \Omega) \\ & -\sin^2\left(\frac{i}{2}\right)\sin^2\left(\frac{\epsilon}{2}\right)\left\{\frac{\cos}{\sin}\right\}(\lambda_{\odot} - \theta - \omega + \Omega) \\ & -\frac{1}{2}\sin(i)\sin(\epsilon)\left[\left\{\frac{\cos}{\sin}\right\}(\lambda_{\odot} - \theta - \omega) - \left\{\frac{\cos}{\sin}\right\}(-\lambda_{\odot} - \theta - \omega)\right] \\ & -\sin^2\left(\frac{i}{2}\right)\cos^2\left(\frac{\epsilon}{2}\right)\left\{\frac{\cos}{\sin}\right\}(-\lambda_{\odot} - \theta - \omega + \Omega) \\ & -\cos^2\left(\frac{i}{2}\right)\sin^2\left(\frac{\epsilon}{2}\right)\left\{\frac{\cos}{\sin}\right\}(-\lambda_{\odot} - \theta - \omega - \Omega), \end{aligned} \tag{87}$$

where $\epsilon$ denotes the obliquity of the ecliptic (23.44°). $\lambda_{\odot}$ is the ecliptic longitude of the Sun, which is calculated using

$$\begin{aligned} \lambda_{\odot} = & \ 279.70 + 0.98564734\,(t_{\mathsf{MJD}} - 15019.5) \\ & +1.92\sin(358.48 + 0.98560027\,(t_{\mathsf{MJD}} - 15019.5)). \end{aligned} \tag{88}$$

The two orbit configurations that were analysed had the modified Julian dates 38400 and 38520. Table 4 presents the state vectors calculated for each satellite epoch using the information given by Slowey [110] using conversion techniques presented by Chobotov [20].

Table 4: *The state vectors obtained for the two epochs.*

| Variable | MJD 38400 | MJD 38520 | Units |
|---|---|---|---|
| $x$ | −5827.82033553 | 7895.58573595 | km |
| $y$ | −6107.82947540 | 6332.61720200 | km |
| $z$ | −5053.75375177 | 727.31583677 | km |
| $\dot{x}$ | 2.46234616 | −0.57894551 | km/s |
| $\dot{y}$ | 2.27553622 | −0.23912932 | km/s |
| $\dot{z}$ | −5.50086435 | 6.21665152 | km/s |

The satellite orbits for the two test cases were propagated by AETHER and the change in the semi-major axis $\mathrm{d}a$ was recorded over a period of one orbit cycle, as shown in Figure 25.

Secular changes of a satellite's orbit are of particular interest when determining long-term atmospheric density changes. Solar radiation pressure can cause a secular change in the

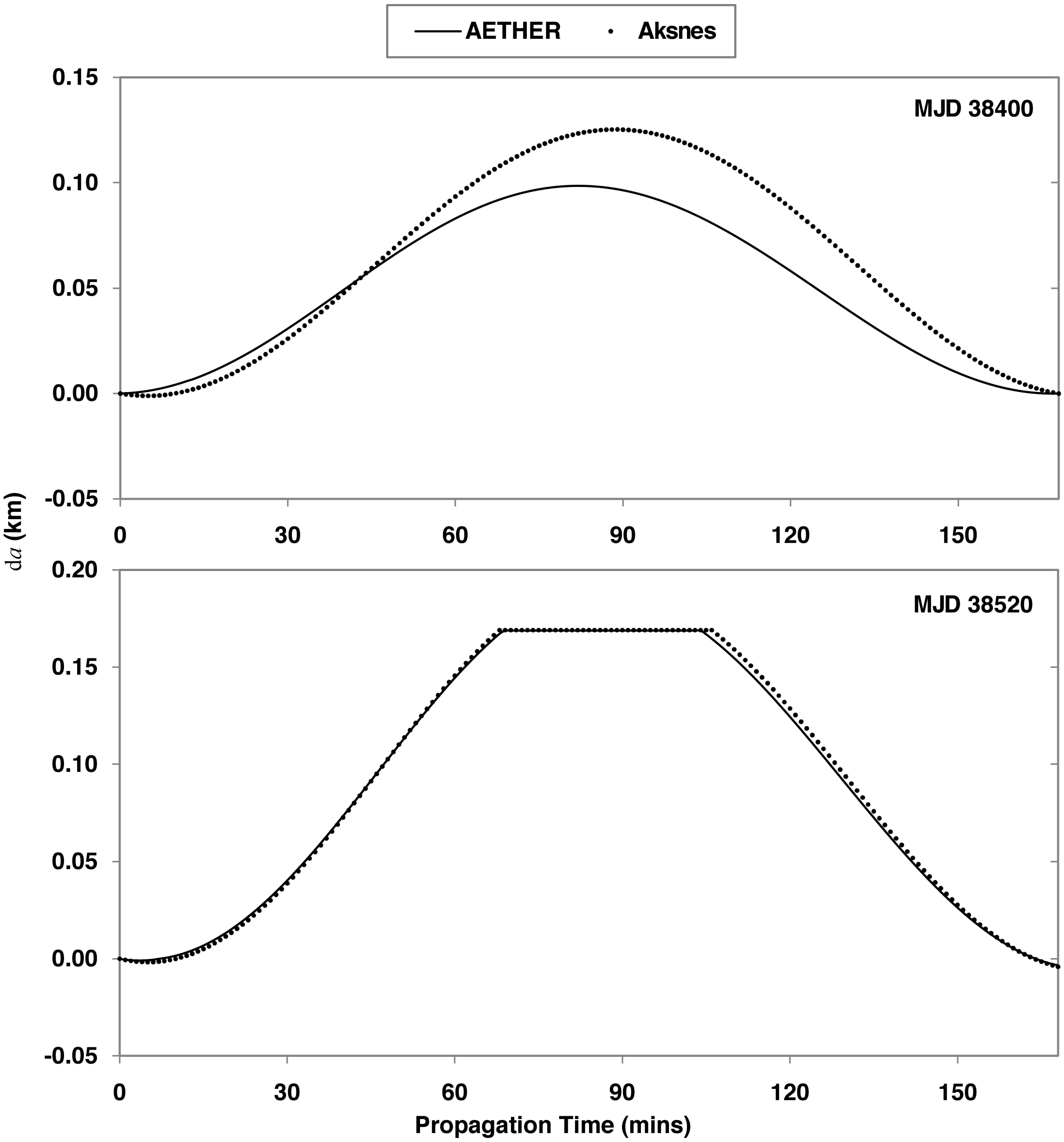

Figure 25: *The change in semi-major axis* $\mathrm{d}a$ *over one orbit cycle. The orbit during the epoch of MJD 38400 is fully illuminated by the Sun, whereas during MJD 38520 the orbit transverses the Earth's shadow shown by the horizontal sections.*

semi-major axis of a satellite's orbit. Therefore, the perturbations due to SRP need to be quantified before inferring changes in the semi-major axis attributable to atmospheric drag. During an orbit in which a satellite is continuously illuminated by the Sun, as in the test case of MJD 38400, there is no net change in the semi-major axis due to SRP. This can be seen from analysing equation (85), where after one orbit cycle $E_2$ would equal $E_1$ and therefore $\mathrm{d}a$ would reduce to zero. As expected, the results from the validation of AETHER produce a zero net change in semi-major axis, as can be seen in Figure 25 for the test case of MJD 38400. After periodic orbit cycles the values of $\mathrm{d}a$ are shown to reduce to zero, by agreement with both

Aksnes and AETHER. Therefore, there will be no artificial secular change due to the SRP perturbations aliased into the analysis of semi-major axis when determining thermospheric density trends.

Comparing the semi-analytical results from Aksnes [4] to those yielded by AETHER gave satisfactory results. However, there was a difference in the maximum $\mathrm{d}a$ between the results of Aksnes and AETHER. This is due to the difference in the methods used to propagate them i.e. semi-analytical versus numerically integration. For the test case of MJD 38400, the maximum deviation between the two results is 0.32 km. An orbit position error of 0.032 km is approximately 30% of the positions errors associated with the TLE ephemerides error. Although not ideal, the key requirement is that no secular change due to SRP is aliased into the variation of semi-major axis, which has already been shown to have been attained.

In the case of MJD 38520, when a passage through the Earth's shadow is applied, good correlation exists between the results Aksnes and AETHER with an acceptable maximum deviation of 0.004 km. The horizontal sections of the curves in Figure 25 signify the shadow passages as there is no perturbation due to SRP. If the satellite's orbit transverses the Earth's shadow then there will be a net change in the semi-major axis over one orbit cycle. This can also be seen from the results of the theory and propagation by AETHER in Figure 25, as the curves of both methods do not return to zero after the orbit propagation. Furthermore, the final value of the net change in semi-major axis for the theory of Aksnes and the numerical predictions by AETHER coincide. This shows good agreement with the numerical methods used by AETHER and the accepted theory of Kozai and Aksnes.

## 5.2 Ballistic Coefficient Determination

This section presents a novel way to estimate a satellite's ballistic coefficient, $\delta$ [107]. This method was peer reviewed and accepted for publication in the Journal of Spacecraft and Rockets in mid-2011. The development of the methodology is described here, along with the tests that were performed throughout the development to ensure that a rigorous and robust approach was applied.

The concept used in this study to determine an empirical ballistic coefficient for a specific satellite, involves a comparison between observational data (TLE sets) and numerically propagated orbit data produced by AETHER. It was a further requirement that the goal of calculating a satellite's ballistic coefficient utilise only observational data from TLE sets. Therefore, achieving this goal was the primary criteria of the method developed here.

TLE data for satellites with known physical parameters were used to develop and test the method. Thirteen satellites with spherical geometry were used as control objects for estimating ballistic coefficients. The use of spherical configurations reduced the unknowns in drag calculations associated caused by shape effects when estimating $\delta$. In addition to these 'control' objects, two other non-spherical satellites were used to show how the method presented here performs on more typical test subjects. Table 5 lists the satellites used and their physical characteristics.

Table 5: *The known physical parameters of the 15 objects used to develop the method of determining an empirical satellite ballistic coefficient.*

| Satellite ID | Satellite Name | Surface Characteristic | Projected Area (m$^2$) | Mass (kg) |
|---|---|---|---|---|
| 02389 | OV3-3 | Solar Cells | 0.404-0.707 | 74.33 |
| 02622 | OV1-9 Atlas D R/B | Stainless Steel | 7.306-64.660 | 2,347.00 |
| 11796 | Yug⋆ | Smooth Surface | 3.142 | 750 ±10 |
| 13750 | Yug⋆ | Smooth Surface | 3.142 | 750 ±10 |
| 13972 | Type 2⋆ | Solar Cells | 3.164 | 750 ±30 |
| 14668 | Type 2⋆ | Solar Cells | 3.164 | 750 ±30 |
| 22990 | ODERACS⋆ | Polished Chrome | 0.008 | 1.48 |
| 22991 | ODERACS⋆ | Sand-blasted Aluminium | 0.008 | 1.48 |
| 22994 | ODERACS⋆ | Polished Chrome | 0.018 | 5.00 |
| 22995 | ODERACS⋆ | Sand-blasted Aluminium | 0.018 | 5.00 |
| 23471 | ODERACS⋆ | Black Iridite | 0.018 | 5.00 |
| 23472 | ODERACS⋆ | White Chemglaze | 0.008 | 1.48 |
| 25769 | Starshine 1⋆ | 878 Mirrors | 0.178 | 39.46 |
| 26929 | Starshine 3⋆ | 1,500 Mirrors | 0.685 | 90.04 |
| 26996 | Starshine 2⋆ | 845 Mirrors | 0.177 | 38.56 |

R/B: Rocket Body
⋆ satellites with spherical geometry

The reason for choosing these satellites was to provide a database to make the analysis more efficient. The OV3-3 satellite and the Atlas D Rocket Body are the non-spherical test subjects. In Table 5 they have been listed with a range of possible cross-sectional areas due to their irregular geometry and the possibility that they are tumbling. All 13 other test subjects have a spherical geometry, with known surface properties and physical characteristics. However, in the case of the Russian Yug and Type 2 satellites, their masses are only known to within the specified tolerance.

The two Type 2 satellites had the most similar physical characteristics and orbits, as shown in Table 6. Therefore, it would be expected that their predicted $\delta$ values would be nearly identical, a feature that was used to demonstrate the consistency of the estimation method. The two Yug satellites have identical satellite characteristics but their orbit inclination and eccentricity vary. This difference may highlight any influence on the predicted $\delta$ values of the differing atmospheric regions through which they travel. Most importantly, it has been shown by Bowman [9] that there is an increase in drag coefficient with increasing altitude, due to variations in flow regime. The ODERACS satellites provide a diverse range of satellite mass and surface properties with nearly identical orbit configurations. These would demonstrate the ability of the estimation method to detect variations in drag coefficient, caused by varying accommodation coefficients associated with different satellite surface characteristics. Finally, the Starshine satellites provide a challenge in the estimation of $\delta$ due to the limited temporal data span.

Table 6: *The orbital parameters from the TLE data of the 15 objects.*

| Satellite ID | Satellite Name | Perigee Range (km) | Eccentricity Range | Average Inclination (°) |
|---|---|---|---|---|
| 02389 | OV3-3 | 348 - 345 | 0.1667 - 0.1595 | 81.4 |
| 02622 | OV1-9 Atlas D R/B | 474 - 473 | 0.2291 - 0.2281 | 99.1 |
| 11796 | Yug | 298 - 155 | 0.0855 - 0.0043 | 82.9 |
| 13750 | Yug | 442 - 149 | 0.0038 - 0.0012 | 65.8 |
| 13972 | Type 2 | 467 - 145 | 0.0033 - 0.0014 | 65.8 |
| 14668 | Type 2 | 468 - 163 | 0.0034 - 0.0014 | 65.8 |
| 22990 | ODERACS | 333 - 166 | 0.0018 - 0.0004 | 56.9 |
| 22991 | ODERACS | 335 - 182 | 0.0017 - 0.0002 | 56.9 |
| 22994 | ODERACS | 340 - 159 | 0.0013 - 0.0007 | 56.9 |
| 22995 | ODERACS | 340 - 176 | 0.0013 - 0.0004 | 56.9 |
| 23471 | ODERACS | 329 - 170 | 0.0017 - 0.0005 | 51.9 |
| 23472 | ODERACS | 325 - 178 | 0.0019 - 0.0002 | 51.9 |
| 25769 | Starshine 1 | 380 - 173 | 0.0013 - 0.0003 | 51.6 |
| 26929 | Starshine 3 | 466 - 185 | 0.0005 - 0.0006 | 67.0 |
| 26996 | Starshine 2 | 362 - 155 | 0.0020 - 0.0004 | 51.6 |

In addition to the varying satellite characteristics, the test subjects were also chosen to cover a range of historical periods and $F_{10.7}$ solar flux levels. Figure 26 shows the $F_{10.7}$ solar flux in conjunction with the historical periods of the TLE data used for each satellite when deriving $\delta$ values.

The concept used here to determine a ballistic coefficient for a specific satellite involves averaging many estimates, each made from a comparison between the observational and numerically derived data. For each estimate, two observations of satellite position are required. These are given by two consecutive TLE sets, $TLE_1$ and $TLE_2$. Two separation periods between

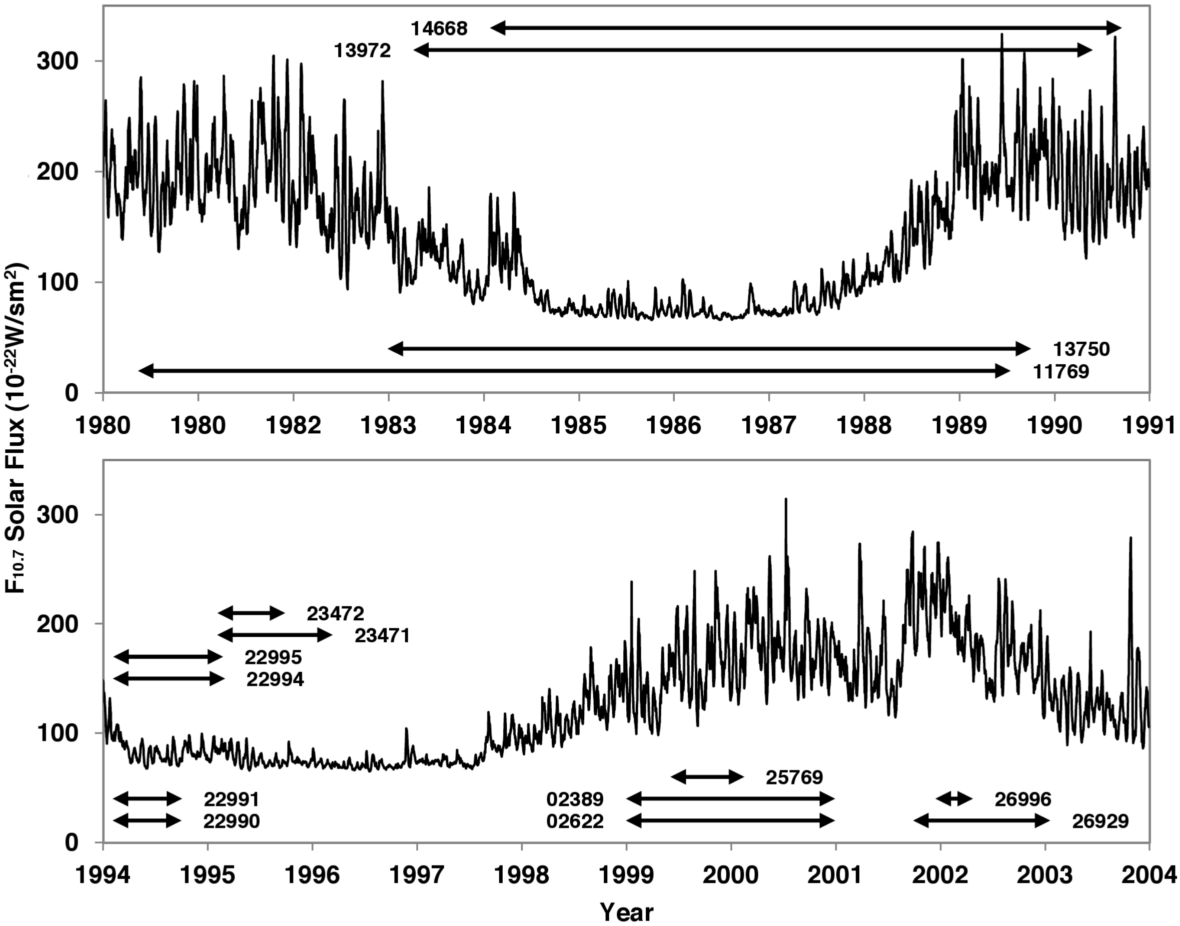

Figure 26: *The $F_{10.7}$ solar flux in conjunction with the historical period of the TLE data used for each satellite when deriving $\delta$ values.*

TLE epochs, of approximately 2 days and 10 days, were chosen for testing. By doing this, the magnitude of the relative changes in semi-major axes could be determined. The knowledge gained would later be valuable when developing the method to infer long-term thermospheric density change.

There were various parameters that could be used as a source of comparison when iteratively determining the ballistic coefficient. These parameters will be discussed later with their advantages and disadvantages. However, here, the comparison parameter will be denoted by $Q$. Once the values of comparison parameters are obtained, the difference is calculated and stored as

$$\Delta(\delta_n) = Q_{\text{AET}} - Q_{\text{TLE}}, \tag{89}$$

where $\Delta(\delta_n)$ denotes the difference between the comparison parameter $Q$ from the numerical data ($_{\text{AET}}$) and that from the observational data ($_{\text{TLE}}$), for a particular value of ballistic coefficient, $\delta_n$. If the comparison yields a large difference between the observational and numerical results, the propagation is re-run and, with the use of the Secant method, a revised value of ballistic coefficient is used,

$$\delta_n = \delta_{n-1} - \frac{\Delta(\delta_{n-1})[\delta_{n-1} - \delta_{n-2}]}{\Delta(\delta_{n-1}) - \Delta(\delta_{n-2})}, \tag{90}$$

where $\delta_n$ represents the updated ballistic coefficient estimate. This is process is repeated iteratively until the difference in the observational and numerical results coincide within a predefined tolerance.

Two options for the comparison parameter were investigated when developing this method. One was to use a satellite's predicted position vector to compare AETHER's results with $\text{TLE}_2$. Another option is to use orbit parameters, such as the semi-major axis. The following sections describe the two approaches.

Before applying the finalised method to all 15 satellites listed above in Tables 5 and 6, the developments initially concentrated on using one satellite. TLE sets from the years 1999 and 2000 were used to predict the ballistic coefficient for the OV3-3 satellite (ID 02389). This satellite was chosen for its relatively well documented ballistic coefficient from previous studies. The values previously attributed to this satellite over the specified periods have been in the range of 0.0181-0.0184 $\text{m}^2$/kg.

### 5.2.1 The Velocity Vector Approach

This approach compared the output position from AETHER ($\mathbf{r}_{\text{AET 2}}$) to the position of $\text{TLE}_2$ ($\mathbf{r}_{\text{TLE 2}}$). There are many different measurements that could have been used to compare the positions from the two sources. Owing to the numerous perturbations that can affect a satellite's position vector, simply using the magnitude of the displacement between $\mathbf{r}_{\text{AET 2}}$ and $\mathbf{r}_{\text{TLE 2}}$ would not provide an efficient parameter with which to estimate the effects of atmospheric drag and hence the ballistic coefficient. A position, relative to the orbit geometry, would more appropriately serve as a comparison parameter. This is because the orbit geometry is not fixed with respect to the reference frame of the Earth, as in the case of the position vectors. One approach is to calculate the number of orbit cycles the satellite completed within the epoch separation of $\text{TLE}_1$ and $\text{TLE}_2$, which would not necessarily be an integer. An obvious parameter to calculate this would be its true anomaly, as this progressively tracks the angular position of a satellite in its orbit. However, in the case of AETHER, the output is given by a state vector describing an osculating orbit. The true anomalies calculated from different osculating orbits are not compatible, as true anomaly is related to the perigee point, which is different for each osculating orbit i.e. from $\text{TLE}_1$ and $\text{TLE}_2$. Therefore, a theoretical plane, normal to the velocity vector of $\text{TLE}_2$ ($\mathbf{v}_{\text{TLE 2}}$), and located at the position vector $\mathbf{r}_{\text{TLE 2}}$, was used to provide a static reference for comparison, as shown in Figure 27. The perpendicular distance of $\mathbf{r}_{\text{AET 2}}$ from this velocity vector reference plane was used as the comparison parameter, $Q$.

The ballistic coefficients that resulted using this velocity vector approach are shown in Figure 28. During the development of this method, the sinusoidal pattern exhibited by the ballistic coefficient predictions were found to coincide with the precession of apsides of the satellite's orbit. This is because the TLEs produce ephemerides at an approximately constant geocentric latitude as previously presented in Figure 5 of Section 2.2 of the Literature Review. Therefore the relative location of the TLE ephemeris on the satellite's orbit would change during apsidal precession. In reality, the ballistic coefficient can never be a negative number. Therefore, the results highlight a deficiency with using the TLE data in this way. The

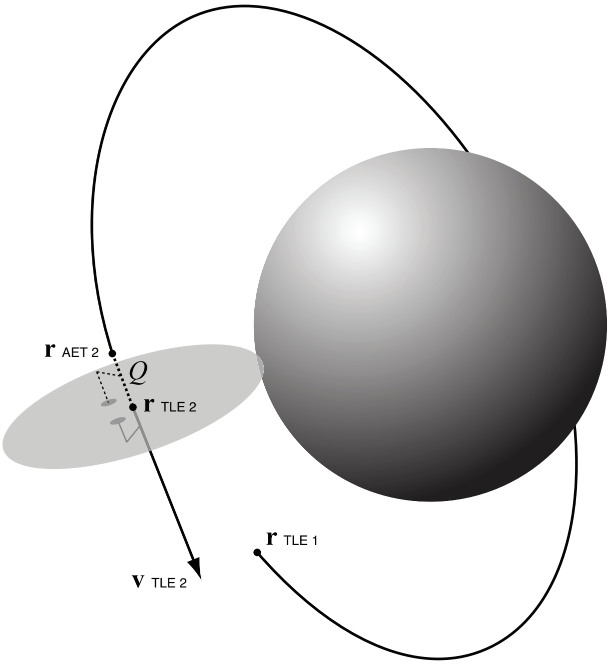

Figure 27: *The velocity vector approach:* $\mathbf{r}_{\text{TLE 1}}$ *and* $\mathbf{r}_{\text{TLE 2}}$ *represents the positions defined by the respective observational TLE sets.* $\mathbf{r}_{\text{AET 2}}$ *represents the satellite's position after propagation via AETHER. Here the positions of* $\mathbf{r}_{\text{TLE 1}}$ *and* $\mathbf{r}_{\text{TLE 2}}$ *are for illustration purposes only, as there are typically many orbit cycles between TLE epochs of 2 and 10 days.*

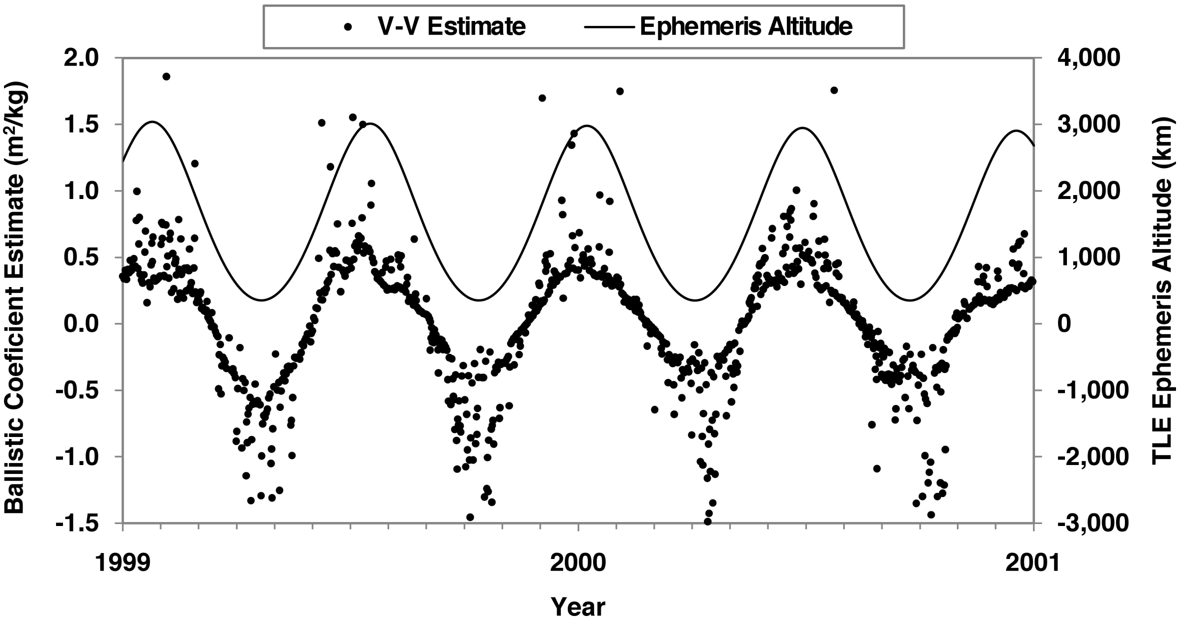

Figure 28: *The ballistic coefficients derived from the velocity vector (V-V) approach. Also shown are the ephemeris altitudes of the TLE data.*

consequence is that at perigee, either the satellite's velocity is underestimated or the estimated altitude is lower than the true altitude, and *vice versa* at apogee. Averaging the comparisons made by using the velocity vector method and the entire TLE data from the years 1999 and 2000 resulted in an estimated ballistic coefficient for satellite 02389 of approximately 0.0572

±21.12 m$^2$/kg, which is over three times larger than the published value, not to mention the associated error. This 1$\sigma$ variance equates to 36,916% of the averaged value 0.0572 m$^2$/kg. Owing to the enormous error margin, this method was not suitable.

### 5.2.2 Matching the Semi-Major Axis

As the velocity vector approach did not yield accurate results and was sensitive to the deficiencies in the TLE data, a better method was required. The method presented in this section is similar in concept to the velocity vector approach. However, the parameter for comparison was the semi-major axis of the satellite's orbit.

An advantage of using the semi-major axis as the parameter for comparison is that, over many orbit cycles, the most significant perturbation causing a secular change is that due to atmospheric drag. This means that when comparing a value of semi-major axis between numerical predictions and observation data, the parameters involved in drag prediction are the most significant. As the ballistic coefficient is directly related to drag effects, changes in the semi-major axis will be sensitive to the numerical value of the ballistic coefficient. This will allow a more accurate estimate of ballistic coefficient to be determined.

The testing of the method using the semi-major axis as the comparison parameter was performed using the same TLE data for the OV3-3 satellite (ID 02389) and yielded the improved results shown in Figure 29. The derived value of the ballistic coefficient for the satellite from the results shown in Figure 29 was 0.0184 ±0.07 m$^2$/kg, within the range expected from previously published values. In addition, no obvious irregularities are observed, with the exception of perhaps a slightly larger variance of ballistic coefficient predictions during times when the TLE ephemerides coincide with the orbit perigee. The results shown demonstrate an improvement in

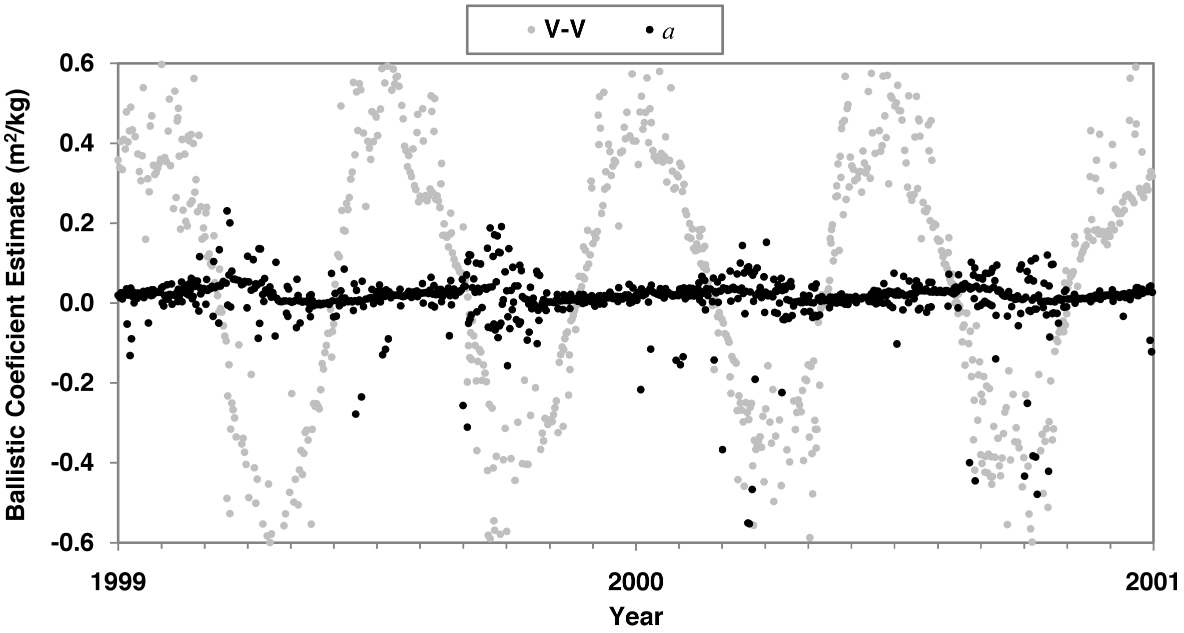

Figure 29: *The ballistic coefficients derived from matching the semi-major axes ($a$) for comparison with the previous results from the velocity vector approach (V-V).*

the variance compared to the velocity vector approach, with $1\sigma$ = 401% of the averaged value 0.0184 m$^2$/kg. Although the accuracy and variance had been significantly improved, the magnitude of the variance was still much larger than the magnitude of the ballistic coefficient estimate, and so further refinement was deemed necessary.

### 5.2.3 Using the Change in Semi-Major Axis

The Kozai mean motion, $n_k$, given explicitly in the TLE data, is used to calculate values of the semi-major axis. The change in these values of semi-major axis from TLE$_1$ to TLE$_2$ was used as the comparison parameter, $Q$. The Kozai mean motion was used, as short term periodicities have been removed. Consequently it most closely represents the secular effect of atmospheric drag on a satellite's orbit. It is important to acknowledge here that ballistic coefficient estimates using this method will be entirely dependent on the empirical atmospheric model used in the propagator. If this method is to be used in a different study, extreme caution must be taken when using the estimates of ballistic coefficients to numerically propagate orbits. Deriving a value for the semi-major axis from $n_k$ uses the expression,

$$a_{\text{TLE}} = \sqrt[3]{\frac{\mu}{n_k^2}}, \tag{91}$$

having converted the units of $n_k$ from revolutions per day to radians per second. The total change in semi-major axis, represented by the observational TLE data, $\Delta a_{\text{TLE}}$, is simply given by

$$Q_{\text{TLE}} = \Delta a_{\text{TLE}} = a_{\text{TLE 2}} - a_{\text{TLE 1}}, \tag{92}$$

The initial conditions for AETHER's numerical propagation, in terms of epoch and state vector, are those given by TLE$_1$. As an initial estimate for the ballistic coefficient, the $B^*$ value from TLE$_1$ is used. In some cases, older TLE sets have a $B^*$ value of +00000-0 (zero), which is obviously not a physical value and so an arbitrary initial guess of 0.01 m$^2$/kg is used. The satellite orbit is then propagated by AETHER from the epoch of TLE$_1$ to that of TLE$_2$. To derive the change in semi-major axis as predicted numerically by AETHER, $\Delta a_{\text{AET}}$, the secular effect on the semi-major axis due to atmospheric drag is integrated to give the total change. Here, the model density errors in the NRLMSISE-00 used by AETHER need to be considered. Estimating ballistic coefficients using the following method assumes that the density given by the NRLMSISE-00 for orbital propagation in AETHER is correct. Here lies the fundamental ambiguity of using a predicted density value to derive an observed density value. Assuming the density model provides a correct estimate of density is a false assumption as there will always be errors and model biases that do not provide a totally accurate estimation of model density. The effect of this is that resulting value of ballistic coefficient estimated is generally irrelevant for the purposes of this study as it is simply used as an appropriate scaling factor to adjust the observable density ratios. However, model bias do have the potential to erroneously affect the trend results derived from the density ratios. Therefore, careful acknowledgement and consideration of the potential of modelled density errors is crucial.

For each integration step of the numerical propagation, the rate of change of the semi-major axis due to atmospheric drag is calculated from King-Hele [61] using

$$\dot{a}_{Drag} = \frac{2a^2 v}{\mu} \ddot{r}_{Drag}. \tag{93}$$

Over the propagation period between $\text{TLE}_1$ and $\text{TLE}_2$ the increments of $\dot{a}$ are summed to derive the total change in the semi-major axis, $\Delta a_{\text{AET}}$, entirely due to drag, giving

$$Q_{\text{AET}} = \Delta a_{\text{AET}} = \int_{\text{TLE 1}}^{\text{TLE 2}} \dot{a}_{Drag} \mathrm{d}t. \tag{94}$$

The right-hand-side of equation (94) is essentially the same integral as was used in the study by Picone *et al.* [92], yet they made use of the SGP4 propagator to perform the integration.

A semi-analytical propagator could be used to calculate the integral given by equation 94. This could potentially increase the efficiency with which the integral is calculated. However, the accuracy would be degraded. Though an analytical propagation could also evaluate the orbital changes from all perturbations, their coupled effects would not be included. For each integration step in a numerical propagation, all perturbations contribute to the change in the acceleration vector. This acceleration vector is then used to determine a new osculating orbit, with new orbital parameters, based on the contributions from all perturbations. As a result, the change in the orbital parameters, such as the semi-major axis, would not evolve in the same way as could be predicted by analytical theory.

Once the values for $\Delta a_{\text{TLE}}$ and $\Delta a_{\text{AET}}$ are obtained, the difference is calculated and stored using the comparison parameters as

$$\Delta(\delta_n) = Q_{\text{AET}} - Q_{\text{TLE}} = \Delta a_{\text{AET}} - \Delta a_{\text{TLE}}, \tag{95}$$

where $\Delta(\delta_n)$ could then be used in the Secant iteration defined previously by equation (90).

Using the change in semi-major axis $\Delta a$, as opposed to the resulting absolute value $a$ after numerical propagation, as the comparison parameter again improved the variance of the ballistic coefficient estimates as shown in Figure 30. The derived value of the ballistic coefficient for the OV3-3 satellite from the results shown in Figure 30 was 0.0189 $\pm$0.0053 $\text{m}^2$/kg. This estimate differed from the previously published values by less than 3%. The $1\sigma$-variance equated to 28% of the averaged value 0.0189 $\text{m}^2$/kg. With the ballistic coefficient estimate being less than 10% of previously published values, this method was deemed a suitably accurate. The errors associated with ephemerides provided by TLE data, as well as the possibility of the varying cross-sectional area caused by satellite tumbling, was the reason why this satellite was chosen as the initial test subject. Choosing a satellite with more well known physical characteristics may have yielded higher accuracy predictions from the previous methods. This could have prematurely halted further development and refinement of the method, which has been shown to be essential to obtain an accurate ballistic coefficient estimate for a satellite with relatively unknown physical characteristics. Hence, using the change in semi-major axis as the comparison parameter is the method by which all ballistic coefficients were estimated in this

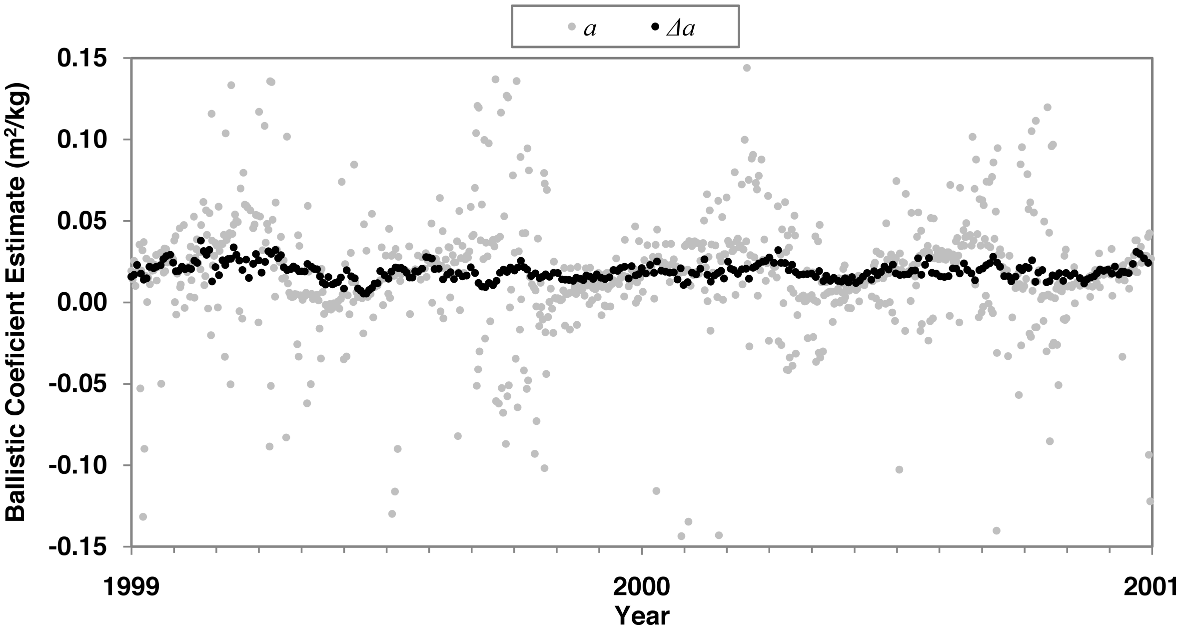

Figure 30: *The ballistic coefficients derived from matching the changing in semi-major axes ($\Delta a$). Also shown are the previous results from comparing the absolute values of semi-major axis ($a$).*

study.

### 5.2.4 The Gaussian Summation Model

A method to effectively extract a single value of ballistic coefficient that can be attributed to a satellite was required upon obtaining numerous empirical estimates from the method described previously. Bowman [7] stated that an average of multiple estimates of ballistic coefficient can provide an accurate estimate of a satellite's true ballistic coefficient. However, for this analysis, a more accurate approach was desired that did not allow extreme values, data skew or outliers, in the estimation process to affect the final attributable value of ballistic coefficient. Therefore, a process of determining the most common value, from a set of empirical estimates, was derived. In some cases the median value was practically coincidental to the mode. However, for other cases there was sufficient skewness in the spread of data to significantly separate the median value from the ultimately more accurate mode. To obtain the most common value from a dataset of discrete values required a statistical method. This method needed to assign a continuous and symmetric distribution to the discrete value, which, when combined with other estimates, would allow the estimate of a most common value. As the combination of the distributions would provide a continuous function, the most common estimate could take any value, which could potentially increase the accuracy of the final estimate.

A symmetric distribution in the form of a modified Gaussian function was applied to each ballistic coefficient prediction, given by

$$g(x,\delta) = \frac{1}{n} e^{-(\frac{x-\delta}{\eta})^2}, \tag{96}$$

where $n$ is the number of ballistic coefficient predictions, $x$ is the variable along which the distribution is plotted, $\delta$ is the specific ballistic coefficient prediction, which acted as the distribution's mean, and $\eta$ is the mean of all the predictions, acting as the distribution's variance. Equation (96) was applied to the entire set of ballistic coefficient predictions (eg. $\delta_{(1,2..n)} \in \delta^*$). They were then added together to give the distribution,

$$G(x,\delta^*) = \frac{1}{n}\sum_{i=1}^{n} e^{-(\frac{x-\delta_i}{\eta})^2}. \tag{97}$$

The maximum value reached by this distribution gives the most common value of ballistic coefficient out of all the predictions. It is important to note that the most common value here is probably not the same as any of the initial estimates. To determine the maxima of $G(x,\delta^*)$, a code was written by the author in C++ to compliment the main program AETHER. Here, this new code was named AETHER$\delta$. The process of calculating the maximum value of the function $G(x,\delta^*)$ involved taking the derivative of equation (97) giving

$$G'(x,\delta^*) = \frac{-2}{\eta n}\sum_{i=1}^{n}(x-\delta_i) e^{-(\frac{x-\delta_i}{\eta})^2}, \tag{98}$$

and finding the roots ($G'(x,\delta^*) = 0$) using a bisection method. Care was taken to ensure the desired root of the function's maximum was selected; it is possible that $G'(x,\delta^*) = 0$ in more than one place. A check was performed to ensure that the limits of the bisection method contained only one root, the maxima of $G(x,\delta^*)$. Figure 31 shows the distribution $G(x,\delta^*)$ and highlights the maxima, and therefore, final $\delta$ that is attributed to the satellite under investigation.

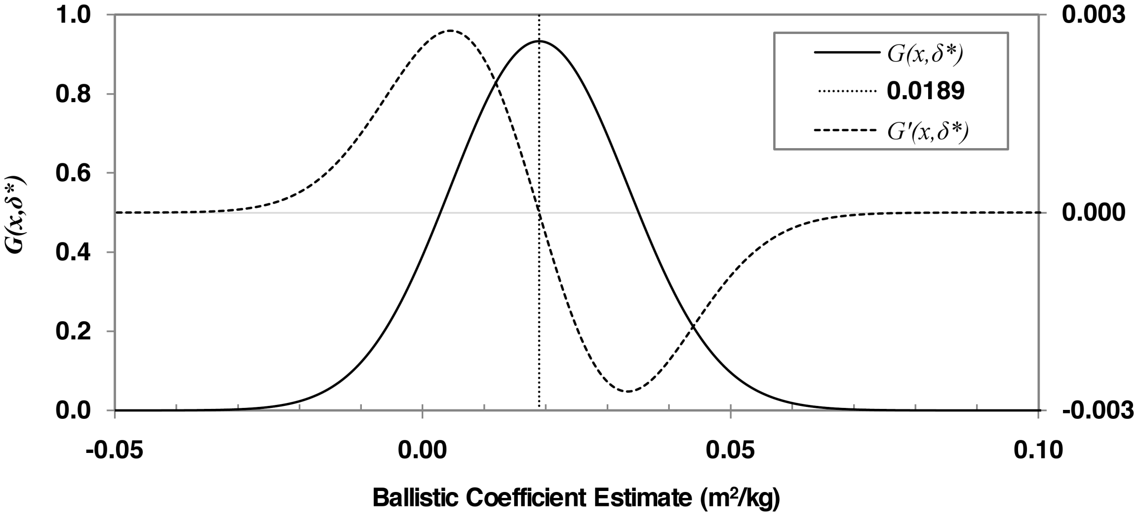

Figure 31: *The distribution $G(x,\delta^*)$ and $G'(x,\delta^*)$ for the OV3-3 satellite. $G(x,\delta^*)$ is the summation of the Gaussian distributions $g(x,\delta)$. Note the maximum of $G(x,\delta^*)$ coincides with the root of $G'(x,\delta^*) = 0$. It is this value at which this maximum occurs that provides the final attributable satellite ballistic coefficient of 0.0189 m$^2$/kg.*

Essentially, this method assumes an uncertainty in the estimate of each value of ballistic coefficient. This uncertainty is modelled using the modified Gaussian distribution. The summation of these modified distributions from all the estimates gives a new distribution that is similar itself to a Gaussian distribution. This new distribution was then used to estimate the 1-$\sigma$ variance in the final ballistic coefficient estimates using

$$\sigma = \sqrt{\frac{1}{n}\sum_{i=1}^{n}(\delta_i - \delta)^2}. \tag{99}$$

In summary, this new distribution was insensitive to outliers from spurious ballistic coefficient estimates. This effectively provided an average of only the ‘good’ estimates, i.e. the non-outliers, of ballistic coefficient.

### 5.2.5 Results and Analysis

Using the method presented above, the predicted ballistic coefficients for the 15 satellites listed in Tables 5 and 6 are given in Table 7. For the 13 spherical satellites, with known surface area and mass, a confident estimate of their respective drag coefficients can be made. However, for the irregularly-shaped satellites, discussion about the area-to-mass ratio and the drag coefficient will be deferred, due to the possibility of tumbling.

Table 7: *The predicted values of $\delta$, inferred drag coefficients and 1$\sigma$ accuracy values.*

| Satellite ID | Satellite Name | Projected Area (m$^2$) | Derived $\delta$ (m$^2$/kg) | Drag Coefficient | 1$\sigma$ Variance (% of $\delta$) |
|---|---|---|---|---|---|
| 02389 | Solar Cells | variable | 0.01886 | - | 28.83 |
| 02622 | Stainless Steel | variable | 0.02509 | - | 31.10 |
| 11796 | Smooth Surface | 3.142 | 0.00834 | 1.99 | 31.31 |
| 13750 | Smooth Surface | 3.142 | 0.00855 | 2.04 | 18.23 |
| 13972 | Solar Cells | 3.164 | 0.00940 | 2.23 | 19.06 |
| 14668 | Solar Cells | 3.164 | 0.00932 | 2.21 | 16.58 |
| 22990 | Polished Chrome | 0.008 | 0.01109 | 2.03 | 12.76 |
| 22991 | Sand-blasted Aluminium | 0.008 | 0.01134 | 2.07 | 13.47 |
| 22994 | Polished Chrome | 0.018 | 0.00731 | 2.00 | 11.88 |
| 22995 | Sand-blasted Aluminium | 0.018 | 0.00758 | 2.08 | 12.33 |
| 23471 | Black Iridite | 0.018 | 0.00681 | 1.87 | 12.02 |
| 23472 | White Chemglaze | 0.008 | 0.01045 | 1.91 | 11.20 |
| 25769 | 878 Mirrors | 0.178 | 0.00962 | 2.13 | 9.52 |
| 26929 | 1,500 Mirrors | 0.685 | 0.01575 | 2.07 | 13.43 |
| 26996 | 845 Mirrors | 0.177 | 0.01008 | 2.19 | 10.28 |

The satellites with spherical geometry were considered first when assessing the performance of this method in deriving a satellite’s ballistic coefficient. This was to evaluate, and validate, the method using the ‘control satellites’ so that the method may then be applied to irregularly-shaped satellites. The following Figures show the initial ballistic coefficient estimates that were made over the time history of the TLE data for each satellite. The estimates are shown for the 2-day and 10-day TLE epoch separations.

As previously described in Section 5.2.3, where the method was introduced, the ballistic coefficient estimates are dependent on the empirical density model used in the propagator. The variation of the ballistic coefficient estimates shown the following Figures not only demonstrate variabilities in the source data, but also it includes differences from the true density experienced by the satellite to the modelled density from the NRLSISE-00 density model.

**The Yug Satellites (IDs 11796 & 13750)**

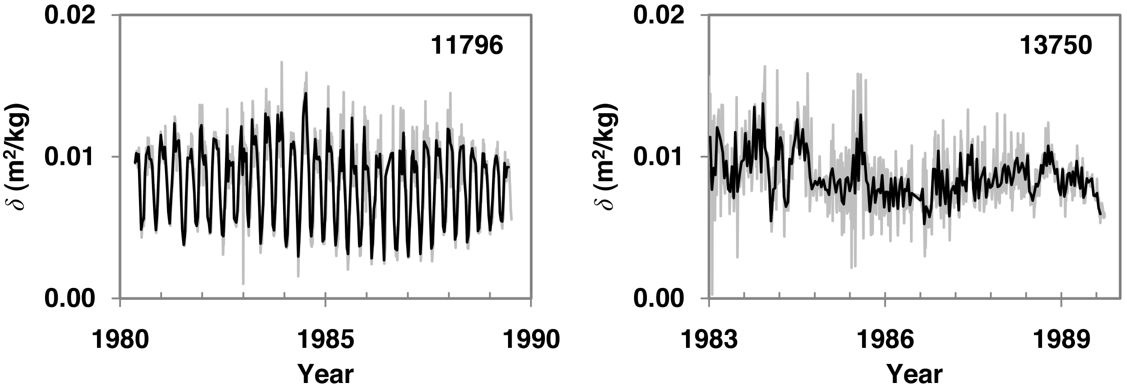

Figure 32: *The derived ballistic coefficients for the Yug satellites 11796 and 13750. The $\delta$ values derived using a TLE epoch separation of 2-days and 10-days are shown by the grey and black plots respectively.*

With the satellites having near-identical physical characteristics, the $\delta$ values obtained are very similar, despite the variation in orbit eccentricity. In Figure 32 the derived $\delta$ values for satellite 11796 show a strong periodic variation in contrast to the derived $\delta$ values of satellite 13750, which show no obvious periodicity. The reason for this difference is discussed later but is believed to be due to the varying orbit geometries and associated TLE ephemeris errors and not a product of surface composition variation. Satellite 13750 has a higher drag coefficient, which is in line with Bowman's work [9], suggesting an increase of drag coefficient with an increase in altitude. However, as the mass is only known to within ±10 kg, a precise value of the area-to-mass ratio is also unknown. Therefore, the variation in $\delta$ value, and hence drag coefficient, derived through the method presented here could possibly be attributed to the unknowns in the area-to-mass ratio. Also, the historical period over which the $\delta$ estimates were made covered a large range of solar flux levels. Bowman [9] also showed a variation in drag coefficient with solar flux, which could also contribute to the relatively large variance in $\delta$ estimates.

**The Type 2 Satellites (IDs 13972 & 14668)**

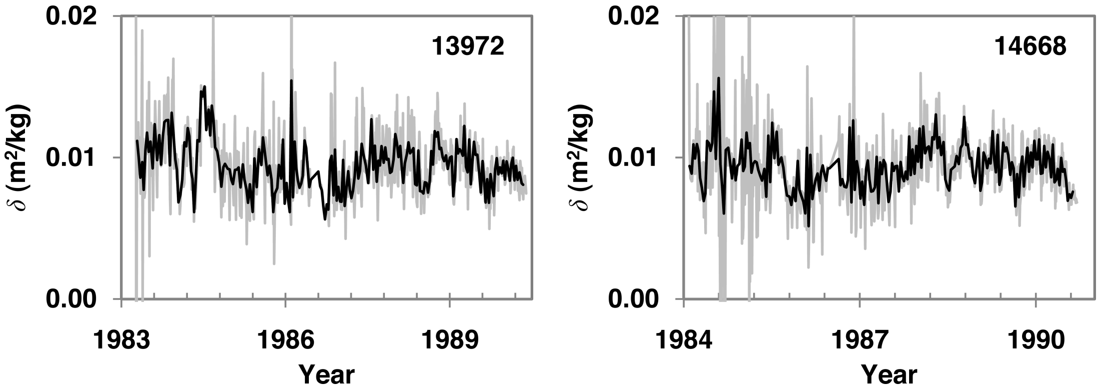

Figure 33: *The derived ballistic coefficients for the Type 2 satellites 13972 and 14668. The $\delta$ values derived using a TLE epoch separation of 2-days and 10-days are shown by the grey and black plots respectively.*

With the closest match of orbit geometry and physical characteristics, the derived $\delta$ values show consistent agreement, considering the margin of error in the area-to-mass ratio. The variances of 19.06 and 16.58% of $\delta$ were generally larger than the variances from the other spherical satellites, with the exception of the Yug satellites. A reason for this is possibly due to these Type 2 satellites also having their $\delta$ values derived over a historical period covering a large range of solar flux levels.

**The ODERACS Satellites (IDs 22990, 22991, 22994 & 22995)**

The derived values of $\delta$ for the ODERACS satellites are presented in Figure 34. Considering these four satellites as pairs with similar surface characteristics, there is evidence that the method can distinguish variations in surface characteristics. Both of the satellites with the sand-blasted aluminium surfaces gave higher drag coefficients compared to those with surfaces of polished chrome. At a microscopic level, all surfaces are generally 'rough' but, it is a case of relative roughness that can account for the changes in drag coefficient. However, as the drag coefficient is partly dependent on the accommodation coefficient, the results support the theory that a surface finish of sand-blasted aluminium would 'accommodate' the incident molecules for longer than in the case of a reflective surface of polished chrome. The greater the length of time the incident flow is 'accommodated' by the surface the greater the accommodation coefficient. This is due to the temperature of the reflected molecules, tending towards the temperature of the satellite's surface molecules during their temporary adhesion. This then reduces the difference between the temperature of the incident molecular flow and that of the reflected flow. The result of this is that the satellite accommodation coefficient (and, thus the value of drag coefficient) for the sand-blasted aluminium surface finish would be greater than that for the polished chrome surface. Also, the rougher surface would influence the direction of the re-emitted momentum compared to the smoother surface, which could also account for the differences between the calculated drag coefficients.

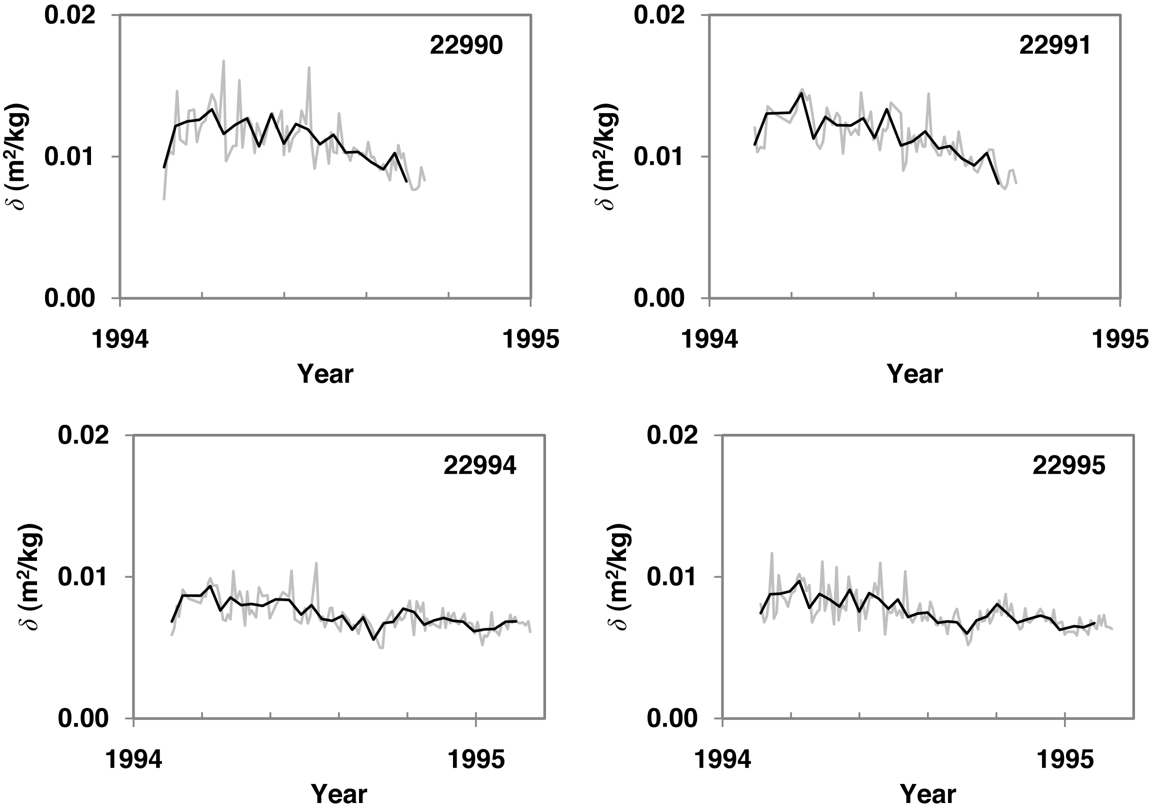

Figure 34: *The derived ballistic coefficients for the ODERACS satellites 22990, 22991, 22994 and 22995. The $\delta$ values derived using a TLE epoch separation of 2-days and 10-days are shown by the grey and black plots respectively.*

**The ODERACS Satellites (IDs 23471 & 23472)**

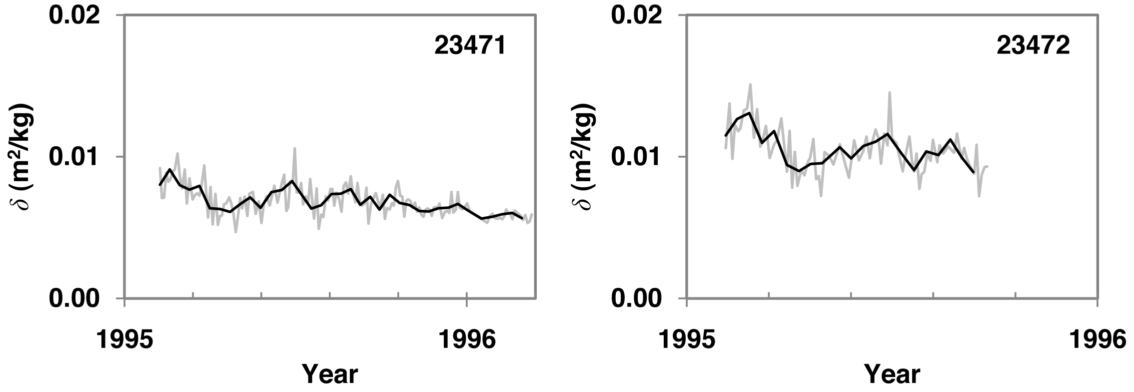

Figure 35: *The derived ballistic coefficients for the ODERACS satellites 23471 and 23472. The $\delta$ values derived using a TLE epoch separation of 2-days and 10-days are shown by the grey and black plots respectively.*

With the same area-to-mass ratios as the previous ODERACS objects, the $\delta$ values derived for satellites 23471 and 23472, presented in Figure 35, imply a non-physical estimation ballistic coefficient. The inferred drag coefficients of both these satellites gave $C_d < 2$, which is impossible. This implies a bias in the atmospheric density predicted by the NRLMSISE-00. However, only the fact that a bias exists can be deduced from this data. No assumption can be made here about the constancy of the bias yet it is imperative to acknowledge it existence. Moe & Bowman [75] showed that the absorption of atomic oxygen on the satellite's surface over time influences the properties of the accommodation coefficient. However, with black iridite (chromate) and white chemglaze (polyurethane) coatings being susceptible to O($^+$) absorption, the effect would be to increase the value of drag coefficient, which does not account for the estimated values being $C_d$ < 2. Once again, this method has demonstrated its ability to highlight anomalies in a satellite's drag coefficient that are most likely due to surface finish.

**The Starshine Satellites (IDs 25769, 26929 & 26996)**

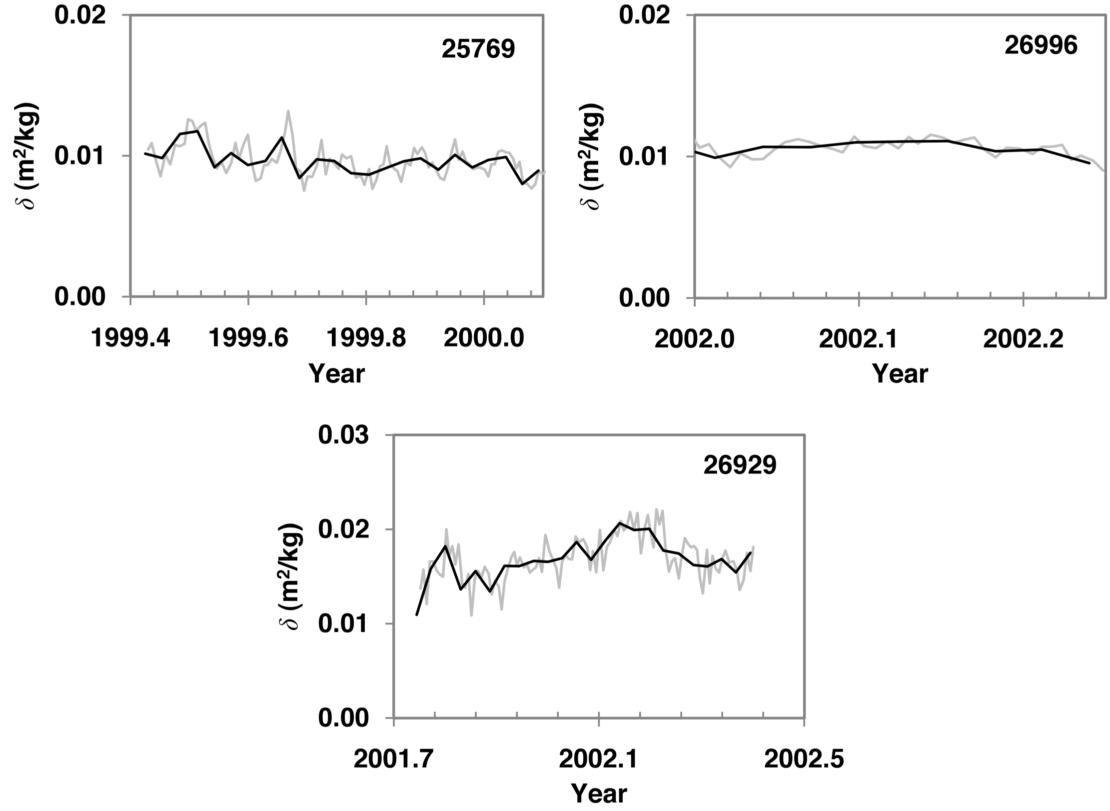

Figure 36: *The derived ballistic coefficients for the Starshine satellites 25769, 26929 and 26996. The $\delta$ values derived using a TLE epoch separation of 2-days and 10-days are shown by the grey and black plots respectively.*

The Starshine satellites successfully demonstrated the performance of the method over smaller historical data spans. Relatively consistent estimates of $\delta$ were obtained for all three Starshine satellites, as shown in Figure 36. Owing to the small number of $\delta$ estimates available, no robust conclusions can be made about the small variances seen in the spread of estimates. These small variances may simply be due to the small data set. However, the consistent estimates of $\delta$ suggests the method can provide accurate results even with small temporal data ranges. This is likely due to the simple geometry of the satellite, and its inability to present varying cross-sectional areas to the incident flow. For more irregular-shaped satellites, a larger data set would probably be required to obtain an accurate estimate of $\delta$.

**Satellites OV3-3 (ID 02389) & Atlas D Rocket Body (ID 02622)**

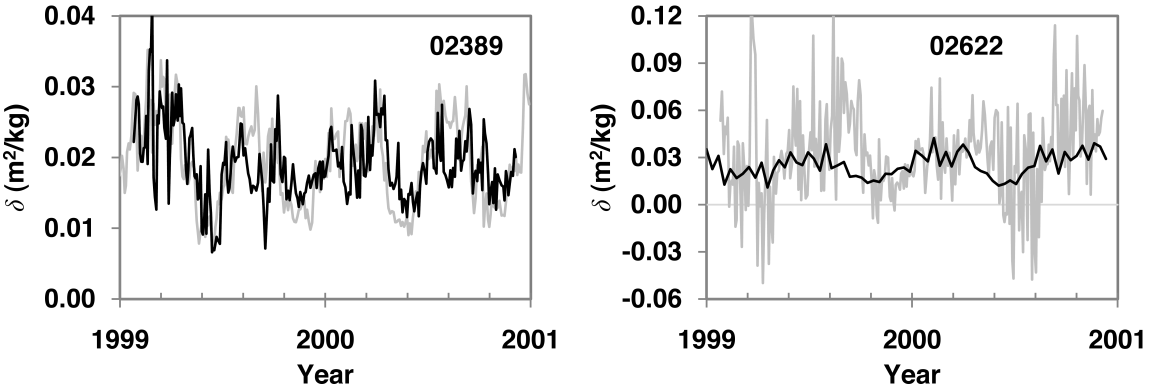

Figure 37: *The derived ballistic coefficients for the OV3-3 satellite 02389 and Atlas Rocket Body 02622. The $\delta$ values derived using a TLE epoch separation of 2-days and 10-days are shown by the grey and black plots respectively.*

Both the OV3-3 satellite and the Atlas D rocket body may have been tumbling throughout the analysed historical period. Therefore, the derivation of a drag coefficient, based on their known physical parameters and derived values of $\delta$, is not as simple as for the spherical satellites. Therefore judging the accuracy of this method for these irregularly-shaped satellites required a different approach.

It is possible to make assumptions about the most likely projected areas based on their moments of inertia and axes of rotation. However, this does not provide a sound foundation on which to assess the method of determining ballistic coefficients presented here. Therefore, by assuming that the method is providing sensible values for $\delta$, as shown in Figure 37, we can use this value of $\delta$ to tell us something about a satellite's orientation and most probable projected area, and then judge whether this assumption is plausible.

The satellites had relatively standard surface characteristics of solar panels, aluminium and stainless steel (the latter being the material for the Atlas D Rocket body). Therefore, the drag coefficient, which is dependent upon the atmospheric composition, the satellite's shape, accommodation coefficient and mode of molecular reflection, can be approximated by $C_d = 2.2$, as previously described in Section 5.1.7. By combining this assumption with the derived values of $\delta$, we can infer the mean projected surface area as shown in Table 8.

Table 8: *The predicted values of $\delta$ and their inferred drag coefficients.*

| Satellite ID Number | Satellite Name | Derived $\delta$ (m$^2$/kg) | Drag Coefficient | Area-to-Mass Ratio (m$^2$) | Projected Area (m$^2$) |
|---|---|---|---|---|---|
| 02389 | Octagonal cylinder | 0.01886 | 2.20 | 0.00857 | 0.65755 |
| 02622 | Circular cylinder | 0.02509 | 2.20 | 0.01141 | 26.76983 |

By calculating the projected areas of these two satellites, assuming an octagonal cylinder for the OV3-3 satellite (ID 02389) and a perfect cylinder for Atlas D rocket body (ID 02622), it can be shown from simple geometry that to project such surface areas as given in Table 8, their axes of symmetry would deviate from the direction of the velocity by no more than 20°. However, there is significant variation in the derived values of $\delta$, as shown in Figure 37, to suggest that the satellites do rotate to present a range of possible projected areas.

In summary, the derived values of $\delta$ are plausible when considering the satellite's geometry and possible projected areas. Complementary to the estimates for the spherical satellites, as well as the accurate estimates for satellite OV3-3 during the development of this, confident estimates of ballistic coefficient may be made for the vast majority of orbiting objects with irregular geometries.

Bowman [9] states that the drag coefficient is dependent on flow regime, and hence, altitude. A drag coefficient variation of 0.08-0.15 per 100 km, dependent on solar flux, was observed. The estimates of ballistic coefficient obtained through testing the method presented here were used to form an independent conclusion about the variation of drag coefficient with altitude. The variation of drag coefficient with flow regime is now well understood, and so identifying a trend of drag coefficient with altitude using the method presented here further validates the process.

Of the 15 satellites analysed here, there are eight whose estimates of $\delta$ were used to infer an altitude dependency of drag coefficient. For this analysis only spherical satellites were considered. In addition to flow regime, Bowman [9] also showed the variation of drag coefficient with solar flux. Therefore, to further reduce any unknowns in the analysis, the estimates of $\delta$ from periods with large variations in solar flux were removed. This meant excluding from the analysis the $\delta$ values derived from the Yug and Type 2 satellites. Finally, of the nine satellites remaining from the selection criteria above, all had perigee altitudes between approximately 380 and 240 km, except Starshine 3 (ID 26929), whose $\delta$ values were also removed from the analysis.

The drag coefficients derived from the initial $\delta$ estimates for the eight satellites were plotted against the associated perigee altitude for each specific $\delta$ estimate, as shown in Figure 38. A linear regression line was fitted to the data to obtain a trend. The linear regression line yielded a trend of 0.42 per 100 km apparent altitude variation in drag coefficient. The description of apparent in the previous sentence is necessary as it is uncertain whether the altitude trend is due to variation in the satellite's drag coefficient, or whether there is a vertical bias in the NRLMISISE-00 empirical density model. It is essentially unnecessary to determine which is the true cause as long as the clear altitude variation is taken into account in some form. Although the regression analysis returned a correlation coefficient of $R^2$ = 0.2882, the trend was highly statistically significant with a P-value of $2.13\times10^{-16}$.

In summary, a trend of drag coefficient with respect to altitude was detected. The results have shown that in addition to distinguishing between satellite surface properties, the method can also detect variations in flow regime when estimating values of ballistic coefficient. The magnitude of the trend is 3-5 times larger than that reported by the detailed study by Bowman. However, the trend determined here is unreliable due to the low value of regression correlation coefficient.

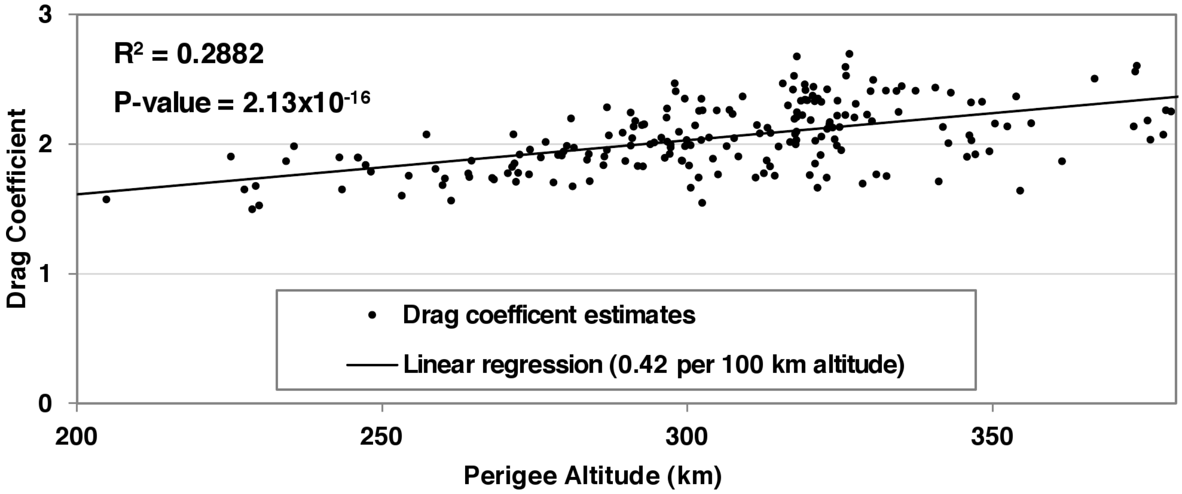

Figure 38: *The drag coefficients derived from the initial $\delta$ estimates for eight satellites plotted against against altitude. The trend yielded a 0.42 per 100 km apparent altitude variation in drag coefficient. The regression analysis gave a correlation coefficient, $R^2$ = 0.2882 and a highly statistically significant P-value of 2.13$\times$ $10^{-16}$.*

### 5.2.6 Discussion of Method

The two main sources of error in this method come from the ephemeris data given by the TLE sets, and from the atmospheric model used to predict local density in AETHER. Errors in the estimation of ballistic coefficient due to TLE ephemeris errors reduce when more TLE sets are used to make the estimation. The process used in this method to average the effect of the TLE ephemeris errors was by using a $TLE_1$-$TLE_2$ epoch separation of 10 days. The $\delta$ estimations for the Type 2 satellite (ID 14668), as shown in Figure 33, are typical examples of the changes that can be achieved by using a larger $TLE_1$-$TLE_2$ epoch separation time. They grey plots denoting the $\delta$ estimations made using the 2-day epoch separation vary significantly more than the black plots denoting the 10-day epoch separation. In this case, the variance when using an epoch separation of 2 days yielded 35%, whereas with a 10-day epoch separation the deviation was reduced to 17%. It is unlikely that the accuracy of the ballistic coefficient estimates improved with the 10-day TLE epoch separation even though the variance decreased, as the use of a 10-day epoch separation essentially removes data that would have been included if a 2-day separation were used. However, seeing as a 10-day separation would later be used to analyse changes in thermospheric density, in additional to easing TLE file sizes, the 10-day separation would continue to be used.

Using an increased $TLE_1$-$TLE_2$ epoch separation to reduce the effect of TLE ephemeris errors has limited effectiveness. This is due to the intrinsic error associated with the precision of the TLE data. The errors associated with this are most apparent when studying high-eccentricity orbits. For example, the epoch of a TLE is given in days to 8 decimal places, so that this could allow for an error of $\pm 5\times 10^{-9}$ days. When passing through its perigee, a satellite in a high-eccentricity orbit can travel at speeds greater than 10 km/s this equates to a position error of approximately 4.2 metres. With angular orbital elements given by the TLE sets to only 4 decimal places, this leads to position uncertainties of 6 metres for LEO satellites and up to 35 meters for satellites in geostationary orbits [121].

The ephemeris for a satellite given by a TLE is always very close to the ascending node as described earlier. By combining this feature with the inaccuracies associated with rounding, a sinusoidal periodicity in phase with argument of perigee is apparent when deriving values for $\delta$. This is due to the precession of apsides. As the Yug satellites 11796 and 13750 have orbit eccentricities of 0.08552 and 0.00385 respectively, but near-identical physical parameters, they are ideal candidates to demonstrate this behaviour. Figure 39 shows the derived values of $\delta$ for the two Yug satellites.

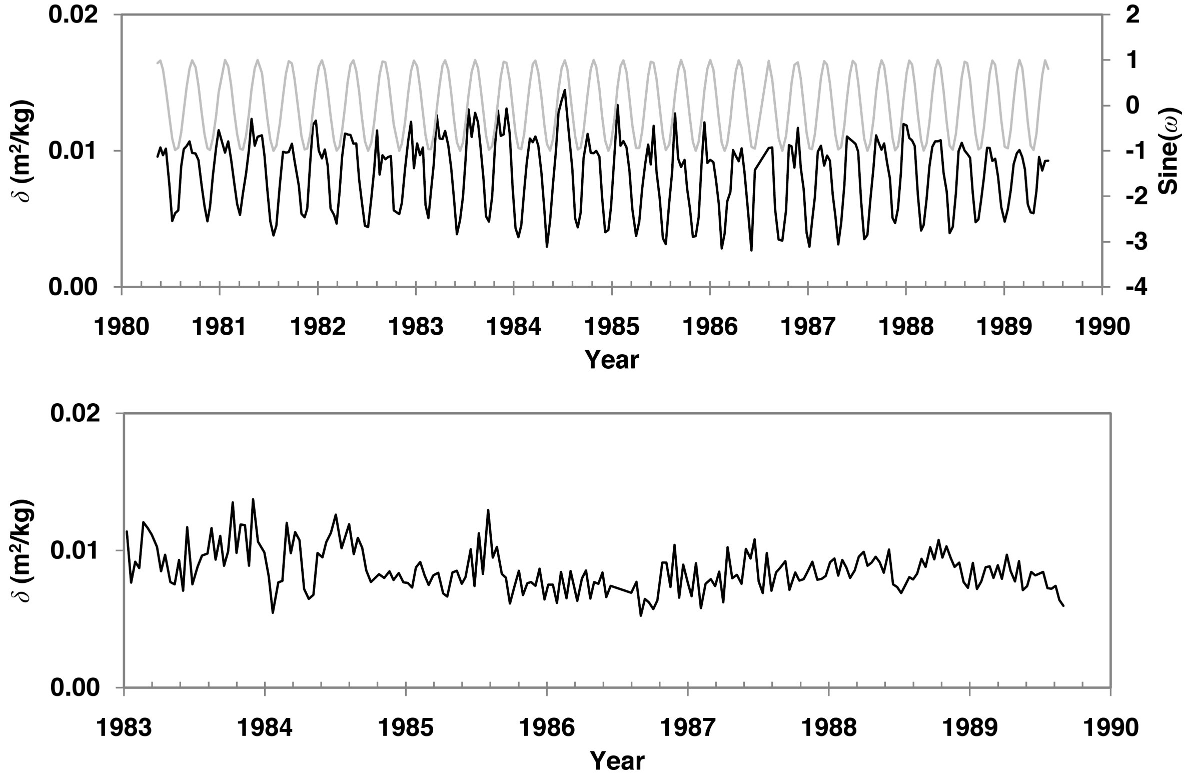

Figure 39: *The difference in derived values of $\delta$ caused by orbit eccentricity. Top: The derived $\delta$ values (black) for Yug 11796, shown with the Sine of the argument of perigee $\omega$ (grey). Orbit eccentricity = 0.08552. Bottom: The derived $\delta$ values (black) for Yug 13750. Orbit eccentricity = 0.00385.*

In Figure 39 there is a periodicity in the derived values of $\delta$, which appears to be in phase with the argument of perigee. Here, the periodicity of the derived values of $\delta$ for the Yug satellite (ID 11796) is approximately 110.2 days. To quantitatively connect this to theory of apsidal precession requires an analysis of the orbit evolution. The precession rate of the argument of perigee of an orbit as presented by Fortescue *et al.* [35] is given by

$$\dot{\omega} = \frac{3}{2}\frac{J_2 R_E^2}{p^2} n_k (2 - \frac{5}{2}\sin^2 i), \tag{100}$$

where $p$ is the semi-latus rectum of the orbit and all other symbols retain their previous meaning. Using equation (100) and average values for inclination and Kozai mean motion, taken directly from the TLE data used to derive the ballistic coefficients, yields an apsidal precession rate of 110.3 days. Therefore, evidence from theory further supports the connection between apsidal precession and TLE ephemeris error. Calculation of the semi-latus rectum also used values of eccentricity taken directly from the TLE data as well as an average semi-major value derived from the Kozai mean motion.

The value of $\delta$ derived for Yug 11796 was still accurate, even with a periodic 1-$\sigma$ variance of 18%. When investigating satellites with eccentric orbits, the uncertainty of the TLE ephemerides will vary sinusoidally depending on the position of the ephemeris relative to the perigee. Therefore, to reduce the effect of these periodicities, a historical TLE data span greater than the period of one apsidal precession must be used.

The second most significant source of error comes from the atmospheric model used to predict local density. As it is impossible to have a drag coefficient of $C_d$ < 2, the results from those satellites yielding $C_d$ < 2 suggest a bias in the atmospheric model. Previous studies have demonstrated the variability of ballistic coefficient and atmospheric density estimates based on data derived from empirical models. In a paper that outlined a method to estimate a satellite's true ballistic coefficient, Bowman [7] presented a correlation between ballistic coefficient estimates and the variation of solar flux over the 11-year solar cycle. The studies into long-term thermospheric density change by Emmert [28 & 30] and Marcos [73] presented a dependency of derived densities with solar flux. Both studies of long-term thermospheric density change showed a significant drop in the derived densities estimated during times of solar minimum. The density ratios were based on data inferred from satellite drag measurements with densities predicted using empirical models. In the paper presenting the JB2008 empirical atmospheric model [11], the variations of density estimates compared between empirical models all demonstrate high errors during times of low solar flux. The inferred drag coefficients of $C_d$ < 2 were from satellites whose data was taken during times of solar minimum. Therefore, the non-physical characteristic of a drag coefficient of $C_d$ < 2 can be attributed, with relatively high confidence, to the errors in density estimates arising from the use of the NRLMSISE-00 empirical atmospheric model during times of low solar flux. As discussed in the introduction, if the NRLMSISE-00 model is used with the derived values of $\delta$ when studying orbit evolution in the upper atmosphere, the errors associated with the atmospheric model density bias will be negligible. However, if the derived values of $\delta$ are used to propagate satellites using an atmosphere model with a different solar flux model, the errors associated with the atmospheric model density bias will be large.

## 5.3 A Demonstration of Orbit Propagation

To asses the performance of AETHER as a whole, along with the method derived for predicting ballistic coefficients, two pre-cursor tests were performed: the first to assess whether AETHER's propagation of TLE sets was suitably more accurate than using the SGP4 propagator; and the second was to predict the re-entry dates for satellites nearing atmospheric re-entry [105]. Both pre-cursor tests highlighted the requirement for an accurate method of estimating ballistic coefficients. When more accurate estimates of ballistic coefficients were possible (as presented in this thesis: Section 5.2 page 73), AETHER demonstrated its ability to accurately propagate satellite orbits.

### 5.3.1 Propagating Two-Line Element Sets

In the field of astrodynamics, it is readily accepted that to propagate an ephemeris using orbit fitted data requires the same propagator that was originally used to create the ephemeris. This is due to the differential numerical process that was used to initially determine the orbital parameters. The adjustment of the parameters to achieve minimum overall error ($\chi^2$-value) can employ non-physical statistical methods. The use of such methods can then compromise the use of the resulting ephemerides with other orbital propagators. This is the situation with using the numerical propagator AETHER to propagate ephemerides generated by the analytical SGP4 propagator.

In terms of propagation accuracy, the advantages of using the numerical propagator AETHER can potentially outweigh the run-time advantages of using the SGP4 propagator. As a result, simulations were performed to demonstrate AETHER's ability to produce accurate orbit evolution data from TLE sets that could then be used in the analysis of long-term thermospheric density change.

The process adopted in this per-cursor test was to use high-accuracy truth orbit ephemerides produced by the Challenging Minisatellite Payload (CHAMP) satellite [17]. In private communication with Doornbos [26], the published Cartesian state vectors from the CHAMP Rapid Science Orbit data sets would be suitable for use in an orbital propagator comparison study. The Cartesian state vectors were then used to calculate values of semi-major axis. Over a 10-day period, the average rate-of-change of semi-major axis was calculated and used as truth data from which one could compare results from AETHER and the SGP4 propagator.

Ten sample TLE sets were selected that provided the initial ephemerides for the comparisons. They were approximately evenly spaced in time with the first being in May 2005 and the tenth in August 2006. These dates were chosen to coincide approximately with solar minimum so that the perturbations from Earth gravity anomalies were relatively larger compared with atmospheric drag perturbations. In addition, the NRLMSISE-00 empirical atmosphere was reported to have the greatest biases when estimating densities during times of low solar activity. Therefore, this gave AETHER the least likelihood of producing a more accurate orbit propagation than the SGP4. For each sample epoch, 10 days of data was obtained from the

CHAMP Rapid Science Orbit data set [18]. The Cartesian state vectors were then used to calculate values for the semi-major axis using

$$a = \frac{\mu r}{2\mu - v^2 r}, \tag{101}$$

where $r$ and $v$ is the magnitude of the geocentric position and velocity vector respectively given by the TLE state vector, with $\mu$ having its usual meaning. Once the values for semi-major axis were calculated, a linear regression line was fitted and an average rate-of-change was calculated.

The propagation via AETHER first required estimations of ballistic coefficients. Therefore, the 30 TLE sets published directly before and after the 10 sample TLE sets were used to estimate ballistic coefficient values for CHAMP using the method described in Chapter 5.2. The resulting estimations of ballistic coefficients for the 10 sample TLE sets are shown below in Figure 40.

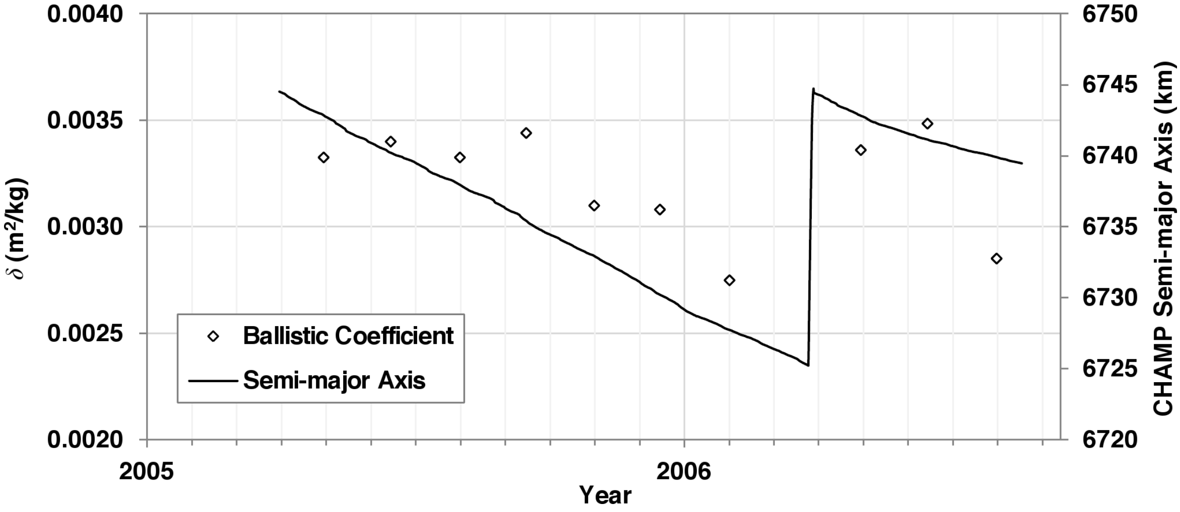

Figure 40: *The estimations of ballistic coefficients for the 10 sample TLE sets that were used in AETHER for the comparison simulations. Also shown for reference are the values of semi-major axis derived from the state vectors of the TLE sets. Note the apparent correlation with altitude of the ballistic coefficient estimates.*

Using the ballistic coefficients estimated for the 10 sample TLE epochs, AETHER then propagated the state vector output from the SGP4 for a 10-day period and returned the variation in semi-major axis. A linear regression line was then fit to the semi-major axis data and an average rate-of-change was calculated.

Finally, propagation data from the SGP4 was required. This was a trivial task whereby the SGP4 propagator integrated the 10 sample TLE sets and produced Cartesian output state vectors. These state vectors were then converted into values of semi-major axis (using equation (101) through which a linear regression line was plotted and an average rate-of-change was calculated.

The percentage difference in the average rate-of-change of semi-major axis were then calculated for all ten sample TLE epochs with the results shown below in Figure 41. The average errors for AETHER and the SGP4 propagations were 13.28% and 9.63% respectively. This resulted in an overall improvement in propagation accuracy of 3.65%. Out of the 10 sample simulations, 7 showed AETHER to gave an improved accuracy propagation compared to the SGP4 propagator. From this, and the overall error improvement of 3.65%, AETHER was considered to be able to obtain sufficiently accurate propagation ephemerides for use when analysing long-term thermospheric density changes.

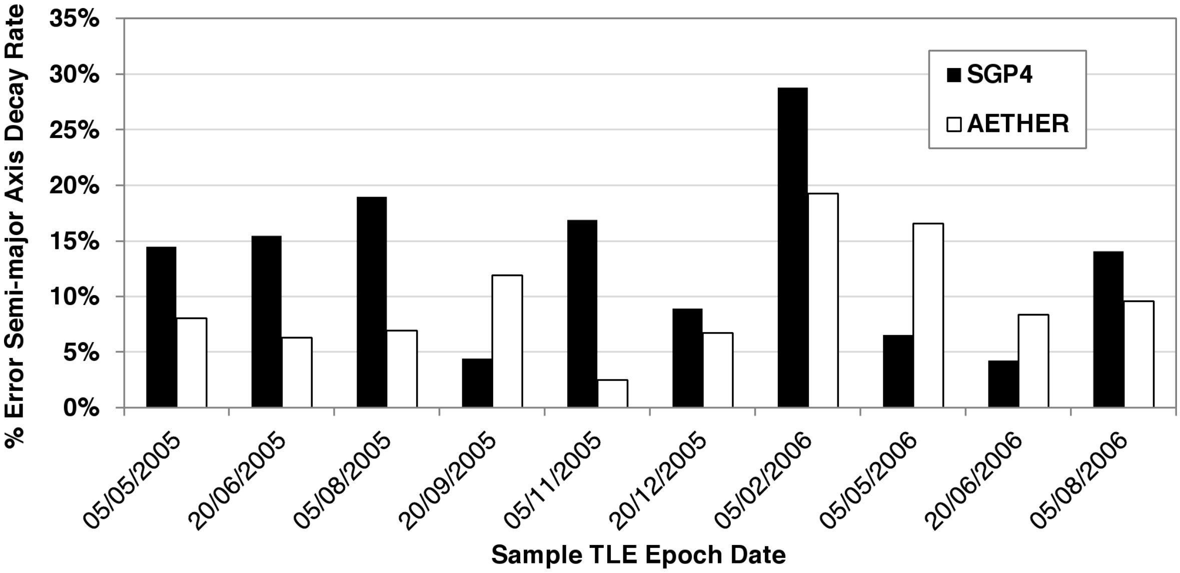

Figure 41: *The percentage difference in the average rate-of-change of semi-major axis between the CHAMP RSO data sets and AETHER and the SGP4 propagators for all ten sample TLE epochs.*

### 5.3.2 Re-entry Predictions

For this pre-curser test of AETHER, only TLE data was used to provide the satellite ephemerides as well as to estimate the satellite's ballistic coefficients. This was done to mimic the practical challenges present when analysing long-term thermospheric density changes.

The validation was made by predicting re-entry dates using TLE data prior to the re-entry of three satellites: an Earth observation satellite (ID 10973 re-entered March 2007); the spent upper stage of a Tsiklon-3 launch vehicle (ID 20967 re-entered January 2007); and a solar observation satellite (ID 26873 re-entered December 2005).

Initially, the ballistic coefficients were calculated from the unreliable $B^*$ values given in the TLEs (using equation (7) on page 22). Due to the unknown orientation, configuration and surface properties of the satellites, three cases were investigated by varying the value for $\delta$ by $\pm$20% [89]; the results are shown in Figure 42.

For all satellites the predicted re-entry dates were later than the actual re-entry. This was believed to be due to the underestimation of the ballistic coefficient from using the $B^*$ value. This result provided the motivation to develop the new method that could derive significantly more accurate estimates of ballistic coefficient. The predicted re-entry dates using the three

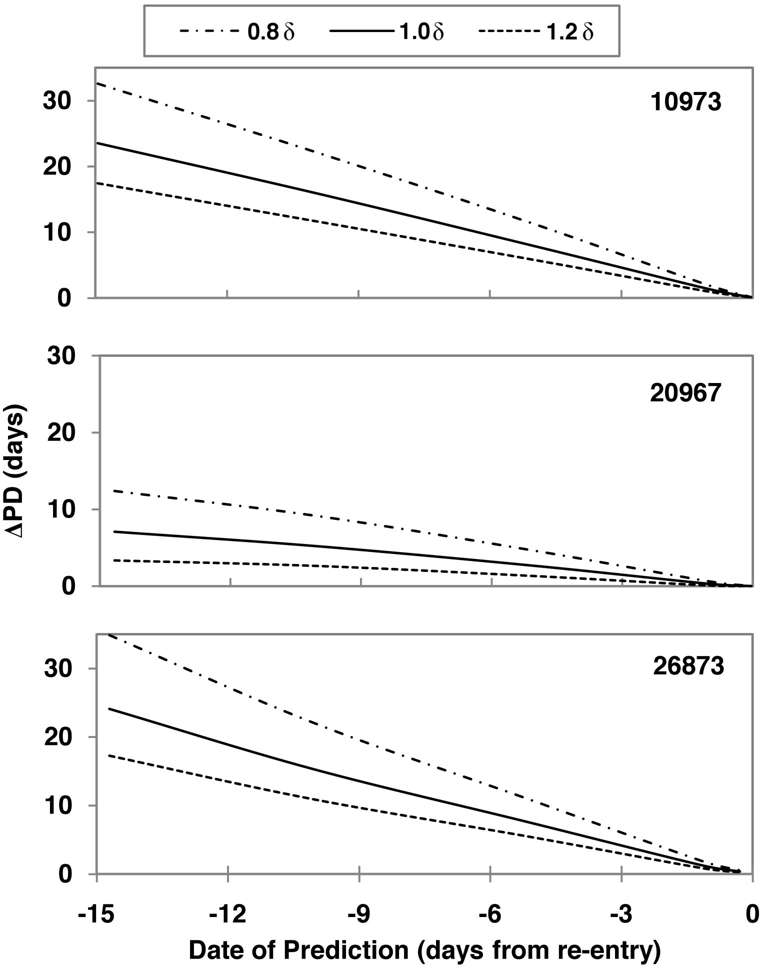

Figure 42: *The re-entry predictions used to validate AETHER. The ballistic coefficients that were used for each satellite were based on the* $B^*$ *value given explicitly in the TLE sets.* $\Delta$*PD denotes the difference between the predicted re-entry date and the true re-entry date*

ballistic coefficients ($\pm$20%) converged as the time to true re-entry decreased. The convergence of the plots demonstrates correct processing of atmospheric drag. The rate of degradation of the semi-major axis is proportional to the drag force, which in turn is proportional to the ballistic coefficient. Reducing the ballistic coefficient, via a reduction in cross-sectional area, reduces the effect of atmospheric drag, which would lead to a slower rate of decay in the semi-major axis. This reduction of decay rate would simulate the satellite remaining in orbit for longer, thus, producing a later re-entry date. An earlier re-entry date would also be expected, due to the same process, for an increase in cross-sectional area.

Subsequently, this exercise was revisited once the method to predict accurate ballistic coefficients had been developed. The tests described above were re-run using the revised values of the ballistic coefficients with improved results. Figure 43 shows the re-entry predictions using the revised estimates of ballistic coeffcient.

The average rate of change of semi-major axis was used to quantitatively assess the magnitude of the improvement. The true average decay rate of the semi-major axis was

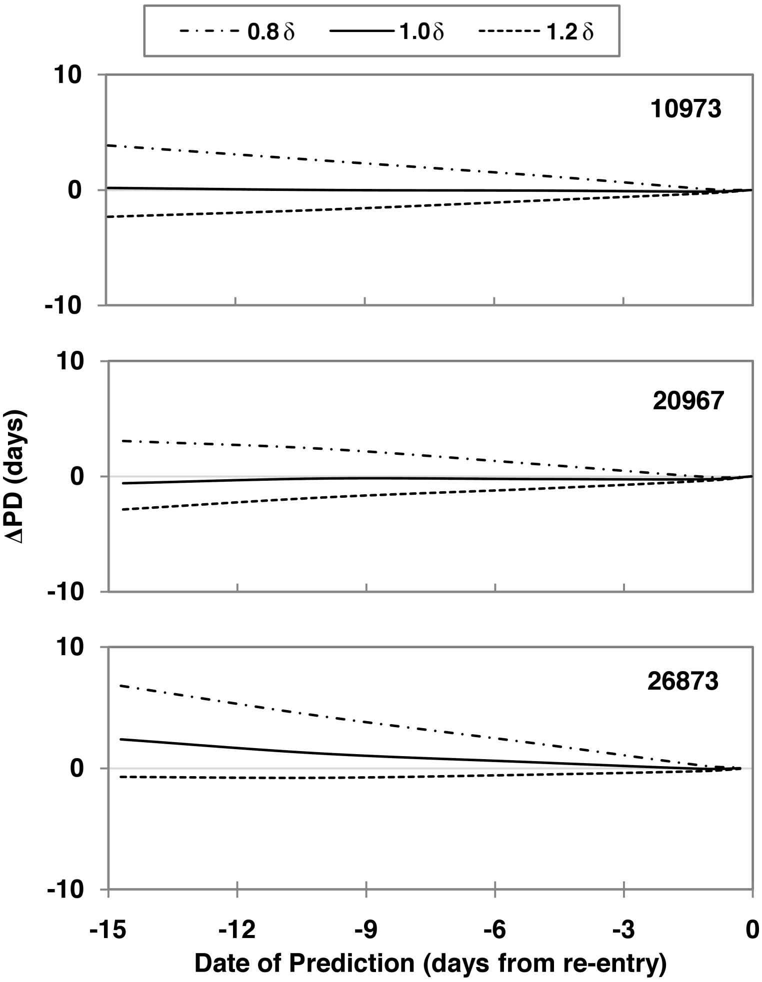

Figure 43: *The revisited re-entry prediction exercise used to validate AETHER. $\Delta$PD denotes the difference between the predicted re-entry date and the true re-entry date.*

calculated using

$$\bar{\dot{a}}_{true} = \frac{a_{15} - a_0}{\Delta t}, \tag{102}$$

where $a_{...}$ is the value of semi-major axis derived from the TLE data at a given number of days, denoted by the subscript, prior to re-entry and $\Delta t$ is time between the TLE sets. Table 9 gives the average decay rates of semi-major axis for the true case, given by the TLE data, and for both the re-entry prediction cases using the different methods of ballistic coefficient estimation.

The use of the ballistic coefficient estimation method developed here reduced the errors in the semi-major axis decay rates to 1.25% at best and 14.20% at worst. This would be directly proportional to errors in the modelled atmospheric drag. An error of 14.20% is less than the assumed variation in project surface area of $\pm$20%. Therefore, having reduced the errors in the modelling of atmospheric drag to less than that intrinsic to the system is satisfactory.

Using the improved method of estimating ballistic coefficients required a large amount of computational effort. More specifically, owing to the iterative method, the calculations of the gravitational harmonics up to order and degree 20 contribute a significant proportion of the total computational run-time. Therefore, in the effort to estimate the satellite ballistic coefficients

Table 9: *The average decay rates of semi-major axis for the true case, given by the TLE data, and for both the re-entry predictions cases using the different methods of ballistic coefficient estimation.*

| Satellite Number | $\bar{\dot{a}}_{true}$ (km/day) | $\bar{\dot{a}}_{B^*}$ (km/day) | $\bar{\dot{a}}_{B^*}$ (% error) | $\bar{\dot{a}}_{AETHER\delta}$ (km/day) | $\bar{\dot{a}}_{AETHER\delta}$ (% error) |
|---|---|---|---|---|---|
| 10973 | -8.38 | -3.25 | 61.24 | -8.28 | 1.25 |
| 20967 | -7.70 | -5.18 | 32.67 | -8.02 | 4.16 |
| 26873 | -6.64 | -2.49 | 62.58 | -5.70 | 14.20 |

$\bar{\dot{a}}_{B^*}$ denotes using $\delta$ from the $B^*$ parameter.

$\bar{\dot{a}}_{AETHER\delta}$ denotes using $\delta$ from the new method.

more efficiently, a further investigation was performed, varying the degree of the calculated gravitational harmonics.

The ballistic coefficients for the three satellites used to make the re-entry predictions were also predicted using varying degrees of gravitational harmonics between order 3,3 up to 20,20. The results shown in Figure 44 are normalised with respect to the ballistic coefficient determined from gravitational harmonics of order and degree 20.

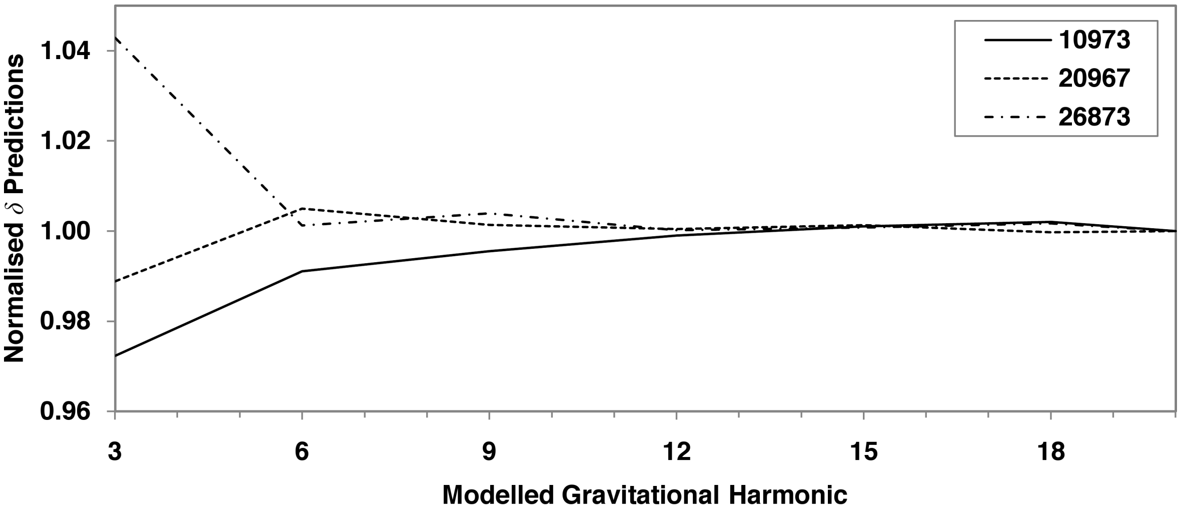

Figure 44: *The estimates of ballistic coefficient normalised to the value obtained using gravitational harmonics of order and degree 20.*

From Figure 44 it is evident that there exists a correlation between the accuracy of the ballistic coefficient estimates and the order and degree of gravitational harmonics included in AETHER's propagation. When modelling Earth gravitational harmonics above order and degree 12, the estimates of ballistic coefficient converge to a single value. Beyond order and degree 20, the error reduces to a value less than 1%. To infer thermospheric density from satellite drag data requires a precise estimate of ballistic coefficient. Therefore, as the accuracy of the ballistic coefficient estimates reduce to 1% only after gravitational harmonic order and degree 20, this level of detail is used in the AETHER perturbation model when predicting the ballistic coefficients for satellites whose data is used to infer thermospheric density changes.

## 5.4 Analysing Thermospheric Density and Deriving a Secular Trend

Based on the requirement of item 4 in the Research Plan (page 35), this Section presents the method used to infer information about thermospheric mass density from TLE data and how this information was used to derive long-term thermospheric density changes.

This point in the thesis marks a subtle shift in the logic surrounding the ambiguity of estimating ballistic coefficients and thermospheric density. So far, we have mainly focussed on assuming a correct model density, derived from the NRLMSISE-00 empirical model, in order to allow predictions of ballistic coefficients. Now, the perspective shifts whereby an analysis has been summarised of the constancy of the ballistic coefficients, and how variations therein are accounted, to allow an analysis of thermospheric density change to be made.

The observational (TLE) and numerically derived (AETHER) data provides the most accurate ephemerides when used in state vector format, as previously described. From these state vectors, osculating orbital elements can be deduced. From the previous Chapters, the change in semi-major axis $\Delta a$ was shown to be a reliable parameter when obtaining accurate estimates of satellite ballistic coefficients. As such, it was also the parameter used to infer information about thermospheric density. The method described here utilises the TLE data in consecutive pairs given by (TLE$_1$ and TLE$_2$) for a particular satellite.

To infer a change in thermospheric mass density required a comparison between density information derived from observational data and data derived numerically. This can be expressed as

$$\zeta = \frac{\rho}{\rho^*}, \tag{103}$$

where $\rho$ denotes the density derived from the observational TLE data and $\rho^*$ is the density derived numerically from the atmospheric model in AETHER. From King-Hele [62], the density at any point on an orbit is

$$\rho = \frac{-\mu \dot{a}_{Drag}}{a^2 v^3 \delta}, \tag{104}$$

where $\mu$ is the gravitational constant of the Earth, $\dot{a}$ is the rate of change with respect to time of the semi-major axis, $a$, $v$ is the satellite's air-relative speed and $\delta$ is the ballistic coefficient of the satellite.

Assuming that the parameters in equation (104) refer to the average values of a satellite's orbit between the epochs TLE$_1$ and TLE$_2$, all the parameters are known except the rate of change of the semi-major axis $\dot{a}$, an average value of which can be calculated by

$$\dot{a} = \frac{a_2 - a_1}{\Delta t} = \frac{\Delta a}{\Delta t}, \tag{105}$$

where $\Delta t$ is the epoch separation between TLE$_1$ and TLE$_2$. Calculating the values of $a_1$ and $a_2$ associated with the epochs of TLE$_1$ and TLE$_2$ respectively from the observational and numerically derived data sources allows the derivation of the densities $\rho$ and $\rho^*$ from equation (104).

The values of $a_1$ and $a_2$ representing the observational data are derived from the Kozai mean motion, given explicitly in the TLE sets, using equation (91) (page 79). From the two estimates of semi-major axis from $\text{TLE}_1$ and $\text{TLE}_2$ the change in semi-major axis, from the observational data, $\Delta a_{\text{TLE}}$ can be calculated.

Via the SGP4 propagator, AETHER uses the state vector of $\text{TLE}_1$, associated with the osculating orbit $\text{O}_1$, to propagate the orbit until the epoch of $\text{TLE}_2$, giving a second osculating orbit $\text{O}_2$. The state vectors from the osculating obits $\text{O}_1$ and $\text{O}_2$ are used to infer a value for the semi-major axis using equation 101. The change in semi-major axis from the orbits $\text{O}_1$ to $\text{O}_2$, provides the numerically derived data $\Delta a_{\text{AET}}$.

Previously, using equation (105), $\dot{a}$ was determined from the observational TLE data. A new average rate of change of semi-major axis for the numerically derived data is given by

$$\dot{a^*} = \frac{\Delta a_{\text{AET}}}{\Delta t}, \tag{106}$$

where $\Delta t$ is the same as used in equation (105). This enables an estimate of density derived from numerical propagation given by,

$$\rho^* = \frac{-\mu \dot{a^*}}{a^2 v^3 \delta}. \tag{107}$$

Equation (103) can be re-written using the information from equations (104)-(107), giving

$$\zeta = \frac{a_2 - a_1}{a_2^* - a_1} = \frac{\Delta a_{\text{TLE}}}{\Delta a_{\text{AET}}}. \tag{108}$$

In equation (108), the change in semi-major axis, $\Delta a_{\text{AET}}$, is caused by many perturbations. To isolate the variation in the semi-major axis caused by atmospheric drag, an analysis of how the semi-major axis is affected by the other perturbations was required. The rate of change of a semi-major axis $\dot{a}$ given by the Lagrange's planetary equations is

$$\dot{a} = \frac{2a^2}{\sqrt{\mu p}} \left\{ f_r e \sin\theta + f_t \left(1 + e\cos\theta\right) \right\}, \tag{109}$$

where $f_r$ denotes the radial forces parallel to the position vector $\mathbf{r}$, $f_t$ denotes tangential forces in plane and perpendicular to $\mathbf{r}$, $p$ is the orbit's semi-latus rectum, $e$ the orbit eccentricity and $\theta$ the true anomaly. King-Hele [61] showed that *only* forces with components tangential to the satellite's velocity vector affect the semi-major axis. His resulting expression showing this is

$$\dot{a} = \frac{2a^2 v}{\mu} f_T, \tag{110}$$

where $f_T$ denotes the force per unit mass parallel to the velocity vector $\mathbf{v}$. Therefore, $f_T$ is simply the sum of accelerations from all perturbations parallel to $\mathbf{v}$. Another way to write equation (110) would then be

$$\dot{a} = \frac{2a^2 v}{\mu} \left( \ddot{r}_{Earth} + \ddot{r}_{Drag} + \ddot{r}_{Moon} + \ddot{r}_{Sun} + \ddot{r}_{SRP} \right), \tag{111}$$

where $\ddot{r}$ is the components of the acceleration vectors parallel to $\mathbf{v}$ due to the various perturbation sources, denoted by the subscripts. For the purposes of determining atmospheric density changes, only the rate of change of semi-major axis due to atmospheric drag is of interest. Therefore, when AETHER propagates a satellite's orbit between the epochs of $\text{TLE}_1$ and $\text{TLE}_2$ the required total change in semi-major axis is therefore

$$\Delta a_{\text{AET}} = \int_{\text{TLE1}}^{\text{TLE2}} \frac{2a^2 v}{\mu} \ddot{r}_{Drag} \mathrm{d}t. \tag{112}$$

Figure 45 shows $\dot{a}$ and the cumulative change in semi-major axis $\Delta a$ over a period of 10 hours by using consecutively published TLE sets for satellite ID 02389. The orbital parameters for this satellite gave a semi-major axis of 8077 km, an eccentricity of 0.1665 and an inclination of 81°.

As Figure 45 shows, over many orbit cycles, the only perturbation causing a significant secular change in the semi-major axis is that due to atmospheric drag. There can also be a secular change in the semi-major axis due to the solar radiation pressure perturbation if a satellite enters Earth's shadow. Errors can be induced in the calculation of the SRP contribution to change in semi-major axis due to the possible mismatch in the position of the discretely-propagated ephemeris with the exact point of shadow entry and exit. From Figure 45, the magnitude of semi-major axis perturbations due to SRP are of the order of $10^{-5}$ km. In general, the magnitude of semi-major axis perturbations due to atmospheric drag is much larger than perturbations due to SRP. However, this does depend in solar activity, as shown previously in Figure 2. At 600 km altitude, the magnitude of the perturbations due to SRP are approximately equal to perturbations from atmospheric drag during times of low solar activity.

The plot of gravity harmonics in Figure 45, shows a large effect on the changes in semi-major axis. If the epochs of $\text{TLE}_1$ and $\text{TLE}_2$ produce a satellite ephemeris which are not closely matched in terms of their geocentric latitude, the contribution from perturbations such as $J_2$ would need to be calculated and subtracted from the total change in semi-major axis before inferring changes due to atmospheric drag. Fortunately, the TLE sets are produced in such a way that their geocentric latitudes are similar, therefore minimising the net effect of gravitational anomalies on the semi-major axis. However, in some cases of TLE ephemerides would not be located at the ascending node, in which case the $J_2$ component is not negligible and would significantly affect the value of semi-major axis. As such, the Kozai mean motion is used to determine value of semi-major axis as the $J_2$ component, as well as higher-order gravitational effects, are largely removed and would be comparable with the drag component derived from AETHER.

Integrating in AETHER the osculating semi-major axis from the state vectors and summing the contribution due to drag gave an estimate of $\Delta a_{\text{AET}}$ and the Kozai mean motion given directly by the TLE sets were used to estimate $\Delta a_{\text{TLE}}$. There is a discrepancy in the magnitudes of the derived values of semi-major axis by using these two different sources. This is because the mean motion given in the TLE sets are inclination and eccentricity specific, due the effects of $J_2$. However, the method presented here only requires the secular *change* in semi-major axis, which is practically equal from the different derivation methods described above.

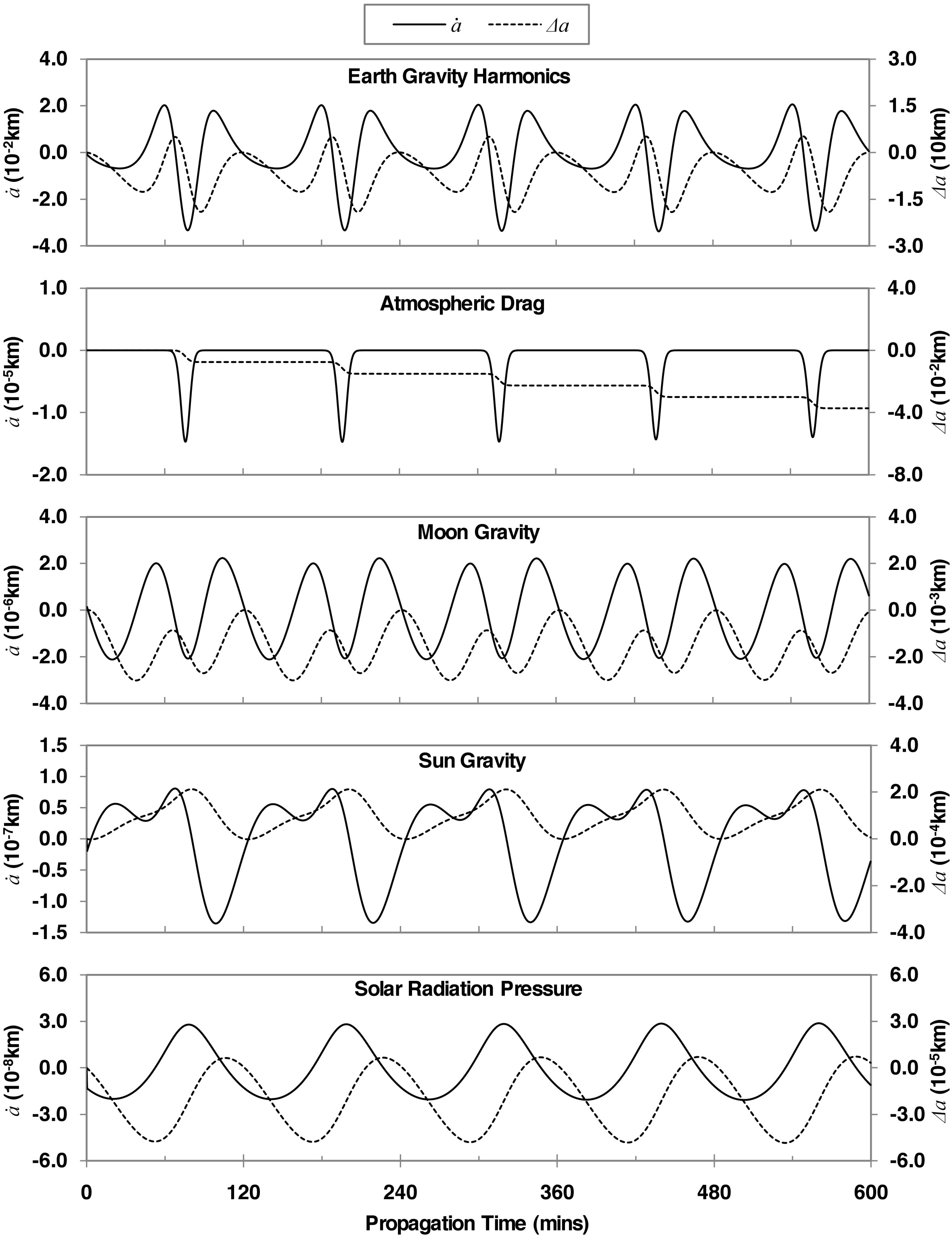

Figure 45: *The rate of change $\dot{a}$ and cumulative change $\Delta a$ in semi-major axis due to the modeled perturbations in AETHER for satellite 02389 between two consecutive TLE sets in January 1999. The units of $\dot{a}$ are shown only in length due to the variability of the integration time step, which was approximately 21 seconds.*

To investigate altitude dependency of long-term thermospheric density changes, a method to associate the density ratios $\zeta$ with a particular altitude, $\zeta_h$, was required. For a satellite orbit that enters the atmosphere, the change in the semi-major axis caused by atmospheric drag can be attributed to a particular height relative to the perigee altitude. This height depends on a parameter given by

$$z = \frac{ae}{H}, \tag{113}$$

where $e$ is the eccentricity of the satellite's orbit and $H$ is the density scale height of the atmosphere at the perigee altitude. King-Hele [64] showed that by assuming a $z > 3$, the associated density altitude can be attributed at approximately half the scale height above the perigee altitude. For satellite orbits with $z < 3$, the perigee altitude was the associated density altitude. As some satellite orbits degraded such that $z > 3$ initially and during, or after, the historical time span reduced to $z < 3$, there lies a discontinuity in the assignment of the associated altitude. However, when the value of $z \to 3$, the associated altitude tends to the perigee altitude, thereby naturally creating a smooth transition between phases.

From King-Hele [60], the density scale height $H$ is a parameter that describes the variation of atmospheric density with altitude. It assumes atmospheric density decays exponentially with altitude and that the Earth is spherical with an inverse-square gravity field. For one density scale height, atmospheric density changes by a factor equal to the exponential mathematical constant $(\exp(1) \approx 2.718)$. The density scale height depends on a number of physical parameters given by

$$H = \frac{1}{\frac{Mg}{RT} - \frac{2}{r}}, \tag{114}$$

where $M$ is the molecular mass of the local atmospheric composition, $g$ is the gravitational acceleration due to the Earth at the local altitude, $R$ is the universal gas constant (8.314 J/kMol), $T$ is the local atmospheric temperature and $r$ is the distance from the centre of the Earth. Equation (114) begins to loose accuracy above altitudes of 500 km due to the increasing mean free path of the atmospheric molecules [60]. The NRLMSISE-00 empirical atmospheric model provides estimates of atmospheric molecular mass as well as local atmospheric temperature and so an estimate of the density scale height can be obtained. However, as the state of the atmosphere depends on solar activity, the density scale height is not constant. Figure 46 shows the variation in density scale height across a range of altitudes for the duration of the historical period analysed in this study.

The estimation of thermospheric density relies heavily on the estimation of ballistic coefficient. It is important to address all aspects that might affect the ballistic coefficient with regards to the derivation of long-term density changes. For this study, TLE sets from the years of 1999 and 2000 with epoch separation of 10-days were used to derive values of satellite ballistic coefficients. This particular historical period provided the required TLE epoch resolution sets the satellites used in this study. In addition, it was a period when solar activity was neither at maximum nor minimum, and therefore represented a relatively 'average' state.

It was important that the estimates of ballistic coefficient were all derived using the same

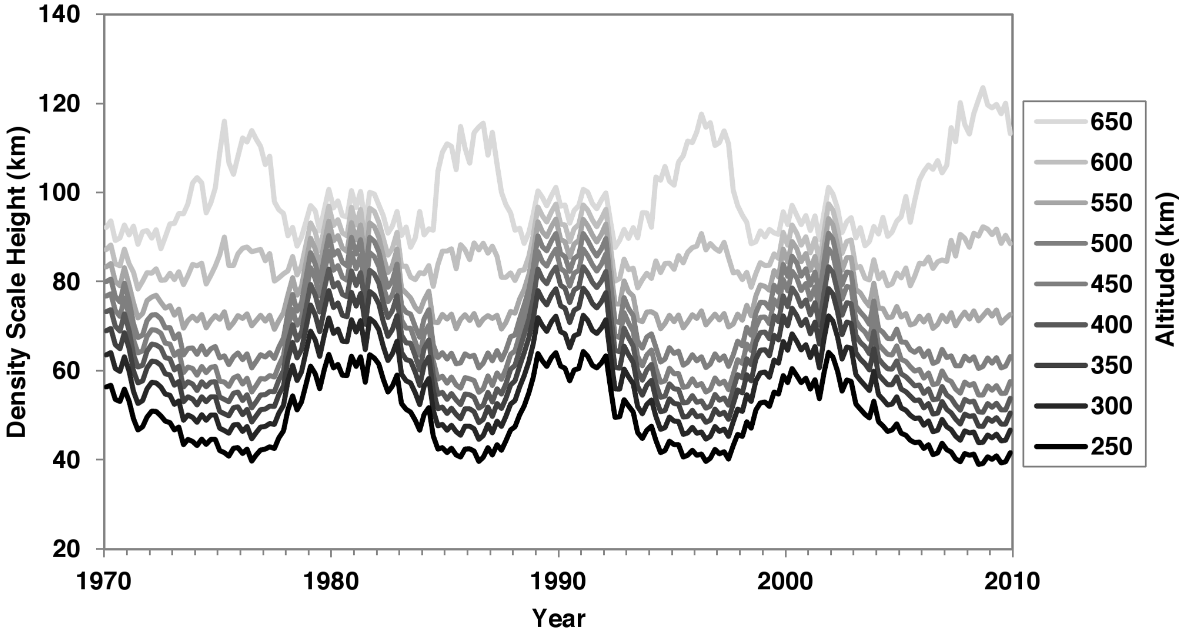

Figure 46: *The variation of density scale height $H$ across a range of altitudes (250-650 km) for the duration of the historical period analysed in this study.*

time period. This is due to the nature in which the ballistic coefficients were estimated and how they would later be put to use. The ballistic coefficients were estimated using observational TLE data, the same data that would be used to infer long-term thermospheric density change. Therefore, to reduce the variations in ballistic coefficient estimates caused by potential atmospheric model biases in AETHER, only a comparatively short historical period of TLE data was used compared to that used to infer long-term density changes. Even so, the ballistic coefficient is essentially a scaling factor used to infer relative changes in thermospheric density. As such, extending the two-year ballistic coefficient estimation period would likely make little difference to the long-term density trend results. This implied that the minimum requirement for the historical database of TLE sets, from which a long-term density changes would be inferred, also needed cover the historical time span between the years 1999-2000.

One of the parameters that affects a satellite's drag coefficient is the atmospheric composition (see Section 2.3 page 21). Depending on what gas species are dominant, the drag coefficient can vary accordingly. As one moves vertically through the atmosphere, the ratios of the different gas species vary approximately according to their molecular mass. This being the case, the drag coefficient can be thought to be altitude-dependent. As well as the gas ratios affecting the drag coefficient, some species directly affect the material surfaces of a satellite; atomic oxygen is one such species. Over time atomic oxygen can adhere to a satellite and alter its surface properties.

Long-term changes in satellite surface properties will affect the drag coefficient, and hence, the ballistic coefficient. However, the magnitude of the changes caused by surface erosion would be significantly less than the magnitude of the variation in projected surface area of the satellite. As both of these parameters contribute to the value of ballistic coefficient, it would be practically impossible to discern changes due to surface erosion from the variability caused by changing projected surface area.

As the semi-major axis of a satellite orbit in an atmosphere reduces over time, so does its associated density altitude. Therefore, when predicting the effects of atmospheric drag in an orbital propagator, such as AETHER, the variation of atmospheric regime and composition would alter the drag coefficient; and so the variation of ballistic coefficient must to be taken into account. For this study, long-term orbit evolution is a key component, with orbit decay playing a vital role that needs to be addressed.

The study by Moe & Bowman [75] showed that for an object with constant mass, geometry and project surface area, the drag coefficient within the lower thermosphere (150-500 km) can reduce by 0.08 up to 0.15 per 100 km for $\mathrm{F}_{10.7}$ solar activity of 200 to 65 ($10^{-22}\mathrm{W/sm}^2$) respectively as shown in Figure 8 (page 24). Due to the lack of available results in this area of study, a linear regression and interpolation analysis was performed to obtain a model of the altitude and solar flux dependency, as shown in Figure 47.

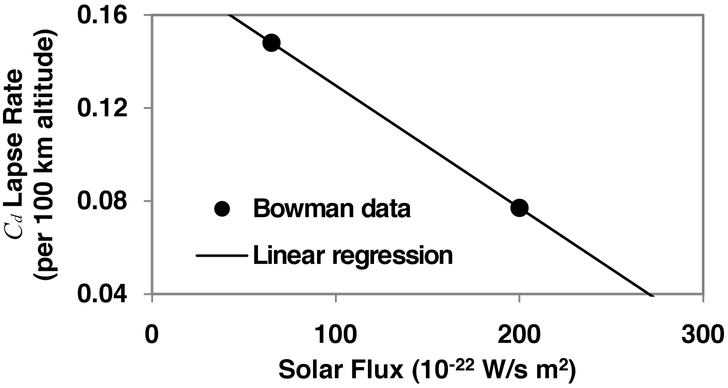

Figure 47: *The linear regression and interpolation analysis used to obtain a model of the altitude and solar flux dependency of drag coefficient. Data points from Bowman [75].*

The function of the linear interpolation line shown in Figure 47 was given by

$$\Delta C_d = -0.000526\mathrm{F}_{10.7} + 0.182185, \tag{115}$$

which could then be used to provide an altitude dependent multiplier for the estimation of the drag coefficient, and therefore ballistic coefficient.

In addition to a ballistic coefficient being estimated for each satellite from the two-year period 1999-2000, a ballistic coefficient reference altitude, $h_\delta$, was also assigned. $h_\delta$ was calculated using the average of all the density altitudes, $h_\zeta$, associated with each density ratio for each satellite. $h_\delta$ could then be used as a reference point from which the values of ballistic coefficients could be varied according to their associated density altitude throughout the historical period used to infer long-term density changes. The derived values of $h_\delta$ for each satellite are shown in Table 12 in Section 11.5 of the Appendix.

Equations (1) and (112) show that as the change in semi-major axis is directly proportional to the drag coefficient, and thus the ballistic coefficient, the density ratios obtained from the observational and numerical data can be manipulated to account for the variation in ballistic coefficient. The manipulation was performed using a ballistic coefficient multiplier, $\Delta\delta$, which used equation (115) to yield an altitude and solar activity dependent function given by

$$\Delta\delta = 0.01(h_\zeta - h_\delta)(-0.000526\mathsf{F}_{10.7} + 0.182185), \tag{116}$$

where $h_\zeta$ (km) denotes the associated density altitude, $h_\delta$ (km) denotes the average associated density altitude during the ballistic coefficient determination period and $\mathsf{F}_{10.7}$ is the solar radio flux ($10^{-22}$W/sm$^2$). The TLE data from the OV3-3 satellite (ID 02389) and historical solar flux data were used to present a typical example of the variation of $\Delta\zeta$ over the 40-year historical period (1970-2010), as shown in Figure 48.

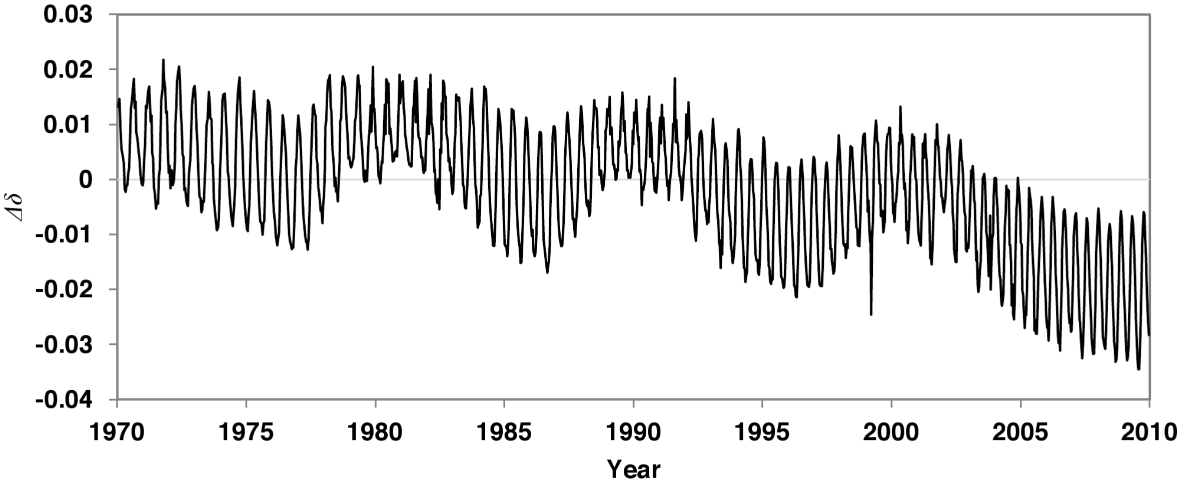

Figure 48: *The typical variation of $\Delta\delta$ over the 40-year historical period (1970-2010) using historical solar flux data and TLE data from the OV3-3 satellite (ID 02389).*

Figure 48 shows a generally declining trend in the multiplier $\Delta\delta$ due to the variations in ballistic coefficient. It is completely independent of any long-term thermospheric density change. Therefore, presenting the typical effect the variation of ballistic coefficient can have demonstrates its importance in deriving long-term changes due to varying thermospheric density. If the variation of ballistic coefficient was not considered, then there would definitely be trends aliased into the analysis that were not due to thermospheric density change.

The multiplication factor $\Delta\delta$ is then scaled using the standard value of drag coefficient of 2.2 to obtain a density ratio multiplication factor $\Delta\zeta$ given by

$$\Delta\zeta = \frac{2.2 + \Delta\delta}{2.2}, \tag{117}$$

Finally, the combination equations (108) and (116) gives

$$\zeta_f = \frac{\zeta}{\Delta\zeta} = \frac{\Delta a_{\mathsf{TLE}}}{\Delta a_{\mathsf{AET}}\Delta\zeta}, \tag{118}$$

where $\zeta_f$ is the final estimate of density ratio. Estimates of $\zeta_f$ from all the satellites studied here were used to determine long-term thermospheric density changes.

## 5.5 Summary

An Earth-orbital propagator for thermospheric analysis (AETHER) has been presented in the preceeding sections. AETHER has the ability to utilise TLE data to propagate satellite orbits. The accuracy with which AETHER can propagate orbits is, at worst, two orders of magnitude better than the accuracy of the TLE ephemeris data. The perturbations due to Earth-gravity harmonics, atmospheric drag, luni-solar gravity and solar radiation pressure are included in AETHER. Where possible, the modelling of each perturbation by AETHER has had its implementation tested, and its accuracy validated, against independent external sources. Initial studies were made before AETHER was used to analyse the full TLE database of the 41 satellites; these will be presented in a later Section. The aim of first study was assess the performance the methods derived in the previous using a small number of satellites. The second study used a larger database of satellite data, building on from the lessons learnt from the first initial study.

The method presented above to empirically determine satellite ballistic coefficients can produce accurate estimates. Furthermore, information about satellite drag coefficients can also be inferred if some information about the physical parameters of the satellite is known. The application of this method could be used in new areas of study as a viable means of investigating satellite drag coefficients.

The 15 objects used to validate the method of ballistic coefficient estimation provide insufficient evidence to rigorously analyse and quantify effects from solar flux and geomagnetic variations in the prediction of ballistic coefficients. However, there have been numerous studies that demonstrate the inaccuracies of empirical atmospheric models arising from varying levels of solar activity. Therefore, methods that predict ballistic coefficients using empirical atmospheric models to estimate density, such as the one developed here, will contain errors connected with the solar flux model dependencies. The errors associated with solar variability when using the method derived here to predict ballistic coefficients were counteracted by carefully selecting the historical time period from which the satellite data is used. By avoiding data derived during times of low solar activity used to predict ballistic coefficients can significantly reduce estimation errors.

The method for predicting ballistic coefficients can be used with any empirical atmospheric models that provide an estimate of local density. The estimated values of ballistic coefficient should be used with caution. If the derived values of $\delta$ are to be used in further atmospheric studies, the same atmospheric model should be used.

This method has demonstrated that accurate ballistic coefficients can be estimated using only raw TLE data. However, care must be taken when selecting the historical span of TLE data for specific satellites, due to the variations associated with high-eccentricity orbits. For satellites with low eccentricity orbits, deriving accurate estimates of ballistic coefficients can be done even if a small temporal span of historical TLE data is available.

The method presented here provides a novel way of predicting satellite ballistic coefficients. By using a dataset of 15 satellites with known physical and orbital parameters, along with previously published studies, the method has been developed to provide ballistic coefficient estimates that can be used in the study of long-term thermospheric density change.

It is important to focus on the goal of this study, which is to deduce and quantify a secular thermospheric density trend, and not to develop a tool to predict absolute thermospheric densities. The difference between the two is subtle, yet they present very different challenges. With the method presented here, sound results for secular thermospheric density change can be successfully achieved without the added complications of producing an absolute value for mass density. Thus, with the ability to analyse thermospheric density and infer long-term changes completes the 4th and final practical objective of the Research Plan.

# 6 Initial Studies Into Long-Term Thermospheric Density Change

This section presents the initial studies that were made in the effort to assess the performance of the methods and tools presented in the previous sections. There are two studies presented here.

The first study was the first attempt at inferring long-term thermospheric density changes. Here, the TLE data for only four satellites were used to give a preliminary view of the performance ability of the methods and tools presented in this report. The utilised TLE data were from the same four satellite as those used by previously published empirical investigations into long-term thermospheric density change. This allowed a direct comparison of the results.

The second study was a more detailed investigation using the TLE data from 29 satellites to analyse long-term density changes in the thermosphere. The larger dataset of satellites gave a better view of the efficiency of the utilised methods and the limitations of the historical TLE dataset before being used on all 41 satellites listed previously in Table 1.

These initial studies provided knowledge on the practical use of the TLE data, their limitations, and how best to overcome their deficiencies. This provided understanding of the TLE data and how best they can be used.

The results of these studies highlighted some improvements that could be made to AETHER, so that the gathering of final results could be done more efficiently.

## 6.1 Preliminary Results of Long-Term Thermospheric Density Change

Using the TLE data of four satellites (IDs 00060, 00614, 02389 & 04430), thermospheric density was analysed and preliminary results were obtained that support existing evidence of a long-term thermospheric density change [106]. The four satellites used here were a subset of the five used by Keating *et al.* [56] and the 27 used by Emmert *et al.* [28], which allowed direct comparison with the results from this study.

A linear regression line was fit to the density ratios derived for each of the four satellites. Table 10 shows the derived trends along with the results from the previously published studies. The plus and minus variabilities stated in the Table were calculated using the maximum and minimum trend value derived from the four satellites in that particular study.

By collating all the results for the individual satellites and applying a linear least-squares regression, a secular decline in thermospheric mass density was determined as shown in Figure 49. Therefore, since 1970 and above an approximate average altitude of 367 km, these studies suggest that thermospheric mass density has reduced by an average rate of -4.1 ±0.7% per decade.

The study by Keating *et al.* gave a value of -3.96 ±2.5% per decade over the 20-year period of 1976-1996 compared to that derived in this study of -3.82 ±1.5% per decade over the same historical time period. The more detailed and robust study by Emmert *et al.* [30], which used more than 5,000 satellites, derived a value of -2.68 ±0.49% per decade, whereas this study yielded the trend of -4.1 ±0.7% per decade. The next step is therefore to perform the analysis using a larger satellite TLE database.

Table 10: *The long-term thermospheric density trends derived from the density ratios obtained from the initial study by Saunders et al. [106]. Results from the previously published studies by Keating et al. [56] and Emmert et al. [28] are also shown for the density trends between the years 1976-1996 with the results from the initial study over the same period.*

| Satellite ID Number | Perigee Altitude (km) | Trend $\dot{\zeta}$ 1970-2000 (% per decade) | Trend $\dot{\zeta}$ 1976-1996 (% per decade) Saunders [106] | Keating [56] | Emmert [28] |
|---|---|---|---|---|---|
| 00060 | 418 - 390 | -4.15 | -3.94 | -3.26 | -6.67 |
| 00614 | 337 - 324 | -3.95 | -4.64 | -3.29 | -7.35 |
| 02389 | 355 - 350 | -4.78 | -4.86 | -7.10 | -5.84 |
| 04330 | 350 - 315 | -3.36 | -1.83 | -2.18 | -8.30 |
| Average | 367 | -4.1 ±0.7 | -3.82 ±1.5 | -3.96 ±2.5 | -7.04 ±1.2 |

Data from the study by Emmert *et al.* was inferred from Figure 9 of their paper [28].

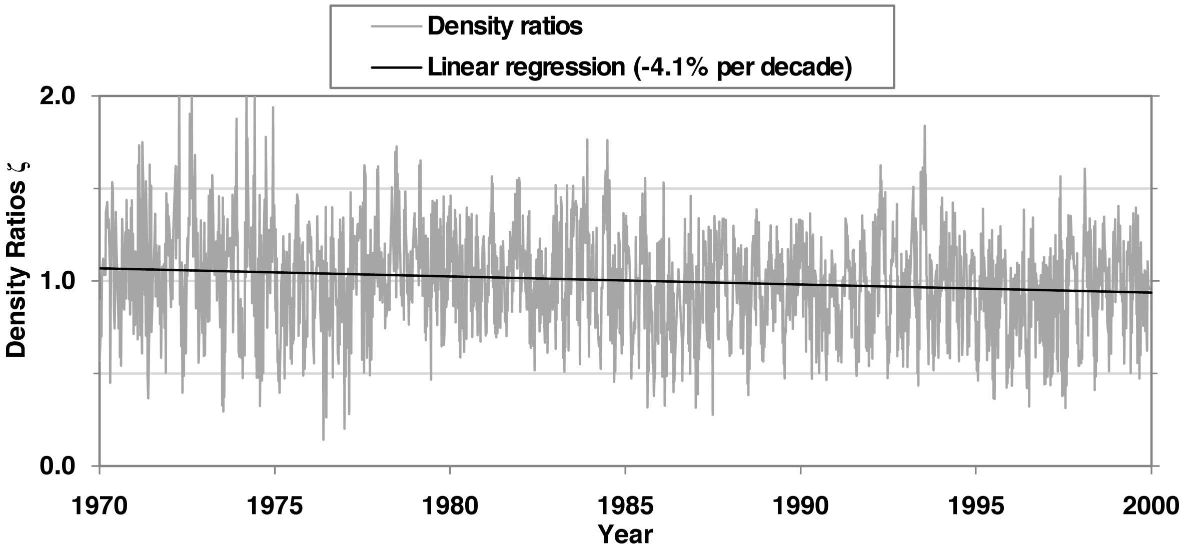

Figure 49: *The density ratios $\zeta$ derived from TLE for all four satellites used in this validation exercise over the historical period of 1970-2000. A linear regression line for the density ratios is plotted showing a secular density decline of approximately -4.1 ±0.7% per decade.*

During the historical time period of 1970-2000, more than two solar cycles occurred. Therefore the data presented here covers all levels of solar variability. It was shown by Emmert *et al.* [28] that thermospheric density variations appeared dependent on solar activity, and therefore this was investigated further. When a 300-day moving average was applied to the density ratios and plotting the result against the $F_{10.7}$ solar flux, a correlation was evident, as shown in Figure 50. A more detailed discussion about this correlation is deferred until the next Section. This apparent dependency of solar flux deserved a more rigorous analysis than could be achieved from the data of four satellites. However, at this point, it was reasonable to draw the conclusion that during periods when $F_{10.7} < 70$, the density ratios were less than the fitted linear trend by approximately 5-10%. In addition, there seemed to be an anti-correlation during periods with $F_{10.7} > 150$. During these periods the density ratios were approximately equal to the fitted linear trend whereas the the periods either side with $70 < F_{10.7} > 150$, the density ratios peaked between 5-9% over the fitted linear trend. Variations in the density ratios could only be due to either the ballistic coefficient or the modelling of atmospheric density by the NRLMSISE-00 empirical model. Previous discussions have described the process of how variations in the ballistic coefficient, due to solar activity, were accounted for in the density ratios. Therefore, the variation in density ratios with solar flux were deemed to be due to the errors associated with the NRLMSISE-00's prediction of density.

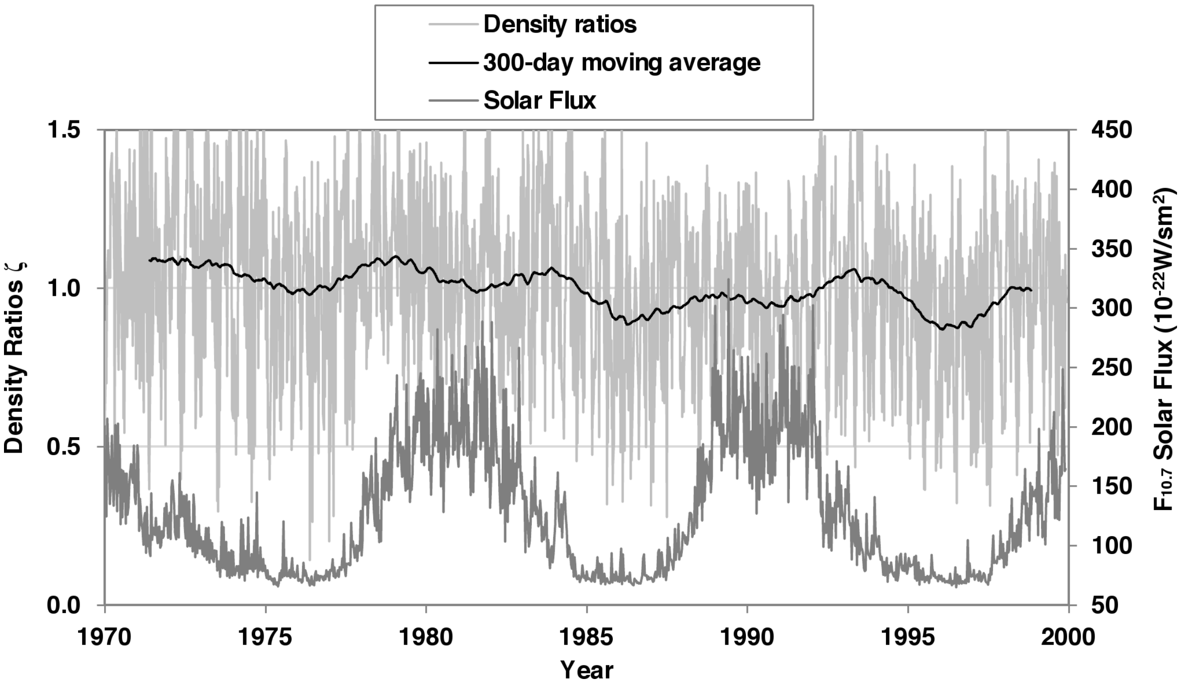

Figure 50: *The 300-day moving average of the density ratios* $\zeta$ *derived from TLE for all four satellites used in this validation exercise over the historical period of 1970-2000. Also shown in the* $F_{10.7}$ *solar flux for the same historical period.*

During the analysis, it became clear that various adjustments in the software AETHER needed to be made in order to increase the efficiency when applying these processes to a larger set of satellite TLE data. With a 2.4 GHz processor computer speed and using a variable integration step size, the computational run-time was an average of 7.5 hours when analysing 30 years of TLE data per satellite. The results of this initial study were used as a datum to assess the alterations to the AETHER software when attempting to improve the efficiency. As briefly mentioned in the demonstration of orbit propagation (Section 5.3.2), improvements in efficiency in AETHER to reduce the computational effort were most beneficial when reducing the degree and order of the Earth's gravitational model used in the acceleration model, as these calculations require the most computational effort.

The magnitude of the secular density trend derived from this initial study was used as a reference value to adjust the detail of the gravitational harmonics modelled in AETHER. The order and degree of gravitational harmonics included in AETHER's perturbation model was varied and the TLE data analysis as previously performed over the 30-year historical period was re-run. Using a perturbation model with the gravitational harmonic of order and degree 2 ($J_{2,2}$)

resulted in a secular density trend 10% greater than the results of this initial study, which modelled gravitational harmonics up to $J_{20,20}$. However, increasing the modelled perturbation detail to $J_{3,3}$, less than 0.04% error in the derived density trends were found. The harmonics of $J_{6,6}$, $J_{12,12}$, $J_{15,15}$ and $J_{18,18}$ were also analysed to ensure that the low error magnitude of using $J_{3,3}$ was not simply a coincidence. The trend error for the harmonics of $J_{6,6}$ and above were less than 0.04%. The analysis of the 30-years of TLE data using the $J_{3,3}$ Earth gravity perturbation model yielded a computational run time of approximately 4 hours; this is about half the time of the previous run-time using a gravity model of order and degree up to $J_{20,20}$. Therefore, when analysing the larger set of satellite TLE data, an Earth gravitational model of $J_{3,3}$ is sufficient. However, when estimating a satellite's ballistic coefficient, a gravitational perturbation model of $J_{20,20}$ is still necessary, based on the results from the first initial study that analysed ballistic coefficient variability with modelled gravitational harmonics.

A correlation appears to exist between the density ratios and solar variability in addition to the secular nature of the long-term trends. Therefore, an additional feature that is included in the next initial study is an attempt to evaluate periodicities in the long-term trends of density ratios.

## 6.2 Further Results of Long-Term Thermospheric Density Change

The second of the initial studies used the TLE data from 29 satellites over the historical period of 1970-2010 to infer a long-term thermospheric density change and was accepted for publication in a special section of the Journal of Geophysical Research - Space Physics, as a paper by Saunders *et al.* [108].

A research objective of this Ph.D study was to analyse the altitude dependency of long-term thermospheric density trends. Methods to infer altitude dependency could be tested with the larger set of satellite TLE data used in this validation exercise. After the 40-year period between 1970-2010 had been analysed by AETHER for all 29 satellites, 33,870 density ratios were obtained, which were unevenly spaced throughout the altitude band 340-640 km.

The density ratios were analysed within overlapping altitude bins, each spanning 40 km. This enabled an analysis of the altitude dependency of the long-term density trends. The overlapping of the bins was done to provide a smoothed set of results from an altitude dependency could be identified. However, the overlapping nature implies re-sampling of the same data, rendering it statistically non-independent. As such, any correlation coefficients derived for any altitude-dependent trend would likely have an artificially inflated correlation coefficient. Figure 51 shows the resulting density ratios contained within the altitude bin of 380-420 km, a 201-day average of the density ratios and a linear regression line applied to the 201-day averages. Linear regression analysis was applied to all the density ratios in each of the 40-km altitude bins. A total of 141 altitude bins were evenly distributed between the altitudes of 360-640 km with their mid-points separated from adjacent bins by 2 km. Figure 52 shows the results of one of these altitude bins as a typical example of the results from other altitude bins, which contained 18 of the 29 total objects analysed.

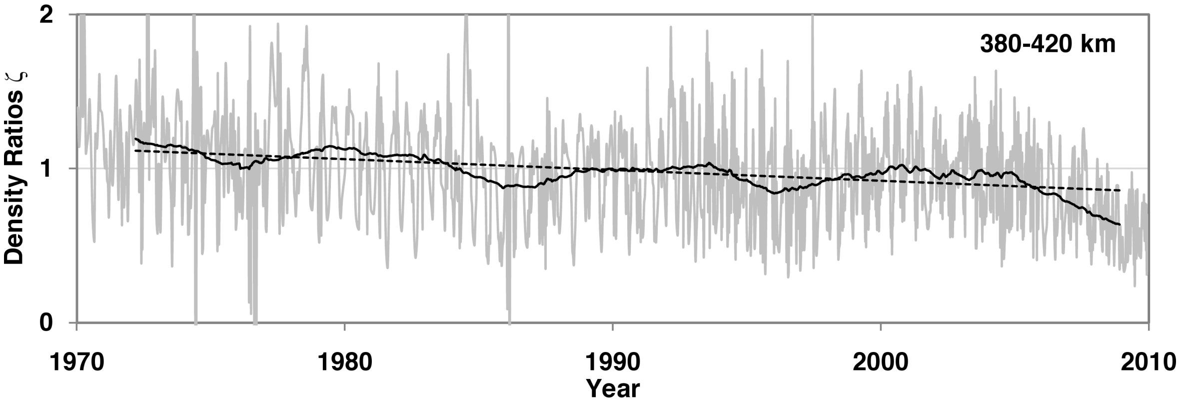

Figure 51: *The resulting density ratios (grey solid line) from 18 out of 29 analysed objects contained within the altitude bin 380-420 km, a 201-day average of the density ratios (black solid line) and a linear regression line applied to the 201-day averages (black dashed line).*

Figure 51 shows the variation of the derived density ratios with the $F_{10.7}$ solar flux intensity at the epoch of derivation of the density ratios. This behaviour can be interpreted in two ways: the NRLMSISE-00 under-predicts atmospheric density for low $F_{10.7}$ intensity ($F_{10.7} < 90$), which would also require a long-term trend in the modelled flux values to be feasible; or there is an increased cooling of the atmosphere at low $F_{10.7}$ intensities, manifesting as a reduction in density. This feature will be discussed in a later section, though this initial study has served to focus attention on this particular area.

The effects of the unevenly spaced density ratios, throughout the historical period and altitude span, are seen around the region of 480 km in the analysis shown in Figure 52. This highlighted the need to develop a way to accurately analyse ‘good’ data and selectively remove outliers. Figure 52 shows an example, in the region of 480 km, of how outliers can manifest into the trend analysis if the statistical methods used to infer trends do not account for outlying data. It was the variation of the number of the density ratios in a particular bin that caused the linear regression analyses to produce poor results. Therefore, during the analysis of the final results, the averages of the density ratios within the temporal and altitude bins were used. This ensured that no artificial trends could be aliased into the results due to the number of density ratios in a particular bin.

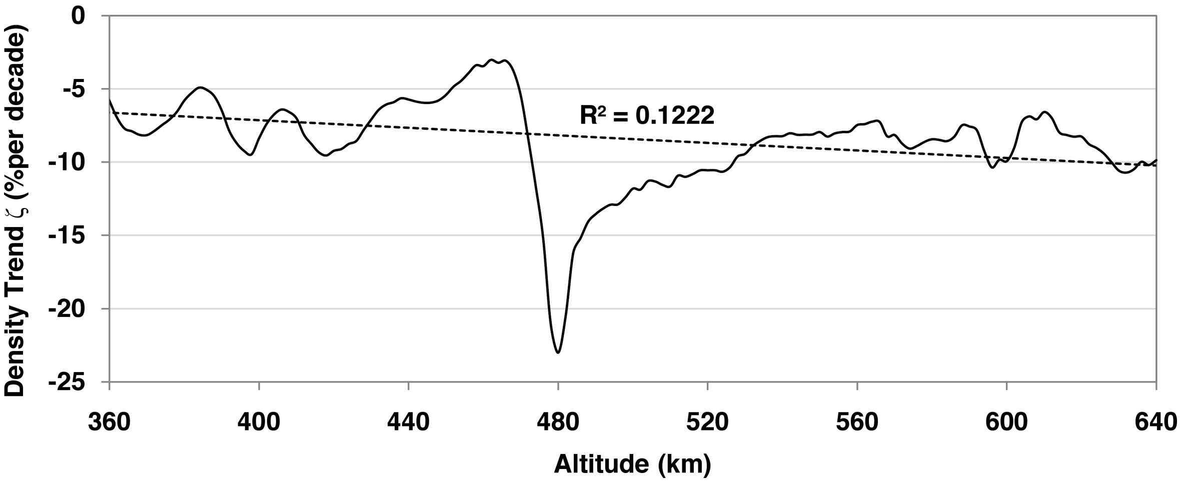

Figure 52: *The altitude variation of the trends of density ratios ($\dot{\zeta}$) derived using overlapping 40-km altitude bins. A linear regression line is shown to highlight the altitude variability. The trough around 480 km is due to the uneven spread of density ratios throughout the historical period analysed.*

The results presented in Figure 52 do show an altitude dependency, although the correlation coefficient of the linear regression was $R^2$ = 0.1222. If the data from the 40-km altitude band of 460-500 km is removed the correlation coefficient rises to $R^2$ = 0.3163. Therefore, the method used in this study has shown its ability to analyse long-term thermospheric density trend variability with respect to altitude. Owing to the nature of atmospheric density decreasing approximately exponentially with altitude, a more sophisticated technique of assigning altitude bins was used to analyse the final results, as opposed to the crude method of a constant 40-km altitude bin height.

The results shown in Figure 51 represent a typical scenario for all altitude bins. All the bins showed the density ratios to vary with similar periodicities. When plotting the results of the previous initial study against $F_{10.7}$ solar flux (Figure 50 page 111) a correlation seemed apparent. As a preliminary analysis of the solar variability dependence of the long-term trend results, a plot of derived density ratios against the $F_{10.7}$ solar flux levels at that time was made from the results of this initial study as shown in Figure 53.

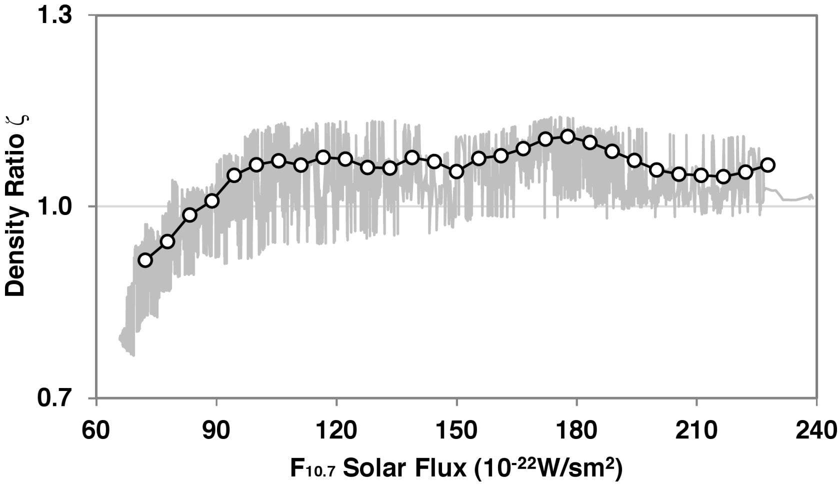

Figure 53: *The density ratios derived in the altitude band 380-420 km plotted against the* $F_{10.7}$ *solar flux levels at the epochs of the density ratios.*

A Fourier spectral analysis was performed on the time series of density ratios to further investigate non-secular historical variation. This showed the periodicities present in the density ratios over time. The method used here to perform a Fourier spectral analysis is taken from [88], which was developed by Lomb [101]. The normalised spectral power as a function of angular frequency $\omega_f$ of a series of unevenly sampled data, such as the time series of the density ratios $\zeta$, is given by

$$P_N(\omega_f) = \frac{1}{2\sigma^2}\left\{\frac{[\sum_j(\zeta_j - \bar{\zeta})\cos\omega_f(t_j-\tau)]^2}{\sum_j \cos^2\omega_f(t_j-\tau)} + \frac{[\sum_j(\zeta_j - \bar{\zeta})\sin\omega_f(t_j-\tau)]^2}{\sum_j \sin^2\omega_f(t_j-\tau)}\right\}, \tag{119}$$

where and $t_j$ is the epoch of the $j$th density ratio and $\tau$ is defined by the relation

$$\tan(2\omega_f\tau) = \frac{\sum_j \sin 2\omega_f t_j}{\sum_j \cos 2\omega_f t_j}. \tag{120}$$

In equation (119) the mean and standard deviation of the density ratios are given respectively by

$$\bar{\zeta} = \frac{1}{N}\sum_1^N \zeta_j, \tag{121}$$

and

$$\sigma^2 = \frac{1}{N-1}\sum_1^{N-1}(\zeta_j - \bar{\zeta})^2. \tag{122}$$

where $N$ is the number of density ratios (33,870). Owing to the nature of this *initial* study, the Fourier spectral analysis described using equations (119)-(122) was only applied to the results from the single altitude bin of 380-420 km. Figure 54 shows the Fourier spectral analysis of the 201-day average variation density ratios as shown in Figure 51.

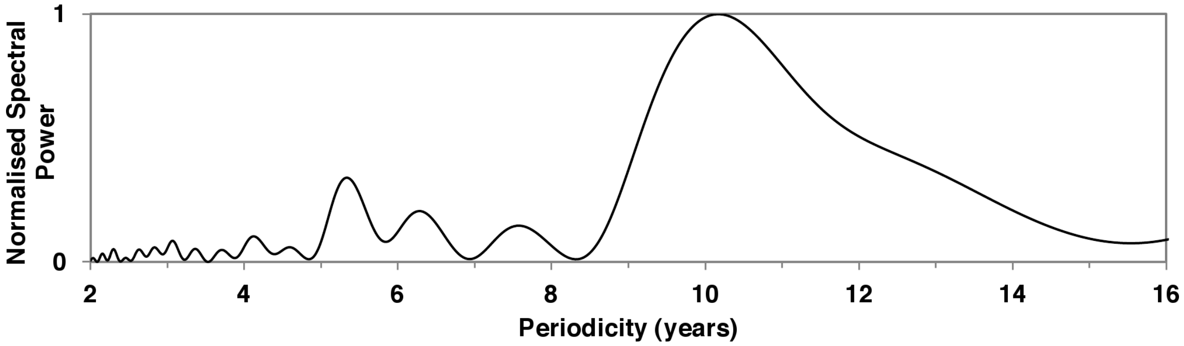

Figure 54: *The normalised spectral power of a Fourier spectral analysis applied to the 201-day average variation density ratios as shown in Figure 51.*

Figure 54 confirms the presence of periodicities in the variation of the density ratios throughout the historical period. The 11-year solar cycle is the strongest component. Comment on other periodicities resulting from Fourier spectral analyses is deferred until a later section whereby the full range of results can be considered.

# 7 Results & Analysis

This section presents the results of applying the methods and tools described in all previous chapters to the TLE data from the 41 satellites. Over the historical period of 1970-2010, this provided 44,843 density ratios. The ballistic coefficients derived using the method presented in Chapter 5.2 and used to predict the effects of atmospheric drag are listed in Table 12 (Section 11.5 of the Appendix). The variance of each ballistic coefficient estimate is also given.

Figure 55 shows the distribution of the 44,843 derived density ratios between the altitudes of 200 and 600 km.

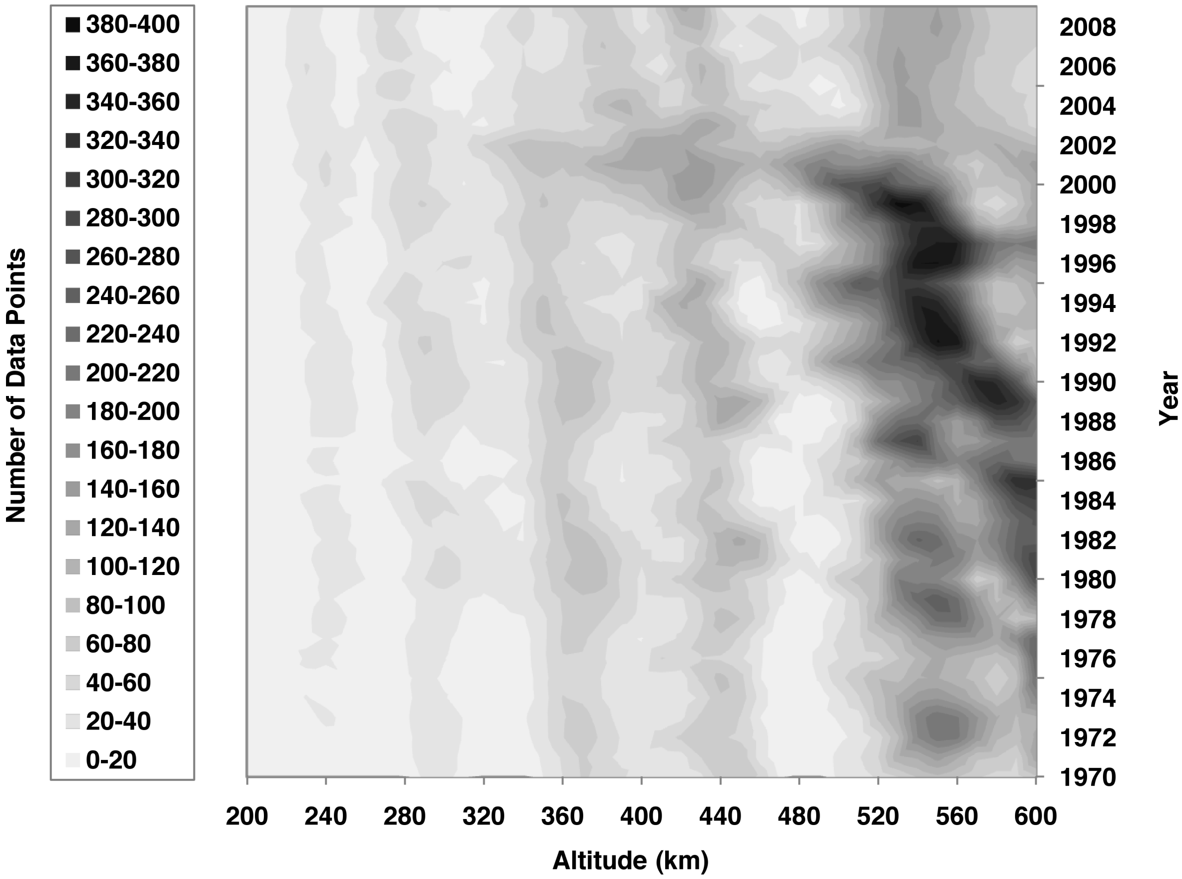

Figure 55: *The number of derived density ratios from the TLE sets of the 41 satellites over the 40 years of historical data.*

A least-squares regression analysis is sensitive to the density of data from a particular region. Regions with high-density data provide a more reliable estimation of the trend in those particular regions, and *vice versa* for regions with low-density data. This meant that the regions of high-density data could increase the uncertainty of the linear regression analysis. Unfortunately, the density ratios derived for trend analysis were not evenly distributed over the historical period. Therefore, a way to smooth the analysis of the density ratios over the entire historical period was to even out the data on which the linear regression is applied. This was done by taking the average of all data points within each bin, which provided a single value of density ratio for the bin. This eliminated any bias in the linear trend analysis caused by an increase in data points in one particular time-span of the historical period. Averaging the density ratios in this way was sensitive to outliers. However, a more sophisticated method of averaging the density ratios that was less susceptible to outliers was not appropriate. This was due to the uncertainty with how to quantify an outlier, as the density ratios were not arranged in any form of distribution that suggested a tendency to a single value. The long-term trends in the derived density ratios were then analysed after the ratios were assigned to their specific altitude and temporal data bins.

The temporal bin size was set at 1 year to obtain gradual changes in the average of density ratios. As atmospheric density reduces with increasing altitude at an approximately exponential rate, a metric that reflected this behaviour was required. Therefore, a constant fraction of the density scale height $H$ was chosen as the altitude bin size to provide a more sophisticated method than that used in the third validation exercise.

To determine a suitable fraction of the density scale height to be used as a altitude bin size, a trade-off was necessary between the number of density ratios available and the percentage change in density covered by the bin height. In order to obtain a high resolution altitude dependent model of thermospheric density change, the height of the altitude bins needed to be relatively small. However, the height of the altitude bin was limited in certain altitude regions due to the low number of available density ratios. Preliminary analyses showed that using altitude bins with less than 20 density ratios returned inconsistent results. Therefore this limit of a minimum of 20 density ratios was set as a criterion for altitude bin sizing. The altitude sizing of the bins was driven by the lower altitude regions where there were fewer available density ratios, as shown in Figure 55. To achieve consistency in the results analysis, an additional criterion of the altitude bin sizing was that whatever method was used in the lower regions also needed to be used in all the other higher altitude regions. This was unfortunate as the higher regions generally contained a greater number of density ratios, which could have produced a higher resolution altitude dependent model. From the criteria described above, it was determined that an altitude bin sizing of 0.5 $H$ would achieve the required number of density ratios per bin. However, this would yield a change in density from the bottom to the top of the altitude bin of approximately 64.87%. Owing to the limited number of density ratios available from the data of the 41 satellites, this meant that only 67.5% of the altitude bands spread over the range of 200-600 km could be used.

The bin coverage encompasses density ratios derived over altitudes extending 0.25 $H$ above and below a particular altitude, i.e. the bins were centred on $H$. This method was applied at 10 km increments between the altitudes of 200 and 600 km, yielding 41 discrete altitude bands. This resulted in some overlap between the bins, which meant that some density ratios contributed to the derived long-term trends via more than one altitude band. Figure 56 demonstrates the altitude coverage resulting from using this method of bin sizing over the historical period. The Figure shows that the width of the altitude bands generally increase with altitude, therefore encompassing a greater number of density ratios.

Figure 56 also shows the value of $H$ tracking the solar cycle. $H$ is calculated using the molecular densities derived from the NRLMSISE-00 empirical atmospheric model, which

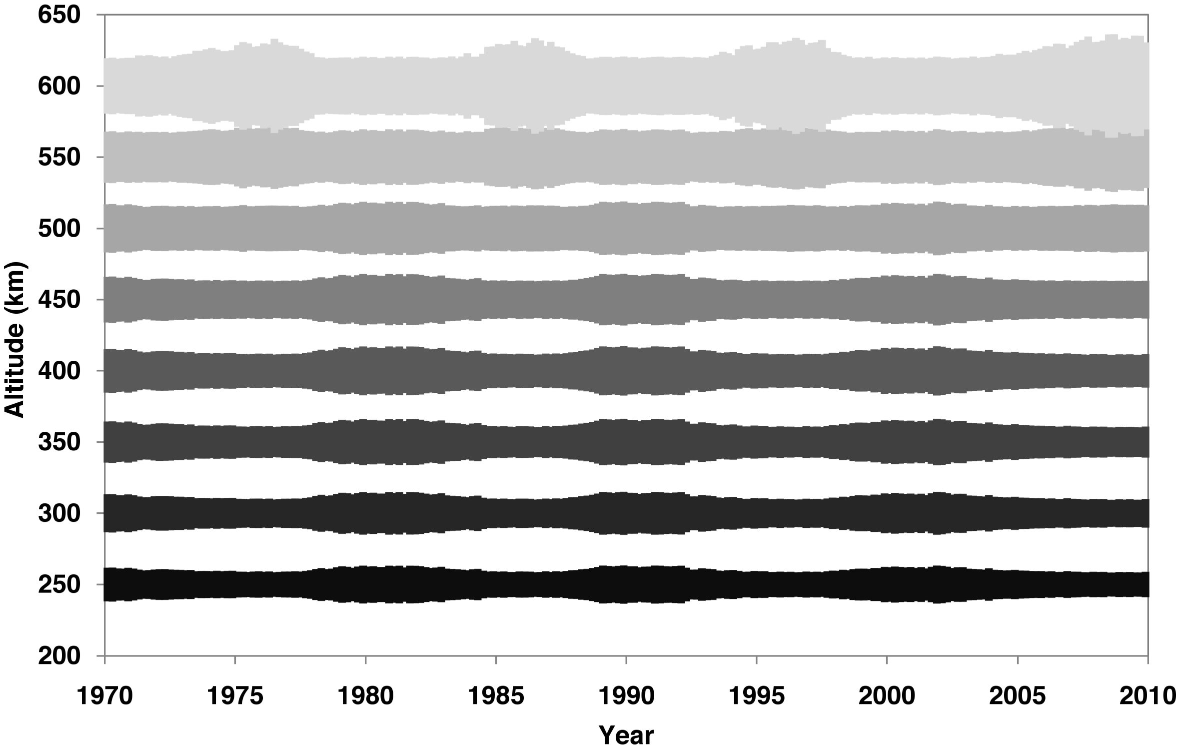

Figure 56: *The historical variation of bin sizing due to varying density scale height shown at sample altitudes.*

depends on solar activity. For the region of approximately 250-500 km, the magnitude of the density scale height is proportional to solar activity. This is shown by an increase in the width of the altitude bands during times of solar maximum, and *vice versa* during solar minimum. At the higher altitude bands, the magnitude of $H$ is inversely proportional as the height of the altitude bands are greatest at times of solar minimum, and *vice versa* during solar maximum.

Grouping the derived density ratios into the 41 altitude bins positioned at 10 km intervals, as well as the 40, 1-year, temporal bins, provided a time series of averaged density ratios per altitude band. Performing linear regression analyses on each time series of density ratios provided estimates of long-term secular trends. The resulting altitude-dependent trends are shown in Figure 57 for the average change in density per decade.

During the minimum of solar cycle 23-24 (2008-2009), the Sun's activity remained very low for a period of time longer than average. As a result, record-low densities were observed in the thermosphere [32]. When the NRLMSISE-00 model was formulated, it was based on empirical data from observations before the year 2000. More specifically, the data set used to obtain the analytical coefficients for the atmospheric model did not contain density values as low as those observed during the minimum of solar cycle 23-24. Therefore, the empirical atmospheric model would be extrapolating atmospheric densities during a time when observed densities reduced below previous records. This would not necessarily provide accurate values, especially considering the biases induced by empirical models at times of low solar activity, as previously discussed. This phenomenon is exhibited in the time series of derived density ratios. The derived density ratios from altitude data bins at 400 and 520 km, shown in Figure 58, are

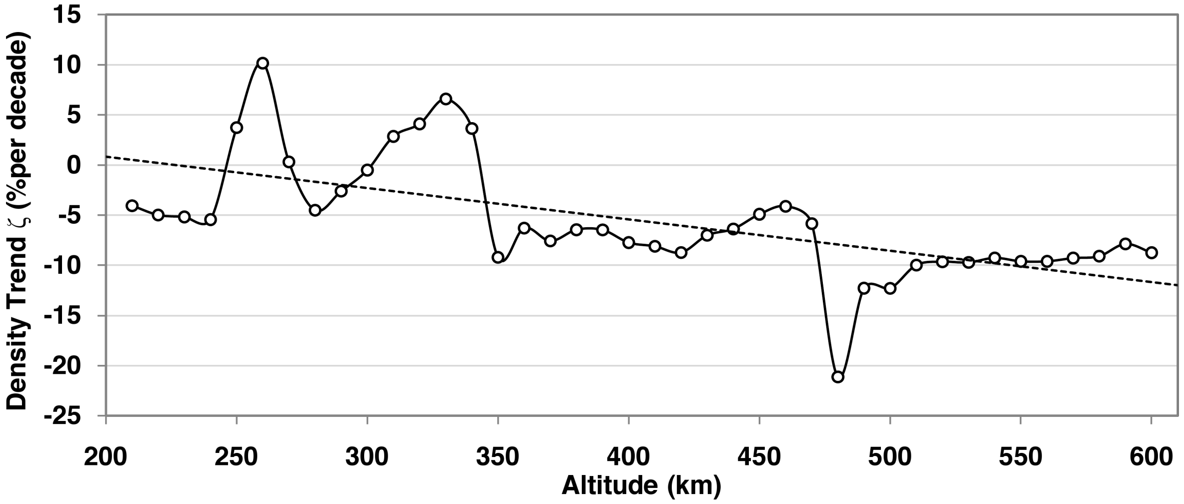

Figure 57: *The altitude-dependency of the secular trends derived from linear regression analyses of all the altitude bins of the entire dataset of density ratios. A linear trend is fitted through the data for illustration purposes only to highlight the altitude-dependent variability.*

used as typical examples that demonstrate the drop in the derived density ratios, apparent during the time of solar cycle minimum 23-24 (2008-2009). The errors bars shown in the Figure represent the $\pm 1\sigma$ variation in averaged derived density ratio.

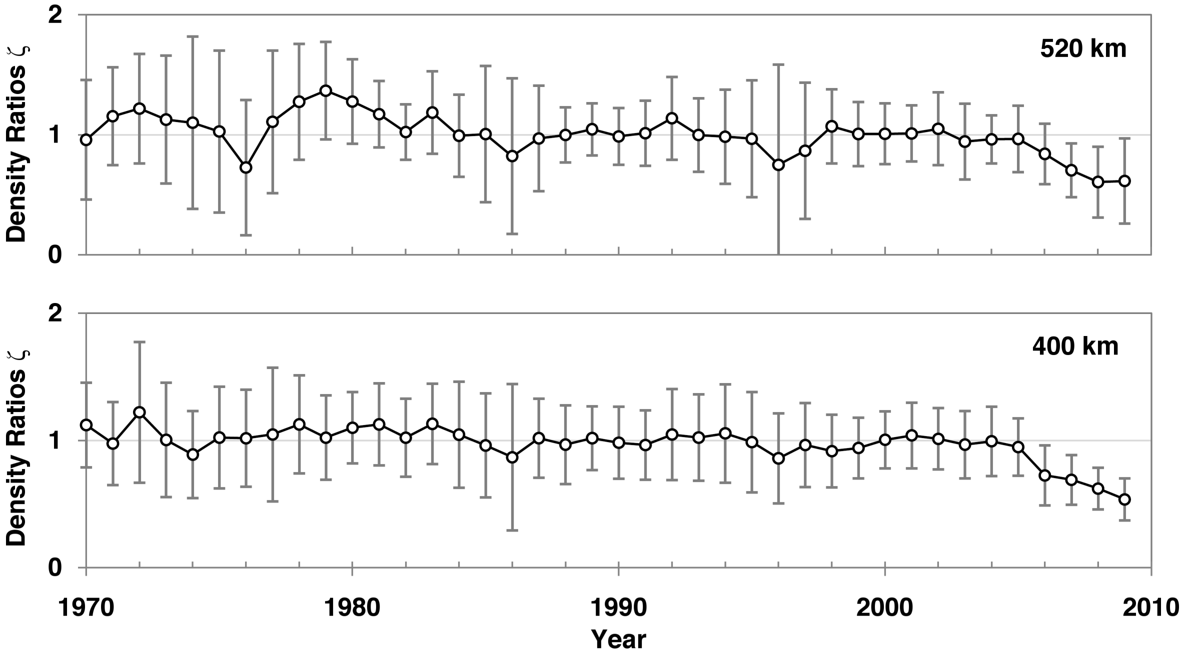

Figure 58: *The drop in derived density ratios during the time of solar cycle minimum 23-24 (2008-2009) demonstrated by the two representative altitude data bins at 400 and 520 km. The errors bars shown represent the* $\pm 1\sigma$ *variation in averaged derived density ratio.*

Owing to these record-low density observations, the density ratios derived in this study from the period of solar minimum cannot be assumed reliable. Therefore, the contribution to the time series of density ratios obtained during the solar minimum of cycle 23-24 were removed.

The resulting 37-year period for the data analysis was from 1970 to the end of 2006. Figure 57 also shows the data contributions from the 32.5% of altitude bands with less than the required number of density ratios, as previously described. Therefore, the contributions from these altitude bins were identified and removed. The resulting altitude-dependent model of long-term secular density change is shown in Figure 59.

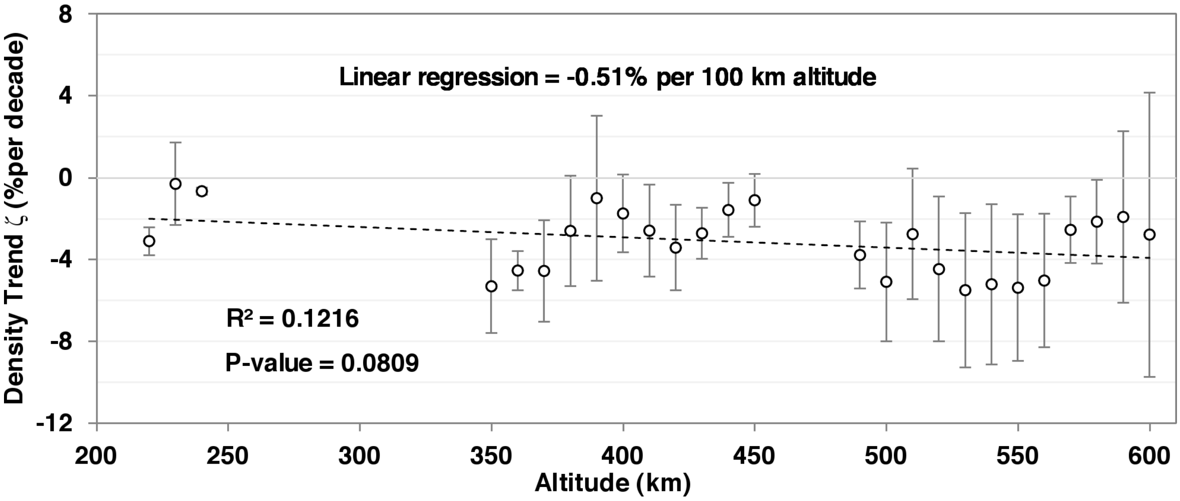

Figure 59: *The altitude-dependent model of long-term secular density change. The data have been reduced to take into account of the abnormal low densities resulting from the solar minimum of cycle 23-24 (2008-2009), as well as incorporating the removal of altitude data bins contained less than the required number of density ratios. The error bars show the* $\pm 1\sigma$ *trend variance. A linear regression is applied to the data yielding an altitude dependency of -0.51% per decade per 100 km increasing altitude, with a correlation coefficient of* $R^2$ *= 0.1216 and significance P-value of 0.0809.*

A linear regression was applied to the resulting data with a correlation coefficient, $R^2$ = 0.1216 (possibly artificially inflated due to the statistically non-independent nature of the multiply-sample data). A statistical significance P-value of 0.0809 gave it more than a 90% statistical probability of there existing an altitude-dependent trend. Long-term thermospheric density has appeared to decline at a rate of approximately -2% per decade at 200 km and increasing to approximately -4% per decade at 600 km. The rate at which the secular trend increases with altitude is approximately -0.51% per decade per 100 km increasing altitude.

Density ratios derived from the altitude bands of 220-240 km inclusive did not meet the requirement of minimum number of density ratios per bin. However, their values of density ratios were much smaller with variances of approximately 35.3% of the variances of density ratios from altitude bands above 350 km. Figure 60 shows the typical trend of density ratios for the data in the low altitude regions (220-240 km) to be compared to those from Figure 58.As a result, the density ratios derived for the altitude regions of 220-240 km were included in the final results to contribute to the model of altitude dependency for the long-term thermospheric density trend analysis.

Owing to the different mechanisms of energy transfer between the various atmospheric constituents, the concentrations of the local gas species are of prime importance when

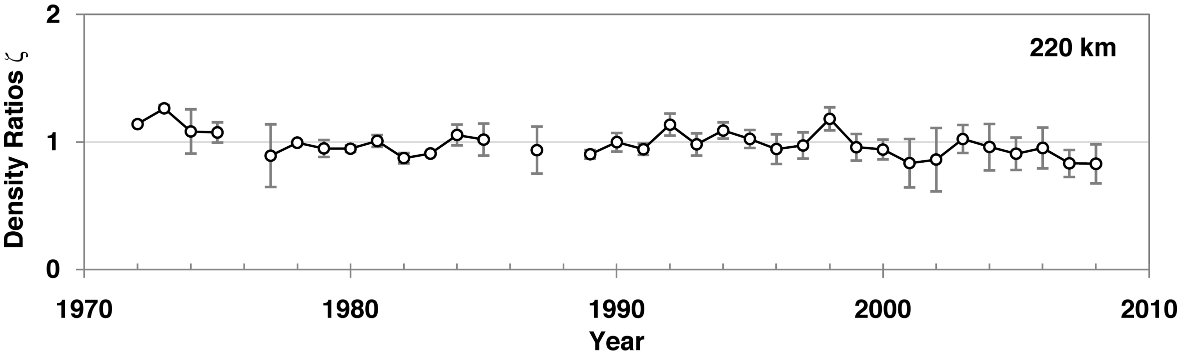

Figure 60: *The typical trend of density ratios for the data in the low altitude regions (210-240 km) to be compared to those from Figure 58. The errors bars shown represent the* $\pm 1\sigma$ *variation in averaged derived density ratio.*

considering radiative transfer. During the 11-year solar cycle, whereby the atmosphere swells and contracts, the relative composition and density of the atmosphere could increase the energy transfer between the molecules of different gas species. Therefore, it is reasonable to assume that during times of varying solar activity, thermospheric cooling would also vary. The initial studies also demonstrated a dependency on solar variability. The method of linear regression was again applied to the derived density ratios, but this time dividing the data into high and low solar activity: $F_{10.7} < 90$ and $> 90$ SU (Standard solar flux units $10^{-22}$W/sm$^2$) respectively. The results gave a reduction in thermospheric cooling during times of high solar activity and an increase in cooling during low solar activity as shown in Figure 61.

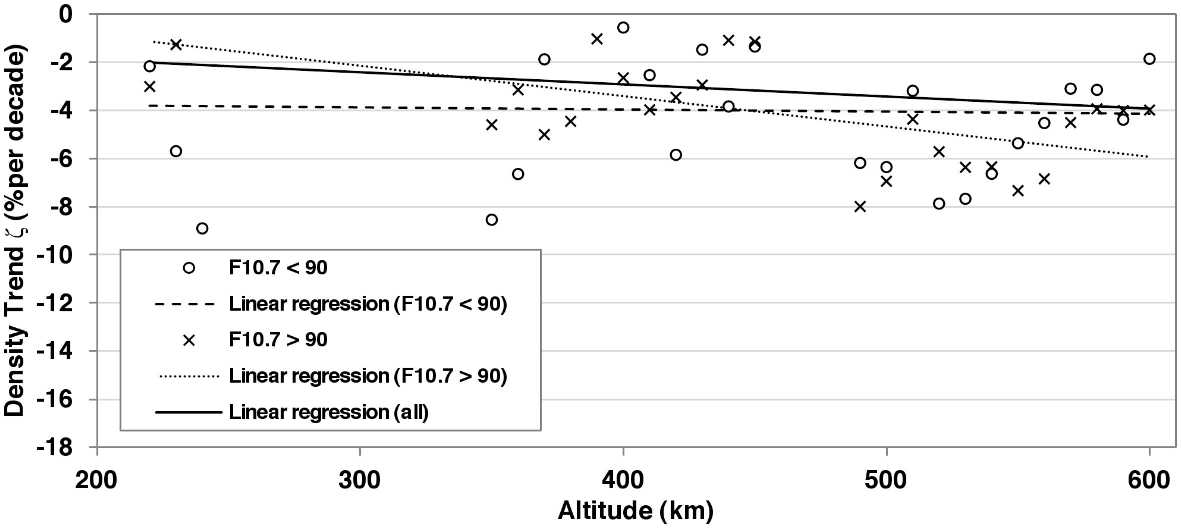

Figure 61: *The* $F_{10.7}$*-dependency of long-term secular density change. The resulting lines from the application of the linear regression analyses are also shown for all the data (as shown in Figure 59) and the data above and below* $F_{10.7} = 90$*. The correlation coefficients were:* $R^2 = 0.0010$ *for* $F_{10.7} < 90$*;* $R^2 = 0.3633$ *for* $F_{10.7} > 90$*.*

During times of low solar activity the reduction in thermospheric density was magnified with a magnitude of -3.8% per decade at 220 km up to -4.1% per decade at 600 km. However, the low number of available density ratios created sparse data yielding a correlation coefficient of $R^2$ = 0.0008 and a very low significance with P-value of 0.8768. During times of high solar activity, variation with altitude is the magnified characteristic but, the magnitudes of thermospheric density decline have reduced to -1.1% per decade at 220 km increasing to -5.9% per decade at 600 km. The correlation coefficient for the regression line during high solar activity was again low with $R^2$ = 0.3633. However, the data gave a much more significant trend with a P-value of 0.0011, giving a 99.89% probability of an altitude dependent trend.

To demonstrate explicitly these results of secular thermospheric mass density change, and their dependency on solar activity, Figure 62 shows the long-term density variation at altitudes of 220, 300, 400, 500 and 600 km using the data from all 41 satellites. The plots of density variation in the Figure assume a 100% density value in the year 1970 and then the relative difference in subsequent years up to the end of 2006.

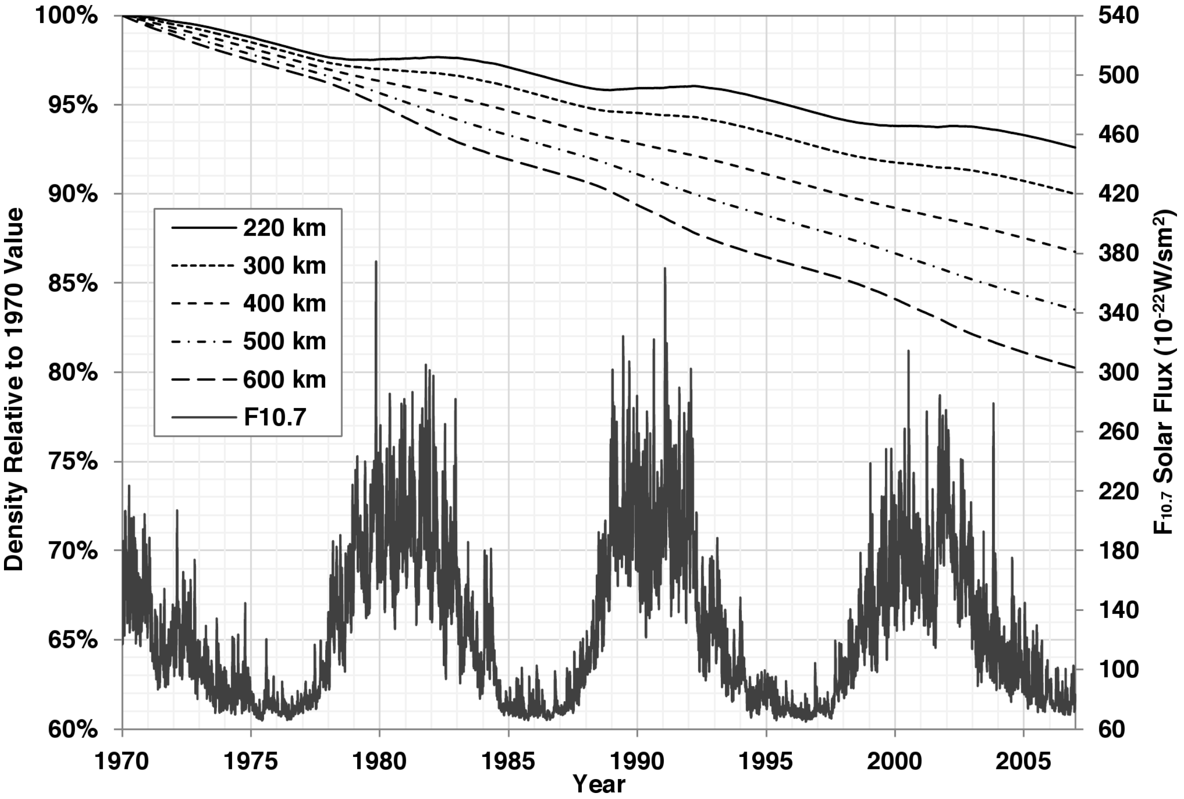

Figure 62: *The long-term density variation at altitudes of 220, 300, 400, 500 and 600 km using the data from all 41 satellites. Also plotted is the historical $F_{10.7}$ solar flux to highlight the rate of density decay in relation to solar activity, i.e. increased cooling at low solar activity and vice versa.*

To investigate whether the variations of long-term thermospheric density change could be connected with periodic natural phenomena, a Fourier spectral analysis was performed on the data from five altitude bands: 380, 400, 430, 560 and 580 km. The bandwidth of periodicities analysed ranged from 0 to 20 years, as any periodicity longer than 20 years would not be unambiguously identifiable within the sample of 40 years. Figure 63 shows the spectral analyses from the five altitude band, normalised to the maximum spectral power from each altitude band.

The five altitude bands analysed show signals of similar periodic behaviour at four distinct

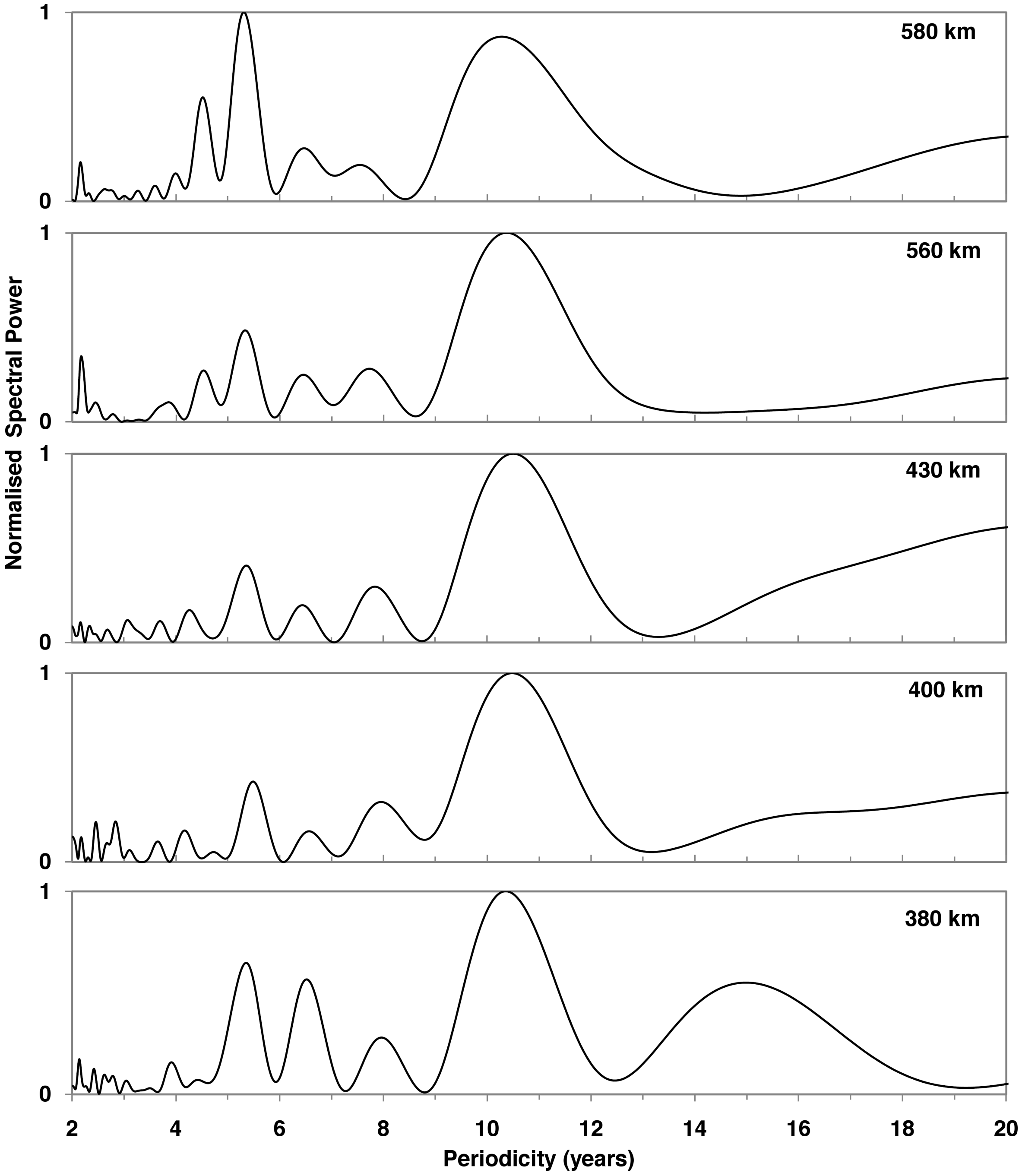

Figure 63: *The results of the Fourier spectral analyses from the five altitude bands. The normalised spectral power is shown in relation to periodicity. The spectral powers were normalised to the value of maximum spectral power for each altitude band.*

periodicities. To refine the general results, the five spectral analyses were multiplied together to highlight the common periodicities. This process removed the altitude dependence so only average thermospheric behaviour could be deduced. Figure 64 shows the combined spectral analyses. From this, four periodicities are seen with a spectral power over 25% of the maximum. The periodicity with the greatest spectral power (equal to unity) coincides with the 11-year solar cycle at 10.47 years. Therefore, this supports the motivation for the previous analysis of long-term secular density change with varying levels of solar flux.

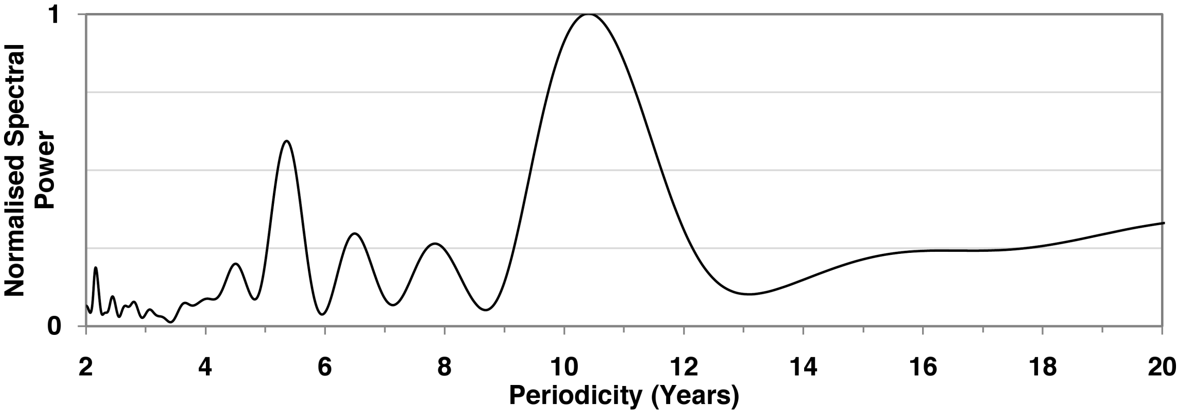

Figure 64: *The combined results of the Fourier spectral analyses from the five altitude bands shown in Figure 63.*

The periodicity with the next highest spectral power occurs at 5.37 years. It shows a strong correlation with semi-solar cycle variation, suggesting a thermospheric reaction during times of transition between high and low solar activity.

The increasing value of spectral power from periodicities of 13 years and longer is possibly a manifestation of the secularly declining nature of the density ratios. It is possible that the results from the Fourier spectral analysis represent the declining trend as an initial part of a waveform with longer periodicity than the historical 40-year period.

There is also a reasonable case for the existence of variations with periodicities of 6.48 and 7.85 years, as these periodicities have a spectral power greater than 25% of the maximum. At present there is no physical explanation for these. It is possible that the combination of the satellite orbits from the 41 satellites produced periodicities that when combined over the 40-year period coincidently manifest as a periodic variations in the density ratios. Only the addition of more satellite data to increase the number of density ratios would show whether this coincidence is true.

The other periodicities with spectral power less than 25% of the maximum may contain periodic atmospheric variations but, explanations are deferred to additional studies and future work. Some periodicities are likely be data noise. However, a significant contribution to the smaller apparent periodicities are likely to be due to variations in the TLE ephemerides that constructively interfere to produce sporadic periodicities.

# 8 Discussion

This section compares the results presented here to those reported in previous studies. Then, a discussion of the errors influencing the production of the results is made.

## 8.1 Comparisons with Previous Studies

Out of all the previous studies into long-term secular changes in thermospheric density, the one that most closely matches the historical and altitude boundaries investigated in this study was reported by Emmert *et al.* 2008 [30]. This identified a secular density change of -2.68 ±0.49% per decade at 400 km, with trends of approximately -5 and -2% per decade at solar minimum and maximum, respectively. Their previous study [28] estimated a density trend of -2% per decade at 200 km altitude, increasing to -5% per decade at 700 km. Linearly interpolating between these two data points yields a density trend of -3.2% per decade at 400 km. The results in this study showed a density trend of -1.90% per decade at 200 km, -2.91% at 400 km and further increasing to -3.92% at 600 km, from the applied linear regression. At 400 km, the results presented here show density trends closer to those from the later study of Emmert *et al.* with a difference of 0.23% per decade as opposed to 0.29% from the earlier study. The differences in trend results may be due to the slight difference in trend period. The study presented here used the 37-year period of 1970-2006 inclusive, whereas the studies by Emmert *et al.* used the 35-year period of 1966-2001. Also, the studies by Marcos *et al.* [73] and Qian *et al.* [94] both obtained a secular density decrease at 400 km of -1.7% per decade, which is 1.21% per decade weaker than the results presented here. Both these studies used the 30-year trend analysis period of 1970-2000. The altitude bins in the region of 350-450 km included in the results presented here show the most variability from the linearly approximated altitude dependent trend. This suggests a large range of possible density trend magnitudes. The theoretical study by Qian *et al.* estimates that if data were used up to the end of solar cycle 24 ( 2008) then the secular trend would be greater at 2.7% per decade. The 2006 theoretical study by Akmaev *et al.* [3] predicted thermospheric density trends of -4% per decade at 200 km. This is 2.1% per decade stronger than the results presented here, which is over twice the magnitude. Agreement with the study by Akmaev is not significant considering the variance of the density trends in the lower altitude regions are generally small with an average variance of ±0.84% per decade for the three lowest altitude bins.

In the 2004 paper by Emmert *et al.* [28] a comparison was presented between the secular density trend results derived from the analysis of four satellites with the results obtained by Keating *et al.* [56] for the same satellites and historical period. Following Emmert *et al.* [28], Figure 65 shows the trend results obtained for the four satellites in the historical period of 1976-1996 along with the results the from previous studies.

The horizontal bars shown in the Figure denote the differences between the trend results derived from the individual satellites (the markers) and the overall trend derived from the entire data set of satellites and trend period of the particular study. They take into account any altitude dependency in the overall trends reported by the study, relative to the average perigee altitude

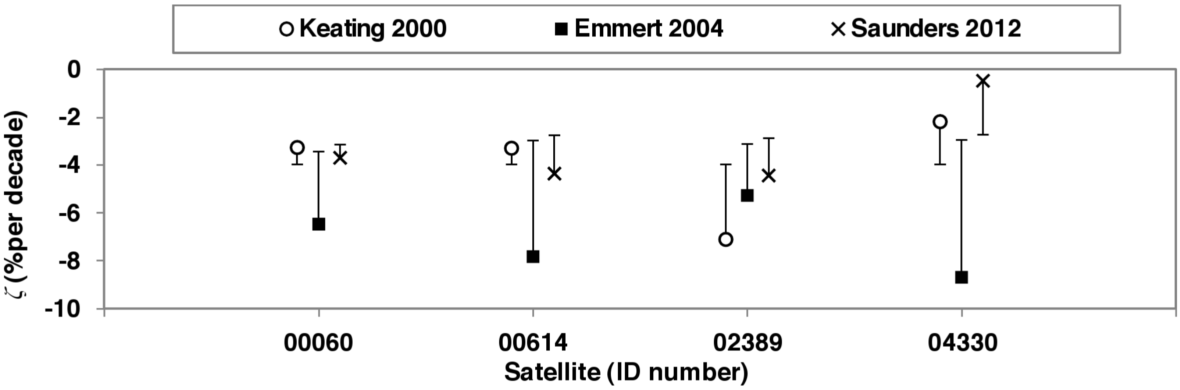

Figure 65: *A comparison of the results from four satellites common to the studies of Keating et al. [56], Emmert et al. [28] and the study presented here. The horizontal bars denote the differences between the trend results derived from the individual satellites (the markers) and the general trend derived from the entire data set of the particular study (horizontal bars), including any reported altitude dependency.*

for each satellite. The magnitudes of the error bars are calculated using a least squares summation of the individual differences given by

$$E_{\%} = \sqrt{\frac{1}{N_{sat}} \sum (\dot{\zeta}_{study} - \dot{\zeta}_{sat})^2}, \tag{123}$$

where $\dot{\zeta}_{study}$ is the density trend derived from the study at the average altitude associated with the particular satellite $\dot{\zeta}_{sat}$ and $N_{sat}$ is the numbers of satellite.

The results derived in this study have the smallest difference with $E_{\%}$=0.81, followed by Keating *et al.* with $E_{\%}$=0.93 and then Emmert *et al.* with $E_{\%}$=2.09. The parameter $E_{\%}$ cannot be used to determine the accuracy of the method, as this would assume that the density trend from the study is the true trend, and all the derived density trends from this study and previous studies have associated errors. However, conclusions can be drawn about the performance of the method presented here. The results of Keating *et al.* only gave an average value for cooling and not an altitude-dependent model of long-term density trends. As such their $E_{\%}$ is not directly compatible as the overall trend is simply an average of the four trend values derived from each satellite. Thus, the variance would naturally be smaller than it would be if the overall trend of the study encompassed a larger set of objects over a longer trend period. Therefore, only the comparison between Emmert *et al.* and this study can provide any real measure of progress. Admittedly, the data set is limited, but these satellites were chosen in the previous studies for their typically representative characteristics of a broader satellite population. As such, these satellites can be used as a source to gauge the performance of the method.

In summary, with a reduction in $E_{\%}$ from the method by Emmert *et al.* to the method used here suggests an improvement in performance. However, the results show relatively large differences in the derived density trends. The results presented here show a stronger decline in thermospheric density than all previously studies over the altitudes analysed. The density trends derived here are approximately equal varying by a factor of 0.05 weaker to 0.9 times stronger than the other empirical studies of Emmert *et al.* with an approximately equal altitude dependency. The results from this study are approximately 1.7 times stronger than the trends derived by Marcos *et al.* and Qian *et al.*. In the lower altitude region of 200 km the trends presented here disagreed, by a factor of 2.35 times weaker than the theoretical study by Akmaev *et al.* [3], who simulated the chemistry of the upper atmosphere to infer long-term trends.

## 8.2 Discussion of Errors

### 8.2.1 Propagation Errors

Determining a secular thermospheric density trend was done by comparing the change in semi-major axes between observational data and numerically derived data. To quantify the errors that arose in the comparison process, and to give an idea of the magnitude of errors expected, an investigation into the semi-major axis variations of two satellites (IDs 02389 & 10973) in different orbits was conducted. A description of the sources of propagation error and their relative magnitudes are listed below.

1. **TLE sets:** as presented in Section 2.2 (page 15) describing the Two-Line Element sets, the TLEs contain ephemeris errors of the order of hundreds of metres to a few kilometres. This translates to an approximate error of 0.05% in both position and velocity of the ephemeris state vector.

2. **Numerical integration:** from Section 5.1.2 (page 43) the numerical integration process used to propagate satellite orbits utilised a variable integration step size. This was done to reduce the computational effort and propagation run-time. The integration step size was determined using a function that yielded a specified accuracy over the entire orbit propagation. The magnitude of the specified accuracy was chosen such that there was a negligible contribution to orbit propagation errors. As a result, the value determined for the specified accuracy was $4.53\times10^{-5}$ km. As the specified accuracy was held constant, it would have the greatest effect on orbits with smaller semi-major axes. Considering a circular orbit with a semi-major axis of 6,778 km (assumed 200 km altitude), the specified accuracy equates to an error in the semi-major axis of $6.68\times10^{-7}$%.

3. **Solar flux variation:** the process of measuring solar flux yields variations in the measured values by approximately 10% from the true value [33]. This would result in satellite propagation errors by altering the density structure of the atmosphere and changing the acceleration due to drag. The change in atmospheric density due to solar flux is not uniform throughout the atmosphere. As a result, predicting the influence that a change in solar flux can have on satellite drag perturbations is difficult to do analytically. Therefore, the empirical approach used in this investigation provides a reasonable means to assess the errors incurred by the variation of solar flux levels.

4. **NRLMSISE-00 empirical model error:** Density predictions using the empirical model NRLMSISE-00 have errors of 8% as discussed in Section 5.1.4 (page 55). Similarly, errors in the calculation of model density would affect the drag perturbations.

5. **Atmospheric drag coefficients $\delta$ & $C_d$:** a satellite's ballistic coefficient can vary by ±20% [89], due to tumbling and/or changes in the drag coefficient, $C_d$, from varying flow regime. The magnitude of acceleration due to atmospheric drag can therefore also change by this amount.

6. **Luni-solar ephemerides:** in this study the method of predicting the relative positions of the Earth, Moon and Sun for the calculations on third body gravity perturbations used a numerical propagation for the Earth and Moon and an interpolation process for the Sun. The maximum position error of the Moon was found to be 0.001% and for the Sun approximately 0.02%. The change in direction of the Moon and Sun, relative to the Earth, of these position errors is $3\times10^{-9}$ and $3\times10^{-12}$ degrees. Therefore third body perturbation inaccuracies caused by errors in luni-solar ephemerides were negligible.

7. **Solar Radiation Pressure:** In the calculation of solar radiation pressure a key parameter is the reflectivity of the satellite, which is composed by the reflectivity coefficient $C_r$ and the surface area projected towards the Sun. Assuming the same rationale as the variation in ballistic coefficient due to tumbling [89], it is equally likely that the projected surface area towards the Sun also varies by ±20%.

The investigation into the variations of semi-major axes, caused by the perturbation inaccuracies listed above, involved propagating the satellites over a period of a one day. Every 15 minutes the semi-major axis $a$ was calculated to produce a time series using

$$a = \frac{\mu r}{2\mu - v^2 r}. \tag{124}$$

Firstly, both satellites (IDs 02389 & 10973) were propagated with all perturbations as performed when deriving thermospheric density ratios. This produced a 'control' time series of the semi-major axis for each satellite. Secondly, the one-day orbit propagations were repeated but the perturbations were varied, in turn, by their associated magnitudes of inaccuracy described above. This created multiple time series for the semi-major axes variation due to the particular perturbations under investigation. It should be pointed out that the errors modelled in this investigation were taken as worst case scenarios. It is unlikely that the perturbation errors would be cumulative and indeed neither would the solar flux and density model errors be constant but, to gather a worst case set of data the assumptions were maintained through the analysis.

The errors that could not be analysed using the above method were those associated with the initial TLE ephemerides. To quantify the sensitivity of these errors in terms of semi-major axes, simple calculations were made using the percentage errors of ±0.03% around the previously stated 0.05%. The physical magnitude of the error is dependent upon where in the orbit the specific TLE ephemeris is associated. For example, the magnitude of a 0.05% error in the position vector at perigee, of a satellite with an orbit eccentricity of approximately 0.1 (i.e. satellite 02389), would be less than the magnitude of a 0.05% error in the position vector at apogee. Figure 66 shows the percentage error in the semi-major axis estimation for various eccentricities due to constant ephemeris position and velocity errors. In general, the most significant change due to a constant percentage error occurs at perigee. An error of 0.05% in the position and velocity of a TLE ephemeris at perigee for satellite 02389 caused a change in semi-major axis of approximately 19 km.

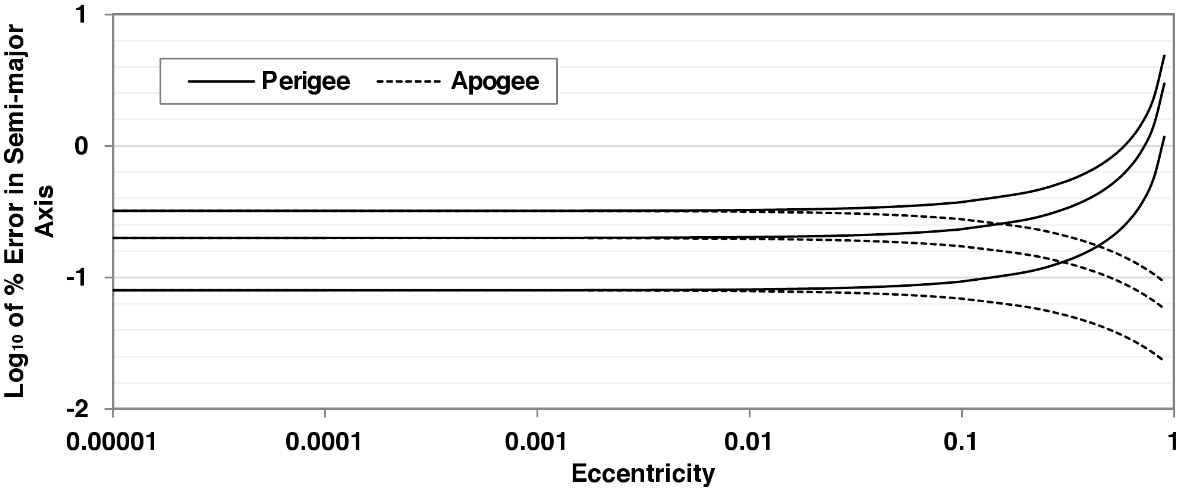

Figure 66: *The dependency of calculation error of the semi-major axis estimate on orbital eccentricity. Three examples of constant percentage errors in the TLE position and velocity vectors are shown, 0.02%, 0.05% & 0.08%. The solid lines denote calculations of semi-major axis when the TLE ephemeris is at the orbit perigee and the dashed lines denote calculations of semi-major axis when the TLE ephemeris is at the orbit apogee.*

The ephemeris errors represent the most significant source of error for this study. The maximum orbit eccentricity of the all 41 satellites used in this study is approximately 0.69. The results presented in Figure 66 show the maximum associated error in the semi-major axis for an orbit eccentricity of 0.69 to be approximately 0.9%. It should be noted that only the orbits of satellites 02643 & 14756 have such high orbital eccentricities. Of the remaining 39 satellites whose TLE data was used to infer thermospheric density ratios, the majority had orbital eccentricities of 0.2 or less.

The one-day variations in semi-major axes for both satellites due to the other perturbations are shown in Figure 67. The propagated errors with magnitudes greater than $10^{-8}$%, as shown in Figure 67, oscillated around a linearly increasing trend with correlations coefficients $R^2$>0.9442. Owing to the assumed linear behaviour of the accumulating propagation errors, the total error for a 10-day propagation was calculated by summing all the cumulative one-day propagated errors and multiplying by 10. Applying this process to the error analyses for both satellites yielded a maximum semi-major axis percentage error of approximately $5\times10^{-5}$% of the semi-major axis. This equated to 0.4 km and 0.35 km error in semi-major axis for the satellites 02389 and 10973 respectively. It was now necessary to assess what error is induced in the *change* of semi-major axis, taking the worst case scenario of 0.4 km error. The difference in density a 0.4-km error can induce may be up to 0.94% at the lower altitude bins of 220 km and 0.64% at 400 km.

A long-term secular thermospheric density decline has been deduced from the analysis of the density ratios with the average trend being approximately -2.91% per decade at 400 km.

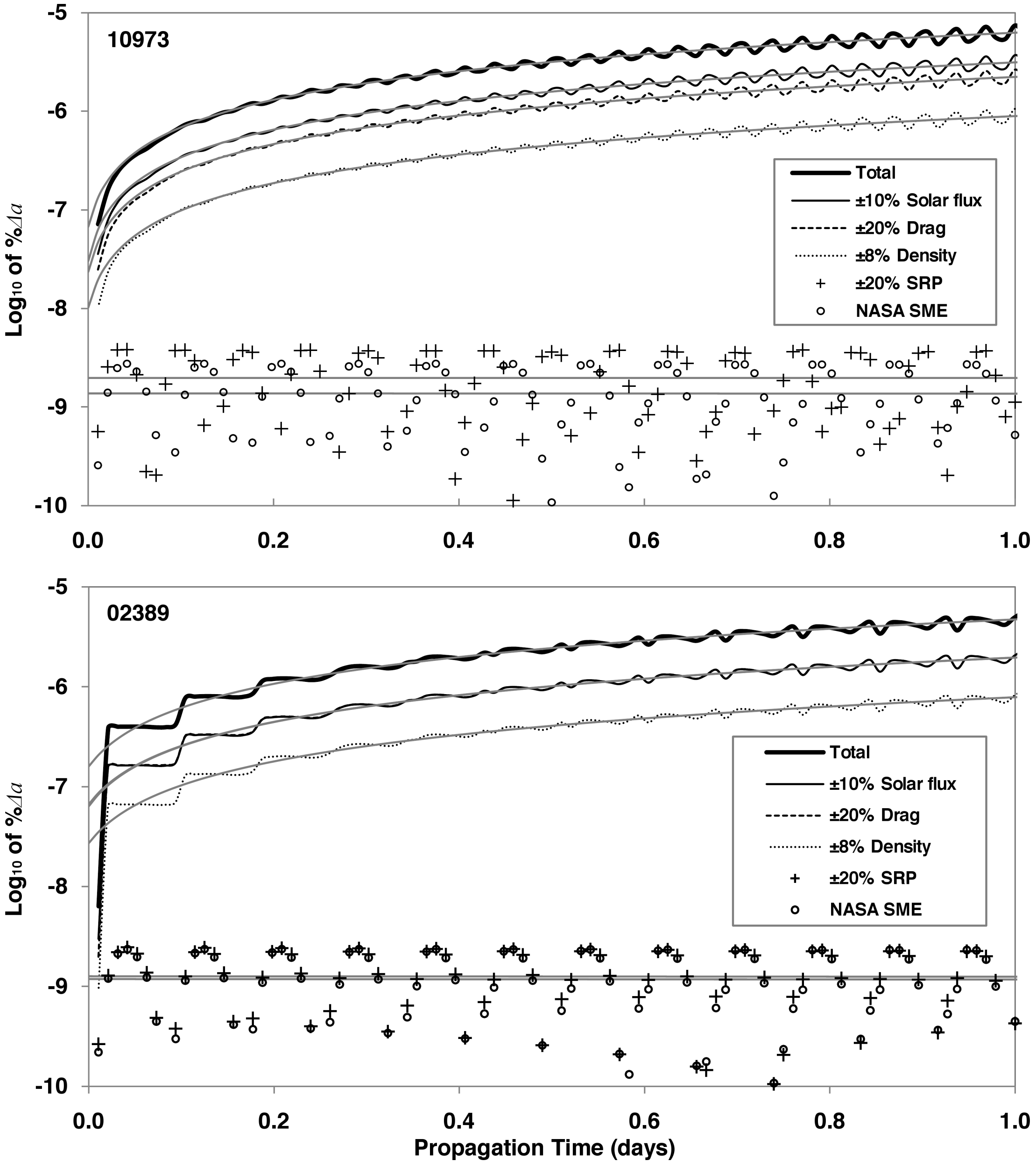

Figure 67: *The magnitudes of the variations in semi-major axis, $\Delta a$, due to perturbations for the satellites 02389 and 10973. 'TOTAL' denotes the magnitude of the combined contributions from the various perturbations, which could take a positive or negative variation. 'NASA SME' denotes the use of the NASA Horizons ephemerides of the Sun, Moon and Earth without the interpolation or propagation by AETHER. The light grey lines are linear approximations to highlight the linear behaviour of the variations over time.*

The density ratios were derived from comparisons of the semi-major axis. This implied that the average difference between the density ratios, and thus difference in semi-major axes, from the beginning of one decade to the end of the same decade was 2.91%. Scaling this magnitude of secular density decline to the time scale of TLE epoch separation (10 days) yielded a density decline of 0.0081% every 10 days. With the maximum possible errors in semi-major axes induced from numerical propagation by AETHER of 0.64%, as previously described, a signal strength of 0.0081% yields a worst-case signal-to-error ratio of approximately 0.0135.

Specifically, the magnitude of the semi-major axis is not the parameter through which the density ratios are defined; it is the *change* in the semi-major axis. However, the magnitude of the semi-major axis still needed to be determined with high accuracy in order to calculate the *change* in the semi-major axis. How the errors associated in the semi-major axis calculation affect the changes in semi-major axis was another issue that needed to be addressed. Will an error in the initial ephemeris conditions provided by the TLE data affect the propagation and hence the change in magnitude of semi-major axis? The answer is yes, but whether this actually affects the final derived density ratio needed to be considered. This is why the method presented in this study analyses *change* in semi-major axis and not magnitude; the *change* in semi-major does not require absolute values of density to be determined. As such, it is a parameter that provides an excellent metric for thermospheric density analysis.

Consider a case whereby there is no long-term thermospheric density change in the atmosphere. There is an orbiting satellite whose orbit is to be numerically propagated to predict its future state. The TLE data for the orbiting satellite provides an ephemeris position at a slightly different position than the true position, due to the errors associated with the TLE data. This erroneous position would result in an erroneous prediction of atmospheric density, for the calculation of atmospheric drag, from the empirical model in the orbital propagator. For ease of comprehension, the integral used to calculate the effects from atmospheric drag during numerical propagation is repeated here and given by

$$\Delta a = -\int_{\text{TLE1}}^{\text{TLE2}} \frac{a^2 v}{\mu} \rho v^2 \delta \mathrm{d}t. \tag{125}$$

After orbital propagation from this erroneous position, the total change in semi-major axis due to atmospheric drag will not be equal to the true change in semi-major axis in the real orbit. This in itself is obvious but, the difference between the changes in semi-major axes from the true orbit evolution to the numerically propagated orbit will not be linearly proportional to the magnitude of the initial position error. This is because atmospheric density varies approximately exponentially with altitude. The error in the semi-major axis associated with the TLE data was previously shown to be 0.05% but, in the case of the error from the change in the semi-major axis due to drag, this error value would not be applicable. It is this facet that accounts for the noisy behaviour of the density ratios from the 41 satellites and was a driving force behind the relatively large altitude bin sizing.

To quantify the error incurred by a 0.05% intrinsic ephemeris error in the TLE data, a more precise estimate of associated density change was required. A position error of 0.05% at LEO altitudes equates to an approximate error of 4 km. Assuming this error is purely in altitude, thereby having the greatest effect on density change, the difference in density is approximately 10%. This value assumed an average level of solar activity and was derived from the NRLMSISE-00 empirical model. Equation (125) shows the change in semi-major axis to be linearly proportional to density. Therefore, the signal-to-error ratio of a secular density decline, with a magnitude of 0.0081% per 10 days, using data that varies by 10% (0.1) was estimated to be of the order of 0.1-0.2. This again shows that the TLE ephemeris errors will contribute to the uncertainty of accurate estimates of long-term density change. In summary, large quantities of source data was one way of reducing the uncertainty and providing a reasonable set of results from which one could draw conclusions. Therefore, the set of TLE data from the 41 satellites used in this study would potentially have yielded more accurate results than could have been achieved from studies with a lesser number of satellites. The larger data set enabled better conclusions to be made about long-term thermospheric density change from the density ratios derived using changes in semi-major axis.

### 8.2.2 Changes in the Solar-Terrestrial Environment

The density structure of the atmosphere has been shown to depend, in part, on solar activity. As the atmosphere swells and contracts during times of high and low solar activity respectively, it is questionable as to whether the secular trends present in the density ratios are due to external forcing from the Sun as opposed to terrestrial influences. Within the irradiance spectrum of the Sun it is the Extreme Ultra-Violet radiation that has the most significant effect on the thermosphere. However, as measurements for EUV flux are unavailable over the historical period analysed in this study, the $F_{10.7}$ will again have to suffice as a proxy measurement of long-term solar variations.

The magnitude of $F_{10.7}$ flux during solar maxima varies greatly. The peak $F_{10.7}$ flux for solar cycles 19, 20, 21, 22 and 23 were approximately 255, 160, 205, 210 and 205 SU respectively. Therefore, attempting to infer any long-term trend in $F_{10.7}$ from the recorded values of the previous five solar cycle maxima would be futile due to the variability. However, the magnitudes of $F_{10.7}$ during the last four solar minima do provide some basis for investigating long-term trends. Figure 68 shows the 81-day averaged $F_{10.7}$ solar flux variation with time. The minima for each solar cycle is plotted and a linear regression is applied. The minimum $F_{10.7}$ value is used to infer long-term changes in the Sun because it represents the quietest possible state of the Sun. This state can then be used as a benchmark to compare any long-term variation.

Figure 68 shows that the solar $F_{10.7}$ flux at the minima of each solar minimum is decreasing. However, the regression analysis gave just over a 60% probability of there existing a trend. Statistically, this is not very significant. The minimum of solar cycle 23-24 is not included in the analysis here as this period did not contribute to the historical period analysed when inferring long-term density changes, due to the Sun's anomalously low activity [32]. The density in the thermosphere can vary by up to an order of magnitude between times of high and low solar activity. During that time, the $F_{10.7}$ solar flux can vary between 60 and 300 SU, approximately. Figure 69 shows the variation of density with $F_{10.7}$ solar flux for the different altitudes, derived from the NRLMSISE-00 empirical model. At 200 km, the change in density per SU of $F_{10.7}$ solar flux is 1.00%. This figure increases to 3.95% at 600 km. A declining trend in $F_{10.7}$ solar flux of 0.43% per decade equates to approximately 0.26 SU per decade. Therefore,

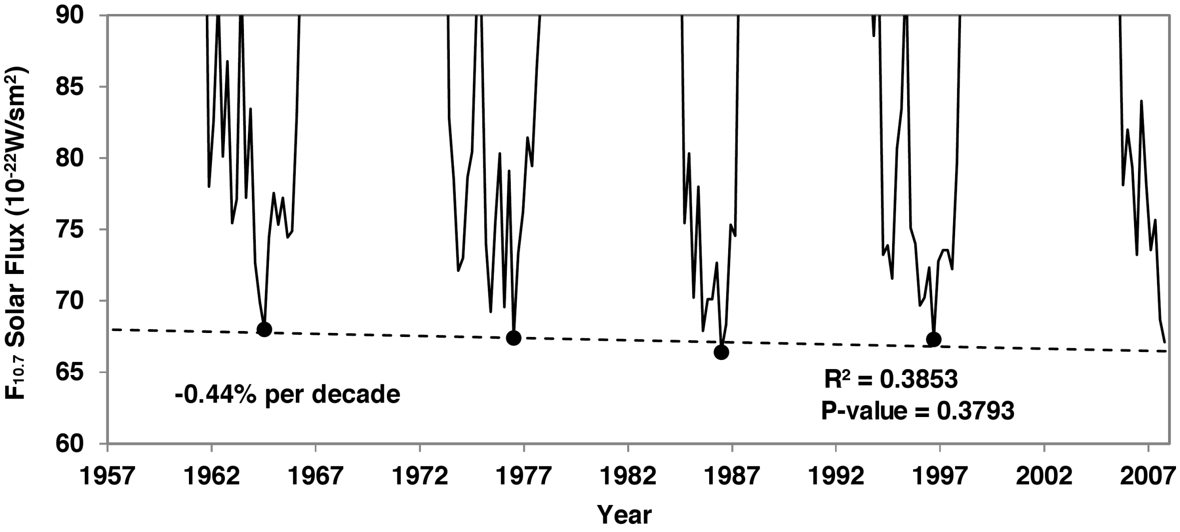

Figure 68: *The 81-day averaged $F_{10.7}$ solar flux variation with time. The minima for each solar cycle is plotted and a least squares best fit is applied resulting in a secular decline of 0.44% per decade of $F_{10.7}$. The linear regression analysis gave a correlation coefficient $R^2$ = 0.3853 and a statistical P-value of 0.3793.*

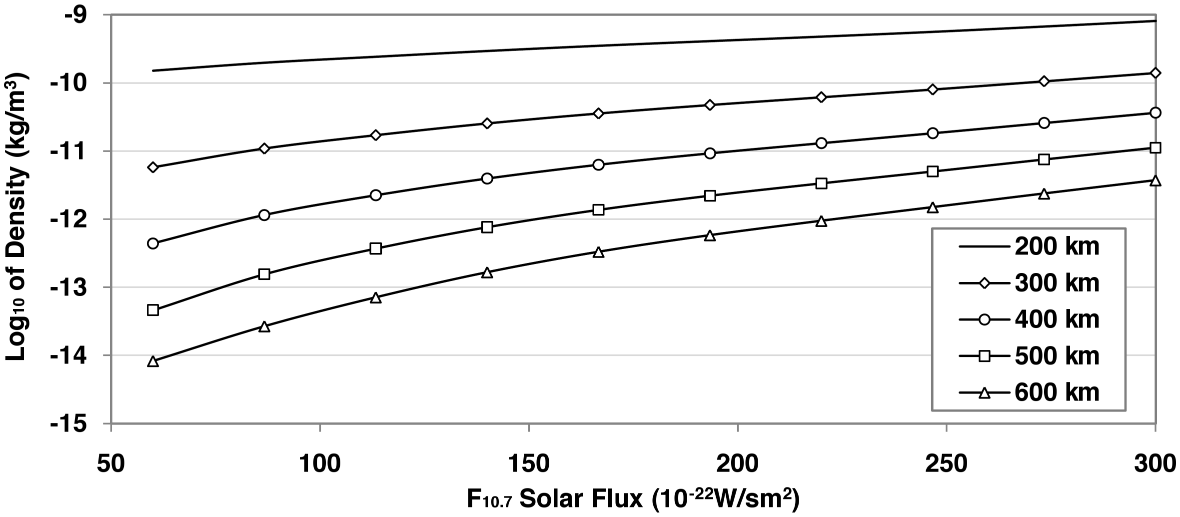

Figure 69: *The variation of density with $F_{10.7}$ solar flux.*

this $F_{10.7}$ decline would yield a secular density decline of 0.26% at 200 km and 1.03% at 600 km. The density trend results derived in this study are greater by over one order of magnitude for the lower altitudes and by a factor of approximately five for the higher altitudes. Therefore, it is possible that a long-term solar irradiance variation may contribution to long-term thermospheric density change but, it is not possible to say whether they could contribute a significant portion of the trends obtained in the results of this study. This analysis assumes the long-term change in solar flux is not captured and removed from the density trend analysis by the NRLMSISE-00 model. This assumption must be false as Figure 69 explicitly demonstrates the ability of the NRLMSISE-00 model to adjust density depending on $F_{10.7}$. As such, the secular declines derived from the variation of $F_{10.7}$ above are highly unlikely, or at least significantly less. Owing to the fact that the density model is responsible for removing the variations due to solar effects, which are two orders of magnitude larger than the apparent secular density trend, the accuracy of the density model's representation of solar effects is crucial when accounting to sources of trend errors.

Other effects of the solar variability include those attributed to the estimation and constancy of the ballistic coefficient. As shown in Figure 53 (see Section 6.2 on page 113), there is a correlation between the density ratio estimates and $F_{10.7}$ solar flux. Bowman *et al.* [11] showed that errors in model densities are highly dependent on solar variability and can therefore have an indirect effect on the constancy of the ballistic coefficient. The solar minimum of cycle 23-24 served to highlight such model variabilities in the NRLMSISE-00 model predictions of interactions between solar irradiance and the upper atmosphere. This is the reason why the $F_{10.7}$ data for the solar cycle minimum of 23-24 was not included in the long-term trend analysis or the linear best fit shown in Figure 68. The density ratios resulting from the abnormally low solar flux emissions during the final years of the historical density analysis demonstrated the erroneous effects that can result from extreme values of $F_{10.7}$. The period through which the ballistic coefficients were estimated was partly selected due to its average solar activity level. This meant that average estimations of ballistic coefficient could be obtained compared to their historical variation during times of solar variation. Therefore, the sharp drop-off in the density ratios plotted in Figure 53 is probably due to increased errors in the NRLMSISE-00 model densities giving erroneous estimates of atmospheric drag, and therefore density ratios. Also, it is likely that the periodicities derived from the Fourier spectral analysis of the trend data that were coincident with solar variation were partly due to errors in the NRLMSISE-00 model.

# 9 Conclusions and Future Work

Two questions that this study set out to answer asked whether the thermosphere was secularly changing, and if so, to what extent. These questions need to be further refined as they do not precisely define what this thesis has ultimately shown. The thermosphere may indeed be secularly changing but, it is the manner in which the change has been caused that is the key issue. This study has shown that the thermosphere is contracting and has quantified the rate at which the contraction is occurring. These questions were derived from motivations to better understand the evolution of our planet and to enable more accurate predictions of the future LEO environment.

Thermospheric cooling and contraction is a real and valid phenomenon to be investigated and is currently actively investigated worldwide. Theoretical and empirical analyses of changes in atmospheric structure predict thermospheric secular change, along with varied views on its long-term outcome. It is hoped that this project will help refine and shape the existing knowledge base of thermospheric evolution.

The concept of long-term thermospheric contraction is not a new idea in this field of research. In this study it is the method of determining a satellite's ballistic coefficient as well as the method utilised to derive density ratios over a long-term historical period that holds significant novelty. In addition to deriving and quantifying long-term thermospheric density changes, one of the aims of this study was to develop an accurate orbital propagator. This has been achieved in AETHER, the results of which have been published along with the novel method of predicting satellite ballistic coefficients solely from TLE data.

From the TLE data of 41 satellites thermospheric density has appeared to decline secularly at a rate of -1.90% per decade at 200 km and increasing to -3.92% per decade at 600 km. The rate at which the secular trend increases with altitude is approximately -0.51% per decade per 100 km. During times of low solar activity the trend in thermospheric density decline appears to increase in magnitude to approximately -4.0% per decade with very little dependency on altitude. During times of high solar activity, declining trends in thermospheric density decreases in magnitude to approximately -1.1% per decade at 200 km with a greater altitude dependency resulting in a trend rate of -5.9% per decade at 600 km. It would be beneficial to apply the models and methods developed in this study to a larger set of TLE data. This would begin to average out erroneous variations due to the deficiencies intrinsic to the TLE data.

Using the data from a much larger set of satellite TLE sets could spur the avenue of research into coupling thermospheric evolution with specific atmospheric forcings. More specifically, the effect of varying concentrations of atmospheric species such as the greenhouse gasses of carbon dioxide, methane and nitrous oxides could be correlated with thermospheric density change to provide a different perspective on climate change and vertical atmospheric coupling.

Periodicities have been detected in the trend data of the density ratios. However, the extent to which these are manifestations of the variation of estimated model parameters aliasing into the trend results is unclear and would require further research to form definitive conclusions. Nevertheless, the periodicities found from the Fourier spectral of the trend data do provide an initial guideline into areas of focus.

Future space debris predictions are highly dependent on density changes in the thermosphere, as atmospheric drag is the only natural sink to remove space debris from orbit. The impact of studies such as the one presented here can make significant changes to spacecraft operations and practices. With prolonged use of satellites for the telecommunications industry, as an example, it becomes essential to maintain the environment in which they operate. Satellite collisions have already occurred, consequently producing thousands of additional pieces of space debris that increase the risk of further collisions. However, removing potentially hazardous objects from the near-Earth environment is extremely expensive and government organisations will only pay for such activities if it shown as a necessity. Long-term density changes in the thermosphere would help demonstrate this necessity through studies, such as those of Lewis *et al.*, which have demonstrated the catastrophic consequences of an over-populated near-Earth environment.

Furthermore, the cause of the density changes may impact areas of life other than those related to satellite orbits and the near-Earth environment. There are many studies showing what can happen with increased greenhouse concentrations in the atmosphere. These studies have been supported by the empirical evidence presented in this study, as well as other studies similar in nature that used in-situ satellite drag data. Concentrations of greenhouse gasses are partly due to anthropogenic activities. Therefore, not only will quantifying changes in thermosperic density impact the practices of satellite operators, it will also impact the way in which we live our lives. Recycling and developing better ways of producing energy that do not emit such vast quantities of greenhouse gasses are ways to reduce greenhouse gas emissions.

Finally, considering a broader view, thermospheric density decline needs to be considered for the space environment to continue to flourish and provide the means for continued scientific, commercial and pleasure usage. Though it is not a directly affecting or obvious variability of life on Earth, long-term thermospheric density change demands the attention, consideration and respect of those who intend to exploit its domain: everyone.

# 10 References

1. Akmaev, R. A. and V. I. Fomichev, (2000), A model estimate of cooling in the mesosphere and lower thermosphere due to the CO2 increase over the last 3-4 decades, *Geophys. Res. Lett.,* 27, 14, doi:10.1029/1999GL011333.

2. Akmaev, R. A., (2003), Thermospheric resistance to ‘greenhouse cooling’: Effect of the collisional excitation rate by atomic oxygen on the thermal response to CO2 forcing, *J. Geophys. Res.,* 108, A7, doi:10.1029/2003JA009896.

3. Akmaev, R. A., V.I. Formichev, X. Zhu, (2006), Impact of middle-atmospheric composition changes on greenhouse cooling in the upper atmosphere, *J. Atmos. & Solar-Terr. Phys.,* 68, 1879-1889,.

4. Aksnes, K., (1974), Short-periodic and long-periodic perturbations of a spherical satellite due to direct solar radiation, *Center for Astrophysics,* Preprint Series No. 230.

5. Analytical Graphics, Inc., (2009), Satellite Tool Kit, www.agi.com.

6. Bowman, B.R., (2001), Atmospheric Density Variations at 1500-4000 km Height Determined from Long Term Orbit Perturbation Analysis, paper presented at the AAS/AIAA Astrodynamics Specialist Conference, Santa Barbara, California, AAS-2001-132.

7. Bowman, B.R., (2002), True satellite ballistic coefficient determination for HASDM, paper presented at the Astrodynamics Specialist Conference, Am. Inst. of Aeronautics and Astronautics, Monterey, California, AIAA 2002-4887.

8. Bowman, B.R., Marcos, F.A. and Kendra, M.J., (2004), A method for computing accurate daily atmospheric density values from satellite drag data, paper presented at the AAS/AIAA Flight Mechanics Meeting, Am. Astron. Soc., Maui, Hawaii.

9. Bowman, B.R. and Moe, K., (2006), Drag Coefficient Variability at 175-500 km from the Orbit Decay Analyses of Spheres, *American Astronautical Society,* AAS 05-257.

10. Bowman, B.R., Tobiska, W.K. and Marcos, F.A., (2006), A New Empirical Thermospheric Density Model JB2006 Using New Solar Indices, *J. Atmos. & Solar-Terr. Phys.,* 70, 774-793.

11. Bowman, B.R., Tobiska, W.K., Marcos, F.A., Huang C.Y., Lin C.S., and Burke, W.J., (2008), A New Empirical Thermospheric Density Model JB2008 Using New Solar and Geomagnetic Indices, paper presented at the Astrodynamics Specialist Conference, Honolulu, Hawaii, AIAA 2008-6438.

12. Brasseur G. and M. Hitchman, (1988), Stratospheric response to trace gas perturbations: Changes in ozone and temperature distributions, *Science,* 240, 634-636.

13. Brodowski, A., (2007), The NRLMSISE-00 model written in C++, http://www.brodo.de/space/nrlmsise/index.html.

14. Brouwer, D., (1959), Solutions of the Problem of Artificial Satellite Theory Without Drag, *Astronomical J.,* Vol. 64(1274): 378-397.

15. Brown, C., (1998), Spacecraft Mission Design, Virginia: AIAA.

16. Bruinsma, S. L. and J. M. Forbes, (2007), Storm-Time Equatorial Density Enhancements Observed by CHAMP and GRACE, *J. Spacecraft & Rockets,* Vol.44 No.6 Nov-Dec. doi: 10.2514/1.28134.

17. Challenging Minisatellite Payload (CHAMP), (2000), http://www-app2.gfz-potsdam.de/pb1/op/champ/

18. CHAMP Rapid Science Orbit Data (CHAMP RSO), (2010), http://thermosphere.tudelft.nl/acceldrag/data.php

19. CIRA-72 COSPAR International Reference Atmosphere (CIRA), (1972), Akademie Verlag, Berlin.

20. Chobotov, V. A., (1996), Orbital Mechanics Second Edition, Virginia: AIAA.

21. Cook, G.E., (1965), Satellite Drag Coefficients, *Planet. Space Sci.,* Vol. 13 pp. 929-946.

22. Dickinson, R.E., Bougher, S.W. (1986), Venus Mesosphere and Thermosphere 1. Heat Budget and Thermal Structure, *J. Geophys. Res.,* 91, A1, doi:10.1029/JA091iA01p00070.

23. Dominion Radio Astrophysical Observatory (DRAO), (2012), http://www.spaceweather.gc.ca

24. Doornbos, E., (2001), Modelling of non-gravitational forces for ERS-2 and ENVISAT, Delft Institute for Earth-Oriented Space Research, Delft University of Technology, The Netherlands.

25. Doornbos, E., (2008), *Private Communication*, Delft Institute for Earth-Oriented Space Research, Delft University of Technology, The Netherlands.

26. Doornbos, E., (2012), *Private Communication*, Delft Institute for Earth-Oriented Space Research, Delft University of Technology, The Netherlands.

27. Dyke, J., (2008), Private Communication, University of Southampton.

28. Emmert, J.T., J. M. Picone, J. L. Lean and S. H. Knowles, (2004), Global change in the thermosphere: Compelling evidence of a secular decrease in density, *J. Geophys. Res.,* 109, A02301, doi:10.1029/2003JA010176.

29. Emmert, J.T., Meier, R.R., Picone, J.M., Lean, J.L. and Christensen, A.B., (2006), Thermospheric density 2002Ű2004: TIMED/GUVI dayside limb observations and satellite drag, *J. Geophys. Res.,* 111, A10S16, doi:10.1029/2005JA011495.

30. Emmert, J.T., J. M. Picone, J. L. Lean and R. R. Meier, (2008), Thermospheric global average trends, 1967-2007, derived from orbits of 5000 near-Earth objects, *Geophys. Res. Lett.,* 35, L05101, doi:10.1029/2007GL032809.

31. Emmert, J.T.,(2008), Private Communication, Naval Research Laboratory.

32. Emmert, J.T., Lean, J.L. and Picone, J.M., (2010), Record low thermospheric density during the 2008 solar minimum, *Geophys. Res. Lett.,* 37, L12102, doi:10.1029/2010GL043671.

33. Erwin, E. H., (2007), NOAA Indices, ftp://ftp.ngdc.noaa.gov/.

34. ESA (2002), Environmental Satellite Mission - Envisat, http://envisat.esa.int/earth/www/category/index.cfm?fcategoryid=87

35. Fortescue, P. W., J. P. W. Stark and G. G. Swinerd, (2003), Spacecraft Systems Engineering, England: Wiley & Sons.

36. van der Ha, J. C. and V. J. Modi, (1977), Analytical evaluation of Solar radiation induced perturbations of space structures, *J. Astronautical Sci.,* XXV, No. 4, 283-306.

37. Gurzadyan, G.A., (2002), Space Dynamics: Advances in Astronomy and Astrophysics, Taylor & Francis.

38. Hedin, A. E., H. G. Mayr, C . A. Rebera and T. W. Spencer, (1974), Empirical Model of Global Thermospheric Temperature and Composition Based on Data From the Ogo 6 Quadrupole Mass Spectrometer, *J. Geophys. Res.,* 79, 1, doi:10.1029/JA079i001p00215.

39. Hedin, A. E., J. E. Salah, J. V. Evans, C. A. Reber, G. P. Newton, N. W. Spencer, D.C. Kayser, D. Alcaydé, P. Bauer, L. Cogger and J.P. McClure, (1977), A Global Thermospheric Model Based on Mass Spectrometer and Incoherent Scatter Data, MSIS 1. N2 Density and Temperature, *J. Geophys. Res.,* 82, 16, doi:10.1029/JA082i016p02139.

40. Hedin, A. E., C. A. Reber, G. P. Newton, N. W. Spencer, H. C. Brinton and H. G. Mayr, (1977), A Global Thermospheric Model Based on Mass Spectrometer and Incoherent Scatter Data MSIS 2. Composition, *J. Geophys. Res.,* 82, 16, doi:10.1029/JA082i016p02148.

41. Hedin, A.E., Niemann, H.B., Kasprzak, W.T. and Seiff, A. (1983), Global Empirical Model of The Venus Thermosphere, *J. Geophys. Res.,* 88, A1, doi:10.1029/JA088iA08p06352.

42. Hedin, A. E., (1983), A Revised Thermospheric Model Based on Mass Spectrometer and Incoherent Scatter Data: MSIS-83, *J. Geophys Res.,* 88, A12, doi:10.1029/JA088iA12p10170.

43. Hedin, A. E., (1987), MSIS-86 thermospheric model, *J. Geophys Res.,* 92, A5 doi:10.1029/JA092iA05p04649.

44. Hedin, A. E., N. W. Spencer and T. L. Killeen, (1988), Empirical global model of upper thermosphere winds based on atmospheric and dynamics Explorer satellite data, *J. Geophys. Res.,* 93, A9, doi:10.1029/JA093iA09p09959.

45. Hedin, A. E., (1988), *High Altitude Atmospheric Modeling*, NASA TM X-100707.

46. Hedin, A. E., M. A. Biondi, R. G. Burnside, G. Hernandez, R. M. Johnson, T. L. Killeen, C. Mazaudier, J. W. Meriwether, J. E. Salah, R. J. Sica, R. W. Smith, N. W. Spencer, V. B. Wickwar and T. S. Virdi, (1991), Revised global model of thermosphere winds using satellite and ground-based observations, *J. Geophys. Res.,* 96, A5, doi:10.1029/91JA00251.

47. Hedin, A. E., E. L. Fleming, A. H. Manson, F. J. Schmidlin, S. K. Avery, R. R. Clark, S. J. Franke, G. J. Fraser, T. Tsuda, F. Vial and R. A. Vincent, (1996), Empirical wind model for the upper, middle and lower atmosphere, *J. Atmos. Terr. Phys.,* 58(13), 1421-1447.

48. Hoots, F. R. and R. L. Roehrhich (1980), Models for propagation of NORAD element sets, Spacetrack Rep. 3, pp 87, Off. of Astrodyn., Aerospace Defense Cent., U. S., Peterson AFB, Colo. (Available at www.celestrak.com)

49. Horn, M. K., (1983), Scaled Runge-Kutta algorithms for handling dense output, SIAM *J. Numer. Anal.,* 20/3, 558-568.

50. Jacchia, L.G., (1970), New static models of the thermosphere and exosphere with empirical temperature models, Technical Report 313, Smithsonian Astrophysical Observatory.

51. Justus, C.G. and Johnson, D.L., (1999) The NASA/MSFC Global Reference Atmospheric Model - 1999 version (GRAM-99), NASA/TM 209630.

52. Kaula, W. M., (1966), Theory of Satellite Geodesy, Waltham MA: Blaisdell Publishing Co.

53. Keating, G.M., Nicholson III, J.Y. and Lake, L.R., (1980), Venus Upper Atmosphere Structure, *J. Geophys. Res.,* 85, AI3, doi:10.1029/JA085iA13p07941.

54. Keating, G.M. and Bougher, S.W., (1992), Isolation of Major Venus Thermospheric Cooling Mechanism and Implications for Earth and Mars, *J. Geophys. Res.,* 97, A4, doi:10.1029/91JA02444.

55. Keating, G. M., J. C. Leary, B. D. Green, O. M. Uy, R. C. Benson, R. E. Erlandson, T. E. Phillips, J. C. Lesho and M. T. Boies, (1998), Neutral and ion drag effects near the exobase: MSX satellite measurements of He and O+, in Astrodynamics 1997: Advances in the Astronautical Sciences, 97(1), edited by F. Hoots, B. Kaufman, P. Cefola, and D. Spencer, pp 549-556, Am. Astronaut. Soc., San Diego, Calif.

56. Keating, G. M., R. H. Tolson and M. S. Bradford, (2000), Evidence of long-term global decline in the EarthŠs thermospheric densities apparently related to anthropogenic effects, *Geophys. Res. Lett.,* 27, doi:10.1029/2000GL003771.

57. Kelso, T.S., (2004), Two-Line Element Set Format, www.celestrak.com.

58. Kelso, T.S., (2004), Orbital Coordinate Systems, Part I, www.celestrak.com.

59. King-Hele, D., (1987), Satellite Orbits in an Atmosphere, Blakie, Glasgow.

60. King-Hele, D., (1987), Satellite Orbits in an Atmosphere: Theory and Applications: Chapter 2.1 The upper atmosphere, Blakie, Glasgow.

61. King-Hele, D., (1987), Satellite Orbits in an Atmosphere: Theory and Applications: Chapter 3, equation 3.57, Blakie, Glasgow.

62. King-Hele, D., (1987), Satellite Orbits in an Atmosphere: Theory and Applications: Chapter 4, equation 4.4, Blakie, Glasgow.

63. King-Hele, D., (1987), Satellite Orbits in an Atmosphere: Theory and Applications: Chapter 10, equation 10.5, Blakie, Glasgow.

64. King-Hele, D., (1987), Satellite Orbits in an Atmosphere: Theory and Applications: Chapter 10.3 Practical formulae for determining air density from $\dot{T}$, Blakie, Glasgow.

65. Klinkrad, H., (1991), DISCOS, ESA's Database and Information System Characterising Objects in Space, *Adv. Space Res.,* 11, 12, pp 43-52.

66. Kozai, Y., (1961), The Motion of a Close Earth Satellite, *Astronomical J.,* 64, 1274: pp 367-377.

67. Kozai, Y., (1961), Second-order solution of artificial satellite theory without drag, *Astronomical J.,* 67: pp 446.

68. Lean, J.L, Picone, J.M., Emmert, J.T. and Moore, G., (2006), Thermospheric densities derived from spacecraft orbits: Application to the Starshine satellites, *J. Geophys. Res.,* 111, A04301, doi:10.1029/2005JA011399.

69. Lewis, H.G., Swinerd, G.G., Ellis, C.S. and Martin, C.E. (2005), Response of the space debris environment to greenhouse cooling, paper presented at the Fourth European Conference on Space Debris, Darmstadt, Germany 18-20 Apr 2005.

70. Lewis, H.G., Swinerd, G.G., Newland, R.J. and Saunders, A. (2009), Active Removal Study For On-Orbit Debris Using DAMAGE, paper presented at the Fifth European Conference on Space Debris, Darmstadt, Germany 30 Mar-02 Apr 2009. European Space Agency.

71. Lewis, H.G., Saunders, A., Swinerd, G.G. and Newland, R.J. (2011), Effect of Thermospheric Contraction on Remediation of the Near-Earth Space Debris Environment, *J. Geophys. Res.,* doi:10.1029/2011JA016482.

72. Liu, L., Wan, W., Ning, B., Pirog, O.M. and Kurkin, V.I., (2006), Solar activity variations of the ionospheric peak electron density, *J. Geophys. Res.,* 111, A08304, doi:10.1029/2006JA011598.

73. Marcos, F.A., Wise J.O., Kendra M.J., Grossbard N.J. and Bowman B.R., (2005), Detection of a long-term decrease in thermospheric neutral density, *Geophys. Res. Lett.,* 32, L04103, doi:10.1029/2004GL021269.

74. McCarthy, D.D., (1996), IERS Conventions, IERS Technical note 21, Central Bureau of IERS - Observatoire de Paris, Paris.

75. Moe, K. and Bowman, B.R., (2005), The Effects of Surface Composition and Treatment On Drag Coefficient on Spherical Satellites, paper presented at the AAS/AIAA Astrodynamics Specialist Conference, Lake Tahoe, California, AAS-2001-132.

76. Montenbruck, O. and Gill. E., (2005), Satellite Orbits: Models, Methods, Applications, Springer Berlin Heidelberg, New York.

77. Montenbruck, O. and Gill. E., (2005), Satellite Orbits: Models, Methods, Applications: Chapter 3 Force Model,
Springer Berlin Heidelberg, New York.

78. Montenbruck, O. and Gill. E., (2005), Satellite Orbits: Models, Methods, Applications: Chapter 3.3.2 Low-Precision Solar and Lunar Coordinates,
Springer Berlin Heidelberg, New York.

79. Montenbruck, O. and Gill. E., (2005), Satellite Orbits: Models, Methods, Applications: Chapter 3.4 Solar Radiation Pressure,
Springer Berlin Heidelberg, New York.

80. Montenbruck, O. and Gill. E., (2005), Satellite Orbits: Models, Methods, Applications: Chapter 3.4.2 Shadow Function,
Springer Berlin Heidelberg, New York.

81. Montenbruck, O. and Gill. E., (2005), Satellite Orbits: Models, Methods, Applications: Chapter 3.5.1 The Upper Atmosphere,
Springer Berlin Heidelberg, New York.

82. Muldoon, A.R., Elkaim, G.H., Rickard, I.F. and Weeden, B., (2009), Improved Orbital Debris Trajectory Estimation Based on Sequential TLE processing, paper presented at the 60th International Astronautical Congress, Daejeon.

83. NASA, (1976), The Theory of Gravitational Potential Applied to Orbit Prediction,
NASA TM X-5818.

84. NASA, (2003), Definition of Two-line Element Set Coordinate System,
http://spaceflight.nasa.gov.

85. National Oceanic and Atmospheric Administration: National Geophysical Data Center: Solar Radio F10.7 Flux Historical Indices, ftp://ftp.ngdc.noaa.gov/STP/SOLAR_ DATA/SOLAR_ RADIO/FLUX/.

86. National Oceanic and Atmospheric Administration: National Geophysical Data Center: Solar Radio F10.7 Flux Adjustments, ftp://ftp.ngdc.noaa.gov/STP/SOLAR_DATA/SOLAR_RADIO/FLUX/docs/ 2800_MHz_SOLAR_FLUX.readme.

87. National Oceanic and Atmospheric Administration: National Geophysical Data Center: Global Geomagnetic Historical Indices, ftp://ftp.ngdc.noaa.gov/STP/GEOMAGNETIC_ DATA/INDICES/KP_ AP/.

88. Numerical Recipes In C: The Art of Scientific Computing: Chapter 13. Fourier and Spectral Applications, Cambridge University Press 1968-1992.

89. Pardini, C. and L. Anselmo, (2001). Re-entry Predictions In Support Of The Inter-Agency Space Debris Co-ordination Committee Test Campaigns, proceedings of the Third European Conference on Space Debris, ESOC, Darmstadt, Germany, pp 521-526.

90. Payne, T., (2009), Private Communication, U.S. Airforce Space Command.

91. Picone, J. M., A. E. Hedin, D. P. Drob and A. C. Aikin, (2002), NRLMSISE-00 empirical model of the atmosphere: Statistical comparisons and scientific issues, *J. Geophys. Res.,* 107, A12, doi:10.1029/2002JA009430.

92. Picone, J. M., J. T. Emmert and J. L. Lean, (2005), Thermospheric densities derived from spacecraft orbits: Accurate processing of two-line element sets, *J. Geophys. Res.,* 110, A03301, doi:10.1029/2004JA010585.

93. Prölss, G. W., (2004), Physics of the Earth's Space Environment: An Introduction. Springer Berlin Heidelberg, New York.

94. Qian, L., R. G. Roble, S. C. Solomon, and T. J. Kane (2006) Calculated and observed climate change in the thermosphere, and a prediction for solar cycle 24, *Geophys. Res. Lett.*, 33, L23705, doi:10.1029/2006GL027185.

95. Richards, P. G., J. A. Fennelly, D. G. Torr, (1994), EUVAC; A Solar EUV Flux Model for Aeronomic Calculations, *J. Geophys. Res.,* 90, A00518, doi:10.1029/94JA00518.

96. Roble, R. G. and R. E. Dickinson, (1989), How will changes in carbon dioxide and methane modify the mean structure of the mesosphere and thermosphere?, *J. Geophys. Res.,* 16, 12, doi:10.1029/GL016i012p01441.

97. Roble, R. G., (1995), The Upper Mesosphere and Lower Thermosphere: A review of Experiment and Theory : Energetics of the Mesosphere and Thermosphere, *Geophys. Monogr.* Ser., 87, 1Ű21.

98. Roble, R. G. and D. S. Ramesh, (2002), Cooling Mechanisms of the Planetary Thermospheres: The Key Role of O Atom Vibrational Excitation of CO2 and NO, *CHEMPHYSCHEM* 2002, 3, 841-843 1 WILEY-VCH Verlag GmbH & Co. KGaA, Weinheim.

99. Roemer, M., (1971), Geomagnetic activity effect on atmospheric density in the 250 to 800 km altitude region, *Space Research* XI, pg.965, Akademie-Verlag, Berlin.

100. Roy, A. E., (1988), Orbital Motion, New York: John Wiley & Sons.

101. Rybicki, G.B., (1989), Computers in Physics, 3, 2, pp 85-87.

102. Saunders, A., (2006), Manned missions to Mars utilizing Aerobraking, University of Southampton, School of Engineering Sciences, UK.

103. Saunders, A., (2007), ExoMars Variant: A balloon platform concept study, University of Southampton, School of Engineering Sciences, UK.

104. Saunders, A., (2008), Nine Month Report, An Empirical Model Of Long-Term Thermospheric Cooling And Contraction, University of Southampton, School of Engineering Sciences, UK.

105. Saunders, A., H.G. Lewis and G.G. Swinerd, (2009), A New Tool for Satellite Re-entry Predictions, paper presented at the Fifth European Conference on Space Debris, Darmstadt, Germany 30 Mar-02 Apr 2009.

106. Saunders, A., Swinerd, G.G. and Lewis, H.G., (2009), Preliminary Results to Support Evidence of Thermospheric Contraction, paper presented at the 10th Advanced Maui Optical and Space Surveillance Technologies Conference, Maui, Hawaii, August-September 2009.

107. Saunders, A., Swinerd, G.G. and Lewis, H.G., (2011), Deriving Accurate Satellite Ballistic Coefficients from Two-Line Element Data, *J. Spacecraft & Rockets,* 2010-12-A32023.

108. Saunders, A., Lewis, H.G. and Swinerd, G.G., (2011), Further Evidence of Long-Term Thermospheric Density Change Using a New Method of Satellite Ballistic Coefficient Estimation, *J. Geophys. Res.,* doi:10.1029/2010JA016358.

109. Schubert, G., Covey, C., Del Genio, A., Elson, L.S., Keating, G., Seiff, A., Young, R.E., Apt, J., Counselman III, C.C., Kliore, A.J., Limaye, S.S., Revercomb, H.E., Sromovsky, L.A., Suomi, V.E., Taylor, F., Woo, R. and VON Zahn, U., (1980), Structure and Circulation of the Venus Atmosphere, *J. Geophys Res.,* Vol. 85, AI3, doi:10.1029/JA085iA13p08007.

110. Slowey, J. W., (1974), Radiation-Pressure and Air Drag Effects on the Orbit of the Balloon Satellite 1963 30D, *Smithsonian Astrophys. Obs.,* Spec. Rep. 356.

111. Solar Heliospheric Observatory, (1995), SOHO Mission, http://sohowww.nascom.nasa.gov/about/about.html.

112. Solomon, S. C., T. N. Woods, L. V. Didkovsky, J. T. Emmert, and L. Qian, (2010) Anomalously low solar extreme-ultraviolet irradiance and thermospheric density during solar minimum, *Geophys. Res. Lett.,* 37, L16103, doi:10.1029/2010GL044468.

113. Space-Track.org, (2004), Space Track: The source for space surveillance data, www.space-track.org.

114. Space-Track.org, (2004), Space Track: TLE Format Description, www.space-track.org/tle_ format.html.

115. Sutton, E. K., R. S. Nerem and J. M. Forbes, (2007), Density and Winds in the Thermosphere Deduced from Accelerometer Data, *J. Spacecraft & Rockets,* 44, 6, doi: 10.2514/1.28641.

116. Storz, M.F., Bowman, B.R. and Branson, J.I., (2002), High Accuracy Satellite Drag Model, paper presented at the AIAA/AAS Astrodynamics Specialist Conference and Exhibit, 5-8 August 2002, Monterey, California, AIAA 2002-4886.

117. Tapley, B. D, M. M. Watkins, J. C. Ries, G. W. Davis, R. J. Eanes, S. R. Poole, H. J. Rim, B. E. Schutz, C. K. Shum, R.S. Nerem, F. J. Lerch, J. A. Marshall, S. M. Klosko, N. K. Pavlis and R. G. Williamson, (1996) The Joint Gravity Model 3, *J. Geophys. Res.,* 101, B12, doi:10.1029/96JB01645.

118. Tapley B.D., J. C. Ries, and M. Cheng, (2007), Neutral Density Measurements from the Gravity Recovery and climate Experiment Accelerometers, *J. Spacecraft & Rockets,*, 44, 6 doi: 10.2514/1.28843.

119. Tobiska, W. K., S. D. Bouwer and B. R. Bowman, (2008), The development of new solar indices for use in thermospheric density modeling, *J. Atmos. & Solar-Terr. Phys.,* 70, 5, pp 803-819.

120. Vallado, D. A., (1997), Fundamentals of Astrodynamics and Applications, Hawthorne CA: Microcosm Press, New York NY: Springer.

121. Vallado, D. A., (1997), Fundamentals of Astrodynamics and Applications: Kepler's Equation and Kepler's Problem: Satellite State Representations: 2-line Element Sets, Hawthorne CA: Microcosm Press, New York NY: Springer.

122. Vallado, D. A., (1997), Fundamentals of Astrodynamics and Applications: General Perturbation Techniques: Forming Analytical Solutions: Kozai's Method, Hawthorne CA: Microcosm Press, New York NY: Springer.

123. Vallado, D. A., (1997), Fundamentals of Astrodynamics and Applications: General Perturbation Techniques: Forming Analytical Solutions: Brouwer's Method, Hawthorne CA: Microcosm Press, New York NY: Springer.

124. Vallado, D. A., (2009), Private Communication, Center for Space Standards & Innovation.

125. Vaisberg, O., (1984), VEGA Mission, http://www.iki.rssi.ru/ssp/vega.html.

126. Williams, D.R. (1978), The Pioneer Venus Orbiter, http://www.nssdc.gsfc.nasa.gov/planetary/pioneer_ venus.html.

127. Woodraska, D. L., T. N. Woods and F. G. Eparvier, (2007), Comparison of TIMED satellite drag with Solar EUV Experiment (SEE) Measurements, *J. Spacecraft & Rockets,* 44, 6, doi: 10.2514/1.28639.

128. Yeomans, D. K. (2009). NASA Horizons System, http://ssd.jpl.nasa.gov/?horizons.

129. Zasova, L.V., Moroz, V.I., Linkin, V.M., Khatuntsev, I.V. and Maiorov, B.S., (2006), Structure of the Venusian Atmosphere from Surface up to 100 km, *Cosmic Research,* 44, 4, pp 364-383.

# 11 Appendices

## 11.1 Trend Data

The Figures in this Section show the full set of density ratios within their respective altitude bins, followed by Figure 70 showing the altitude bin's statistical P-value of the linear regression analysis.

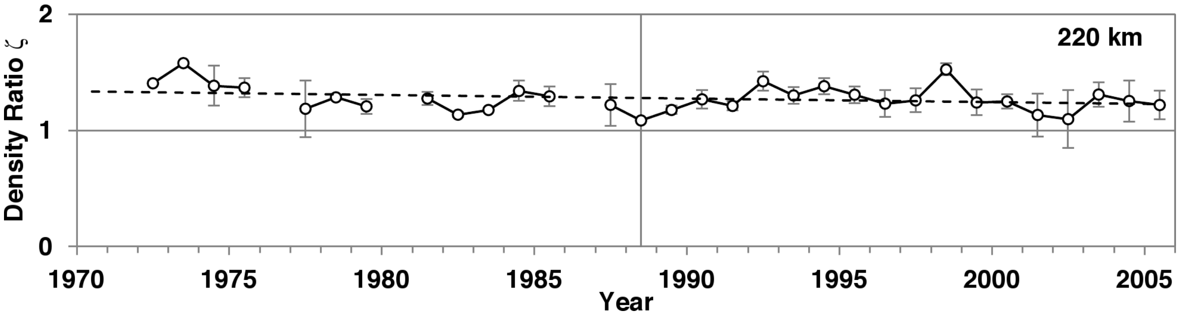

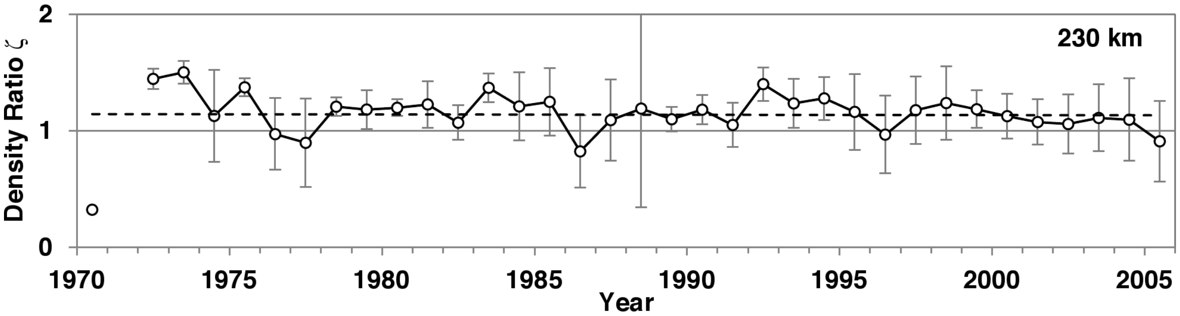

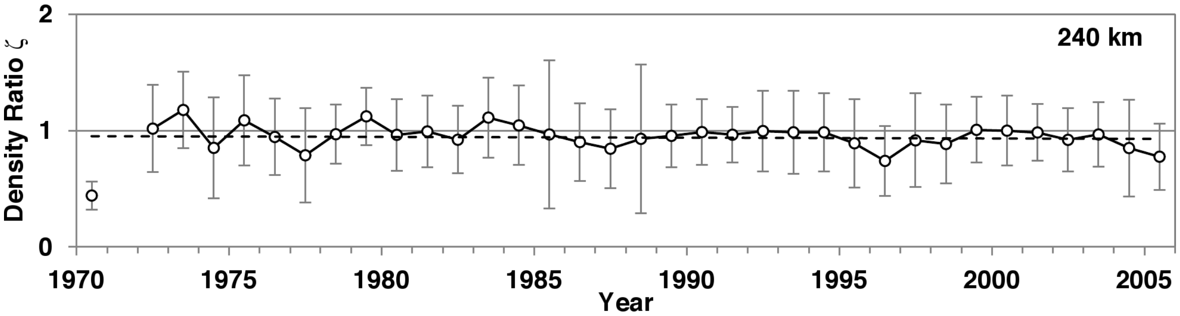

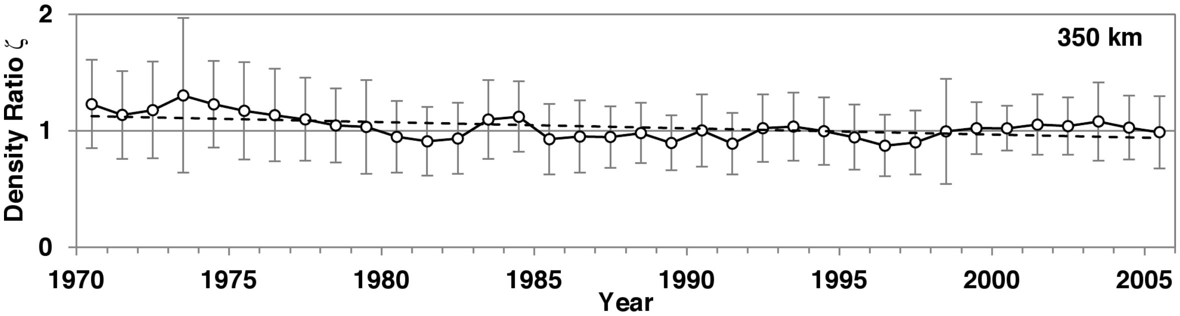

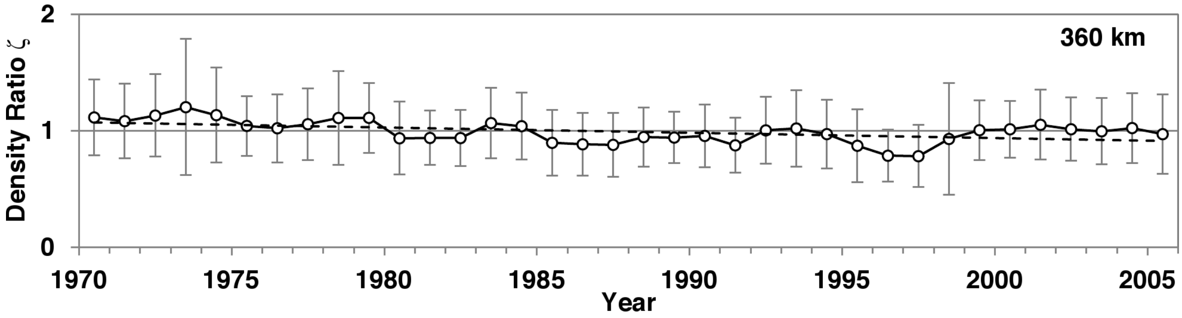
360 km
Density Ratio ζ
2
1
0
1970
1975
1980
1985
1990
1995
2000
2005
Year

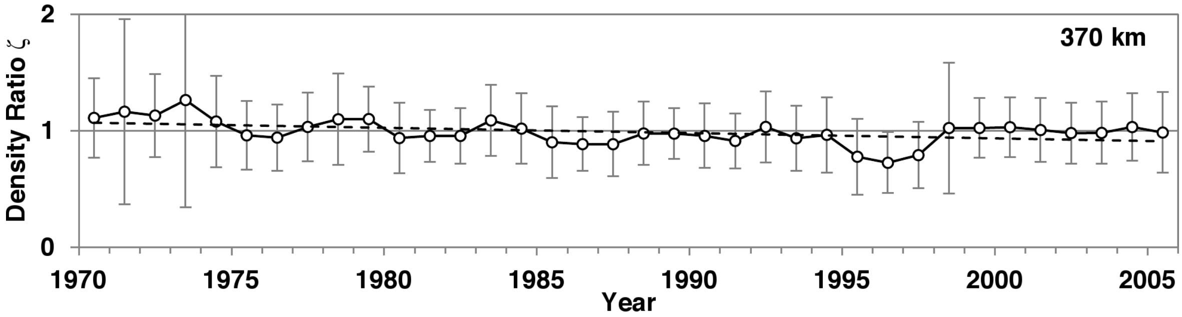
370 km
Density Ratio ζ
2
1
0
1970
1975
1980
1985
1990
1995
2000
2005
Year

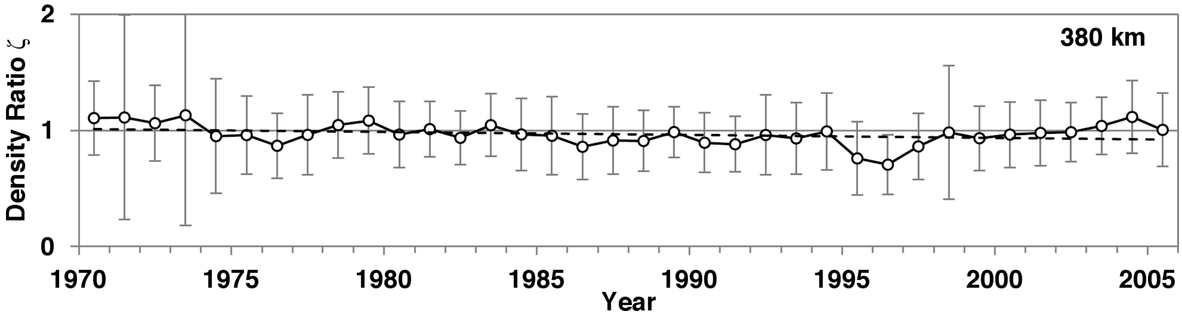
380 km
Density Ratio ζ
2
1
0
1970
1975
1980
1985
1990
1995
2000
2005
Year

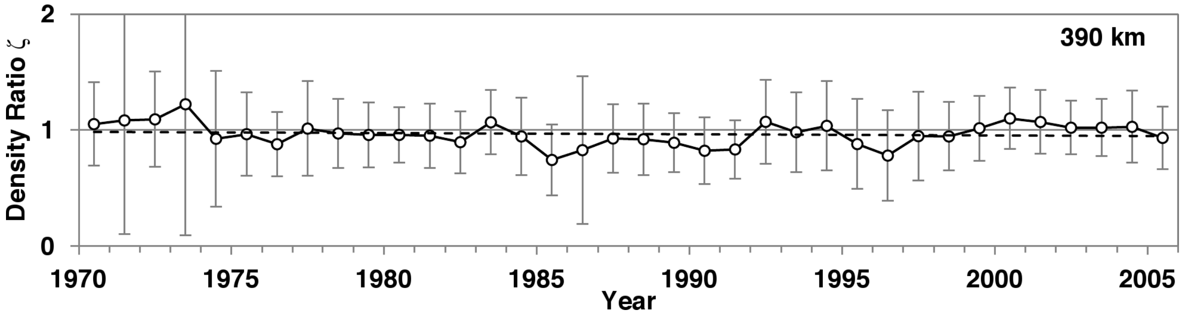
390 km
Density Ratio ζ
2
1
0
1970
1975
1980
1985
1990
1995
2000
2005
Year

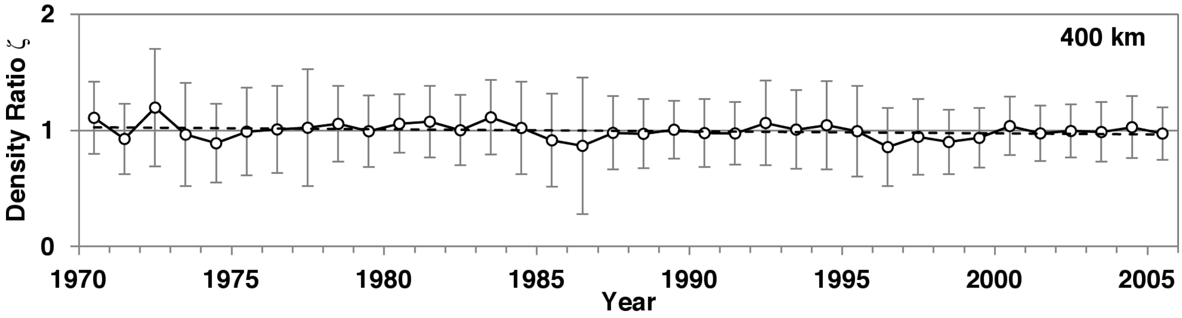
400 km
Density Ratio ζ
2
1
0
1970
1975
1980
1985
1990
1995
2000
2005
Year

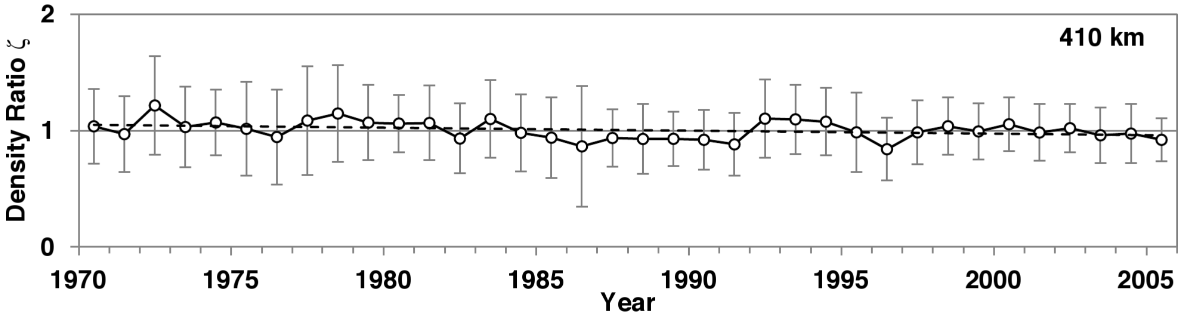
410 km
Density Ratio ζ
Year
0
1
2
1970
1975
1980
1985
1990
1995
2000
2005

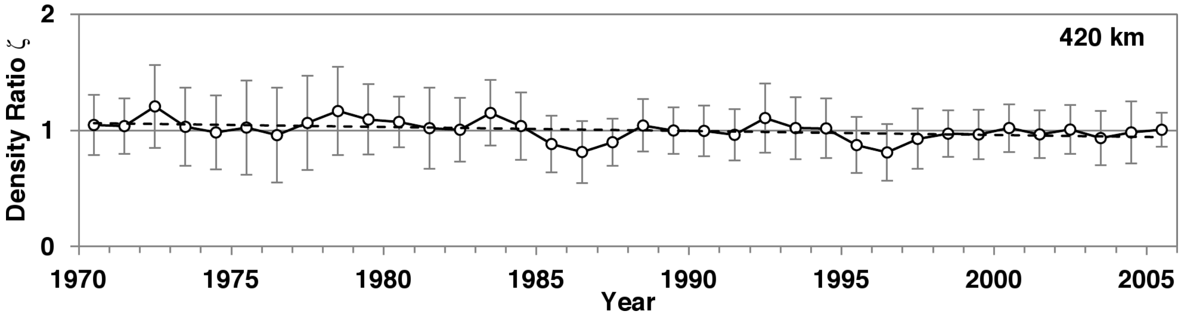
420 km
Density Ratio ζ
Year
0
1
2
1970
1975
1980
1985
1990
1995
2000
2005

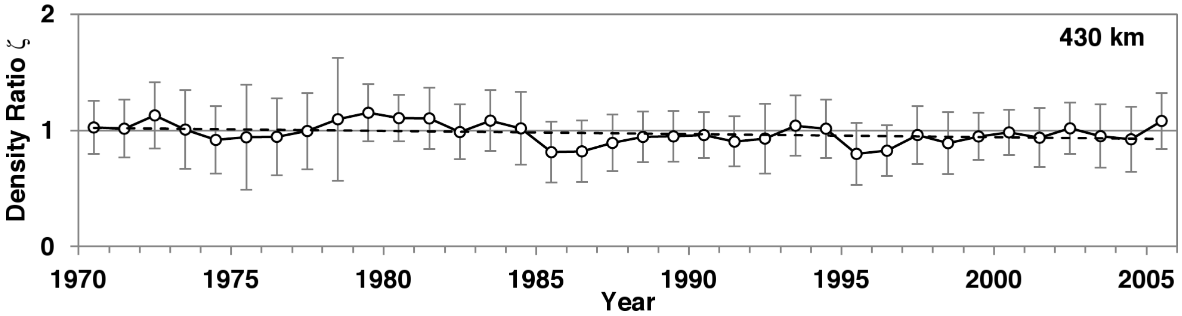
430 km
Density Ratio ζ
Year
0
1
2
1970
1975
1980
1985
1990
1995
2000
2005

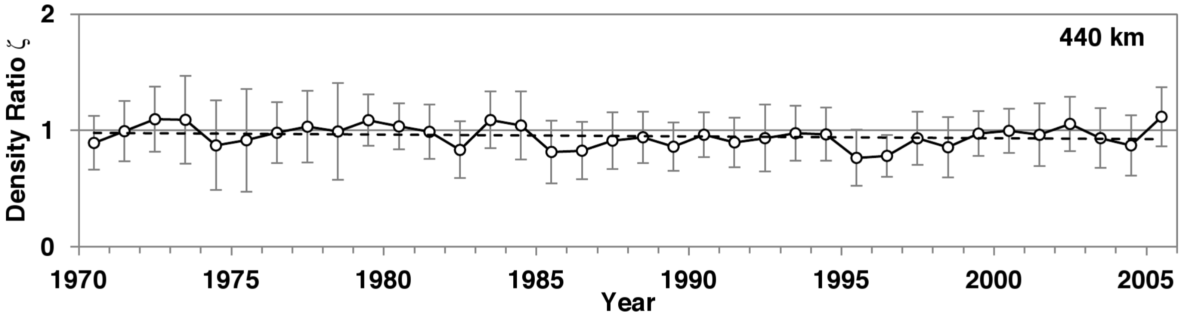
440 km
Density Ratio ζ
Year
0
1
2
1970
1975
1980
1985
1990
1995
2000
2005

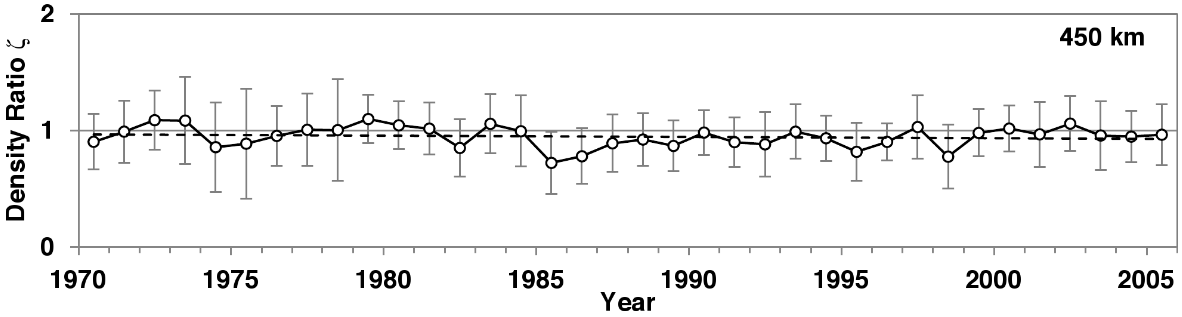
450 km
Density Ratio ζ
Year
0
1
2
1970
1975
1980
1985
1990
1995
2000
2005

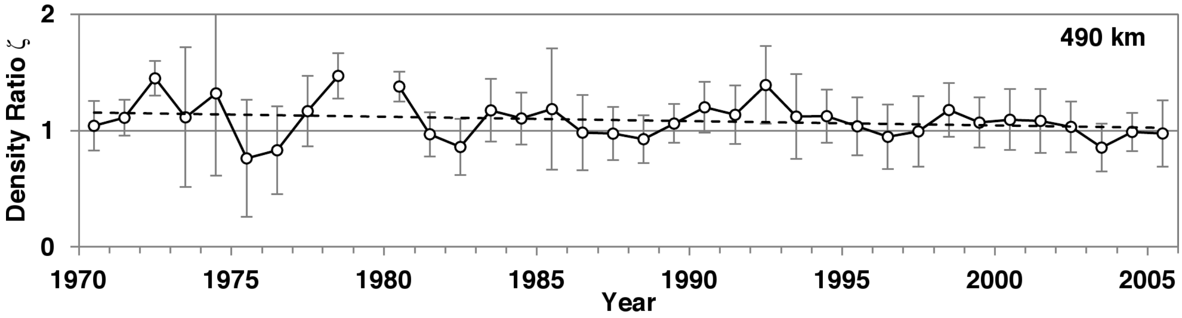
490 km
Density Ratio ζ
0
1
2
1970
1975
1980
1985
1990
1995
2000
2005
Year

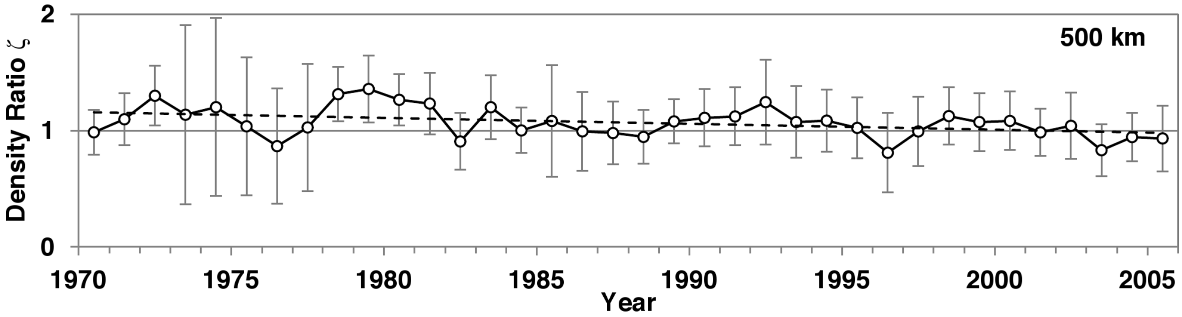
500 km
Density Ratio ζ
0
1
2
1970
1975
1980
1985
1990
1995
2000
2005
Year

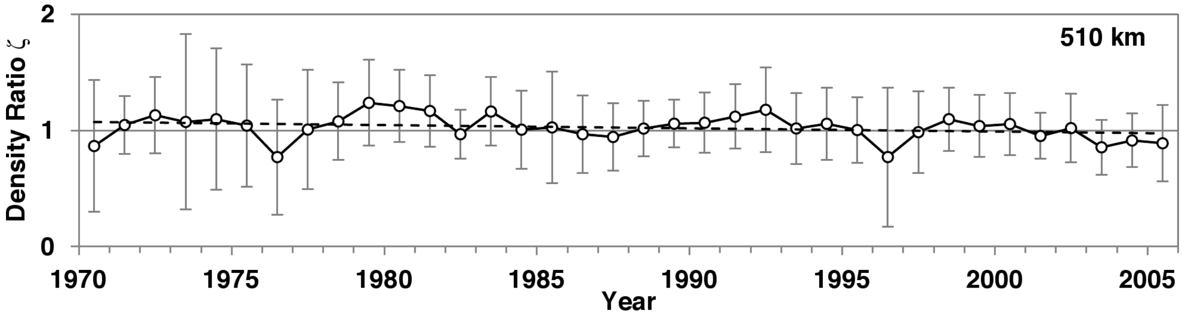
510 km
Density Ratio ζ
0
1
2
1970
1975
1980
1985
1990
1995
2000
2005
Year

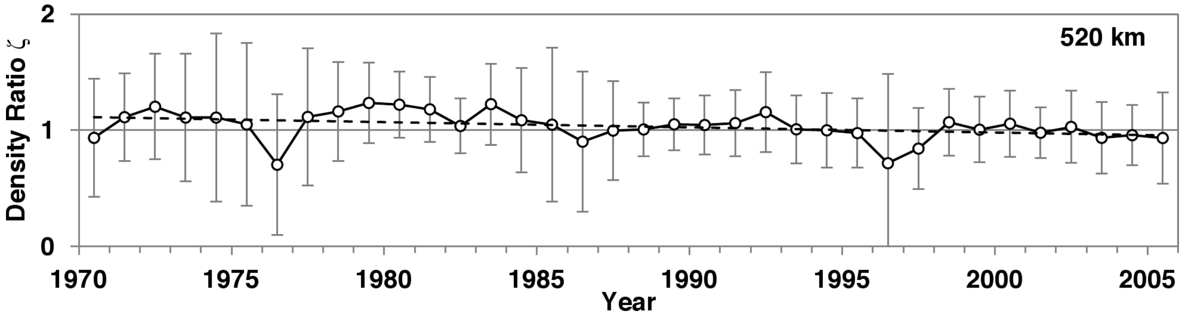
520 km
Density Ratio ζ
0
1
2
1970
1975
1980
1985
1990
1995
2000
2005
Year

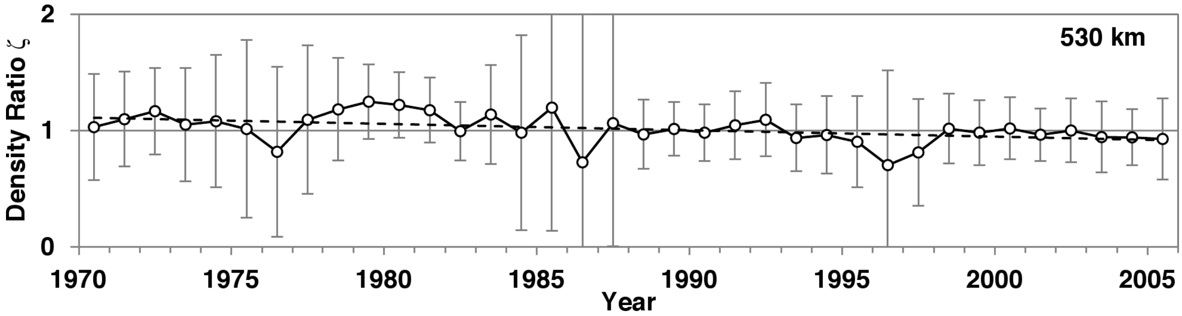
530 km
Density Ratio ζ
0
1
2
1970
1975
1980
1985
1990
1995
2000
2005
Year

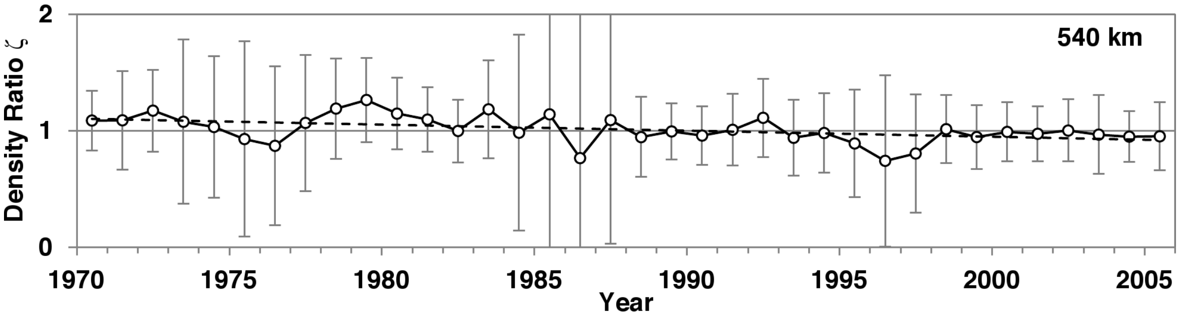
540 km
Density Ratio ζ
0
1
2
1970
1975
1980
1985
1990
1995
2000
2005
Year

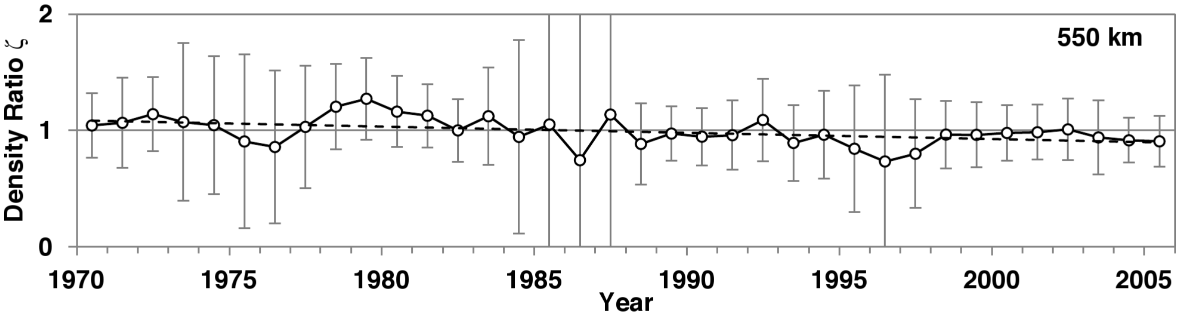
550 km
Density Ratio ζ
0
1
2
1970
1975
1980
1985
1990
1995
2000
2005
Year

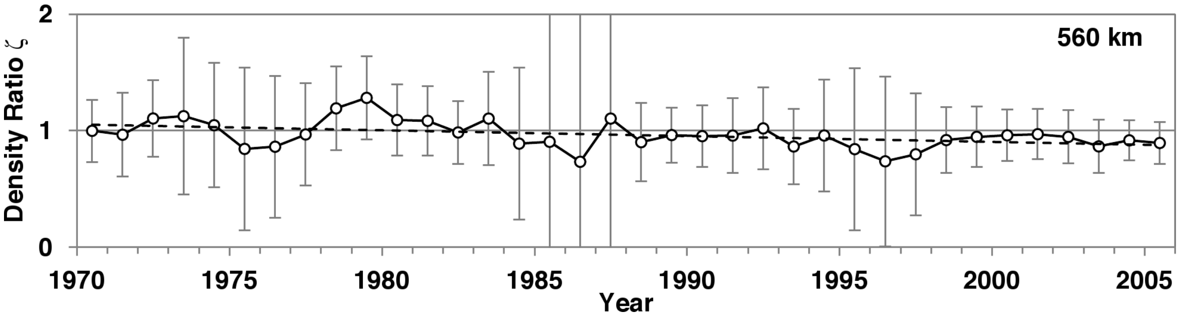
560 km
Density Ratio ζ
0
1
2
1970
1975
1980
1985
1990
1995
2000
2005
Year

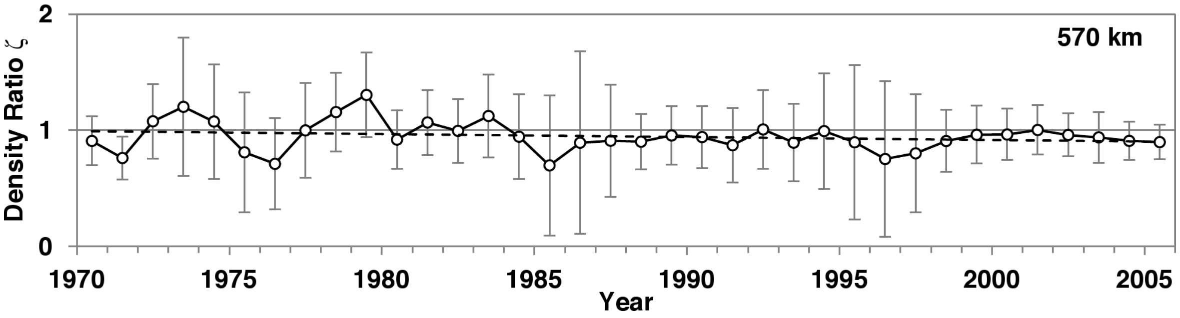
570 km
Density Ratio ζ
0
1
2
1970
1975
1980
1985
1990
1995
2000
2005
Year

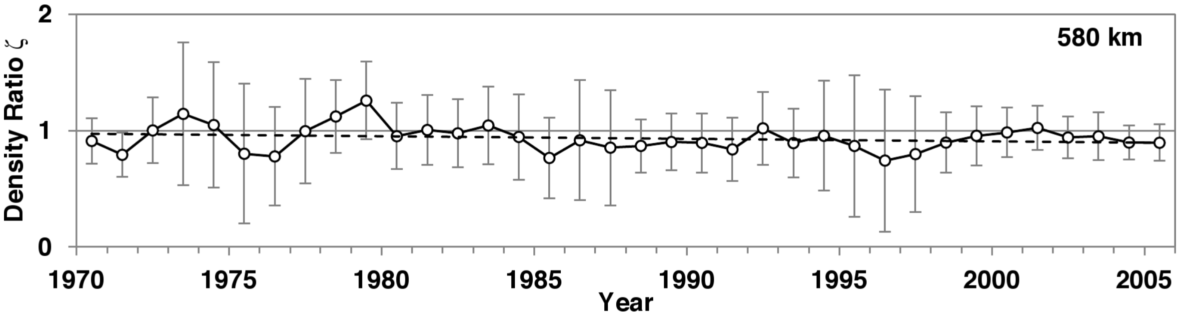
580 km
Density Ratio ζ
0
1
2
1970
1975
1980
1985
1990
1995
2000
2005
Year

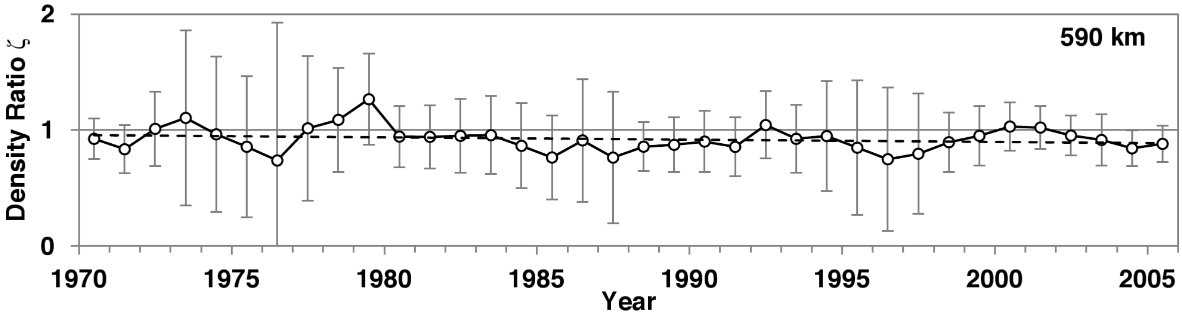

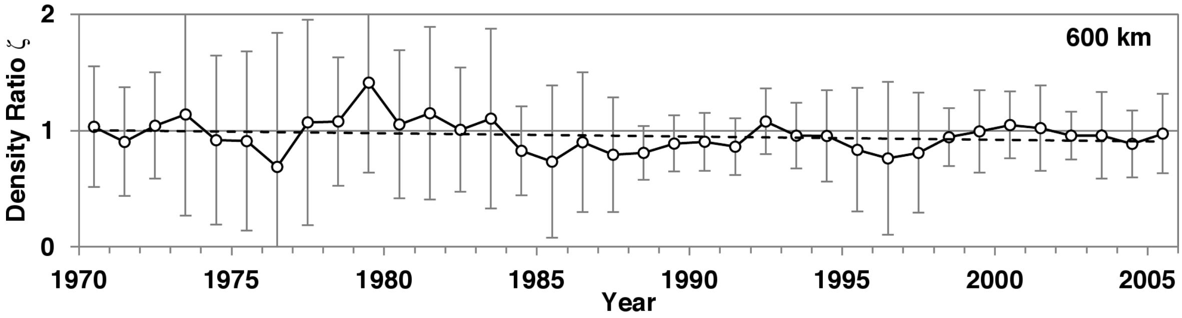

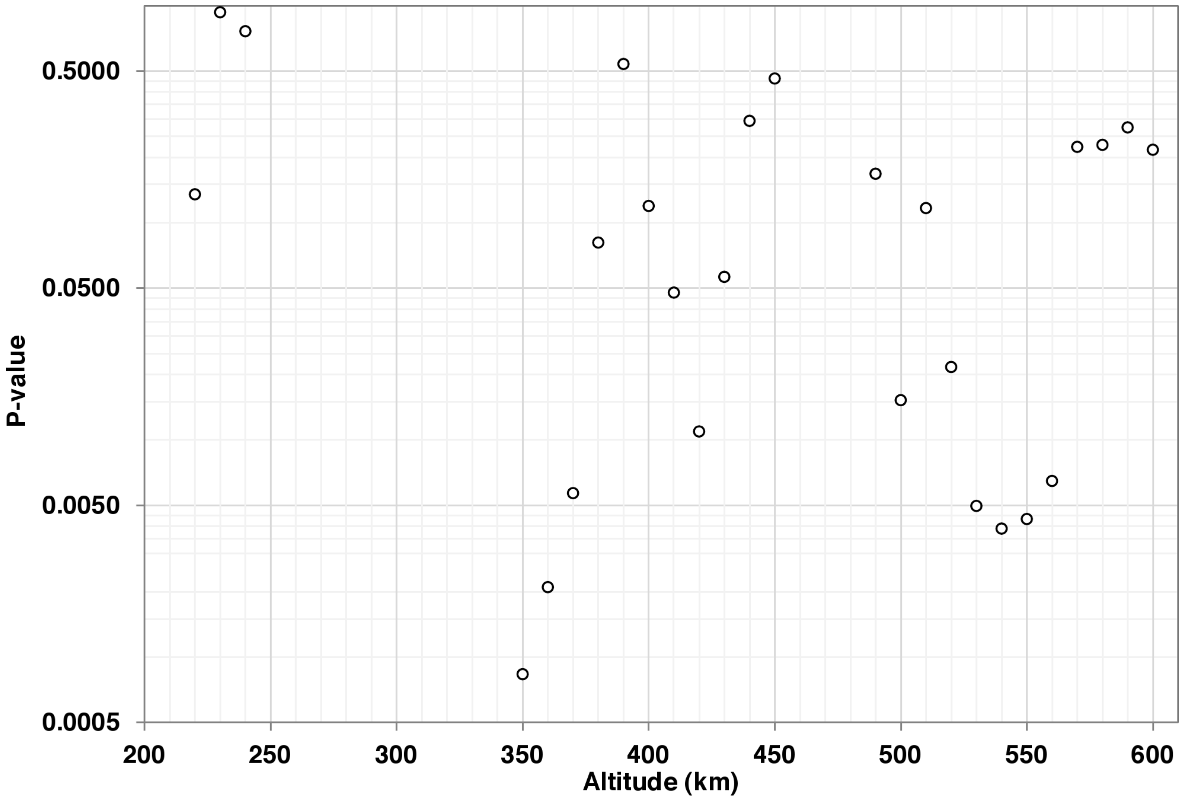

Figure 70: *The individual P-values for the linear regression analysis of the density trend altitude bins.*

## 11.2 AETHER Code

### 11.2.1 AETHER Initialisation Code

```
// AETHER Orbital Propagator
// For secular density trend determination
// Author: Arrun Saunders
// 12th April 2010

#include "functions.h"
#include <cmath>
#include <cstdio>
#include <cstdlib>
#include <windows.h>
#include <iostream>
#include <string.h>

#ifdef _WIN32
#include <io.h>
#endif

#include <conio.h>
#include "sgp4ext.h"
#include "sgp4unit.h"
#include "sgp4io.h"

// All units in kilometres //

// Earth's Characteristics (km)
#define mu 398600.4415
#define Er 6378.1363

int main()
{
    int i;
    // Time Variables and counters
    double t;

    // State Vector
    double S[6];        //The pos/vel state vector at TLE 1
    double dS[6];       //The pos/vel state vector at TLE 2
    double SME[15];     //3D pos of sun, pos/vel of moon/earth

    // Initial Orbit Parameters
    double B[2];
    double T[7];        //Temporal parameters of TLE 1
    double T2[7];       //Temporal parameters of TLE 2
    int PERT[5];        //Switches for orbital perturbations
    double fT[1];       //Individual perturbation magnitudes
    double amag;        //Acceleration magnitude

```

```
    // LAT-LONG Coordinates
    double phi;          //Geographic + Sidereal Latitude
    double geolng;       //Geographic Longitude
    double sidlng;       //Sidereal Longitude
    double greenwich_sidereal_time;

    // SGP4 variables
    double ro[3];
    double vo[3];
    char longstr1[130];
    char longstr2[130];
    elsetrec satrec;

    char bcstr[50];
    long int satreg;

    double DT;
    double day;
    double dayfrac;
    double TLE1days;
    int TLE1years;

    double am, Da_drag, a, e, V;
    double perigee, apogee, H, Z;
    double a1TLE, a2TLE;
    double Da_TLE;
    double zeta;

    // Timing Code Variables
    LARGE_INTEGER startTime;
    LARGE_INTEGER endTime;
    LARGE_INTEGER timerFrequency;
    double runTime;

    // File pointers
    char infilename[15];
    char filename[256];
    char bcfilename[15];
    FILE *infile;
    FILE *bcfile;
    FILE *fp;

    // Switching Perturbations
    PERT[0] = 1;    //Earth Gravity
    PERT[1] = 2;    //Atmospheric Drag
    PERT[2] = 1;    //Moon Gravity
    PERT[3] = 1;    //Sun Gravity
    PERT[4] = 1;    //Solar Radiation Pressure
    fT[0] = 0.0;    //Dummy initial value
    //fT[1] = 0.0;    //Dummy initial value
```

```
//----------------------//
printf("\n Input TLE filename: ");
scanf( "%s", infilename);               //-
//strcpy(infilename,"01981_10.tle");    //+
//printf(" %s\n", infilename);            //+
infile = fopen(infilename, "r");

fgets(longstr1, 130, infile);
fgets(longstr2, 130, infile);
tleread(satrec, longstr1, longstr2);
twoline2rv(satrec);
for(i=0; i<3; i++){
    ro[i] = 0.0;
    vo[i] = 0.0;
}
sgp4(satrec,  0.0, ro,  vo);
//----------------------//
// State Vector
S[0] = ro[0];    //r1 (X)
S[1] = ro[1];    //r2 (Y)
S[2] = ro[2];    //r3 (Z)
S[3] = vo[0];    //v1 (X)
S[4] = vo[1];    //v2 (Y)
S[5] = vo[2];    //v3 (Z)
//----------------------//
if(satrec.epochyr < 50)
    T[0] = satrec.epochyr + 2000;
else
    T[0] = satrec.epochyr + 1900;
TLE1years = satrec.epochyr;
TLE1days = satrec.epochdays;
day = satrec.epochdays;
dayfrac = modf(day, &T[1]);
T[2] = dayfrac*86400.0;
//----------------------//
T[3] = juliandate(T);
T[5] = T[3];
//----------------------//

strcpy(bcfilename,"BCs.txt");
bcfile = fopen(bcfilename, "r");
satreg = 99999;
while(satreg != satrec.satnum) {
    fgets(bcstr, 50, bcfile);
    sscanf(bcstr,"%5ld %15lf", &satreg, &B[0]);
}

// Initial semi-major axis from TLE 1
a1TLE = semimajor_n(satrec.no);

```

```
    // Calculating the Sun/Moon/Earth positions at start Epoch/JD
    ssb(SME, T);
    // Output file header for the thermospheric density comparison
    sprintf(filename, "AETHERst_%05d.txt", satrec.satnum);
    if((fp = fopen(filename, "a")) != NULL){
        fprintf(fp,"Ballistic Coefficient = %16.8e"
            "\n TLE1 Epoch       TLE1 JD          TLE2 JD
                 Da_TLE       Da_drag     Zeta   Perigee   Apogee
                 H    z*_Alt   Z", B[0]);
    }
    fclose(fp);
    // Start of the program timer
    QueryPerformanceFrequency(&timerFrequency);
    QueryPerformanceCounter(&startTime);
    // While loop to start working through the list of TLEs
    while (feof(infile) == 0){

        fgets(longstr1, 130, infile);
        fgets(longstr2, 130, infile);
        tleread(satrec, longstr1, longstr2);
        twoline2rv(satrec);
        for(i=0; i<3; i++){
            ro[i] = 0.0;
            vo[i] = 0.0;
        }
        sgp4(satrec, 0.0, ro, vo);
        // Calulcating the semi-major axis of TLE 2
        a2TLE = semimajor_n(satrec.no);

        //  Assigning the time variables of TLE 2 (T2)
        if(satrec.epochyr < 50)
            T2[0] = satrec.epochyr + 2000;
        else
            T2[0] = satrec.epochyr + 1900;

        day = satrec.epochdays;
        dayfrac = modf(day, &T2[1]);
        T2[2] = dayfrac*86400.0;
        T2[3] = juliandate(T2);
        T2[5] = T2[3];

        // Time Step
        T[4] = 20.0;    //seconds
        T2[4] = T[4];
        t = 0.0;

        //Integration Time between TLE epochs (seconds)
        DT = (T2[3] - T[3])*86400.0;

        T[6] = 1.0;
```

```

        Da_TLE = a2TLE - a1TLE;
        Da_drag = 0.0;

        printf("\n TLE2 Epoch \%02d\%06.2lf",
                satrec.epochyr, satrec.epochdays);

        ///////////////////////////////////////////////////////////
        ///////////////////////////////////////////////////////////
        // Orbital propagation

        while(TRUE){

            T[5] = T[3] + (t/86400.0);

            // State Vector to LAT-LONG coordinates
            phi = latitude(S);
            sidlng = longitude(S);
            greenwich_sidereal_time = gst(T);
            geolng = sidlng - greenwich_sidereal_time;
            if(geolng < 0.0)
                geolng += 360;

            // Setting the variable time step
            for(i=0; i<6; i++)
                dS[i] = S[i];    // dS: Dummy state vector
            // Send to the perturbation model satrhs()
            satrhs(dS, SME, T, B, PERT, geolng, fT);
            amag = Amagv(dS);    // amag: Magnitude of acc. vector
            // Assigning the time step
            T[4] = 0.484744320043329*(pow(amag, -0.798900546961359));

            // Seconds adjustment over midnight
            if(T[2]+T[4] < 86400.0)
                T[2] += T[4];
            else {
                T[1] += 1;
                T[2] = T[2] + T[4] - 86400.0;
            }

            if((t+T[4])<DT)
                t += T[4];
            else {
                T[6] = (DT - t)/T[4];
                t += T[6]*T[4];
                rkfh(S, SME, T, B, PERT, geolng, fT);
                T[5] = T[3] + (t/86400.0);

                // Semi-major axis calculations
                a = semimajorS(S);         //Instant. 'a' from SV
```

```
            V = Amagv(S);              //Instant. scalar of vel.
            am = ((2.0*a*a*V)/mu);     //Instant. change in 'a'
            Da_drag += am*fT[0]*T[6]*T[4];  //AETHER derived drag
            zeta = Da_TLE / Da_drag;        //Density change

            //Orbital Parameters
            e = eccentricity(S);
            perigee = (a*(1.0-e)) - Er;
            apogee = 2*a - (a*(1.0-e)) - Er;
            H = dsh(S, T, perigee);
            Z = (a*e)/H;

            if((fp = fopen(filename, "a")) != NULL) {
                fprintf(fp,"\n NUMBER FORMAT",
                    TLE1years, TLE1days, T[3], T2[3], Da_TLE,
                    Da_drag, zeta, perigee, apogee, H,
                    (perigee+0.5*H), Z);
            }
            fclose(fp);
            TLE1years = satrec.epochyr;
            TLE1days = satrec.epochdays;
            break;
        }

        if(altitude(S) < 90.0)
            break;

        //-----------------------//
        rkfh(S, SME, T, B, PERT, geolng, fT);
        sun(SME, T[5]);
        rk2(SME, T);
        //-----------------------//
        a = semimajorS(S);
        V = Amagv(S);
        am = ((2.0*a*a*V)/mu);
        Da_drag += am*fT[0]*T[4];
    }
    ////////////////////////////////////////////////////
    ////////////////////////////////////////////////////

    //Transfer of variables
    t = 0.0;
    for(i=0; i<6; i++){
        T[i] = T2[i];
    }
    for(i=0; i<3; i++){
        S[i] = ro[i];
        S[i+3] = vo[i];
    }
    for(i=0; i<6; i++){
```

```
            dS[i] = 0.0;
            T2[i] = 0.0;
        }
        ssb(SME, T);
        a1TLE = 0.0;
        a1TLE = a2TLE;
    }

    QueryPerformanceCounter(&endTime);
    runTime = double(endTime.QuadPart - startTime.QuadPart);
    runTime = runTime / (double)timerFrequency.QuadPart;
    printf("\n\n NUMBER FORMAT sec. \n", runTime);
    if((fp = fopen(filename, "a")) != NULL) {
        fprintf(fp,"\n\nRun Time\n NUMBER FORMAT secs", runTime);
    }
    fclose(fp);

    return 0;
}
```

### 11.2.2 J2000.0 to TEME Matrix Rotation

```
void convertZX(double *r, double zrad, double xrad)
{
    double convzx[3][3];
    int i;
    //    convx[row][column]
    //    [0][0]    [0][1]    [0][2]
    //    [1][0]    [1][1]    [1][2]
    //    [2][0]    [2][1]    [2][2]

    convzx[0][0] = cos(zrad);
    convzx[0][1] = -sin(zrad)*cos(xrad);
    convzx[0][2] = sin(zrad)*sin(xrad);
    convzx[1][0] = sin(zrad);
    convzx[1][1] = cos(zrad)*cos(xrad);
    convzx[1][2] = -cos(zrad)*sin(xrad);
    convzx[2][0] = 0;
    convzx[2][1] = sin(xrad);
    convzx[2][2] = cos(xrad);

    for(i=0; i<3; i++)
        r[i] = convzx[i][0]*r[0] + convzx[i][1]*r[1] + convzx[i][2]*r[2];
}

// Rotation is positive clockwise looking down the axis towards origin
// Equinox to epoch
zrad = 0.017453292519943296*(2000.0-(JD_of_Epoch)*0.013846153846153846153);
// Ecliptic to equatorial
xrad = 0.017453292519943296*23.44;
```

### 11.2.3 4th Order Runge-Kutta Technique

```
void rk(double *y, double h)
{
    int x = 15;
    int z = 0;
    double k1[15];
    double k2[15];
    double k3[15];
    double k4[15];
    double a1[15];
    double a2[15];
    double a3[15];
    double a4[15];
    int i;

    /////////////////////////////////////////
    //////////// K1 Definition //////////////
    for(i=z; i<x; i++){
        a1[i] = y[i];
    }
    smerhs(a1);
    for(i=z; i<x; i++){
        k1[i] = h*a1[i];
    }
    /////////////////////////////////////////
    //////////// K2 Definition //////////////
    for(i=z; i<x; i++){
        a2[i] = y[i]+(k1[i]/2.0);
    }
    smerhs(a2);
    for(i=z; i<x; i++){
        k2[i] = h*a2[i];
    }
    /////////////////////////////////////////
    //////////// K3 Definition //////////////
    for(i=z; i<x; i++){
        a3[i] = y[i]+(k2[i]/2.0);
    }
    smerhs(a3);
    for(i=z; i<x; i++){
        k3[i] = h*a3[i];
    }
    /////////////////////////////////////////
    //////////// K4 Definition //////////////
    for(i=z; i<x; i++){
        a4[i] = y[i]+k3[i];
    }
    smerhs(a4);
    for(i=z; i<x; i++){
```

```
        k4[i] = h*a4[i];
    }

    for(i=z; i<x; i++){
        y[i] += (1.0/6.0)*(k1[i] + (2.0*k2[i]) + (2.0*k3[i]) + k4[i]);
    }
}
```

### 11.2.4 7th Order Runge-Kutta-Fehlberg-Horn Technique

```
double aij[6][6] = {
    { 0.000000000000000,  0.00000000000000,  0.00000000000000,
      0.000000000000000,  0.000,  0.0},
    { 0.250000000000000,  0.00000000000000,  0.00000000000000,
      0.000000000000000,  0.000,  0.0},
    { 0.093750000000000,  0.28125000000000,  0.00000000000000,
      0.000000000000000,  0.000,  0.0},
    { 0.879380974055530, -3.27719617660446,  3.32089212562585,
      0.000000000000000,  0.000,  0.0},
    { 2.032407407407410, -8.00000000000000,  7.17348927875244,
     -0.205896686159844,  0.000,  0.0},
    {-0.296296296296296,  2.00000000000000, -1.38167641325536,
      0.452972709551657, -0.275,  0.0}
};

void rkfh(double *y, double *y2, double *T, double *B, int *PERT,
          double geolng, double *fT)
{
    double k[7][6];
    double x0[6];
    double x1[6];
    double x2[6];
    double x3[6];
    double x4[6];
    double x5[6];
    double x6[6];
    double sum;
    double sumv[6];
    double b[7];
    int q, r, s;

    /////////////////////////////////////////
    //////////// K0 Definition //////////////
    s = 0;
    B[1] = 1.0;
    for(q=0; q<6; q++){
        x0[q] = y[q];
    }
    satrhs(x0, y2, T, B, PERT, geolng, fT);
    for(q=0; q<6; q++){
```

```
        k[s][q] = x0[q];
    }
    B[1] = 0.0;
    /////////////////////////////////////////
    //////////// K1 Definition //////////////
    s = 1;
    for(q=0; q<6; q++){
        sum = 0.0;
        for(r=0; r<s; r++){
            sum += aij[s][r]*k[r][q];
        }
        x1[q] = y[q] + T[4]*sum;
    }
    satrhs(x1, y2, T, B, PERT, geolng, fT);
    for(q=0; q<6; q++){
        k[s][q] = x1[q];
    }
    /////////////////////////////////////////
    //////////// K2 Definition //////////////
    s = 2;
    for(q=0; q<6; q++){
        sum = 0.0;
        for(r=0; r<s; r++){
            sum += aij[s][r]*k[r][q];
        }
        x2[q] = y[q] + T[4]*sum;
    }
    satrhs(x2, y2, T, B, PERT, geolng, fT);
    for(q=0; q<6; q++){
        k[s][q] = x2[q];
    }
    /////////////////////////////////////////
    //////////// K3 Definition //////////////
    s = 3;
    for(q=0; q<6; q++){
        sum = 0.0;
        for(r=0; r<s; r++){
            sum += aij[s][r]*k[r][q];
        }
        x3[q] = y[q] + T[4]*sum;
    }
    satrhs(x3, y2, T, B, PERT, geolng, fT);
    for(q=0; q<6; q++){
        k[s][q] = x3[q];
    }
    /////////////////////////////////////////
    //////////// K4 Definition //////////////
    s = 4;
    for(q=0; q<6; q++){
        sum = 0.0;
```

```
        for(r=0; r<s; r++){
            sum += aij[s][r]*k[r][q];
        }
        x4[q] = y[q] + T[4]*sum;
    }
    satrhs(x4, y2, T, B, PERT, geolng, fT);
    for(q=0; q<6; q++){
        k[s][q] = x4[q];
    }
    /////////////////////////////////////////
    //////////// K5 Definition //////////////
    s = 5;
    for(q=0; q<6; q++){
        sum = 0.0;
        for(r=0; r<s; r++){
            sum += aij[s][r]*k[r][q];
        }
        x5[q] = y[q] + T[4]*sum;
    }
    satrhs(x5, y2, T, B, PERT, geolng, fT);
    for(q=0; q<6; q++){
        k[s][q] = x5[q];
    }
    /////////////////////////////////////////
    //////////// K6 Definition //////////////
    s = 6;
    for(q=0; q<6; q++){
        sum = 0.0;
        x6[q] = y[q] + T[4]*(0.16666666666666666667*k[0][q]
                            +0.16666666666666666667*k[4][q]
                            +0.66666666666666666667*k[5][q]);
    }
    satrhs(x6, y2, T, B, PERT, geolng, fT);
    for(q=0; q<6; q++){
        k[s][q] = x6[q];
    }
    /////////////////////////////////////////
    //////////// B*'s Definition ////////////
    b[0] = 1 - T[6]*(2.50833333333333 + T[6]*(-2.49074074074074
                                              +T[6]*0.8638888889));
    b[1] = 0.0;
    b[2] = T[6]*(5.03017543859649 + T[6]*(-7.98440545808967
                                          +T[6]*3.47321637426901));
    b[3] = T[6]*(-3.41638755980861 + T[6]*(8.85730108098529
                                          -T[6]*4.93478203083466));
    b[4] = T[6]*(1.14 + T[6]*(-3 + T[6]*1.68));
    b[5] = T[6]*(-1.74545454545455 + T[6]*(3.63636363636364
                                          -T[6]*1.85454545454545));
    b[6] = T[6]*(1.5 + T[6]*(-4.0 + T[6]*2.5));

```

```
    for(q=0; q<6; q++){
        sumv[q] = 0.0;
        for(r=0; r<7; r++){
            sumv[q] += b[r]*k[r][q];
        }
        y[q] += T[6]*T[4]*sumv[q];
    }
}
```

### 11.2.5 Satellite Acceleration Calculations

```
// All units in kilometres

// Earth's GM (km)
#define mu 398600.4415
#define Er 6378.1363

/////////////////////////////////////////////////////////////
// Indices for the JGM-3 geopotential model up to order 20 //
int cnm[4][4] = {
                {0,0,0,0},
                {0,0,0,0},
                {-484165368, -187, 2439261, 0},
                {957171, 2030137, 904706, 721145}
};              // ...and continued up to n=20

int snm[4][4] = {
                {0,0,0,0},
                {0,0,0,0},
                {0, 1195, -1400266, 0},
                {0, 248131, -618923, 1414204}
};              // ...and continued up to n=20

////////////////////////
// Factorial Function //
double factorial(double x)
{
    double y;

    if(x==0)
        x=1;
    else{
        for(y=(x-1); y>0; y-=1){
            x = x*y;}}
    return x;
}

//////////////////////////
// Normalising Function //
```

```
double normalise (int n, int m)
{
    double norm;
    double z, fp, fn;
    int dm;

    if(m==0)
        dm=1;
    else
        dm=0;

    fp = factorial(double(n+m));
    fn = factorial(double(n-m));
    z = (double((2-dm)*(2*n+1)*(fn)))/double(fp);

    norm = sqrt(z);

    return norm;
}

//////////////////////////////
// Geopotential using JGM-3 //
void satrhs(double *z, double *sme, double *T, double *B, int *PERT,
            double geolng, double *fT)
{
    // Variables for Aerodrag
    double x[6];
    double aerodrag[3];
    double rscalar;
    double vscalar;
    double vvector[3];
    double rho;
    double M, Sc, Ar, V[3], v;
    double W[3];
    double pi = 3.14159265358979323;

    double output[11];
    double input[7];
      double flags[24];
    double ap[7];
    int i;
    int day = int(T[1]);

    // Variables for Sun/Moon gravity perturbations
    // Directional Vectors from bodies to satellite
    double sssb[3], mssb[3], essb[3];
    double esc[3], emc[3];
    double r[3];
    double G = 6.6725985e-20;
    double sun = 1.98891691172466e+30;
```

```
double moon = 7.34766310628125e+22;
double emcc, escc, rc;
double e_r[3], e_m[3], e_s[3];
double moonacc[3];
double sunacc[3];
double zrot, xrot;    // Axes rotations in radians

///////////////////////////////////
// Variables for the geopotential //
int n, m;
double phi, lambda;
double dudrnm, dudphinm, dudlambdanm;
double dudrsum, dudphisum, dudlambdasum;
double dudr, dudphi, dudlambda;
double Gamma;
double pnmp1;    // For the case of P_n,m+1 where m>n.
double s, c;
double e = 1e-12;
double p[4][4];
double geoidacc[3];

//////////////////////////
// Variables for the SRP //
double nu, AtoM;
double Cr = 1.25;         //typical reflectivity of satellite
double AU = 1.49597870691e8;
double srp_P = 4.56e-3;    // N/km2 Where N = kgkm/s2
double srp_a, srp_b, srp_c;
double srp_x, srp_y;
double ssc[3];        //satellite -> sun vector
double rs;
double A;
double srpacc[3];

/////////////////////////////////////////
// Calculating Sun/Moon/Earth/Sat vectors
for(i=0; i<3; i++){
    // Sun
    sssb[i] = sme[i];
    // Moon
    mssb[i] = sme[i+3];
    // Earth
    essb[i] = sme[i+9];
    // Satellite
    r[i] = z[i];
    vvector[i] = z[i+3];
}

// Directional Vectors
dirvec(emc, mssb, essb);    // Moon pos, origin at Earth
```

```
    dirvec(esc, sssb, essb);    // Sun pos, origin at Earth
    dirvec(ssc, esc, r);        // Sun pos, origin at satellite

    // Need to rotate the sun and moon vector
    // Rotation is +ve clockwise looking down the axis towards origin
    // Equinox to epoch
    zrot = 0.017453292519943296*((2000.0-(T[0]
        + (T[1]/365.25)))*0.013846153846153846153);
    // Ecliptic to equatorial
    xrot = 0.017453292519943296*23.43929111;
    convertZX(emc, zrot, xrot);
    convertZX(esc, zrot, xrot);

    // Magnitude
    emcc = Amag(emc);
    escc = Amag(esc);
    rc = Amag(r);

    // Unit Vectors
    for(i=0; i<3; i++){
        e_r[i] = r[i]/rc;
        e_m[i] = emc[i]/emcc;
        e_s[i] = esc[i]/escc;
    }
    if(PERT[2]==1){
        moonacc[0] = (((G*moon*rc)/(pow(emcc, 3)))*
                     (-e_r[0]+3*e_m[0]*e_m[0]*e_r[0]));
        moonacc[1] = (((G*moon*rc)/(pow(emcc, 3)))*
                     (-e_r[1]+3*e_m[1]*e_m[1]*e_r[1]));
        moonacc[2] = (((G*moon*rc)/(pow(emcc, 3)))*
                     (-e_r[2]+3*e_m[2]*e_m[2]*e_r[2]));
    }
    else{
        moonacc[0] = 0.0;
        moonacc[1] = 0.0;
        moonacc[2] = 0.0;
    }
    if(PERT[3]==1){
        sunacc[0] = (((G*sun*rc)/(pow(escc, 3)))*
                    (-e_r[0]+3*e_s[0]*e_s[0]*e_r[0]));
        sunacc[1] = (((G*sun*rc)/(pow(escc, 3)))*
                    (-e_r[1]+3*e_s[1]*e_s[1]*e_r[1]));
        sunacc[2] = (((G*sun*rc)/(pow(escc, 3)))*
                    (-e_r[2]+3*e_s[2]*e_s[2]*e_r[2]));
    }
    else{
        sunacc[0] = 0.0;
        sunacc[1] = 0.0;
        sunacc[2] = 0.0;
    }
```

```

// Turning the atmospheric effects on/off
  for (i=0;i<24;i++)
      flags[i]=1;
flags[9]=-1;

x[0]=z[0];    //r1 (X)
x[1]=z[1];    //r2 (Y)
x[2]=z[2];    //r3 (Z)
x[3]=z[3];    //v1 (X)
x[4]=z[4];    //v2 (Y)
x[5]=z[5];    //v3 (Z)

//printf("\n \%9.4lf \%9.4lf \%9.4lf \%9.4lf \%9.4lf \%9.4lf",
                    x[0], x[1], x[2], x[3], x[4], x[5]);

rscalar = Amag(z);
vscalar = Amagv(z);

// Input values
input[0]= T[2];                   //sec
input[1]= altitude(z);            //alt
input[2]= latitude(z);            //g_lat
input[3]= geolng;                 //g_long
phi = input[2]*(1.74533e-2);      //geo lat
lambda = input[3]*(1.74533e-2);   //geo long
input[4]= lst(input);             //local solar time (lst)
input[5]= f107a(T);               //f107A
input[6]= f107d(T);               //f107
geomag(ap, T);                    //ap

if(PERT[1]==1 || PERT[1]==2){
    // Geomagnetic Indices
    //geomag(ap, T);            //ap

    // Thermospheric Neutral Density
    //printf("\n %9.4lf %9.4lf", rscalar, vscalar);
    gtd7d(input, day, ap, flags, output);
    rho = output[5]*1e12; //kg/km3
    B[1] = rho;

    if(PERT[1]==2){
        // Atmospheric Rotation
        M = 1/(sqrt(x[0]*x[0] + x[1]*x[1]));
        Sc = 2.0*pi*rscalar*cos(phi);
        // Local Atmospheric rotation km/s
        Ar = Sc*1.1605775033656747597e-5;

        W[0] = -x[1]*M*Ar;  // x-component of atmospheric rotation
        W[1] =  x[0]*M*Ar;  // y-component
```

```
            W[2] = 0.0;         // z-component
        }
        else{
            for(i=0; i<3; i++)
                W[i] = 0.0;
        }

        for(i=0; i<3; i++)
            V[i] = x[i+3] - W[i];
        v = Amag(V);

        aerodrag[0] = -0.5*rho*v*B[0]*V[0];
        aerodrag[1] = -0.5*rho*v*B[0]*V[1];
        aerodrag[2] = -0.5*rho*v*B[0]*V[2];
    }
    else{
        aerodrag[0] = 0.0;
        aerodrag[1] = 0.0;
        aerodrag[2] = 0.0;
    }

    if(PERT[4]==1){
        // SRP assuming e=0.2 and CD=2.2
        AtoM = B[0]/2.2;
        rs = Amag(ssc);
        srp_a = asin(6.96e5/rs);
        srp_b = asin(Er/rc);
        srp_c = acos(-(Adot(r, ssc))/(rc*rs));

        if(srp_c >= (srp_a + srp_b))
            nu = 1.0;        //satellite in sunlight
        else{
            if(fabs(srp_a - srp_b) >= srp_c)
                nu = 0.0;    //satellite in umbra
            else{
                srp_x = (srp_c*srp_c + srp_a*srp_a
                       - srp_b*srp_b)/(2*srp_c);
                srp_y = sqrt(srp_a*srp_a - srp_x*srp_x);
                A = srp_a*srp_a*acos(srp_x/srp_a)
                  + srp_b*srp_b*acos((srp_c - srp_x)/srp_b)
                  - srp_c*srp_y;
                //satellite in penumbra
                nu = 1 - (A/(pi*srp_a*srp_a));
            }
        }

        srpacc[0] = -nu*srp_P*Cr*AtoM*ssc[0]*AU*AU/(pow(rs, 3.0));
        srpacc[1] = -nu*srp_P*Cr*AtoM*ssc[1]*AU*AU/(pow(rs, 3.0));
        srpacc[2] = -nu*srp_P*Cr*AtoM*ssc[2]*AU*AU/(pow(rs, 3.0));
    }
```

```
    else{
        srpacc[0] = 0.0;
        srpacc[1] = 0.0;
        srpacc[2] = 0.0;
    }

///////////////////////////////////////////////////////////////////////
///////////////////////////////////////////////////////////////////////
/////////////////////////////// JGM3 /////////////////////////////////

    if(PERT[0]==1){
        s = sin(phi);
        c = cos(phi);

        dudrsum = 1.0;
        dudphisum = 0.0;
        dudlambdasum = 0.0;

        ///////////////////////////////////////////////
        // The Legendre Polynomials p[n][m]sin(phi) //
        for(i=0; i<4; i++) {
            p[0][i] = 0.0;
            p[1][i] = 0.0;
        }
        p[2][0] = 0.5*(3*s*s-1);
        p[2][1] = 3*c*s;
        p[2][2] = 3*c*c;
        p[2][3] = 0.0;

        p[3][0] = 0.33333333333333333333*(5*s*p[2][0]-2*s);
        p[3][1] = c+5*c*p[2][0];
        p[3][2] = 5*c*p[2][1];
        p[3][3] = 5*c*p[2][2];      // ...and continued up to n=20

        for(n=2; n<=20; n++)
        {
            for(m=0; m<=n; m++)
            {
                Gamma = normalise(n, m);

                //////////
                // DuDr //
                dudrnm = (pow((Er/rscalar), n))*(1+n)*p[n][m]*Gamma*
                         ((cnm[n][m]*e*cos(m*lambda))
                       + (snm[n][m]*e*sin(m*lambda)));
                dudrsum = dudrsum + dudrnm;

                ////////////
                // DuDphi //
                if((m+1) > n)
```

```
                    pnmp1 = 0.0;
                else
                    pnmp1 = p[n][m+1]*Gamma;
                dudphinm = (pow((Er/rscalar), n))*(pnmp1 - m*tan(phi)*
                            p[n][m]*Gamma)*((cnm[n][m]*e*cos(m*lambda))
                         + (snm[n][m]*e*sin(m*lambda)));
                dudphisum = dudphisum + dudphinm;

                ///////////////
                // DuDlambda //
                dudlambdanm = (pow((Er/rscalar), n))*m*p[n][m]*Gamma*
                              ((snm[n][m]*e*cos(m*lambda))
                            - (cnm[n][m]*e*sin(m*lambda)));
                dudlambdasum = dudlambdasum + dudlambdanm;
            }
        }

        dudr = -(mu/(rscalar*rscalar))*dudrsum;
        dudphi = (mu/rscalar)*dudphisum;
        dudlambda = (mu/rscalar)*dudlambdasum;


        geoidacc[0] = ((dudr/rscalar)
     - (x[2]/(rscalar*rscalar*sqrt(x[0]*x[0]+x[1]*x[1])))*dudphi)*x[0]
     - (dudlambda/(x[0]*x[0]+x[1]*x[1]))*x[1];
        geoidacc[1] = ((dudr/rscalar)
     - (x[2]/(rscalar*rscalar*sqrt(x[0]*x[0]+x[1]*x[1])))*dudphi)*x[1]
     + (dudlambda/(x[0]*x[0]+x[1]*x[1]))*x[0];
        geoidacc[2] = (dudr/rscalar)*x[2]
     + ((sqrt(x[0]*x[0]+x[1]*x[1]))/(rscalar*rscalar))*dudphi;
    }
    else{
        geoidacc[0] = -(mu*x[0])/(pow(rscalar, 3.0));
        geoidacc[1] = -(mu*x[1])/(pow(rscalar, 3.0));
        geoidacc[2] = -(mu*x[2])/(pow(rscalar, 3.0));
    }

//////////////////////////////////////////////////////////////////////
//////////////////////////////////////////////////////////////////////

    z[0] = x[3];
    z[1] = x[4];
    z[2] = x[5];
    z[3] = geoidacc[0] + aerodrag[0] + moonacc[0]
         + sunacc[0] + srpacc[0];
    z[4] = geoidacc[1] + aerodrag[1] + moonacc[1]
         + sunacc[1] + srpacc[1];
    z[5] = geoidacc[2] + aerodrag[2] + moonacc[2]
         + sunacc[2] + srpacc[2];

```

```
    // The velocity tangential acceleration of atmospheric drag
    if(B[1]>0.0){
        //Contribution of atmospheric drag
        fT[0] = (Adot(aerodrag, vvector))/vscalar;
    }
}
```

### 11.2.6 $F_{10.7}$ Solar Flux Calculations

```
int f107[19416] = {
2517, 2508, 2590, 2618, 2663, 2417, 2268, 2130, 1976, 1966,
1985, 1884, 1802, 1743, 1679, 1770, 1852, 1962, 2127, 2035,
2058, 2122, 2295, 2113, 2195, 2158, 1886, 1795, 1713, 1603,
1793, 1656, 1683, 1647, .... };

double f107a(double *T)
{
    double JDinteg, JDfrac;
    int JDint, JDdoy;
    int JDstart = 2435841; // Midday on 02/01/1957
    int i;
    int favg=0;
    double f107a;

    JDfrac = modf(T[5], &JDinteg);
    if(JDfrac >= 0.5)
        JDinteg = JDinteg + 1;
    else
        JDinteg = JDinteg;

    JDint = int(JDinteg);
    JDdoy = JDint - JDstart;

    for(i=-40; i<41; i++){
        favg += f107[JDdoy+i];
    }
    f107a = double(favg)/810.0;

    return f107a;
}

double f107d(double *T)
{
    double JDinteg, JDfrac;
    int JD1, JD2;
    double f107_1, f107_2;
    int JDstart = 2435841; // Midday on 02/01/1957
    double f107s;

```

```
    JDfrac = modf(T[5], &JDinteg);

    JD1 = int(JDinteg) - JDstart - 1;
    JD2 = int(JDinteg) - JDstart;

    f107_1 = double(f107[JD1])/10.0;
    f107_2 = double(f107[JD2])/10.0;

    f107s = f107_1 + (JDfrac*(f107_2 - f107_1));

    return f107s;
}
```

### 11.2.7 $a_p$ Solar Flux Calculations

```
int ap[155328] = {
 9,  6,  9, 48, 12,  9, 56, 48,
22, 12,  9, 15,  9,  5,  5,  6,
 5,  6,  7,  7,  3,  4,  3,  4,
 4,  4,  4, ...     };

void geomag(double *api, double *T)
{
    double JDc;
    double JDstart = 2435840.6250;
    double JDspec, JDint, rem;
    double x, y, z;
    int zi;

    JDc = T[5] - JDstart;
    rem = fmod(JDc, 0.125);
    JDc -= rem;
    JDspec = modf(JDc, &JDint);

    x = JDspec/0.125;
    y = JDint*8.0;
    z = x + y;
    zi = int(z);

    api[0] = (ap[zi] + ap[zi-1] + ap[zi-2] + ap[zi-3] + ap[zi-4]
            + ap[zi-5] + ap[zi-6] + ap[zi-7] + (rem*(ap[zi+1]
            - ap[zi-7])))/8.0;
    api[1] = ap[zi] + (rem*(ap[zi+1] - ap[zi]));      // Current Time
    api[2] = ap[zi-1] + (rem*(ap[zi] - ap[zi-1]));    // 3hrs before CT
    api[3] = ap[zi-2] + (rem*(ap[zi-1] - ap[zi-2]));  // 6hrs before CT
    api[4] = ap[zi-3] + (rem*(ap[zi-2] - ap[zi-3]));  // 9hrs before CT
    // Ave of 12hrs (4) to 33hrs (11) before CT
    api[5] = (ap[zi-4] + ap[zi-5] + ap[zi-6] + ap[zi-7] + ap[zi-8]
            + ap[zi-9] + ap[zi-10] + ap[zi-11] + (rem*(ap[zi-3]
```

```
            - ap[zi-11])))/8.0;
    // Ave of 36hrs (4) to 57hrs (11) before CT
    api[6] = (ap[zi-12] + ap[zi-13] + ap[zi-14] + ap[zi-15] + ap[zi-16]
            + ap[zi-17] + ap[zi-18] + ap[zi-19] + (rem*(ap[zi-11]
            - ap[zi-19])))/8.0;
}
```

### 11.2.8 Luni-Solar Ephemerides Calculations

```
// Solar System Propagator with only Sun/Moon/Earth
// Start date of ephemeris data = JD 2435850.0
// End date of ephemeris data = JD 2455200.0

// Ephemeris Data SUN/MOON/EARTH
// SRX, SRY, SRZ,
// MRX, MRY, MRZ, MVX, MVY, MVZ,
// ERX, ERY, ERZ, EVX, EVY, EVZ.
// SSB10_SME.xlsx
double sme[29040] = {
    1.20324454753788E+06,    3.15361499142559E+05,    ...,    ...,
    1.20273440850611E+06,    3.26902213748453E+05,    ...,    ...,
    1.20205915258952E+06,    3.38442470389027E+05,    ...,    ...,
    1.20122351392318E+06,    .................... };

void sun(double *sunvec, double JD)
{
    int i;
    double JD10, fracJD, intJD;
    int JDstart10 = 243585; // (JD: 11/01/1957 12:00)*0.1
    int JD1, JD2;

    JD10 = JD*0.1;
    fracJD = modf(JD10, &intJD);

    JD1 = int(intJD) - JDstart10;
    JD2 = JD1 + 1;

    for(i=0; i<3; i++){
        sunvec[i] = sme[JD1*15+i]
                   + fracJD*(sme[JD2*15+i]
                   - sme[JD1*15+i]);
    }

}

void ssb(double *vr, double *T)
{
    int i, JDtar, reverse;
    double fracJDtar, JDint;
```

```
int JDstart = 2435850; // 11/01/1957 12:00
double JDd10;
double intTime, steps, intsteps, fracsteps, endstep;
double dt = 30.0;
double JDsun;

JDtar = 0;

//////////////////////////////////////////////////
// Calculating which side of 10 days is closer. //
JDd10 = T[5]*0.1;
fracJDtar = modf(JDd10, &JDint);
JDtar = int(JDint) - 243585;
// Which side to propagate from.
if(fracJDtar > 0.5){
    JDtar++;
    reverse = 1;}
else
    reverse = 0;

// Retrieving ephemeris data for target JD
for(i=0; i<15; i++)
    vr[i] = sme[JDtar*15+i];

if(reverse==1){
    for(i=0; i<3; i++){
        // Reversing the velocity vectors of M&E
        vr[i+6] = -vr[i+6];
        vr[i+12] = -vr[i+12];
    }
    // Calculating the time steps to reach JD
    intTime = (1.0-fracJDtar)*864000;
}
else{
    // Calculating the time steps to reach JD
    intTime = fracJDtar*864000;
}

steps = intTime*0.033333333333333333333;
            // Number of 30 second steps
fracsteps = modf(steps, &intsteps);
endstep = fmod(intTime, 30);

//////////////////////////////
// Assigning the ephemerides
for(i=0; i<intsteps; i++){
    rk(vr, dt);
        // Calculating the Sun's step ephemeris
    if(reverse==1)
        JDsun = JDint*10 - (i*dt)/86400;
```

```
        else
            JDsun = JDint*10 + (i*dt)/86400;
        sun(vr, JDsun);
    }
    rk(vr, endstep);
    JDsun = T[5];
    sun(vr, JDsun);

    //////////////////////////////
    // If propagation is reversed
    if(reverse == 1){
        for(i=0; i<3; i++){
            vr[i+6] = -vr[i+6];
            vr[i+12] = -vr[i+12];
        }
    }
}
```

### 11.2.9 Luni-Solar Accelerations

```
void smerhs(double *z)
{
    int i;
    double gamma = 6.6725985e-20;        \\ Universal Grav.
    double sun = 1.98891691172466e+30;   \\ Sun's mass
    double moon = 7.34766310628125e+22;  \\ Moon's mass
    double earth = 5.97369125232005e+24; \\ Earth's mass
    double smc, mec, esc;
    double er[3], ev[3], mr[3], mv[3], sr[3];
    double sm[3], me[3], es[3];

    for(i=0; i<3; i++){
        // Sun
        sr[i] = z[i];
        // Moon
        mr[i] = z[i+3];
        mv[i] = z[i+6];
        // Earth
        er[i] = z[i+9];
        ev[i] = z[i+12];
    }

    // Directional Vectors
    dirvec(sm, mr, sr);
    dirvec(me, er, mr);
    dirvec(es, sr, er);

    smc = Amag(sm);
    mec = Amag(me);
```

```
    esc = Amag(es);

    for(i=0; i<3; i++){
        // No computed accelerations Perturbing the SUN

        // Accelerations Perturbing the MOON
        z[i+6] = (((gamma*earth)/(pow(mec, 3)))*me[i])
                -(((gamma*sun)/(pow(smc, 3)))*sm[i]);
        z[i+3] = mv[i];
        // Accelerations Perturbing the EARTH
        z[i+12] = (((gamma*sun)/(pow(esc, 3)))*es[i])
                 -(((gamma*moon)/(pow(mec, 3)))*me[i]);
        z[i+9] = ev[i];
    }
}
```

### 11.3 $b_i^*$ Formulae

The required $b_i^*(\tau)$ coefficients during the RKFH numerical integration method are given by

$$b_1^*(\tau) = 1 - \tau\left(\frac{301}{120} + \tau\left(-\frac{269}{108} + \tau\frac{311}{360}\right)\right), \tag{126}$$

$$b_2^*(\sigma) = 0, \tag{127}$$

$$b_3^*(\tau) = \tau\left(\frac{7168}{1425} + \tau\left(-\frac{4096}{513} + \tau\frac{14848}{4275}\right)\right), \tag{128}$$

$$b_4^*(\tau) = \tau\left(-\frac{28561}{8360} + \tau\left(\frac{199927}{22572} - \tau\frac{371293}{75240}\right)\right), \tag{129}$$

$$b_5^*(\tau) = \tau\left(\frac{57}{50} + \tau\left(-3 + \tau\frac{42}{25}\right)\right), \tag{130}$$

$$b_6^*(\tau) = \tau\left(-\frac{96}{55} + \tau\left(\frac{40}{11} - \tau\frac{102}{55}\right)\right), \tag{131}$$

and

$$b_7^*(\tau) = \tau\left(\frac{3}{2} + \tau\left(-4 + \tau\frac{5}{2}\right)\right). \tag{132}$$

### 11.4 $a_{ij}$ Coefficients

The coefficients required in calculating the gradients in the RKFH integration method are displayed Table 11.

| $i$ | $a_{i0}$ | $a_{i1}$ | $a_{i2}$ | $a_{i3}$ | $a_{i4}$ |
|---|---|---|---|---|---|
| 0 | $0$ | | | | |
| 1 | $\frac{1}{4}$ | | | | |
| 2 | $\frac{3}{32}$ | $\frac{9}{32}$ | | | |
| 3 | $\frac{1932}{2197}$ | $-\frac{7200}{2197}$ | $\frac{7296}{2197}$ | | |
| 4 | $\frac{439}{216}$ | $-8$ | $\frac{3680}{513}$ | $-\frac{845}{4104}$ | |
| 5 | $-\frac{8}{27}$ | $2$ | $-\frac{3544}{2565}$ | $\frac{1859}{4104}$ | $-\frac{11}{40}$ |

Table 11: Coefficients required for the RKFH method.

## 11.5 Satellite Properties

Table 12: *The estimated values of ballistic coefficient for the 41 satellites used in this study, along with the variances of the estimations.*

| Satellite Number | Historical Period Covered | $\delta$ (m$^2$/kg) | $\delta$ Variance (% of $\delta$) | $h_\delta$ (km) |
|---|---|---|---|---|
| 00060 | 1970 - 2010 | 0.0275 | 43.35 | 425.21 |
| 00063 | 1970 - 2010 | 0.0184 | 20.25 | 539.37 |
| 00165 | 1970 - 2010 | 0.0683 | 27.40 | 634.26 |
| 00229 | 1970 - 2002 | 0.0667 | 22.06 | 579.05 |
| 00614 | 1970 - 2010 | 0.0146 | 23.45 | 357.60 |
| 00750 | 1970 - 2010 | 0.0865 | 14.37 | 425.67 |
| 01335 | 1970 - 2010 | 0.1051 | 35.42 | 635.81 |
| 01370 | 1970 - 2004 | 0.1499 | 26.44 | 549.20 |
| 01616 | 1970 - 2010 | 0.0237 | 23.80 | 439.00 |
| 01685 | 1970 - 2010 | 0.0455 | 24.57 | 613.88 |
| 01808 | 1970 - 2002 | 0.1611 | 25.53 | 502.03 |
| 01843 | 1970 - 2002 | 0.0127 | 18.87 | 439.41 |
| 01857 | 1970 - 2010 | 0.0696 | 26.58 | 629.56 |
| 01981 | 1970 - 2010 | 0.0376 | 30.35 | 598.63 |
| 02016 | 1970 - 2010 | 0.0350 | 28.55 | 537.61 |
| 02129 | 1970 - 2002 | 0.0490 | 22.23 | 527.17 |
| 02153 | 1970 - 2010 | 0.0359 | 34.64 | 541.71 |
| 02389 | 1970 - 2010 | 0.0189 | 28.12 | 383.08 |
| 02611 | 1970 - 2002 | 0.0264 | 22.11 | 522.18 |
| 02622 | 1970 - 2002 | 0.0264 | 30.29 | 512.09 |
| 02643 | 1970 - 2010 | 0.0251 | 25.48 | 373.37 |
| 03019 | 1970 - 2010 | 0.0506 | 17.80 | 406.15 |
| 03038 | 1970 - 2002 | 0.0098 | 53.32 | 622.91 |
| 03462 | 1970 - 2010 | 0.2163 | 24.98 | 606.98 |
| 03523 | 1970 - 2010 | 0.0256 | 24.96 | 513.64 |
| 03524 | 1970 - 2001 | 0.1889 | 19.47 | 469.86 |
| 03553 | 1970 - 2001 | 0.1284 | 25.76 | 542.75 |
| 03608 | 1970 - 2004 | 0.1633 | 33.48 | 511.12 |
| 03717 | 1970 - 2010 | 0.0899 | 26.45 | 506.23 |
| 03835 | 1970 - 2001 | 0.1248 | 40.49 | 540.97 |
| 04053 | 1970 - 2010 | 0.0167 | 17.30 | 285.99 |
| 04119 | 1970 - 2010 | 0.0063 | 34.65 | 495.01 |
| 04221 | 1970 - 2002 | 0.0155 | 29.58 | 408.50 |
| 04330 | 1970 - 2010 | 0.0225 | 21.25 | 346.11 |
| 04726 | 1970 - 2003 | 0.0282 | 18.62 | 496.87 |
| 04849 | 1970 - 2001 | 0.1527 | 24.09 | 524.03 |
| 04940 | 1971 - 2005 | 0.0141 | 22.18 | 512.76 |
| 05977 | 1970 - 2001 | 0.1588 | 24.10 | 326.06 |
| 05998 | 1970 - 2010 | 0.0345 | 19.30 | 278.00 |
| 06073 | 1970 - 1999 | 0.0347 | 28.56 | 237.75 |
| 14756 | 1972 - 2010 | 0.0035 | 27.15 | 278.67 |